THE UNIVERSITY OF
WARWICK

AUTHOR: **Jennifer Wooldridge** DEGREE: **Ph.D.**

TITLE: **Superconductivity and Magnetism in Sodium Cobaltate Oxyhydrate**

DATE OF DEPOSIT: .....

I agree that this thesis shall be available in accordance with the regulations governing the University of Warwick theses.

I agree that the summary of this thesis may be submitted for publication.

I **agree** that the thesis may be photocopied (single copies for study purposes only).

Theses with no restriction on photocopying will also be made available to the British Library for microfilming. The British Library may supply copies to individuals or libraries. subject to a statement from them that the copy is supplied for non-publishing purposes. All copies supplied by the British Library will carry the following statement:

> "Attention is drawn to the fact that the copyright of this thesis rests with its author. This copy of the thesis has been supplied on the condition that anyone who consults it is understood to recognise that its copyright rests with its author and that no quotation from the thesis and no information derived from it may be published without the author's written consent."

AUTHOR'S SIGNATURE: .....

USER'S DECLARATION

1. I undertake not to quote or make use of any information from this thesis without making acknowledgement to the author.
2. I further undertake to allow no-one else to use this thesis while it is in my care.

DATE SIGNATURE ADDRESS

.....

.....

.....

.....

.....

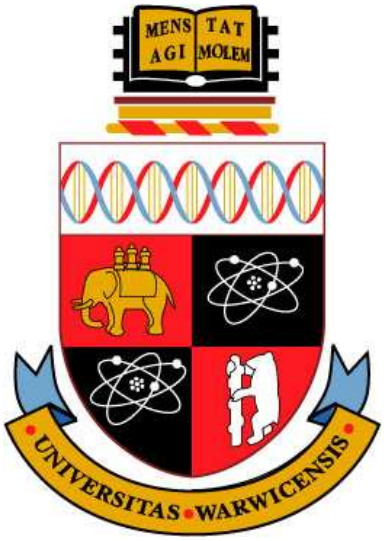

Superconductivity and Magnetism in Sodium Cobaltate Oxyhydrate

by

Jennifer Wooldridge

Thesis

Submitted to the University of Warwick

for the degree of

Doctor of Philosophy

Department of Physics

November 2006

THE UNIVERSITY OF WARWICK

Contents

List of Figures

List of Tables

Acknowledgments

I'd like to thank the following people, who have made positive contributions to this thesis, and my Ph.D. experience in general, over the past three years. First and foremost I'd like to thank my supervisor Martin Lees, for his support, guidance and patience with all things laboratory based, for insightful discussions on anything to do with magnetism or superconductivity and for having a great sense of humour especially whilst on experiment (when one is needed). I am indebted to the help with sample preparation given by Geetha Balakrishnan, for being able to see things in the crystal flux that no one else can... I am grateful to Oleg Petrenko for his helpfulness in answering all my neutron scattering queries and being prepared to give up his time to assist on doomed experiments at PSI. I'd also like to thank Don Paul for his contribution to the work presented in chapter 6, especially during the production of the associated paper. Many thanks to Tom Orton for his help around the lab. The final thanks at Warwick go to my mezzanine mates Sonya Crowe, Nic Wilson, Andy Crichton and more recently Dan O'Flynn, for being a pleasant distraction to the incessant noise from the lab!

The neutron scattering experience was made less painful by the helpfulness of a number of local contacts. I am particularly thankful to Philippe Bourges at LLB, Chris Frost at ISIS, Denis Sheptyakov at PSI and Garry McIntyre at the ILL, without whom the work presented in this thesis would not have been possible. Jim Hague was a great help in providing a user friendly introduction to linear spin wave theory. I'm also grateful to Jon Duffy and Stephen Dugdale for the brief introduction to the world of Compton scattering, and for the opportunity to travel to SPring-8.

$\Theta\alpha\ \acute{\eta}\theta\epsilon\lambda\alpha\ \nu\alpha\ \epsilon\upsilon\chi\alpha\rho\iota\sigma\tau\acute{\eta}\sigma\omega\ \tau\sigma\nu\ M\acute{\alpha}\rho\iota\sigma\ \gamma\iota\alpha\ \tau\eta\nu\ \alpha\gamma\acute{\alpha}\pi\eta\ \kappa\alpha\iota\ \upsilon\pi\sigma\sigma\tau\acute{\eta}\rho\iota\xi\eta\ \tau\sigma\upsilon$, $\kappa\alpha\iota\ \epsilon\pi\iota\pi\lambda\acute{\epsilon}\sigma\nu\ \gamma\iota\alpha\ \tau\sigma\ \tau\zeta\alpha\tau\zeta\acute{\iota}\kappa\iota\ \tau\sigma\upsilon$. Finally, I'd like to thank my family for their continuous support and encouragement throughout my time at university.

Declarations

The material presented in this thesis consists of introductory information in chapters 1-3 that does not represent my own research, followed by four chapters of experimental work carried out during the period Sept. 2003 to Sept. 2006. All of the work presented constitutes new and original scientific research on samples produced by myself, under the guidance of Dr. Geetha Balakrishnan. The material presented in chapter 4 and sections 5.1, 7.1 and 7.2 represents work carried out at the University of Warwick under the supervision of Dr. Martin Lees. The remainder of research comprises work completed at neutron scattering facilities (the Paul Scherrer Institut (Switzerland), ISIS (UK), the Laboratoire Léon Brillouin (France) and the Institut Laue Langevin (France)) where, in collaboration with a local instrument scientist, I was either the sole experimentalist or the leading member of an experimental team. Finally, the information presented in section 2.3 was completed as part of an experimental team at the SPring-8 synchrotron (Japan). The results were analysed by a group at the University of Bristol and do not represent my own work, and so have been presented as additional introductory material. No part of the work detailed in chapters 4-7 has been submitted for examination at any other institute.

Some of the research outlined in chapter 4 and section 5.1 has been published as:

- J. Wooldridge, D. McK. Paul, G. Balakrishnan and M. R. Lees. Investigation of the spin density wave in Na_xCoO_2. *J. Phys.: Condens. Matter*, 17:707, 2005.

- J. Wooldridge, D. McK. Paul, G. Balakrishnan and M. R. Lees. The magnetic field and pressure dependence of the magnetic ordering transition in Na_xCoO_2 (0.6<x<0.72). *J. Phys.: Condens. Matter*, 18:4731, 2006.

A paper detailing the research discussed in chapter 5 is currently under construction. Additionally, the work presented in chapter 6 has been submitted to Physical Review B and is currently available in pre-print format:

- J. Wooldridge, G. Balakrishnan, D. McK. Paul, C. Frost, P. Bourges and M. R. Lees. Intraplanar Magnetic Excitations in $Na_{0.5}CoO_2$: An Inelastic Neutron Study. cond-mat/0608196, 2006.

The work described in this thesis has also been presented in posters at the following four conferences:

- J. Wooldridge, M. R. Lees, G. Balakrishnan and D. McK. Paul. Magnetic Susceptibility & Heat Capacity Measurements of Single Crystal $Na_xCoO_2 \cdot yH_2O$. *Condensed Matter and Materials Physics Conference*, University of Warwick, 4-7 April 2004.

- J. Wooldridge, G. Balakrishnan, D. McK. Paul, D. Sheptyakov and M. R. Lees. The Magnetic Phase Diagram of Na_xCoO_2. *Condensed Matter and Materials Physics Conference*, University of Warwick, 10-15 April 2005.

- J. Wooldridge, G. Balakrishnan, D. McK. Paul and M. R. Lees. Magnetism in Sodium Cobalt Oxide. *ESF Workshop - Highly Frustrated Magnetism*, La Londe les Maures, 6-9 November 2005.

- J. Wooldridge, M. R. Lees, G. Balakrishnan, D. McK. Paul, G. McIntyre, D. Sheptyakov, C. Frost, P. Bourges. The Phase Diagram of Sodium Cobaltate. *Condensed Matter and Materials Physics Conference*, University of Exeter, 19-21 April 2006.

Abstract

$Na_xCoO_2 \cdot yH_2O$ has a rich phase diagram inclusive of spin density wave (SDW) magnetic ordering at 0.68$< x <$0.75, exotic superconductivity in the water intercalated compound at $x \sim$0.3 and antiferromagnetism (AFM) with a metal-insulator transition (MIT) at x=0.5. The significance of this system in the understanding of superconductivity in the cuprates and thermopower in the related system Li_xCoO_2 (used commercially in battery cathodes) is unquestionable. The structure comprises layers of CoO_2 separated by Na channels, and produces strong electron correlations that dominate the magnetic and superconducting properties.

The macroscopic properties in the sodium doping range of 0.5$< x <$0.72 are presented. SDW magnetic ordering is confirmed at $x \sim$0.7, via anomalies in the magnetic, thermal and transport measurements, the properties of which are anisotropic. The results indicate the material is intrinsically phase separated into magnetic and non-magnetic subsystems, suggesting the SDW material exists as a point compound. Further modifications to the magnetism occur at 10 and 4 K, with the onset of ferrimagnetism and a glassy ground state. The AFM and MI transitions of the $x = 0.5$ system are also discussed.

The crystal structure of Na_xCoO_2 is investigated by powder neutron diffraction. The predicted phase separation is identified; two systems exist with different morphologies of NaO_6 octahedra. A transfer of Na between the phases is seen at temperatures at which anomalies occur in the heat capacity and transport data. An orthorhombic Na ordering at x=0.5 is recorded, and a lattice contraction around the MIT is observed. Bond valence calculations indicate static charge ordering on the Co sites is not the origin of the insulating behaviour.

An investigation is made into the intra-planar magnetic excitations in the half doped system using inelastic neutron scattering. Scattered intensity is visible above an energy gap of 11.5(5) meV at points above the supercell ordering reflections. Preliminary investigations reveal the *c*-axis dispersion to be significant and indicative of the three dimensional magnetism seen in the SDW phase.

Finally, magnetic and heat capacity studies on the superconducting compound are presented. The system is proven to be an extreme type II superconductor, with weak flux pinning effects. Single crystal neutron diffraction confirms the presence of supercell ordering due to short-ranged correlations between the intercalated water molecules as predicted by powder diffraction studies.

List of Symbols

$2\Delta\,(T)$	The temperature dependent superconducting gap.
2θ	Diffraction scattering angle.
$\mathbf{a}$, $\mathbf{b}$, $\mathbf{c}$	The real space lattice vectors.
$\mathbf{a}^*$, $\mathbf{b}^*$, $\mathbf{c}^*$	The reciprocal space lattice vectors.
a	A sample dimension within the Bean model.
a,*b*,*c*	The lattice parameters.
$a_i^{[\dagger]}$	The spin wave annihilation[creation] operator for the a spin subset.
$a_q^{[\dagger]}$	The Fourier transformed spin wave annihilation[creation] operator for the a spin subset.
A	The absorption factor.
b	The neutron scattering length; a sample dimension within the Bean model.
$b_i^{[\dagger]}$	The spin wave annihilation[creation] operator for the b spin subset.
$b_q^{[\dagger]}$	The Fourier transformed spin wave annihilation[creation] operator for the b spin subset.
$b^{+[-]}$	Scattering lengths for nucleus-neutron systems with a spin of $\boldsymbol{I} + [-]\frac{1}{2}$.
$b_{coh[inc]}$	The coherent[incoherent] neutron scattering length.
b_n	The background fit coefficients in a Rietveld refinement.
$\boldsymbol{B}$	The magnetic induction.
B_i	The thermal parameter of the i^{th} atom.
C'	An estimate of the phonon contribution to the specific heat.
C_{CW}	The Curie-Weiss constant.
$C^{D[E]}$	The Debye[Einstein] approximation to the specific heat.
$C_{el[es]}$	The electronic heat capacity [in the superconducting state].
C_{Sch}	The heat capacity of a Schottky system.
C_{mag}	The magnetic contribution to the heat capacity.
$C_{V[P]}$	The specific heat at constant volume[pressure].
d	The spacing between planes of atoms; the spin dimensionality; the superconducting sample size.
dS	An elemental area.

D The magnetic anistropy parameter; the crystal dimensionality; the spin wave stiffness or velocity.

e The electronic charge.
E The energy; an electric field.
E_f The final neutron energy.
E_F The Fermi energy.
E_g An energy gap.
E_i The incident neutron energy.

$f(T)$ A function of temperature.
$\boldsymbol{F}_P$ The flux pinning force per unit volume.
F The Helmholtz free energy.
F_{hkl} The nuclear structure factor of reflection (hkl).
$|F_{hkl}|_{C[O]}$ The calculated[observed] nuclear structure factor.
$F_N(\boldsymbol{q})$ The nuclear structure factor.

$g_{ab[c]}$ The Landé g-factor resolved within the *ab* plane [along the *c*-axis].
g_J The Landé g-factor.
$G(\boldsymbol{r}, t)$ The time pair correlation function.
$G(\theta)$ The reflection profile function.

(hkl) Miller indices.
$\boldsymbol{H}$ The external magnetic field.
H The Heisenberg hamiltonian.
H_C The thermodynamic superconducting critical field.
$H_{C1[2]}$ The lower[upper] critical field in a type II superconductor.
H_{irr} The irreversibility field.
H_P The Pauli paramagnetic critical field.
H_{sf} The spin-flop field.

$\boldsymbol{I}$ The nuclear spin.
I The current.
$I_{c(hkl)[o(hkl)]}$ The calculated[observed] intensity of reflection (hkl).
I_i Intensity at the i^{th} step in 2θ.

$\boldsymbol{J}$ The total angular momentum.
$\mathbf{J}$ The Heisenberg exchange integral.
$\mathbf{J}_{ab[c]}$ The Heisenberg exchange integral for interactions in the *ab* plane [along the *c*-axis].
J The magnitude of $\boldsymbol{J}$.
$J(\boldsymbol{k}_i, \boldsymbol{k}_f)$ The neutron scattering function multiplied with the TAS resolution functions.
$\boldsymbol{J}_C$ The superconducting critical current density.

$\boldsymbol{J}_S$ The supercurrent density.

$\boldsymbol{k}$ A vector in reciprocal space.
$\boldsymbol{k}_f$ The final neutron wavevector.
$\boldsymbol{k}_i$ The incident neutron wavevector.
k_B Boltzmann's constant.
k_F The electron momentum at the Fermi level.

l The angular momentum quantum number; the distance from sample to detector.
$\boldsymbol{L}$ The orbital angular momentum.
L The magnitude of $\boldsymbol{L}$; a distance.
L_{hkl} The geometerical corrections for reflection (hkl), containing the Lorentz, polarisation and multiplicity factors.

m The mass of an electron; the sample mass.
m^* The effective mass of an electron.
m_l The magnetic quantum number.
m_N The neutron mass.
m_s The spin magnetic quantum number.
$\boldsymbol{M}$ The bulk magnetisation.
M A characteristic amount of iodine used in the deintercalation process.
$M_{ab[c]}$ The magnetisation resolved along the *ab* plane [*c*-axis].
$\tilde{\boldsymbol{M}}(\boldsymbol{q})$ The magnetic structure factor.

n The principal quantum number; the number of magnetic atoms; an integer; the number of data points in a Rietveld refinement.
n_i The fractional occupancy of the i^{th} atom.
N The number of diffracted neutrons; the number of acoustic phonon modes per formula unit; the number of magnetic atoms in a Schottky system; the number of atoms.
N_A Avagadro's number.
$N(E)$ The density of states at energy E.

p The number of refined parameters in a Rietveld refinement.
P The pressure.
P_{hkl} The preferred orientation correction to reflection (hkl).

$\boldsymbol{q}$ The wavevector in reciprocal space.
$\boldsymbol{q}_{\parallel[\perp]}$ The wavevector in reciprocal space resolved parallel[perpendicular] to $\boldsymbol{k}_i$.
$\boldsymbol{Q}(\boldsymbol{q})$ The magnetic interaction vector.
Q A quantity of heat.

$\boldsymbol{r}$ The neutron position vector.

r The distance of an electron from the nucleus; the distance between magnetic moments; the scaling coefficient between C and C'.

R The molar gas constant; the resistance.

$\boldsymbol{R}_i$ The position vector of the i^{th} atom.

R_B The Bragg factor parameter in a Rietveld refinement.

R_E The expected profile parameter in a Rietveld refinement.

R_{wp} The weighted profile parameter in a Rietveld refinement.

s The spin quantum number.

s_N The neutron spin.

$\boldsymbol{S}$ The spin angular momentum.

S The magnitude of $\boldsymbol{S}$; the entropy.

$S_{+[-]}$ The spin raising[lowering] operator.

$S(\boldsymbol{q}, \hbar\omega)$ The scattering function.

S_y The difference between the observed and calculated intensities in a Rietveld refinement.

t The time; the reduced temperature parameter.

$t_{m[ch]}$ The time-of-flight from the moderator to the chopper [moderator to the sample].

T The temperature.

T^* A sodium ordering transition temperature.

T_C The Curie temperature; the superconducting critical temperature.

T_{irr} The irreversibility temperature.

T_M The magnetic ordering temperature.

T_{MI} The temperature of the MIT.

T_N The Néel temperature.

T_{Na} A sodium ordering transition temperature.

T_{peak} The temperature of the peak in χ_{ac}.

T_R The reaction temperature.

T_{SDW} The SDW transition temperature.

$\boldsymbol{u}_{1[2]}$ Orthogonal viewing axes in the mslice program.

v The neutron velocity; the velocity of sound in a crystal.

V The sample volume.

$\widehat{V}_N$ The neutron scattering potential.

V_0 The volume of the crystallographic unit cell.

W The number of indistinguishable configurational microstates.

$W_i(\boldsymbol{q})$ The Debye-Waller factor.

$\boldsymbol{x}, \boldsymbol{y}, \boldsymbol{z}$ Cartesian coordinate vectors.

x The sodium concentration.

(x_i, y_i, z_i) The atomic position of the i^{th} atom in the unit cell.

y The number of water molecules per formula unit; the reduced value of x after sodium deintercalation.

y_{ib} The background intensity at the i^{th} step in 2θ.

$y_{ic[io]}$ The calculated[observed] intensity at the i^{th} step in 2θ.

z Oxonium concentration.

$z_{\uparrow\downarrow[\uparrow\uparrow]}$ The number of antiparallel[parallel] nearest neighbours.

Z The atomic number.

α The ratio of the nn and nnn magnetic exchange integrals; a label denoting the O3 crystallographic structure; the angle of the monochromator on a TAS.

α' A label denoting the O1 crystallographic structure.

$\alpha_q^{[\dagger]}$ The Bogoliubov transformation of $a_q^{[\dagger]}$.

β The critical exponent of the magnetisation; a label denoting the P3 crystallographic structure; the angle of the analyser crystal on a TAS; the temperature coefficient of volume expansion; the phononic specific heat constant.

$\beta_q^{[\dagger]}$ The Bogoliubov transformation of $b_q^{[\dagger]}$.

γ The critical exponent of the isothermal susceptibility; a label denoting the P2 crystallographic structure; the electronic specific heat constant.

$\gamma_{n[s]}$ The electron specific heat constant in the normal[superconducting] state.

$\boldsymbol{\delta_{ij}}$ The vector between the i^{th} and j^{th} spin sites.

δ The ESR skin depth.

Δt_{ch} The opening time of the chopper.

Δt_m The width of the pulse of neutrons from the moderator.

$\Delta\theta_i$ The 2θ value at the i^{th} step corrected for the zero-point shift of the detector.

ϵ The energy scale of the Zeeman splitting within a Schottky system.

η The mixing parameter in a pseudo-Voigt function.

θ The magnetic ordering temperature.

$\theta_{D[E]}$ The Debye[Einstein] temperature.

θ_q A phase factor in the Bogoliubov transformation.

κ The GL parameter.

κ_T The isothermal compressibility.

λ The wavelength.

λ_L The London penetration depth.

λ_N The neutron wavelength.

μ The magnetic moment.
μ_0 The magnetic permeability of free space.
μ_B The Bohr magneton.
μ_{eff} The effective magnetic moment.

ξ The superconducting coherence length.
$\xi_{ab[c]}$ The superconducting coherence length resolved within the *ab* plane [along the *c*-axis].

ρ The resistivity.
ρ_{dc} The dc resistivity.
$\rho_{H[0]}$ The resistivity in an applied field H[a zero field].

σ The neutron scattering cross section.
$\sigma_{coh[inc]}$ The coherent[incoherent] neutron scattering cross section.
$\sigma_{ip[ib]}$ The standard deviation in the intensity[background] at the i^{th} step in 2θ.

τ A characteristic timescale.

φ The SDW phase factor; the angle between μ and H; a rotation angle.
ϕ An axis of rotation in an Eulerian cradle.
Φ_0 The flux of incident neutrons; the magnetic flux quantum.
Φ_S The rate of neutron scattering events.

χ The magnetic susceptibility; an axis of rotation in an Eulerian cradle.
χ^2 The goodness of fit parameter.
χ_0 A constant susceptibility.
$\chi_{ab[c]}$ The susceptibility resolved along the *ab* plane [along the *c*-axis].
$\chi_{ac[dc]}$ The susceptibility in an $ac[dc]$ field.
χ_{dia} The diamagnetic susceptibility.
χ_{para} The parmagnetic susceptibility.
χ_{pauli} The Pauli paramagnetic susceptibility.

Ψ The magnetic order parameter; the superconducting order parameter.
$\Psi_{inc[sc]}$ The incident[scattered] neutron wavefunction.

ω The rotational angular velocity; and axis of rotation in an Eulerian cradle; the half-width-half-maximum of a Bragg reflection; the spin wave frequency.
$\omega_{D[E]}$ The Debye[Einstein] frequency.
ω_i The weighting factor at the i^{th} step in 2θ.
ω_L The Larmor frequency.
Ω A solid angle.

List of Abbreviations

AFM	Antiferromagnetic; antiferromagnetism.
ARPES	Angle resolved photoemission spectroscopy.
BCS	Bardeen, Cooper & Schriefer.
BZ	Brillouin zone.
CCD	Charge coupled device.
CCR	Closed cycle refrigerator.
CO	Charge ordered; charge ordering.
EDX	Energy dispersive x-ray analysis.
EPR	Electron paramagnetic resonance.
ESR	Electron spin resonance.
FC	Field cooled.
FIP	Far infrared peak.
FM	Ferromagnetic; ferromagnetism.
FS	Fermi surface.
G	A gaussian function.
GL	Ginzburg-Landau.
GMR	Giant magnetoresistance.
HS	High spin.
HTSC	High temperature superconductor.
ICDD	International centre for diffraction data.
ICP-AES	Inductively coupled plasma atomic emission spectroscopy.
ILL	The Institut Laue Langevin.
INS	Inelastic neutron spectroscopy.
IR	Infrared.
ISIS	A neutron spallation source.
L	A lorentzian function.

LDA Local density approximation.
LLB The Laboratoire L$\acute{e}$on Brillouin.
LS Low spin.

MIT Metal to insulating transition.
ML Mass loss.
MPMS Magnetic properties measurement system.
MR Magnetoresistance.
MS Medium spin.
μSR Muon spin resonance.

NMR Nuclear magnetic resonance.
nn Nearest neighbour.
nnn Next nearest neighbour.
NQR Nuclear quadrupole resonance.

PDF Powder diffraction file.
PG Pyrolytic graphite.
PPMS Physical properties measurement system.
PSD Position sensitive detector.
PSI The Paul Scherrer Institut.
pV A pseudo-Voigt function.

RAL Rutherford Appleton Laboratory.

SCES Strongly correlated electron systems.
SDW Spin density wave.
SEM Scanning electron microscope.
SQuID Superconducting quantum interference device.
SRO Short range ordering; short range ordered.

TAS Triple axis spectrometer; triple axis spectrometry.
TEM Transmission electron microscopy.
TGA Thermogravimetric analysis.
TOF Time of flight.

VSM Vibrating sample magnetometer.

WHH Wertham, Helfand & Hohenberg.

YBCO $YBa_2Cu_3O_{7-\delta}$.

ZFC Zero field cooled.

Chapter 1

Introduction

The physical properties of condensed matter materials depend strongly on the behaviour of the electrons present in the system. The ability to conduct electricity and heat, as well as to exhibit effects like magnetism and superconductivity is fundamentally linked to the electronic dynamics and interactions with the atomic nuclei and other electrons. Materials in which the latter interaction becomes a sizable fraction of the former are called *strongly correlated electron systems* (SCES). This chapter sets out the fundamental principles of the physics of SCES and their interaction with neutrons, a common probe used in condensed matter. The derivations of the equations presented below may be found in any standard text on magnetism [1, 2], superconductivity [3] and neutron scattering theory [4, 5] and the references included therein.

1.1 Theory of Magnetism

A magnetic moment originates from the angular momentum of a charged particle. In quantum magnetism there are two components that make up the total angular momentum $\boldsymbol{J}$ and define the magnetism: the orbital angular momentum $\boldsymbol{L}$, whose total magnitude is equal to $\hbar\sqrt{l\,(l+1)}$, and the spin angular momentum $\boldsymbol{S}$ with a magnitude of $\hbar\sqrt{s\,(s+1)}$. The projection of $\boldsymbol{L}$ and $\boldsymbol{S}$ along the *z*-axis is $\hbar m_l$ and $\hbar m_s$ respectively. The principal (n), angular (l), magnetic (m_l), spin (s) and spin

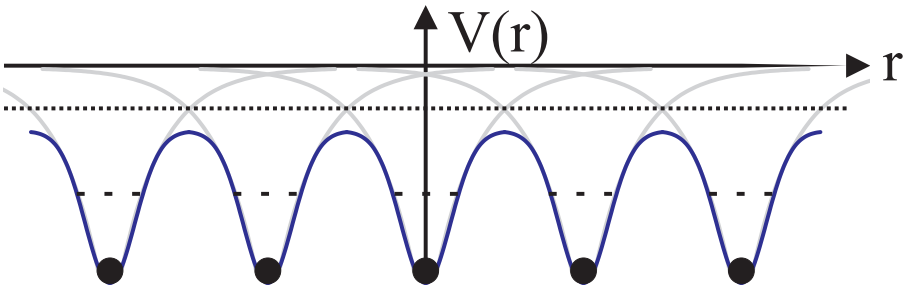

Figure 1.1: A schematic diagram of the individual atomic potentials (grey) and the total lattice potential (blue) according to the tight binding model. Free and bound electron states are denoted by the dotted and dashed lines respectively.

magnetic (m_s) quantum numbers define the quantum state of an electron; the Pauli exclusion principle, which states that electrons occupying the same position in space and time must differ by at least one quantum number, is one of the characteristics that defines the electronic properties of solid state materials. The sequence of occupation of localised electrons in an atom is governed by *Hund's rules*. They are as follows:

1. The lowest energy configuration is one in which the multiplicity (spin) is maximised.

2. The subsequent configuration with the largest angular momentum has the lowest energy.

3. If the shell (denoted by principal quantum number n) is less[more] than half full, the lowest energy configuration has the smallest[largest] total momentum $\boldsymbol{J}$.

In a crystalline material the electrons are subject to strong periodic oscillations of potential as a result of the Coulomb interaction with the lattice ions and the periodicity of the localised electronic density. The total crystal potential constitutes a superposition of the independent atomic potentials as shown in figure 1.1. The application of this periodic potential results in the splitting of individual electronic energy levels into bands in $\boldsymbol{k}$ space. Depending on the particular

characteristics of the ionic lattice potential, the electron orbitals may either be *localised* or *delocalised* (*itinerant*) as indicated by the dashed and dotted lines in the figure. Completely filled bands do not contribute to the angular momentum $\boldsymbol{J}$ and thus do not exhibit a magnetic moment; consequently magnetism is found in atoms with incomplete shells and therefore unpaired electrons. How the moment responds to the presence of a magnetic field is described by a quantity known as the *magnetic susceptibility* (χ) which depends on whether the band contributing to the magnetic moment is localised or itinerant as well as the interaction between it and other magnetic particles in the lattice.

1.1.1 The Magnetic Response to an External Field

Diamagnetism and *paramagnetism* describe two types of magnetic response to an applied field and are characterised by negative and positive susceptibility respectively. The first of these two effects results in the magnetic polarisation opposing the applied field. It is explained in classical electrodynamics by *Lenz's rule*. A magnetic field induces circular currents in a material which creates a field that opposes the applied field. In quantum electrodynamics the same effect is described by the *Larmor theorem*; electrons precess around the direction of their spin in the presence of the magnetic field with a frequency equal to $\omega_L = eH/2m$ where H is the magnitude of the applied field, m is the mass of the electron and e the electronic charge. The resulting negative susceptibility is:

$$\chi_{dia} = \frac{-\mu_0 n Z e^2}{6m} \left\langle r^2 \right\rangle \tag{1.1}$$

where μ_0 is the magnetic permeability of free space, n the number of magnetic atoms in the sample, Z is the atomic number of the atom and $\langle r^2 \rangle$ the mean square distance of the electron from the nucleus.

Paramagnetism is a consequence of the unordered moments already present in the system aligning with the field, the cumulative effect serving to enhance the external field. The paramagnetic susceptibility of a set of localised, weakly

interacting moments is described by the Brillouin function and can be approximated for low fields and moderate temperatures as:

$$\chi_{para} = \frac{n\mu_0\mu_{eff}^2}{3k_BT} \tag{1.2}$$

where μ_{eff} is the effective magnetic moment on each of the n sites, k_B is Boltzmann's constant and T the temperature. This is known as *Curie's Law* and enables an estimate of the magnetic moment on each atom to be made from the experimental magnetic susceptibility data. The effective magnetic moment is related to the total angular momentum by:

$$\mu_{eff} = g_J\mu_B\sqrt{J\left(J+1\right)} \tag{1.3}$$

where g_J is the Landé g-factor (discussed further in section 4.1.1), μ_B the Bohr magneton and J the magnitude of the total angular momentum, equal to $L \pm |S|$. The paramagnetic susceptibility of itinerant electrons is derived from the free electron gas model. It calculated to be:

$$\chi_{pauli} = \mu_0\mu_B^2 N\left(\epsilon_F\right) \tag{1.4}$$

where $N\left(\epsilon_F\right)$ is the density of states (inversely related to the bandwidth of the electronic energy bands) at the Fermi level; χ_{pauli} is therefore a temperature independent parameter. However, the free electron gas is not a good model for a crystalline lattice, as mentioned above. A correction to χ_{pauli} needs to be made to account for the periodic lattice potential which leads to the inclusion of a factor of $\left(1-\frac{1}{3}\left(\frac{m}{m^*}\right)^2\right)$. This additional term in the Pauli paramagnetic susceptibility therefore adds a diamagnetic contribution which includes the effective mass of the conduction electrons (m^*) and consequently the band structure effects.

Generally, materials exhibit both diamagnetic and paramagnetic behaviour, although the former is more often than not a far weaker effect than the latter. In a real material, the magnetism is investigated by the measurement of the bulk magnetisation $\boldsymbol{M}$, defined as the number density of the magnetic dipole moments.

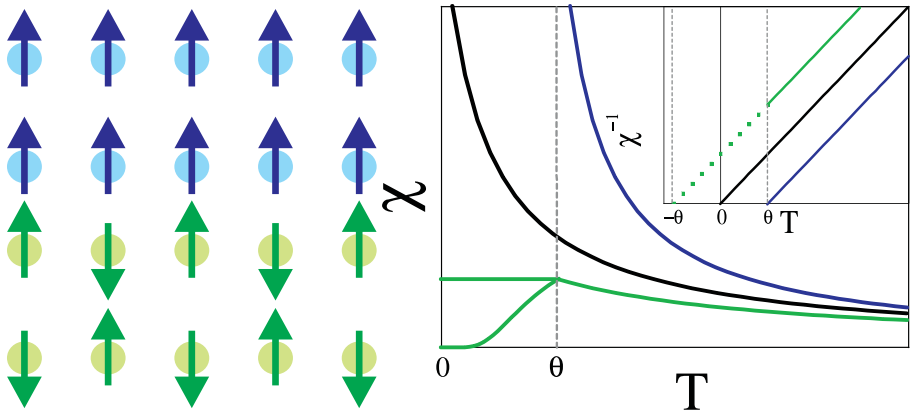

Figure 1.2: A schematic diagram of the magnetic order (left) and the measured susceptibility (right) of a ferromagnet (blue) and an antiferromagnet (green). The susceptibility curve of a paramagnet (black) is shown for comparison. Inset: the x-axis intercept of the inverse magnetic susceptibilities occurs at the Curie or Néel temperature (θ or $-\theta$).

It is related to the external field ($\boldsymbol{H}$) and the magnetic induction within the sample ($\boldsymbol{B}$) by:

$$\boldsymbol{B} = \mu_0 \left(\boldsymbol{H} + \boldsymbol{M} \right) \tag{1.5}$$

with the magnetic susceptibility defined as $\chi = \boldsymbol{M}/\boldsymbol{H}$. The paramagnetic magnetisation measured as a function of field should be linear at small $\boldsymbol{H}$; the inclusion of higher order terms resulting in deviations from linearity are caused by spin fluctuations and other excitation processes that are not treated correctly in the mean-field approximation that was used to derive equation 1.2.

1.1.2 Magnetic Order

Some materials display finite magnetism in the absence of applied fields as a result of strong interactions between the magnetic atoms. The most common ordering patterns for the magnetic moments in a material are termed *ferromagnetic* (FM) and *antiferromagnetic* (AFM). The former refers to the parallel alignment of all the spins along a unique direction and the latter to two interpenetrating, counter-oriented FM lattices which lead to a zero net magnetisation. The presence of interactions between the moments in a material leads to a non-zero abscissa of

	2D Ising	3D Ising	XY	Heisenberg	Mean Field
Spin dimensionality (d)	1	1	2	3	-
Crystal dimensionality (D)	2	3	3	3	-
β	0.125	0.326	0.345	0.367	0.5
γ	1.75	1.2378(6)	1.31(6)	1.3888(3)	1

Table 1.1: Critical exponents for a variety of magnetic models, after reference [1].

the inverse magnetisation at zero temperature (shown in figure 1.2). Below a critical ordering temperature (termed the *Curie temperature* (T_C) in FM and the *Néel temperature* (T_N) in AFM), the moments in the sample align as indicated in the figure. Above these ordering temperatures the moments display no long range order but may be aligned with an applied field according to the Curie-Weiss law:

$$\chi \, \alpha \, \frac{1}{T - \theta} \tag{1.6}$$

where θ is equal to the Curie temperature or the negative of the Néel temperature. Weiss attempted to explain these phenomena using classical thermodynamics by the invention of an internal molecular field, strong enough to be capable of creating spontaneous magnetic order. The theorem explains phenomenologically the appearance of magnetic order, however the calculated molecular fields for average ferromagnets were unfeasibly large (for example $\sim 2 \times 10^4$ kOe in cobalt). The problem was subsequently solved by Heisenberg by the introduction of a quantum mechanical exchange interaction **J**. To first order it is an electrostatic interaction and not magnetic. The magnetic dipole-dipole interaction varies as $1/r^3$; the weakness of this type of interaction is the origin of the overestimation of the magnetic molecular field proposed by Weiss. The Heisenberg model also differs from the Weiss model in that it describes interactions between specific magnetic sites in the system, rather than applying an averaged "mean field" approximation. The theory describes excitations of the whole spin system and is discussed further in section 1.1.4.

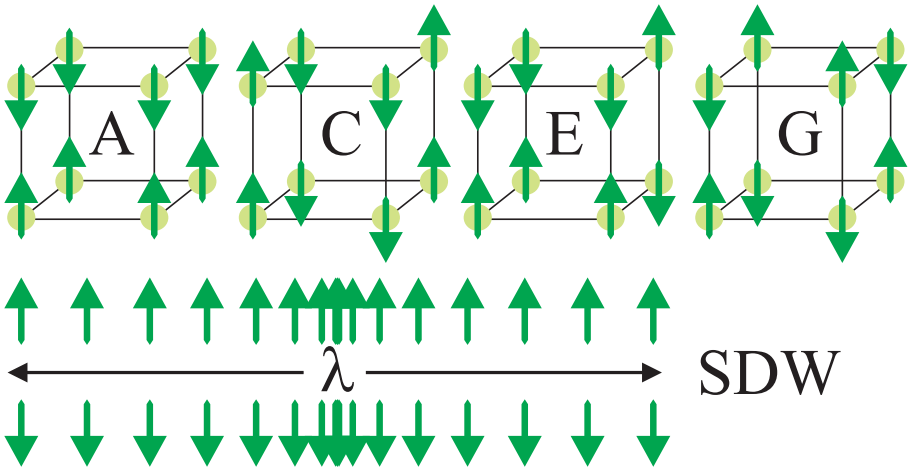

Figure 1.3: A schematic diagram of the magnetic ordering in A, C, E and G-type antiferromagnets within the local moment model (top row). Spin density wave ordering occurs in anisotropic itinerant systems and consists of a sinusoidal modulation of the density of spins in the conduction bands.

Specific approximations to the Heisenberg model include the *Ising model*, in which the spin vector operator is one dimensional and has only two states ("spin up" and "spin down" aligned along a particular crystallographic direction) and the *XY model*, in which the two dimensional spin operator allows the moments to rotate in the (x, y) plane. The onset of magnetic order in any of these approximations may be estimated by examining the behaviour of the free energy above and below the transition temperature. How a physical quantity of the system varies around the critical temperature is defined by its *critical exponent*; the exponents for the magnetisation $\boldsymbol{M}$ [and therefore magnetic order parameter Ψ] $\left(\boldsymbol{M}\left[\Psi\right] \alpha \left(T_C - T\right)^{\beta}\right)$ and the isothermal susceptibility $\left(\chi \alpha \left(T - T_C\right)^{-\gamma}\right)$ are listed in table 1.1. A comparison with experimental data enables the determination of the nature of the phase transition to be made.

1.1.3 Antiferromagnetic Order

As mentioned above, the AFM lattice can be considered as the sum of two interpenetrating FM lattices. Depending on the configuration of the crystal lattice and

the symmetry breaking involved in the magnetic ordering transition, there may be many different ways of arranging an equal number of up and down moments onto a three dimensional set of magnetic atoms. Four types of ordering that are found in orthorhombic crystal settings are shown in figure 1.3. The type of ordering present in a real magnetic system depends on the *exchange pathways* and the number of nearest neighbours. Below the Néel temperature, the magnetisation depends on how the applied field is oriented with respect to the moments. If the field is aligned perpendicular to the spin polarisation axis, the moments will tilt towards $\boldsymbol{H}$ leading to a roughly temperature independent susceptibility. With the field aligned along the magnetisation direction of one lattice (and hence antiparallel to the second lattice) the application of a field at zero temperature will have no net effect resulting in zero magnetic susceptibility. Increasing the temperature produces thermal agitations of the spins that will increase the magnetisation until the temperature reaches an energy equal to the strength of the exchange integral at T_N.

The antiferromagnetic order discussed so far has referred to the spatial orientation of localised spins on crystallographic sites. A common magnetic ground state of AFM metals is the spin density wave (SDW), which consists of a spatially dependent modulation of the density in the spins (and therefore of the overall charge) of the conduction electrons in itinerant systems or alternatively a spatially dependent modulation of the magnitude of the moment on each magnetic site in localised materials. A schematic diagram of the former is presented in the lower half of figure 1.3. The formation of a SDW is due to strong electron-electron interactions and is frequently found in highly anisotropic materials that have Fermi surfaces (FS) with parallel planes that enable *nesting*; the inverse of the reciprocal lattice vector spanning the nested FS sheets gives the modulation of the SDW in real space and is therefore not necessarily commensurate with the underlying crystal lattice. The formation of the SDW is also accompanied by the opening of a gap in the single particle excitation spectrum at the Fermi level;

extremely anisotropic systems may experience the complete removal of the FS at the ordering temperature T_{SDW} resulting in a metal to insulator (MI) transition. The total moment in the system (in one dimension) is equal to :

$$\boldsymbol{M} = 2\,|S|\,g_J\mu_B\cos\left(2k_F x + \varphi\right) \tag{1.7}$$

where k_F is the (x-component of) the electron momentum at the Fermi level and φ is a phase factor. Spin density waves are strongly affected by magnetic impurities. The phase of the SDW couples directly to the impurity potentials within a sample resulting in the destruction of long-range order and the introduction of finite phase correlation lengths that are related to the mean free path between impurities.

1.1.4 Linear Spin Wave Theory

Static magnetic order of the kind represented in figure 1.3 exists only at zero temperature. The addition of heat to a system results in perturbations on the magnetic order, that may propagate through the crystal. The dynamics of these *magnetic excitations* are determined by the type and strength of exchange coupling between the spins which is described by the Heisenberg model. The general Hamiltonian for a system of interacting magnetic moments is:

$$H = -2\mathbf{J}\sum_{<ij>}^{nn}\boldsymbol{S}_i.\boldsymbol{S}_j - 2\mathbf{J}\alpha\sum_{<ij>}^{nnn}\boldsymbol{S}_i.\boldsymbol{S}_j - D\sum_i \boldsymbol{S}_{iz}^2 \tag{1.8}$$

where **J** is the exchange integral (negative for antiferromagnetic interactions and positive for ferromagnetism) and $\boldsymbol{S}_{i[j]}$ is the atomic spin at the $i^{th}[j^{th}]$ site. The exchange interaction is a direct result of the Pauli exclusion principal, which forbids fermions (particles with half integer spin) with the same spin quantum number to exist in the same position and time, and simple electrostatic Coulomb repulsion. The exchange interaction requires the overlap of electron orbitals and is therefore a short ranged effect. Exchange may be mediated through a diamagnetic atom, such as oxygen, known as superexchange. Close examination of a crystal structure is necessary for the successful formulation of a physically realistic Hamiltonian. In

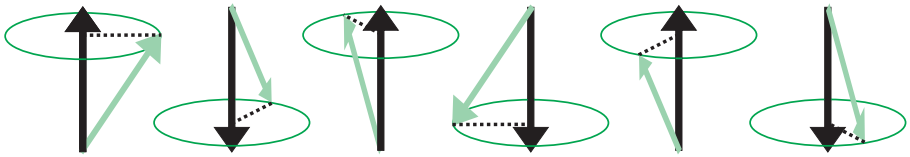

Figure 1.4: A schematic diagram of a linear antiferromagnetic ground state (black arrows) and its excitation (green arrows).

any case, because the extent of such exchange pathways are limited, it is usual to consider just nearest neighbour (nn) and possibly next nearest neighbour (nnn) magnetic atoms in the summation. The parameter α therefore denotes the relative strengths of the nn and nnn interactions. D describes the magnetic anisotropy, modelling the tendency of spins to align in a particular plane or direction. In equation 1.8 the moments are assumed to lie along the *z*-axis.

The propagation of the perturbation of the magnetic ground state is known as a *spin wave* or *magnon* if its energy is quantised. A low energy excitation for a linear antiferromagnetic chain is pictured schematically in figure 1.4; the spins precess around the *z* axis with the phase of the rotation increasing as a function of distance along the chain. The formalism for working out the energy dependence of spin waves requires the spin vector operators to be written in terms of spin creation and annihilation operators. These are transformed into reciprocal space (the Fourier transform is taken) and related to the reciprocal crystal lattice. The change of an individual state in real space (for example, the reversal of one spin in an Ising system) can therefore be described by the sum of an infinite number of spin waves in reciprocal space that have the periodicity of the crystal lattice. In order to perform the transformation to the reciprocal space operators, only the lowest terms in the expansion are used; the approximation gives its name to *linear spin wave theory*. It remains valid for excitations that are small in comparison to the total spin $2S$. The full derivation of the theory, and its application to real systems is outlined in appendix A.

1.2 Introduction to Superconductivity

A superconducting phase transition exhibits itself in a material in two ways. Below a *critical temperature* T_C, the resistivity drops abruptly to zero and any external magnetic fields are excluded from within the system. According to the second of these two properties and equation 1.5, the magnetisation and applied fields must be equal and opposite, in other words the material demonstrates perfect diamagnetism with $\chi = \boldsymbol{M}/\boldsymbol{H} = -1$. Superconductivity is destroyed by the application of a large enough field (the *critical field* H_C); the value of the field needed to return a material to its normal resistive state varies as a function of temperature:

$$H_C(T) \cong H_C(0)\left[1 - \left(\frac{T}{T_C}\right)^2\right] \tag{1.9}$$

Approximately forty years after the discovery of superconductivity a second type of superconducting state was discovered, where the complete expulsion of the magnetic flux density within a sample (known as the *Meissner state*) exists up to a certain critical field H_{C1}, above which discrete lines of magnetic flux (vortices with normal state cores) may enter the bulk whilst the remainder of the sample remains superconducting. As the field is increased further, more flux vortices enter the sample till a critical flux density is reached at H_{C2}, after which the normal state is present once again. The behaviour of both types of superconductors as a function of field is shown schematically in figure 1.5.

The ability of type I superconductors to expel magnetic flux was first explained by London and London in 1935. They assumed a two fluid model in which normal and superconducting electrons exist simultaneously in varying fractions. Magnetic flux is removed by circulating supercurrents with a density $\boldsymbol{J}_S$ that flow near the surface of the sample (within the *London penetration depth* λ_L); the fields created by these supercurrents cancel the externally applied field, the magnitude of which decays exponentially with distance into the material. The theoretical framework of London and London may also be applied to the case of type II su-

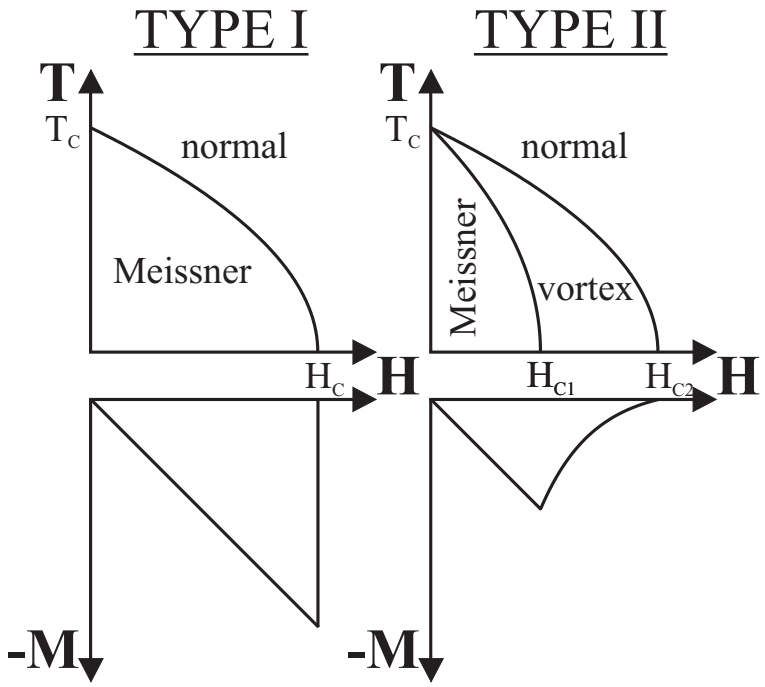

Figure 1.5: The temperature-field and magnetisation-field phase diagrams (top and bottom respectively) for a type I (left) and type II (right) superconductor.

perconductors in the vortex (or mixed) state, since a vortex with a normal core may be supported by supercurrents that circulate around it.

1.2.1 Theoretical Models of Superconductivity

The theory of superconductivity was advanced by Ginzburg and Landau, by the introduction of a *superconducting order parameter* Ψ which increases from zero at T_C to a maximum value at 0 K, similar to the onset of magnetic order parameters as described in section 1.1.2. Along with Ψ, another important parameter was introduced: the *coherence length* of a superconductor describes the distance over which the order parameter varies. Despite the advances made by both the London and Ginzburg-Landau (GL) theories, an understanding of the origin of superconductivity was yet to be identified. Several empirical relations had been made that hinted at the importance of the crystal lattice to superconductivity. Firstly, the critical temperatures of type I superconductors and their room temperature resis-

tivities are inversely related. In fact, superconductivity does not exist in some of the best normal conductors such as Cu, Ag and Au. Secondly, T_C is also made to vary monotonically by changing the isotope of an element within a sample. Both facts indicate that electronic coupling to the lattice is an important factor in the superconducting phase transition. The nature of its relevance to superconductivity was revealed by the theory of Bardeen, Cooper and Schriefer (BCS).

The BCS theory postulates that the superconducting state is comprised of pairs of coupled electrons, known as *Cooper pairs*. The underlying electron pairing mechanism is due to the electrostatic attraction between the electron and the cations that comprise the crystal lattice. As an electron travels through the crystal it distorts the lattice, creating a phonon that is absorbed by a second electron at some later time. The difference in the speed of propagation between an electron and a phonon ($\sim 10^6 \mathrm{ms}^{-1}$ and $\sim 10^3 \mathrm{ms}^{-1}$ respectively) makes the electron-phonon interaction possible and ensures that the mean distance between the two electrons is large. The net result is that this interaction potential outweighs the screened electronic Coulomb repulsion and hence the system is unstable to the formation of Cooper pairs. Symmetry and energy considerations within BCS theory require that the two electrons have opposite wavevectors (so that the total momentum in the centre-of-mass frame is zero) and spins, and have energies within $\hbar\omega_D$ of the Fermi energy E_F, where ω_D is the Debye frequency of the phonons, as discussed further in chapter 4.

The onset of superconductivity is accompanied by the opening of a temperature dependent energy gap $2\Delta(T)$ at the Fermi level; the energy cost from the increase in kinetic energy that is associated with the occupation of states above E_F is also outweighed by the reduction in energy achieved by the formation of the Cooper pairs. Therefore, $2\Delta(T)$ defines the amount of energy needed to break the paired electron state. If $k_B T$ is smaller than the gap, the superconducting electrons are not excited by thermal vibrations of the lattice. The presence of the gap also provides an explanation as to why superconductivity is not seen in magnetic

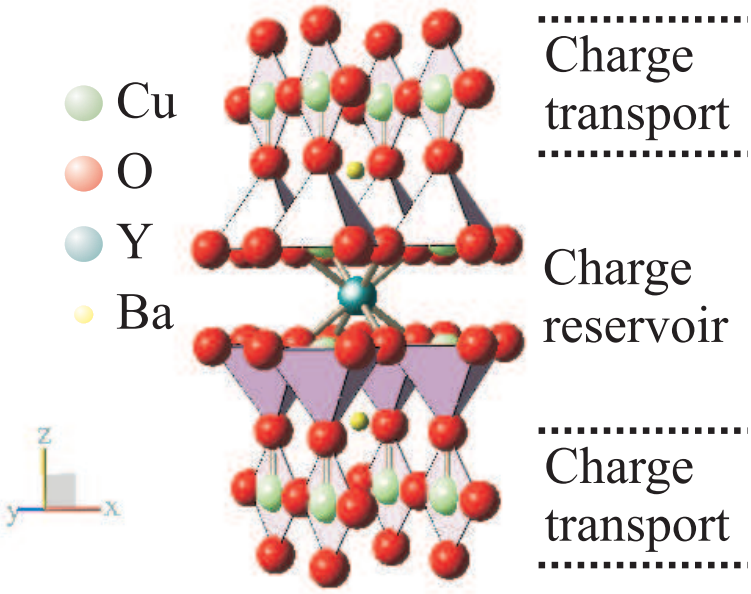

Figure 1.6: The crystal structure of YBCO. Superconductivity occurs within the copper oxide planes (marked charge transport); the CuO_2 planes are separated by charge reservoir layers consisting of barium, yttrium and oxygen.

elements such as Fe or Co, and is strongly suppressed by the presence of magnetic impurities within other superconducting materials, since the magnetic energy of each electron in the Cooper pair is defined by its relative orientation to the local magnetic field. If the difference in magnetic energy between the two electrons is larger than $2\Delta\left(T\right)$, the superconductivity is destroyed and the magnetism is said to be a *pair breaking mechanism*.

1.2.2 Exotic Superconductivity

The BCS theory adequately explains the properties of conventional type I and II superconductors in which electron pair formation is mediated by phonons. The strength of this coupling mechanism sets an upper limit on the critical temperature of approximately 40 K. Attempts were made to enhance the electron-phonon coupling parameter by the Jahn-Teller effect in order to reach higher critical temperatures which led to the discovery of the new class of high temperature superconductors (HTSCs) in 1986. The HTSCs are made mostly all cuprates and

have complex layered crystallography based on the *perovskite* structure that show anisotropic magnetic and superconducting behaviour. The underlying mechanism for Cooper pair formation in the HTSCs is not yet known, although a theory known as the *charge transfer model* indicates the layered structure of the cuprates to be the key to superconductivity. The crystal structure of one of the most famous HTSCs, $YBa_2Cu_3O_{7-\delta}$ (YBCO), is shown in figure 1.6. It is thought that the superconductivity is confined to the CuO_2 *charge transport* planes, which are isolated from each other over large distances by *charge reservoir* layers, so called because changing the chemical content in the unit cell in these rare earth oxide layers results in a change in the valence state of the Cu in the charge transport layers via the overlapping oxygen $2p$ orbitals. Therefore, the isolation planes not only separate the conduction planes but provide charge carriers and possibly the coupling mechanism for superconductivity.

The dominant theory of the pairing mechanism in the HTSCs is the *spin wave model*, in which the formation of Cooper pairs, i.e. the electron-electron interaction required to the screened Coulomb repulsion, is mediated by magnons that have exchange energies typically four times the size of phonon energies, capable of supporting the higher critical temperatures. In conventional BCS superconductors, the pairing wavefunction and the energy gap are spherically symmetric; it is named s-wave pairing in analogy with the shape of atomic orbitals. The pair binding state in unconventional superconductors can either have a total spin of zero or one, known as spin singlet and spin triplet pairing respectively. The fact that the overall wavefunction is antisymmetric under particle exchange requires that the singlet[triplet] pairing wavefunctions have an even[odd] orbital momentum number. The net effect is that the unconventional superconducting order parameter has a more complicated structure that is a function of $\boldsymbol{k}$. It is clear that the strong electron correlations found in the cuprates and the enhanced Coulomb repulsion that accompanies it favour pairing states with non-zero angular momentum.

1.3 Neutron Scattering Theory

In order to understand the physical properties of crystalline systems, it is necessary to obtain information on the positions of the atoms in a material as well as details of the individual and collective dynamics in the system. Neutron scattering is a useful tool used to obtain such information, although its use is not just confined to the study of the structural and magnetic properties of crystals. The properties of the neutron also make it a useful application to the fields of biology (for example in determining the structure of proteins), physical chemistry (in the study of polymers and gels), materials science (with the measurements of stresses, strains and textures) and disordered materials (liquids and glasses).

1.3.1 Properties of the Neutron

A beam of neutrons with a single energy E_i, travelling in a direction defined by the wavevector $\boldsymbol{k}_i$ will either pass through a material undisturbed, be absorbed or scattered. The scattering process involves a change in direction of the wavefunction (denoted by a final wavevector $\boldsymbol{k}_f$) and/or a change in energy to E_f. The purpose of neutron scattering is to link the characteristics of the scattered neutrons to the order and dynamics of the scattering atoms within the sample. This is made possible using *thermalised neutrons*, which have four useful properties:

1. They have energies of the order of $300k_B$ with corresponding wavelengths λ_N of a few ångström, comparable to the interactomic distances of most crystalline materials (the relative size of the wave and the scattering object determines whether diffraction will occur). The energy of thermal neutrons is also of the same order of magnitude as the typical excitation energies of the scattering systems, enabling a strong coupling between the neutrons and the excitation modes that allows the characteristics of the excitations to be accurately determined.

2. The neutron itself carries no electrical charge and therefore does not exhibit

any electrostatic interaction with the electron cloud of an atom in direct contrast to x-ray scattering in which the probability of scattering is proportional to the square of the atomic number. Rather, the neutron interacts with the atomic nucleus via the *strong nuclear interaction*, a very short ranged force. Neutrons are therefore highly penetrating; measurements from the bulk of the sample are obtainable, again in contrast to x-ray scattering which requires very high energy x-rays to penetrate more than just the surface of a material.

3. The strength of the nuclear force is determined by both the number of nucleons present and the occupied energy levels within the nucleus. The neutron-nucleus interaction strength as a function of atomic number has an irregular profile and even varies dramatically between isotopes of the same element. It is therefore possible to determine the positions of very light elements such as hydrogen, which are almost invisible to x-rays.

4. The neutron is made from one *up* and two *down quarks* and hence has a total spin $s_N = \hbar/2$. The magnetic moment associated with this spin couples to the local fields of magnetic atoms that are created by the presence of unpaired electrons. The theory of the magnetic interaction between a neutron and the magnetic atom allows the study of magnetic order.

Typically, the characteristics of structural and/or magnetic order are determined by using neutron diffraction (the process defined by $E_i = E_f$) and the structural and/or magnetic excitations are probed with inelastic scattering (in which $E_i \neq E_f$).

1.3.2 The Scattering Process

The interaction between a neutron and a scattering atom is defined by a quantity known as the *differential cross section*, which is equal to the ratio of the number of neutrons scattered per second (Φ_S) into a particular solid angle ($d\Omega$) and the

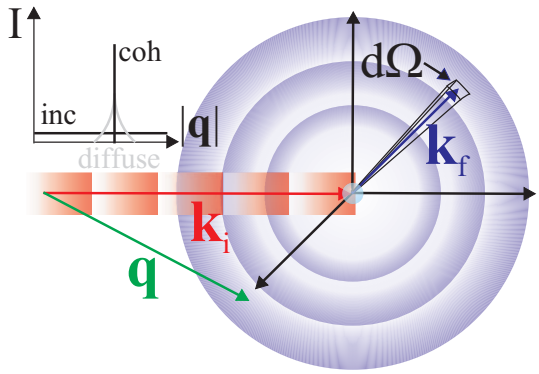

Figure 1.7: A plane wave of incident neutrons (red) is scattered from a single, bound nucleus; the outgoing wave (blue) is spherically symmetric. The difference between the incoming and outgoing wavevectors ($\boldsymbol{k}_i$ and $\boldsymbol{k}_f$) as measured through an incremental solid angle $d\Omega$ defines the momentum transfer vector $\boldsymbol{q}$. Inset: The total scattering from a set of N nuclei contains an isotropic incoherent (inc) term, coherent (coh) scattering in Bragg directions and diffuse scattering around Bragg reflections that corresponds to structural irregularities.

incident flux (Φ_0):

$$\frac{d\sigma}{d\Omega} = \frac{\Phi_S}{\Phi_0} \tag{1.10}$$

The scattering cross section defines the effective area perpendicular to the incident beam that is "visible" to the neutron and hence the overall probability of a scattering event taking place. $d\sigma/d\Omega$ has the dimensions of square metres accordingly, although it is most frequently defined in barns where 1 barn $= 10^{-24}$ cm^2. The analysis of this scattering function may also include the condition of the scattered neutron having a final energy $E \geq E_f \geq E + dE$; the probability of scattering is now termed the *partial differential cross section*:

$$\frac{d^2\sigma}{d\Omega dE_f} = \frac{\Phi_S}{\Phi_0} \tag{1.11}$$

The strong nuclear force has a range of approximately 10^{-15} m, small in comparison to the average nuclear radius ($\sim 10^{-14}$ m) and tiny with respect to λ_N ($\sim 10^{-10}$ m); the interaction potential can therefore be represented as point-like, and is known as the *Fermi pseudo-potential*. A neutron, with an incident plane wave function oriented along $\boldsymbol{z}$ (i.e $\Psi_{inc} = \exp(i\boldsymbol{k}.\boldsymbol{z})$), that is scattered from a

single bound nucleus has a scattered wavefunction which is isotropic within the centre-of-mass system (known as s *wave scattering* since no orbital angular momentum is involved) equal to $\Psi_{sc} = -b/r \exp(i\boldsymbol{k}.\boldsymbol{r})$ (shown in figure 1.7). The scattering potential is defined by:

$$\widehat{V}_N(\boldsymbol{r}) = \frac{2\pi\hbar^2}{m_N} b_i \delta(\boldsymbol{r} - \boldsymbol{R}_i) \tag{1.12}$$

where $\boldsymbol{r}$ is the position vector of the neutron, m_N the neutron mass, b_i the scattering length and $\boldsymbol{R}_i$ the position vector of the i^{th} scatterer. The scattering length, in analogy to the nuclear cross section, can be considered the effective distance within which the neutron must pass to facilitate scattering. It is a complex number, the real part of which is independent of the energy or wavevector of the incident neutron. The real part relates to the strength of $\widehat{V}_N$ and may be positive or negative (corresponding to an attractive or repulsive interaction respectively), whereas the imaginary part relates to the probability that the neutron will be absorbed instead of scattered.

1.3.3 Coherent and Incoherent Scattering

The incident flux is defined as $\Phi_0 = v|\Psi_{inc}|^2$ where v is the neutron velocity. The number of scattered neutrons passing through an elemental area dS is therefore $vdS|\Psi_{sc}|^2 = vb^2 d\Omega$. From equation 1.10:

$$\frac{d\sigma}{d\Omega} = \frac{vb^2 d\Omega}{v d\Omega} = b^2 \tag{1.13}$$

Integrating over all angles gives a value of the total scattering cross section of $\sigma = 4\pi b^2$. This cross section is made from two constituent parts termed *coherent* and *incoherent* i.e. $\sigma = \sigma_{coh} + \sigma_{inc}$. If the sample is a crystal consisting of only one non-magnetic element, with no isotopic variation, whose atoms are placed at the nodes of a regular lattice, the resulting spherical scattered waves from each atom will exhibit a definite phase relationship with one another and will be out of phase with respect to the incoming plane wave by an amount proportional to the coherent

scattering length b_{coh}. In certain directions the waves interfere constructively and the amplitude of the outgoing wave in that direction contains a contribution from all of the scatterers. In other words the scattered waves behave in a coherent manner. This process is known as Bragg diffraction and discussed in further detail in section 3.2. The number of neutrons scattered in a Bragg direction is known as the *coherent differential scattering cross section* $(d\sigma_{coh}/d\Omega)$ and is proportional to the square of the amplitude of the scattered neutron wavefunction and therefore b_{coh}^2.

In reality, crystal systems may contain more than one constituent element and different isotopes of each element. The system can be modelled by assuming the scattering lengths fluctuate randomly around a mean value $\overline{b}$:

$$b_i = \overline{b} + \delta b_i \tag{1.14}$$

where the incremental variations sum to zero over N lattice sites i.e. $\sum_i^N \delta b_i = 0$. Each lattice site may therefore be represented as having two scatterers, one with a scattering length of $\overline{b} \equiv b_{coh}$ and another with $b = \delta b_i$, a value that varies randomly and has no correlation between sites i and $i+1$. Since the change in phase of the scattered wave is proportional to b, as mentioned above, the scattered waves from these second scatterers do not undergo coherent interference. Instead, the resulting intensity in all directions is just the sum of the individual intensities from each second scatterer; the overall intensity from this "incoherent" scattering is therefore isotropic. The *incoherent differential scattering cross section* $(d\sigma_{inc}/d\Omega)$ is proportional to:

$$\sum_i^N \delta b_i^2 = N\left[\overline{\left(b_i - \overline{b}\right)^2}\right] = N\left[\overline{b^2}_i - \overline{b}^2\right] \tag{1.15}$$

The incoherent scattering length per nucleus is therefore defined as $b_{inc} = \sqrt{\overline{b^2}_i - \overline{b}^2}$. The variations in scattering lengths between different sites occur for two reasons. As previously mentioned, the strong nuclear force is dependent on the number of nucleons present and therefore varies between isotopes of the same element.

Secondly, the interaction potential is dependent on the relative orientation of the neutron spin $\boldsymbol{s}_N$ and the nuclear spin $\boldsymbol{I}$, if present. There are now two values for the scattering lengths, b^+ and b^-, according to whether the spins are parallel (in which case the total spin is $\boldsymbol{I}+1/2$) or antiparallel (giving a total spin of $\boldsymbol{I}-1/2$). If the spins of neither the incident neutron beam, nor the nuclear moments are aligned, the scattering by b^+ or b^- occurs randomly. Magnetic order within a crystal defines the polarisation of the nuclear moments, the use of a polarised beam of neutrons can consequently provide useful information on such order.

The variation in scattering lengths between sites is thus the result of chemical and magnetic disorder which results in the isotropic background from the incoherent scattering. Magnetic order, on the other hand, will change the symmetry of the crystal structure and therefore add to the coherent scattering. Positional disorder in the crystal structure modifies the coherent scattering and adds intensity around the sharply defined Bragg peaks. This is described as *diffuse scattering* and is shown in the inset of figure 1.7.

In summary, the total differential cross scattering values for both coherent and incoherent scattering are:

$$\sigma_{coh} = 4\pi\overline{b}^2, \qquad \sigma_{inc} = 4\pi\left(\overline{b^2}_i - \overline{b}^2\right) \tag{1.16}$$

The coherent scattering is dependent on the correlation between the positions of the same nucleus at different times as well as correlations between the position of different nuclei at different times. The incoherent scattering is dependent only on correlations between the positions of the same nucleus at different times. These ideas are best expressed in terms of *pair correlation functions*. The time pair correlation function ($G(\boldsymbol{r},t)$) defines the probability of finding an atom at position $\boldsymbol{r}$ and time t, given that there was an atom at the origin at $t=0$:

$$G(\boldsymbol{r},t) = \left(\frac{1}{2\pi}\right)^3 \int \sum_{ij} e^{-i\boldsymbol{q}.\boldsymbol{r}} \left\langle e^{-i\boldsymbol{q}.\boldsymbol{r}_j(0)} e^{i\boldsymbol{q}.\boldsymbol{r}_i(t)} \right\rangle d\boldsymbol{q} \tag{1.17}$$

The Fourier transform of $G(\boldsymbol{r},t)$ determines the scattering function $S(\boldsymbol{q},\hbar\omega)$, i.e.

the quantity calculated from the measured cross sections during an experiment:

$$\begin{aligned} \frac{d^2\sigma}{d\Omega dE_f} &= \sum_{ij} b_i b_j \frac{k_f}{k_i} S\left(\boldsymbol{q}, \hbar\omega\right) \\ \text{where } S\left(\boldsymbol{q}, \hbar\omega\right) &= \frac{1}{2\pi\hbar} \int G\left(\boldsymbol{r}, t\right) e^{i(\boldsymbol{q}.\boldsymbol{r}-\omega t)} d\boldsymbol{r} dt \end{aligned} \tag{1.18}$$

Through the evaluation of the scattering function and its Fourier transform, a link between the data measured in a neutron scattering experiment and the properties of the physical system under study may be ascertained.

Chapter 2

The Phase Diagram of Sodium Cobaltate

In recent years, sodium cobaltate has become one of the most intensely investigated strongly correlated electron systems due to its remarkable electronic properties. A cousin to the commercially used cathode material Li_xCoO_2, its unusually high thermopower and low resistivity [6] make it a potentially viable thermoelectric material. Additionally, the surprise discovery of superconductivity in the hydrated compound [7] in 2003 highlighted similarities to the high temperature superconductors and ignited a debate into the origin of the pairing mechanism. Experimental and theoretical studies undertaken during the last three years have unveiled a complex phase diagram in which sodium doping is key to the magnetic and superconducting properties. Understanding of the physics driving the extraordinary properties in Na_xCoO_2 has been hampered by the difficulty in producing high quality samples and the misidentification of the doping concentration in many early publications. The following chapter sets out the currently available experimental data and theoretical concepts that define the present understanding of the phase diagram.

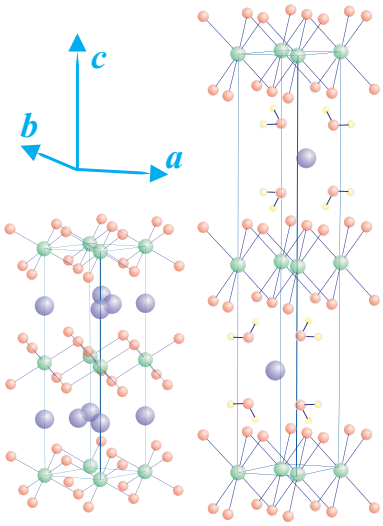

Figure 2.1: Left: The crystal structure of $Na_xCoO_2 \cdot yH_2O$. Sheets of edge sharing CoO_6 octahedra (green and red) are separated by layers of Na ions (blue) positioned on three different sites. Right: In the water intercalated compound, four H_2O or D_2O molecules (yellow and red) per unit cell are positioned either side of the sodium ions, which occupy only the $2c$ or $6h$ site for x ~0.3, resulting in a doubling of the *c*-axis lattice parameter. Structure reproduced from ref. [8].

2.1 The Crystal Structure of Sodium Cobaltate

Na_xCoO_2 belongs to the general class of A_xBO_2 *bronzes* first identified by Jansen and Hoppe [9]. It has a highly anisotropic structure, with two dimensional sheets of CoO_6 octahedra stacked along the *c*-axis and intermittent layers of sodium ions (as shown in figure 2.1). There are three sites on which the sodium may reside; the $2b$ site located directly above and below the cobalt atoms in the adjacent layers, the $2c$ site situated equidistant between the six nearest neighbour cobalts and the $6h$ site, a slightly displaced position from the higher symmetry $2c$ site. The distance between the CoO_6 layers [10] is larger than the ionic radius of sodium (0.97 Å) which is therefore expected to be highly mobile along the basal planes of the material. This mobility also permits a series of different crystallographic stacking sequences of the cobalt oxide and sodium layers to be formed during the crystal growth procedure. The different crystallographic phases were first identified by Fouassier [11] who labelled each phase with a Greek letter and identified the dependence of the stacking sequences on the total sodium concentration x and reaction temperature T_R. The phases are defined more formally by the letters P and O, which describe the alkali ion environment (trigonal prismatic and octahedral respectively) and by a figure denoting the number of cobalt oxide layers included

x	0.55-0.60	0.75	0.90-1.00
Phase label	β (P3) if $T_R \leq$650°C γ (P2) if $T_R \geq$650°C	α' (O1)	α (O3)

Table 2.1: The phases of sodium cobaltate and their dependence on the total sodium concentration x, after reference [11]. Samples with a nominal x value in between the values given above are deemed to be phase separated combinations of the α, α', β or γ phases.

in the crystallographic unit cell. The labels for each structure are recorded in table 2.1. Fouassier suggested that samples with x values in the gaps between the ranges he specified for the α, α', β and γ phases were simply mixtures of the two closest permitted phases in the correct ratio. The γ (P2) phase is described by the space group $P6_3/mmc$, and is the phase under investigation in this work. The other phases of sodium cobaltate exhibit characteristics similar to those described in this thesis; confusion between these phases and the existence of intrinsic phase separation between different x compositions within the same sample have led to conflicting experimental reports in the literature, as discussed in section 4.6.

The crystallographic structure may host intercalated heavy water within the NaO_2 layers, as shown in the right hand side of figure 2.1. The amount of intercalated water is variable; thermogravimetric analysis (TGA) [12] shows stable phases exist with $y = 0.1$, 0.3, 0.6 and 1.4, where y represents the number of water molecules per formula unit. Knowledge of the *c*-axis lattice parameters for each hydrated phase enables the volume fraction of each phase in a sample to be identified with x-ray or neutron diffraction. Within a given hydrated phase, the structure supports a variable amount of sodium, x [13]. The exact coordination of the water to the crystal structure is currently under debate, and is discussed in chapter 7.

2.2 The Magnetic and Superconducting Phase Diagram

The electronic structure of sodium cobaltate is dependent on the sodium concentration. The properties of the 3d transition metal oxides are characterised by the behaviour of the electrons in the crystal field split upper e_g and lower t_{2g} bands; the latter are further split by a trigonal distortion of the cobalt oxide octahedra into an upper a_{1g} band and two lower e'_g bands. In the simple ionic picture, the electronic properties of Na_xCoO_2 are tuned by the addition of x sodium atoms which, via a redox reaction in the oxygen $2p$ orbitals, is equivalent to doping $(1-x)$ holes onto the cobalt triangular lattice by the removal of electrons from the upper, fully occupied a_{1g} band. This introduces a mixed valency to the cobalt system that has a formula of $Na_xCo^{3+}_xCo^{4+}_{1-x}O_2$, where the trivalent cobalt is non-magnetic, and the tetravalent cobalt may exist in its low spin $\left(t^5_{2g}e^0_g\right)$, medium spin $\left(t^4_{2g}e^1_g\right)$ or high spin $\left(t^3_{2g}e^2_g\right)$ state. In reality, this doping model does not adequately describe the Co d orbitals, in which intra-atomic electron correlations and spin-orbit coupling should be accounted for. However, direct measurements of the cobalt valency as a function of doping by iodometric titration measurements [14] show that the general relation between sodium doping and cobalt valence holds true, despite an observed decrease in the total formal valence due to oxygen non-stoichiometry within the samples.

The fully stoichiometric system is, as predicted, a non-magnetic band insulator [15]. As the doping level decreases towards $x = \frac{1}{2}$, the system exhibits Curie-Weiss paramagnetism, with reported values for the unordered moment clustered around the expected moment for a $(1-x)$ fraction of low spin ($S = \frac{1}{2}$) Co^{4+}. At low temperatures, the system is magnetically ordered. Inelastic neutron spectroscopy [16] has characterised the magnetic interactions and identified the magnetic structure as A-type antiferromagnetism, however, the unexpectedly small size of the total ordered moment of just 0.13(2) μ_B per Co [17] has made the identification of the ordered structure by neutron diffraction problematic. The

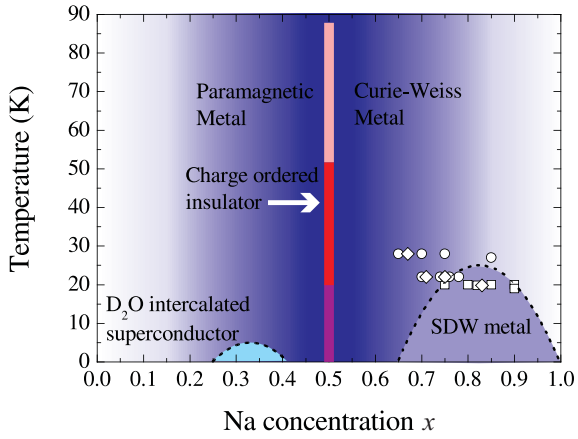

Figure 2.2: The magnetic phase diagram of Na_xCoO_2. The symbols on the right depict the reported SDW transition temperatures (circles - powder samples, squares - single crystals, diamonds - crystals in this work), set against the proposed dome shaped phase. The half doped phase exhibits antiferromagnetic ordering at 88 K (pink) followed by a MI transition at 53 K (red) and a second magnetic transition at ∼20 K (purple) of unknown origin. At $x \sim \frac{1}{3}$, superconductivity exists in the hydrated/deuterated compound.

magnetic coupling constants calculated from the neutron spectroscopy studies also predict remarkably isotropic magnetic interactions for a system with such highly anisotropic macroscopic properties. In fact the simple magnetic structure used to simulate the spin wave dispersions required the sample to be phase separated into areas of spin half Co^{4+} and non-magnetic Co^{3+}, rendering the analysis of the magnetic interactions somewhat in doubt. The authors acknowledge the possible need for a more itinerant model with a small charge disproportionation. The question of itinerancy is also raised in the explanation of the large conductivity that gives sodium cobaltate such a high thermopower, in comparison to the localised magnetic characteristics; the $x > \frac{1}{2}$ system is therefore commonly referred to as a "Curie-Weiss metal". In all other investigations, the magnetic ordering is ascribed to a spin density wave (SDW), with the polarisation vector along the *c*-axis perpendicular to the propagation of the wave in the basal planes. The exact details of the SDW transition as a function of doping are currently under debate. The vast majority of experimental reports place the critical temperature at 22 K [18, 19, 20, 21, 22, 23] for the doping range around x ∼0.75. A few reports

of different ordering temperatures of 20 K [24, 25] or 28 K [26] exist, although early indications suggest these different magnetic ordering temperatures belong to phases other than the P2 'γ' structure. The reported ordering temperatures as a function of sodium concentration are included in the phase diagram in figure 2.2. Despite any concrete evidence, the SDW phase was reported to be dome shaped with respect to x [25, 27], though later evaluations of the phase diagram [10] acknowledge the SDW phase as a point compound at x =0.75 and 22K.

Whatever the nature of the SDW ordering, most authors agree that it is present down to a Na concentration of ∼0.65 where upon the system becomes paramagnetic once more. At $x = \frac{1}{2}$ a special state is realised and new type of magnetic ordering presents itself at 88 K. It has recently been identified as G-type AFM by neutron diffraction [28] although, once again, the measured moment is less than predicted at just 0.13(1) μ_B per Co. The system undergoes a metal-insulator transition at 53 K and angle dependent giant magnetoresistance (GMR) [29] that indicates an unusually strong spin-charge coupling. At lower temperatures still, a further modification to the magnetism is apparent at ∼20 K, although the origin of this low temperature state has yet to be identified. It is known that there exists long-ranged ordering of the Na cations [30] into quasi one dimensional chains along *a*, enabling the crystal structure to be reclassified into an orthorhombic super-cell of dimensions $\left(2a \times \sqrt{3}a \times c\right)$. In this crystal setting, there are now two Co sites. This led to speculation that the above transitions were the results of charge ordering (CO) in the CoO_2 planes, probably due to the influence of charge modulations in the Na layer. More recently, however, the notion of a charge ordered Mott-like transition has been disputed. Nuclear magnetic resonance (NMR) measurements [31] did not deduce any large difference in charge state between the two sites. Crystal structure determination by powder neutron diffraction [32] also failed to find a significant difference between the Co-O hybrization on the two sites. A clear picture of the role of spin and orbital ordering in $Na_{\frac{1}{2}}CoO_2$ has yet to be defined.

Below $x = \frac{1}{2}$ electronic correlation effects are weaker and the system becomes Pauli paramagnetic. The interest in this section of the phase diagram is generated by the presence of superconductivity in the hydrated or deuterated compound at $x \sim \frac{1}{3}$. Early indications show sodium cobalt oxyhydrate to be an extreme type II superconductor [33, 34], with most reported Meissner screening fractions in the range of 10-20$\%$ [7, 33, 35, 36] suggesting the material is non-BCS, the measurement suffers from flux pinning and/or weak link effects or more simply, just a fraction of the sample volume is exhibiting superconductivity due to sample inhomogeneity. The average reported critical temperature is 4.5 K, although this is dependent on both the sodium and water content. Superconductivity is found in the $y = 1.4$ phase only, suggesting that two dimensionality in the CoO_2 planes is enhanced due to the water shielding the Coulomb potential in the Na layer, and the increase in the *c*-axis lattice parameter is critical to the superconducting pairing mechanism. Initial confusion over whether the superconducting phase diagram was dome shaped [37] or constant [38] with respect to sodium concentration was resolved by Milne et al. [36] and Sakurai et al. [39] who discovered the intercalation of water is accompanied by oxonium (H_3O^+) ions. Acting as an additional dopant, the correct chemical formula of the superconducting compound is written $Na_x(H_3O)_zCoO_2 \cdot yH_2O$. The cobalt valence is determined not only by the sodium content x, but by the ratio of oxonium to sodium z/x. The true superconducting phase diagram is evidently complex and both dome shaped and constant doping may be obtained via different projections of the $x - z - T$ phase diagram onto the $x - T$ plane.

2.2.1 The Superconducting Pairing Mechanism

The origin of superconductivity in this system is a topic currently under debate. At first sight, many analogies to the high T_C cuprates may be drawn. Firstly, the layered structure consisting of electronically active cobalt oxide layers separated by the doping layer of Na ions merits the application of the charge-transfer model

to this system. The apparent existence of an optimal electronic doping that leads to a maximum superconducting transition temperature also closely resembles the physics of the HTSCs. The system differs however, in the arrangement of the cobalt onto a triangular lattice rather than the nearly square lattice as found in the cuprates and the fact that in this system, there are two bands intersecting the Fermi surface, neither of which are half filled. The inclusion of oxonium doping into the phase diagram, and careful measurements performed by redox titration [36] placed the optimal cobalt valence at 3.3, rather than 3.7 as suggested by the simple ionic model presented above. This is the doping phase at which the SDW magnetic ordering is observed and has led to speculation that the superconductivity arises from the presence of FM correlations found in the *ab* planes of the anhydrous compound [40], as predicted by LDA calculations performed by Singh et al. [41], suggesting a p-wave spin-triplet pairing mechanism. Alternatively, superconductivity may be achieved by modifications to the strong electronic correlations, also found at $x \sim$0.7, during the hydration process.

Experimental studies designed to elucidate the nature of the pairing mechanism have produced conflicting results. Some muon spin relaxation (μSR), NMR and nuclear quadrupole resonance (NQR) measurements found non-exponential behaviour below T_C, incompatible with a conventional s-wave, fully gapped state [42, 43]. Contrary to this, another study observed the coherence peak in the spin-lattice relaxation curve below T_C [44], absent in the previous two reports, which does indicate a spin-singlet s-wave pairing mechanism. Conclusions based on low temperature heat capacity data are also varied amongst different authors, with some proposing a line-nodal order parameter [35, 45, 46] whilst others suggest spin singlet pairing [47] and even two gap superconductivity as seen in MgB_2 [48]. It is evident that the real origin of the superconductivity in sodium cobalt oxyhydrate currently remains elusive, with both experimental and theoretical investigations in their infancy. The conflicting experimental evidence almost certainly results from the sensitivity of the system to all three of the variable parameters in the doping

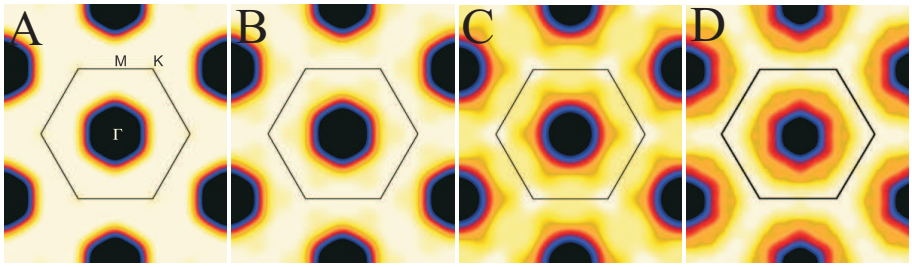

Figure 2.3: Fermi surface reconstructions of Na_xCoO_2 with $x = 0.74$ (A), $x = 0.51$ (B), $x = 0.38$ (C) and the deuterated compound with $x = 0.35$ (D). The black lines indicate the boundary of the first Brillouin zone.

phase diagram - x, z and y.

2.3 The Fermi Surface Topology

The majority of experimental reports deduce spin triplet pairing for the Cooper pair formation mechanism. As discussed in section 1.2.2, the orbital angular momentum must consequently take an odd value, with either p- or f-wave symmetry. All the possible pairing states allowed by the hexagonal symmetry of the system are discussed by Mazin et al. [49], who deduce f-wave pairing to be most likely from the currently available experimental evidence. The Cooper pair attraction results from an instability at the FS of the system, and hence a detailed knowledge of the electronic structure is necessary. The predicted FS of sodium cobaltate [50, 51] is characterised by a large hexagonal hole sheet centered around the Γ point with predominantly a_{1g} symmetry surrounded by six smaller elliptical e'_g hole pockets directed along the (110) or ΓK directions, for x values smaller than $\sim$0.6. Many of the proposed theories on the nature of the superconductivity, rely heavily on the existence of the e'_g pockets as the nodes of possible nesting vectors, which have hitherto not been detected despite numerous angle resolved photoemission spectroscopy (ARPES) experiments [52, 53, 54, 55], casting doubt on the validity of the previous LDA results. Several adaptations to the theoretical electronic structure were made in order to understand the properties of sodium cobaltate in

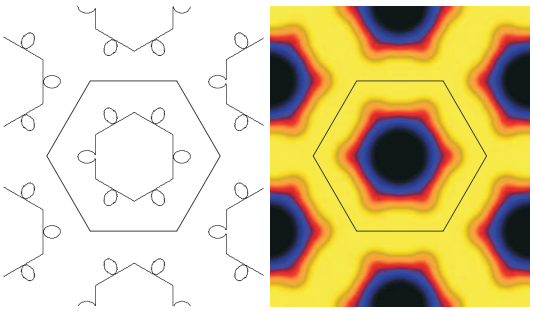

Figure 2.4: Left: A simulation of the boundaries of the Fermi surface (including the large hexagonal sheet and the six small pockets). Right: A convolution of the experimental resolution function with the simulated FS produces an occupational density map similar to those presented in figure 2.3.

the absence of the hole pockets [56, 57], however, these studies acknowledge the sensitivity of ARPES measurements to the surface state of a sample, including possible relaxation of the CoO_6 octahedral trigonal distortions and Na disorder, that may destroy the e'_g pockets altogether.

Figure 2.3 shows the experimentally obtained Fermi surface reconstructions made from the electron momentum distribution in both the anhydrous and deuterated systems measured from single crystals produced at Warwick using the technique of x-ray Compton scattering [58]. A Compton profile is a bulk measurement and represents a one dimensional projection of the electron momentum density. Given the hexagonal symmetry of the underlying crystallographic structure and electronic properties, a reconstruction of the entire FS was made possible by taking just five equally spaced measurements between ΓK and ΓM. The results clearly show the distortion of the a_{1g} sheet by the hole pockets for $x \leq 0.6$ as indicated by the convolution of the experimental resolution to the predicted FS shown in figure 2.4. It is important to note that the hole pockets are still evident in the deuterated compound and may well play a significant role in the formation of the superconducting state.

Chapter 3

Crystal Growth and Experimental Techniques

3.1 Polycrystalline Sample Preparation

The Na_xCoO_2 material was synthesised in a polycrystalline form by means of a solid state reaction of Na_2CO_3 and CoO mixed in a sodium to cobalt ratio of x:1. The powders were calcined at 750°C for 12 hours in an alumina crucible in an oxygen atmosphere, i.e. heated to a temperature below that at which the reaction takes place but high enough to decompose the carbonate:

$$Na_2CO_3 \rightarrow Na_2O + CO_2 \tag{3.1}$$

The resulting mixture, which is reground to ensure homogeneity, now contains the correct starting compounds necessary to make sodium cobaltate. The powder was heated in oxygen to 850°C for 24 hours, during which time the following reaction takes place:

$$\left(\frac{x}{2}\right) Na_2O + CoO + \left(1 - \frac{x}{2}\right) O \rightarrow Na_xCoO_2 \tag{3.2}$$

As discussed in section 2.1, these materials were first made by Fouassier et al. [11], who noted that this reaction is stable only for x $\geq$ 0.6. Indeed, attempts to make samples with lower sodium content produced a powder containing an x $\sim$0.7 sodium cobaltate phase and cobalt oxide impurity made from the remainder of the

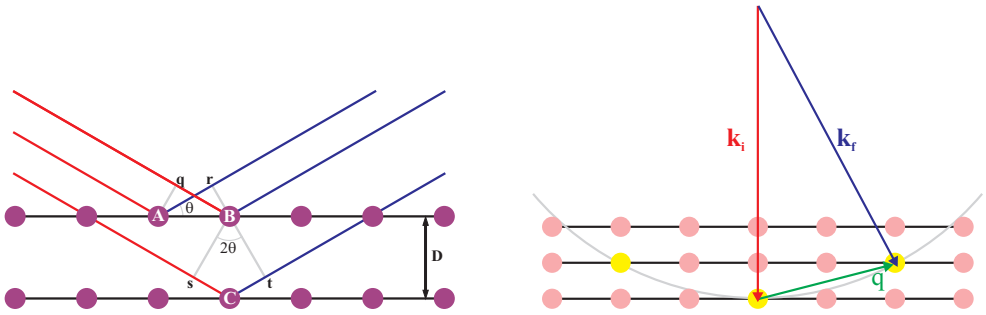

Figure 3.1: The diffraction process in real (left) and reciprocal (right) space. Parallel, monochromatic x-rays (red) are incident on planes of atoms (purple spheres). The scattered rays that are in phase with one another are shown in blue. In reciprocal space, planes of atoms are denoted by points (pink spheres). Only those reciprocal lattice points that are intersected by the Ewald sphere (yellow spheres) satisfy the Bragg condition.

Co in the starting material. All powders were therefore synthesised with x $\cong$ 0.75 and the sodium removed at a later time, as described in section 3.5.

Compounds containing sodium are very volatile and the bulk sodium content is lowered during both the above procedures. To minimize the amount of Na lost, the powders were placed in the furnace after the temperature set point had been reached. Since the composition of the product is non-stoichiometric, the exact amount of sodium lost is not important as the concentration can be measured after the manufacturing process (see section 3.6). It is necessary therefore to start with excess sodium carbonate; typically a starting mixture with x = 0.77 will produce powder with a sodium level of $\sim$0.75.

3.2 X-ray Characterisation

If a sample is bathed in a parallel beam of monochromatic x-rays, the incident rays will scatter isotropically from the atoms in the sample. If the sample also exhibits crystalline order, the x-rays scattered in certain directions will be in phase, reinforcing one another to produce a measurable signal. Consider a set of parallel atomic planes, on which a beam of x-rays is incident at an angle θ as shown in figure 3.1. The x-rays hit atoms A and B and scatter in all directions. The path

difference between the trajectories of the two waves that hit A and B that are reflected at the same angle (as shown by the blue lines) is equal to:

$$qB - rA = AB\cos\theta - AB\cos\theta = 0 \tag{3.3}$$

and so the top two "blue" x-rays will be in phase with each other and interfere constructively. In fact, rays scattered by all the atoms in the first plane that are parallel to the blue rays will have a zero path length difference and so contribute to the diffracted beam. Path length differences for rays between the first and second layers will be equal to:

$$sC + Ct = D\sin\theta + D\sin\theta \tag{3.4}$$

and will also contribute to the total diffracted beam intensity, so long as the quantity in equation 3.4 is equal to a whole number of wavelengths, i.e. $n\lambda$, where n is an integer. Therefore diffracted x-rays from a periodic array of atoms have definite phase relations between them. Higher order reflections (i.e. $n >$1) can be considered as a first order reflection from planes (real or imaginary) spaced at distances of $1/n$ times the original spacing D. The relation derived in equation 3.4 can therefore be expressed as:

$$\lambda = 2d\sin\theta \tag{3.5}$$

where $d = D/n$. This is known as Bragg's law and is the essential condition which must be met if diffraction is to occur. This is true of any scattering mechanism, be it light, x-rays or neutrons.

The diffraction process is neatly described using the Fourier transform of the real space lattice. Planes of atoms in real space are described by points in reciprocal space at a distance of $1/d$ from the origin in a direction perpendicular to the original reflecting planes. If the incident beam is plotted in a direction parallel to its real space equivalent, with a length of $1/\lambda$ Å^{-1}, terminating at the origin of the reciprocal crystal lattice, the three dimensional locus of vectors with the same length and origin as $\boldsymbol{k}_i$ will indicate all the possible configurations of $\boldsymbol{k}_f$ for

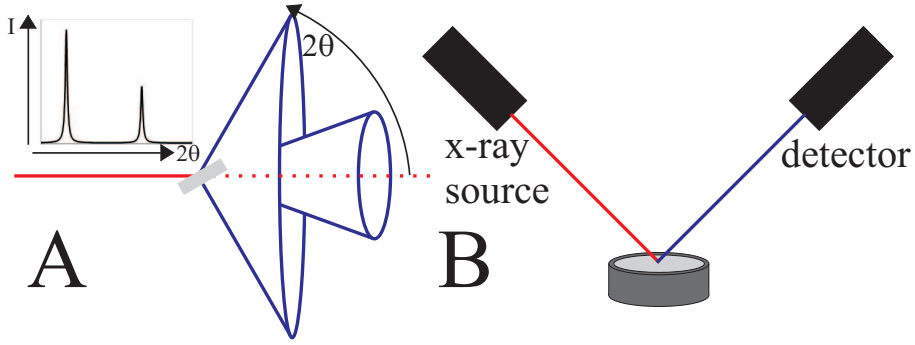

Figure 3.2: Panel A: The scattering (blue ray) of an incident x-ray (red) from a set of reflecting planes in a crystallite (grey). Random orientations of the polycrystalline particles within the sample result in cones of diffracted rays. The resulting intensity versus 2θ curve is shown in the inset. Panel B: The experimental set up of a powder diffraction experiment. Both the x-ray source and the detector are scanned through values of θ.

elastic scattering. This is known as the Ewald sphere construction and is shown (in two dimensions) on the right hand side of figure 3.1. Only the reciprocal lattice points that intersect with the Ewald sphere will be capable of satisfying the Bragg condition and contributing to the coherent scattering.

It is clear therefore, that diffraction provides a technique for determining the spacing between lattice planes in a crystalline sample, from which the crystal symmetry and lattice constants may be deduced. There are several laboratory techniques for measuring x-ray diffraction, corresponding to the variation of the two independent parameters in equation 3.5. In powder x-ray diffraction, the wavelength of the radiation is kept constant and the diffraction angle 2θ is varied. A polycrystalline powder sample consists of small crystallites, aligned randomly with respect to one another. Consider panel A in figure 3.2. The incident (red) and reflected (blue) rays are coplanar with the vector normal to the diffracting planes in the sample; the random alignment of the many micro-grains circumscribe all the possible orientations of the blue x-ray onto the surface of a cone. The process measured in this experiment is that of elastic scattering and hence the red and blue vectors must be of equal magnitude. Therefore planes with larger d spacings will

produce cones with smaller solid angles. The detector is scanned from the straight through beam with increasing values of 2θ; a peak is observed each time the camera intersects one of these scattering cones. The measurements are carried out in a Bruker D5005 diffractometer using a rotating anode source with a Cu target and a scintillation counter detector. Both the x-ray source and the detector are rotated during the measurement. Information of powder diffraction data for most compounds can be obtained from The International Centre for Diffraction Data (ICDD) Powder Diffraction File (PDF) database. A program searches the sample diffraction pattern for a list of peaks, which is compared to the PDF library. The purity of the sample under study can then be ascertained; a calculation of the volume fraction of any impurities is made possible by comparing the intensity ratios of the strongest peaks in the diffraction patterns. Signal to noise ratios for typical measurements enable impurity levels of greater than $\sim 2\%$ to be identified.

3.3 Single Crystal Production - The Floating Zone Method

The powders were isostatically pressed into cylindrical rods 1 cm in diameter and 7 cm in length. A previously grown crystal (or another polycrystalline rod) was mounted directly underneath and used as a growth "seed". The two rods were then enclosed within a quartz tube that was pressurised to 2.5 atmospheres of O_2 in order to suppress the loss of sodium. The furnaces make use of the heat of IR emitting halogen lamps, the rays of which are focused on the ends of the rods by the use of ellipsoidal mirrors, which produce enough heat to melt the sample. Chen et al. [38] determined this temperature to be $\sim$1100°C using thermogravimetric analysis. Direct temperature measurement in the image furnace by pyrometry is not possible since, by definition, all viewing axes inside the mirrors are focused on the image of the lamps. It is therefore the lamp temperature, rather than the sample temperature that is probed. The two molten rods are brought together, whilst rotating in opposite directions at 30 rpm to ensure a homogeneous mix of

material and stability of the molten crystal. This "floating zone" is then scanned along the entire length of the polycrystalline rod. At first, the crystal growth rate was set at the high value of 10 mm hr^{-1} to minimise the loss of sodium from the sample. After the growth, the quartz tube was covered in a film of white powder, identified as Na_2O by x-ray powder diffraction analysis[1]. Later crystal growths were done in two stages. The powder rod was first solidified with a "fast scan" of the zone at 30 mm hr^{-1} in order to densify the crystal starting material. This rod was then inverted and scanned at much slower rate of 2 mm hr^{-1}. Measurement of the masses before and after growth revealed that the maximum sodium loss in both the fast and slow methods was $\sim 1\%$ and must occur as the material is being heated rather than as a function of time whilst molten. The resulting crystal boule was usually oriented with a^* along the length of the crystal and with c^* perpendicular to the growth axis which could be identified by the visible facets on the boule surface. Single crystals were cut by taking slices along the boule with a circular diamond saw and cleaving perpendicular to c^* with a razor. The resulting crystals were rectangular in habit with dimensions as large as 8×12 mm^2 in the *ab* plane and 2 mm along *c*. The edges of the crystal boules usually contained volumes of crystal domains that were misaligned along *c* and hence a large volume of crystal had to be produced in order to collect a reasonable mass of single crystal that could be used in the experiments described in this thesis. A total of 18 crystal boules were therefore made over the course of two and half years.

Cleaved crystals were examined in a JEOL 6100 scanning electron microscope (SEM) with the incoming electron beam oriented perpendicular to the crystallographic *c*-axis. The backscattered electron density measures electrons that have direct collisions with atoms and can thus differentiate between atoms of different atomic species since the number of scattered electrons is proportional to the size of the electron cloud of the atom. Analysis of the images taken in

[1]The diffraction pattern was identified as that of Na_2CO_3 by comparison to ICDD powder diffraction file 19-1130. No carbonate impurity existed in the crystal precursor material or in the furnace atmosphere and it is therefore assumed that sodium oxide is produced during the crystal growth which then reacts with carbon dioxide once the furnace is opened.

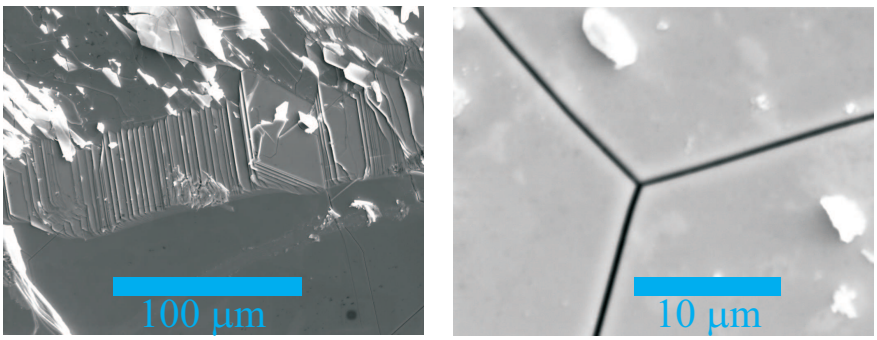

Figure 3.3: Two SEM pictures of a $Na_{0.7}CoO_2$ crystal. The image on the left shows an inclusion of misaligned crystallites with planar spacings of $\sim$3 μm. The second image shows a dislocation in the *ab* plane with hexagonal symmetry. Microcrystals, also identified to be Na_xCoO_2 are visible on the surface.

backscattered mode reveal the crystal surface to be single phased with no evidence of impurities. The SEM was then switched to secondary electron mode with an incident electron energy of 22 kV. Secondary electrons occur when an incident electron passes near enough to an atom to impart some of its energy to an atomic electron. This results in a slight change in direction of the original electron and the ionisation of the bound electron state, the secondary electron. These electrons have very small energies and hence only those within $\sim$10 nm of the surface of the sample can escape and be detected. Any feature of the surface that is larger than 10 nm will change the yield of secondary electrons so that the surface morphology can be imaged. Whilst the majority of the crystal surface is mostly featureless, occasionally crystal growth faults are visible. Images of two such faults are shown in figure 3.3. Inclusions of misaligned crystallites are most likely a result of the fast growth rates used. Dislocations in the basal planes are more common and show up the hexagonal symmetry of the underlying crystal structure. These dislocations, if they persist through the depth of the crystal, are probably the cause of the multiple domains seen in the neutron scattering study in chapter 6 and will also have an effect on the value of the resistance measurements reported in chapter 4.

X-rays are also emitted when an outer electron recombines with the hole

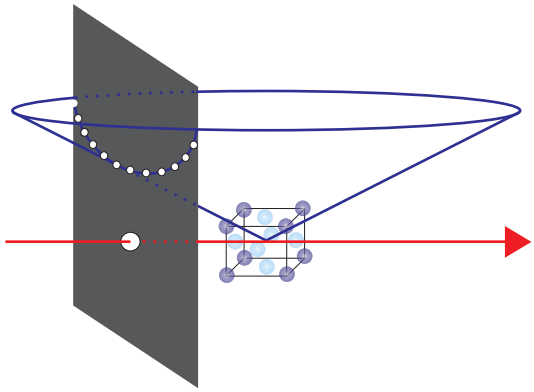

Figure 3.4: A schematic diagram of an x-ray Laue experiment. A white beam of x-rays illuminates a crystalline sample and the diffracted beams are visible as a series of spots on a photographic film or CCD camera. The method pictured above utilises back-scattering geometry; measurements may also be taken in transmission.

produced by the creation of the secondary electron. The energy of these x-rays are specific to the energy levels of each atom and therefore permit quantitative analysis of the chemistry of the sample under study. This process is known as energy dispersive x-ray analysis (EDX) and was used to determine the amount of sodium in the crystal, discussed in section 3.6.

3.4 X-ray Laue photography

The complementary x-ray diffraction technique to that described in section 3.2, used for the characterisation of single crystal samples, is x-ray Laue photography. A white beam of x-rays is incident on a crystal, having passed through a hole in a photographic film or CCD camera, and diffracted rays are emitted in all directions in three dimensions in which the Bragg condition is satisfied. The incident beam contains a continuum of wavelengths; in reciprocal space this conforms to a continuous distribution of Ewald spheres so that many diffracting planes satisfy Bragg's law simultaneously. An alternative way of viewing the process is that θ is fixed for every diffracting plane, each one selects the particular wavelength for Bragg diffraction producing a spot on the photographic film. The spots on any one

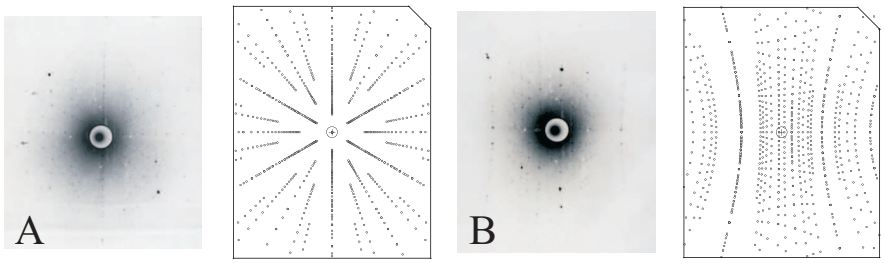

Figure 3.5: Two Laue photographs of $Na_{0.7}CoO_2$ taken with a voltage of 40 kV, a current of 100 mA and 10 minutes exposure time. Pictures A and B relate to two different orientations of the crystal to the incident beam. Knowledge of the space group, lattice parameters and reciprocal lattice directions of the crystal enable simulations to be made for comparison. Note: The images are electronic copies of photographic film, and whilst the image colours have been inverted to improve clarity, the high colour contrast makes it difficult to appreciate the full range of visible spots.

curve, as shown in figure 3.4, belong to the same zone (for example $[00l]$) since these reflections lie on the surface of an imaginary cone whose zone axis is coincident with the cone axis. The symmetry of the pattern of spots depends on the symmetry of the crystal as viewed down the camera axis. Analysis of the patterns allows the crystallographic axes of the sample to be identified. Two such patterns from a Na_xCoO_2 crystal are shown in figure 3.5, along with simulated patterns using the crystallographic indexing software "OrientExpress" [59]. In panel A, the x-ray beam was oriented along the *c* axis of the crystal; the hexagonal symmetry of the lattice in the *ab* plane is evident in the diffraction pattern. Panel B shows an image taken with the crystal rotated through 90°. The sharp array of spots in the pattern, and the good match to the simulation, show that the crystal has clear, long-ranged order. However, x-rays penetrate only the surface of the material. To ensure the sample is a single crystal throughout, images must be taken along the length of the sample and along equivalent directions.

3.5 Sodium Deintercalation Technique

In order to access a large portion of the magnetic phase diagram, sodium was removed from the $Na_{0.75}CoO_2$ materials using a chemical deintercalation technique. Crystals were immersed in solutions of either Br_2:CH_3CN or I_2:CH_3CN. The use of halogens to oxidise metals (producing halides as a byproduct) is a relatively simple laboratory technique, however bromine and iodine are both toxic and caustic materials, and care must be taken when handling the chemicals. The deintercalation process is described by:

$$Na_xCoO_2 + \frac{1}{2}Br_2/I_2 \rightarrow Na_{(x-y)}CoO_2 + yNaBr/I \tag{3.6}$$

Full deintercalation to a stoichiometry of $x = 0$ is theoretically made possible by using a Br/I concentration of $y = x$. With knowledge of the starting composition x, the mass of the crystal and the molecular masses of the compounds in equation 3.6, the amount of Br/I needed to achieve a new sodium concentration of $(x - y)$ is easily computed. In reality a much stronger concentration is necessary as the majority of the halogen remains in the acetonitrile (CH_3CN) solution without reacting with the sodium cobaltate. The deintercalation technique was optimsed using I_2 as an oxidising agent and an empirical relation was found where a 1:1 mass ratio of $Na_{0.75}CoO_2$ to I_2 produces a change in sodium concentration of $(x - y) = 0.2$. The addition of acetonitrile was necessary to dissolve the iodine and provide a solution for the deposition of the sodium halide. The exact amount used is unimportant, but was kept constant at ∼40 ml per gram of Na_xCoO_2.

The kinetics of the sodium removal process is still unclear. Initial experimental results using powders reported deintercalation processes taking between one and five days [10]. The equivalent process for single crystal samples was estimated to have deintercalation times an order of magnitude greater. In fact, the large spacing between the CoO_2 layers enables high ionic mobility within the $(hk0)$ planes. Typical deintercalation times for single crystal samples reported in

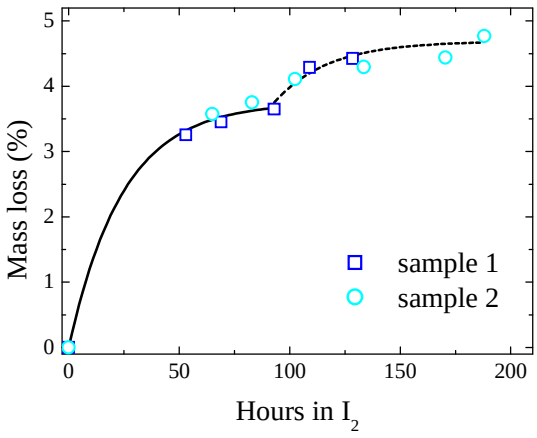

Figure 3.6: The mass lost from two large single crystal samples placed in two different strengths of iodine-acetonitrile solutions are plotted as a function of time. The percent reduction in the total crystal mass decreases with increasing time; the entire process is complete after just one week. The black line is a fit to the data, the dashed line is a copy of the first fit, scaled to the relative strength of the new solution.

the literature are of the order of one or two weeks [25]. To test this, two large (3.2 g and 4.6 g) crystal boules were placed in I_2:CH_3CN solution with the aim of changing x from 0.75 to 0.50, and the amount of sodium removed was monitored by measuring the mass lost from the sample (see section 3.6) at regular intervals. The mass loss (ML) with respect to time (t), shown in figure 3.6, fitted an inverse exponential decay law $ML = ML_0 + Aexp\,(-t/\tau)$ where ML_0 is the mass loss related to the value of $(x - y)$, A is a constant and τ a characteristic timescale. The deintercalation process is predicted to be complete after $\sim$165 hours, in good agreement with the reported values. However, after 100 hours the crystals were placed in a new I_2:CH_3CN solution with just one third of the iodine mass used previously, in order to attain $\sim 5\%$ total mass loss in accordance with a value of $(x - y) = 0.25$. The data from the fit obtained previously was scaled along ML by a factor of a third, and the origin of the curve translated to the last measured values of (ML, t). The mass loss was monitored for a further 100 hours; the data for both samples fit remarkably well to the empirical fit.

A second technique for the removal of sodium in Na_xCoO_2 is described

in reference [60]. The process uses the sodium cobaltate crystal as an anode in an electrochemical cell with NaOH as the electrolyte solution, with a Pt cathode and a Ag/AgCl reference electrode. Sodium is deintercalated through the reaction $Na_xCoO_2 + \delta\,(OH)^- \rightarrow Na_{x-\delta}CoO_2 + \delta\,(NaOH) + \delta e^-$ by the application of small voltage across the Na_xCoO_2-Pt circuit.

3.6 Doping Level Monitoring Techniques

The magnetic properties of sodium cobaltate are highly sensitive to the exact level of sodium within the system. An accurate determination of x for each sample is imperative for the characterisation of the magnetic phase diagram. The lack of clarity in the determination of the exact sodium content of a sample is almost certainly the origin of the large number of conflicting results in experimental reports on studies of samples with nominal x values, as discussed in chapter 2. There are two main techniques used to measure x that are used widely in the literature.

The first is Inductively Coupled Plasma Atomic Emission Spectroscopy (ICP-AES). The samples are dissolved in nitric acid to produce an aqueous solution, before being introduced into the core of an inductively coupled plasma (usually argon at $>$8000°C). The thermal excitation of each element in the sample results in the emission of light at characteristic wavelengths. The full spectrum is passed through a diffraction grating so that a profile of light intensity as a function of λ may be obtained. The relative intensities for each element produce a mass ratio for all the elements in the sample, when calibrated with a sample of known elemental concentration. The necessary equipment to carry out this procedure is not readily available to the Superconductivity $\&$ Magnetism Group and so the samples were analysed by Warwick Analytical Services [61]. A series of samples, both polycrystalline and single crystal, were sent for analysis in order to determine the characteristics of the sodium deintercalation process. The process suffers from several drawbacks. Firstly, this is a destructive measurement technique; it is more

useful to determine x before the measurements are made rather than afterwards. Secondly, although the technique is relatively precise (with an error in x of just 5%) the absolute accuracy depends on a calibration to a standard sample. During the powder reaction processes, an unknown quantity of sodium is lost, and so the production of a standard to calibrate the other measurements against is difficult. Thirdly, the process describes the bulk measurement of the elemental concentrations for the whole sample: any information about Δx across the sample is lost. Finally, the subcontracting of measurements to a private company is both costly and time consuming.

The second technique, energy dispersive x-ray analysis (EDX), was described in section 3.3. Although time consuming, this process provides a measure of the elemental mass ratios in an area localised to the finite size of the x-ray beam. The spread in sodium concentration across the surface of a sample can therefore be measured. Typically distributions in sodium content were found to be of the order of $\Delta x = 0.01$. EDX probes just the sample surface. In order to verify the crystals were single phased throughout the layers, several samples were cleaved in half. The stoichiometry of the freshly cleaved phases was found to agree well with the value measured for the outside of the crystal.

Several other techniques for estimating x were developed throughout the course of this thesis work. The first relies on the rather obvious fact that as sodium is removed from the sample, the mass decreases. This enables the deintercalation process to be monitored as a function of time, as shown in diagram 3.6. The change in mass (Δm) can be related to the change in sodium content ($x - y$) with knowledge of the molar masses of Na, Co and O:

$$y = \frac{1}{m\,(Na)}\left[\Delta m\, x\, m\,(Na) + (\Delta m - 1)\, m\,(CoO_2)\right] \tag{3.7}$$

Again, this technique relies on knowledge of the starting composition x, and the results therefore must be calibrated against other measurements. For instance, if a large group of samples ($\sim$15) are subject to deintercalation with a range

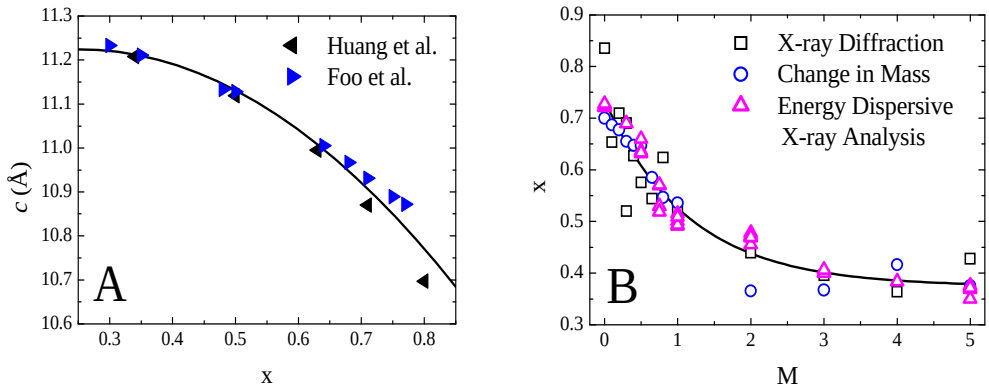

Figure 3.7: Panel A: The relationship between the *c*-axis lattice parameter and the sodium content x; reproduced from Huang et al.[10] and Foo et al. [25]. Panel B: Measurements of x on a set of crystals deintercalated in increasing strengths of I_2:CH_3CN solution (M denotes the amount of I_2 theoretically needed to remove all the sodium).

of strengths of Br_2/I_2 solutions, the magnetic susceptibility of each one can be measured and the sample with the largest indication of the magnetic ordering found at $x = \frac{1}{2}$ assigned to that particular stoichiometry.

The final technique used to determine the sodium content of samples makes use of the well characterised variation of the *c*-axis lattice parameter as a function of x. It is known that the reduction in sodium content produces an increase in the NaO_2 layer because of a reduced interlayer Coulomb attraction that is not offset by the small decrease in the CoO_2 layer caused by the decrease in the cobalt valence. Using the results of neutron and x-ray powder diffraction [10, 25] a calibration curve of *c* versus x may be produced (as shown in panel A of figure 3.7). The *c*-axis reflections are measured using the diffractometer described in section 3.2, from which *c* and therefore x may be determined.

Panel B of figure 3.7 shows results obtained for a set of crystals placed in increasing strengths of I_2:CH_3CN solutions, where $1M$ denotes the amount of I_2 theoretically needed to remove all of the sodium in the sample (equivalent to $y = x$ in equation 3.6), left for sufficient time for the full deintercalation process to take place. Measurements of x were obtained by measuring the change in mass, EDX measurements and *c*-axis lattice parameter measurements. It is clear that

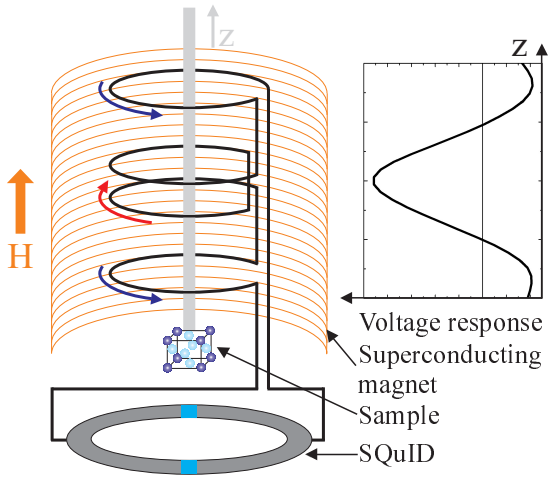

Figure 3.8: A schematic diagram of a SQuID magnetometer (not to scale). The sample is scanned along z through the pick-up coils. The change in current within the detection system is measured by the SQuID sensor, which is located inside a superconducting shield (not shown). The measured voltage response curve is fitted and a value of the magnetisation computed.

all three techniques give results generally in good agreement with one another. It is through the crystal characterisation using these three techniques that the relationship between iodine concentration and change in x, as stated in section 3.5, was obtained. The deintercalation process as a function of I_2 concentration was repeated a further two times, with identical results obtained showing that the process is repeatable and sample independent.

3.7 Magnetisation Measurements

3.7.1 The SQuID Magnetometer

A magnetometer uses the principle of Faraday's Law of electromagnetic induction in order to measure the magnetisation of a sample using a set of pick-up coils. The detection coil is superconducting itself, and wound in the formation of a second-derivative gradiometer. The sample is step-scanned through the gradiometer, the change of magnetic flux associated with this movement produces a change in the persistent current. These pick-up coils are inductively coupled via a set of superconducting wires to a Superconducting Quantum Interference Device (SQuID) located inside a magnetic shield below the sample space. A SQuID consists of a superconducting ring with two Josephson junctions in parallel; variations in the current in the detection coils result in proportional variations in the

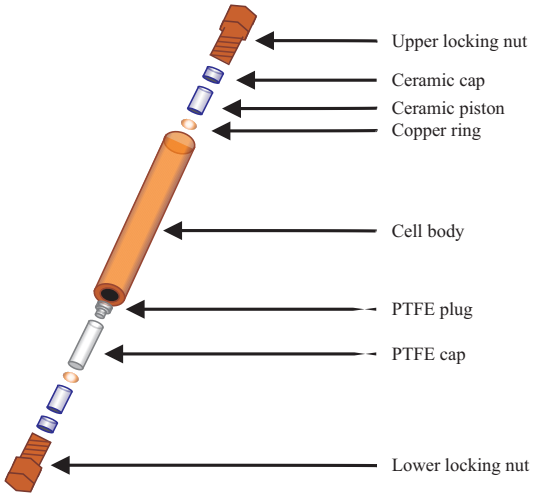

Figure 3.9: The components of the Mcell10 hydrostatic pressure cell, reproduced from reference [62].

SQuID output voltage. The calibration of this voltage response curve to a sample of known mass and magnetic susceptibility enables the measurement of magnetic moments in other samples. The SQuID essentially acts as an extremely sensitive flux-to-current-to-voltage converter and is capable of resolving moments as small as 5×10^{-7} emu. The measurements may be taken over a temperature range of 1.8 - 400 K, with an externally applied field of up to 50 kOe.

3.7.2 Magnetisation Measurements Under Pressure

Magnetisation measurements made under external pressures of up to 10 kbar were made using the easyLab Technologies' Mcell 10 hydrostatic pressure cell [62]. The cell is designed for use with the Quantum Design MPMS SQuID magnetometer as described in section 3.7.1, a schematic diagram of the equipment is shown in figure 3.9. The sample is loaded in a PTFE capsule filled with Daphne oil (the pressure transmitting medium). Pressure is applied to the capsule via the two ceramic pistons using a hydraulic press, and maintained by tightening the end locking nuts. The pressure is measured in situ via the use of a Sn manometer placed alongside the sample, using knowledge of the variation in the superconducting critical tem-

perature of tin as a function of pressure. The method of data collection makes use of the automatic background subtraction feature of the MPMS magnetometer, in which the voltage response curves for the empty cell are recorded at the relevant temperatures and fields and then subtracted from the total voltage response from the cell plus the sample. The fit of the difference curve therefore gives the value of the moment in the sample. In order to carry out this subtraction procedure effectively a dummy capsule, shorter in length than the real capsule, is used in the background measurements in order to mimic the change in length with applied pressure. Using this method, magnetic moments as low as 1×10^{-5} emu may be measured.

3.7.3 The Vibrating Sample Magnetometer

In the Vibrating Sample Magnetometer (VSM), the sample is mounted equidistant between two pick-up coils wound in opposite senses, and vibrated about this central position with a known frequency (usually in the audio range). The induced a.c. voltages in each coil are added together and the signal amplified and recorded. The use of a heavy frame ensures the vibrating motor and the pick-up coils are vibrationally isolated from one another and the whole system is mounted on a concrete platform so that external vibrations are also strongly damped. Calibration of the voltage to a sample of known mass and magnetisation enables the output of magnetic moments for the sample under study to an accuracy of 5×10^{-6} emu. As in the SQuID magnetometer, a superconducting solenoid is placed outside of the pick-up coils and produces a vertical field of up to 120 kOe. The temperature control system facilitates the taking of measurements between 1.4 and 300 K.

3.7.4 χ_{ac} Magnetometry

ac magnetic susceptibility was measured using a standard mutual inductance technique. A primary coil provides an alternating field in a frequency range of 20-20000 Hz with typical excitation fields of a few oersted. Inside the primary coil lies

a secondary (pick-up) coil, which consists of two coils wound in opposite senses. The sample is placed inside the first area of the pick-up coil and the voltage measured. It is then moved to the second area and the voltage measured once more. The difference between these two measurements is equal to twice the voltage induced in the pick-up coil from the sample alone and enables the background signal to be eliminated.

It is the dynamics of the magnetisation that are under investigation in a χ_{ac} measurement; the measurement is sensitive to dM/dH rather than the absolute value of $M(H)$ so that small changes in the magnetisation are apparent. Both the magnitude of the susceptibility and the phase shift relative to the driving frequency are measured, yielding both the real and imaginary parts to χ_{ac}. The second of these two quantities describes the dissipation of the moments within the sample and is therefore an important measurement in systems such as spin glasses.

3.8 Heat Capacity Measurements

The measurement procedure employed in the Physical Properties Measurement System (PPMS) is a pulse-relaxation calorimetry technique. The sample is mounted on a platform (using Apeizon H or N grease to ensure good thermal contact) to which a heater and thermometer are attached. The platform is suspended from the sample puck by wires, which supply the heating power as well as providing thermal contact to the cryogenic bath (the puck). Heat is applied to the platform at a constant rate until T has increased by a designated proportion of the set point (typically 1%). The heating power is then removed and the sample and platform temperature relaxes exponentially back to the set point. The measurement of the temperature versus time can then be fitted using a two-tau relaxation model. The exponential decay consists of two decay modes, one related to the thermal conductivity between the platform and the puck and another proportional to the heat capacity of the sample. The first quantity is estimated from a background

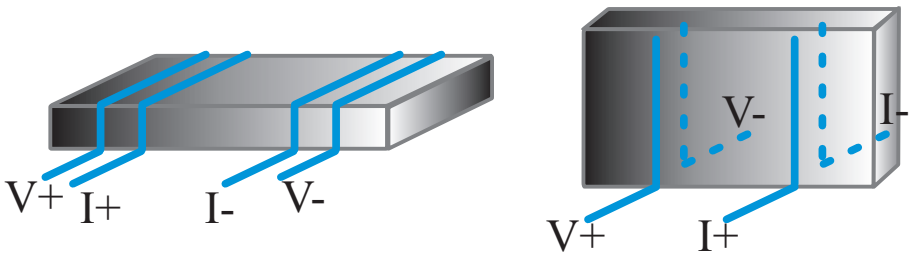

Figure 3.10: Experimental arrangements for anisotropic resistivity measurements, with the current flowing in the *ab* planes (left) and along the *c*-axis (right).

measurement of the platform and Apeizon grease under the same conditions as the actual measurement. The sample heat capacity can then be calculated. This measurement technique relies on the presence of a good vacuum (less than 1 mTorr) to ensure no thermal link to the bath exists through residual helium in the sample space. The thermal diffusion time in the sample must be small in comparison to the time constant; i.e. the platform-sample system must be capable of reaching thermal equilibrium quickly since the presence of persistent high temperature gradients within the sample results in inaccurate measurements.

Measurements made using the PPMS may be obtained over a temperature range of 400 mK to 400 K using both a standard ^{4}He system and a ^{3}He insert. The magnet is capable of providing external fields of up to 90 kOe and measurements may be taken with the sample oriented with the *c*-axis either parallel or perpendicular to H.

3.9 Transport Measurements

Measurements of the dc resistivity (ρ_{dc}) were made in a Quantum Design PPMS under applied fields of up to 90 kOe and a temperature range of 1.8 - 400 K. Current densities in the range of 0.2 - 2 A cm^{-2} were applied to single crystal samples through fine silver wires attached to the sample with silver epoxy. A standard four probe geometry was used for the measurements of ρ in the *ab* plane.

Measurements along the *c*-axis were made with the current (I) contacts attached to the *ab* planes of the crystals and the voltage leads also on the *ab* faces (as shown in figure 3.10). Measurements were made with the field oriented both parallel and perpendicular to *c*, in order to probe the nature of the magnetoresistance (MR) in Na_xCoO_2.

3.10 Constant Wavelength Neutron Diffraction

Neutrons are produced in two different ways, through the fission of ^{235}U in a nuclear reactor (as used at the *Institut Laue Langevin* (ILL) and the *Laboratoire Léon Brillouin* (LLB) in France) or through a spallation process which involves the collision of high energy protons that have been accelerated in a synchrotron with a heavy metal target (as at *ISIS* in the UK or the *Paul Scherrer Institut* (PSI) in Switzerland). Both processes require the use of a room-temperature moderator, in which the neutrons are slowed to thermal velocities via collisions with light atoms such as deuterium. The resulting neutron flux has a Maxwellian distribution of energies, the central energy value corresponding to the temperature of the moderator. For diffraction experiments, as is the case for the x-ray diffraction measurements described in section 3.2, the wavelength should be kept constant whilst the diffraction angle is varied. The beams are therefore monochromated by diffraction from high quality crystals or a mechanical rotating device known as a *chopper*, which permits neutrons that are travelling at the correct velocities to pass through a small window. In the first case, higher order diffraction with wavelengths of λ_N/n also occurs. These secondary wavelengths must be removed by filters, but monochromation of this kind results in a continuous beam and is the method used at PSI. The second method, used at ISIS, results in a pulsed neutron beam with an error in λ_N related to the width of the chopper window. A pulsed neutron beam necessitates an analysis method known as *time-of-flight*. In the detector system of the instrument, the neutrons are counted both as a function

of position and time. The time taken (t) for the neutron to travel a distance L from the chopper to the sample to the detector can be used to determine the magnitude of $\boldsymbol{k}_f$ via the relation $|\boldsymbol{k}_f| = m_N L/\hbar t$.

Any sections of the sample environment or mounting through which the incident and scattered neutron beams must pass are made from aluminium which has a negligible absorption and incoherent scattering cross section. Any sections of the sample mounting equipment which the experimenter wishes to remain "hidden" from the neutron beam are wrapped in cadmium, which has an exceptionally high absorption cross section. The detectors in all of the neutron scattering instruments used in this thesis work were position sensitive ^{3}He detectors (PSD). When a neutron enters the detector, the helium gas inside the chamber is ionised via the following reaction:

$$^3_2He + n \rightarrow ^3_1 H + p + 0.77\,MeV \tag{3.8}$$

If a voltage is applied across the gas chamber, the emitted charged He ions result in a measurable electrical pulse.

In a powder neutron diffraction experiment, an array of ^{3}He detectors are placed on an arc, each one equidistant from the sample. Rather than scanning a detector through a range of 2θ values, data at each angle are collected simultaneously. In a single crystal diffraction experiment, the sample is rotated through the Bragg condition and a plot of neutron counts versus rotation angle is recorded. The resulting curve is fitted to a Gaussian or Lorentzian distribution and the integrated area used to determine a quantity known as the *nuclear structure factor*, defined as:

$$F_N(\boldsymbol{q}) = \sum_i \overline{b}_i e^{i\boldsymbol{q}.\boldsymbol{R}_i - W_i(\boldsymbol{q})} \tag{3.9}$$

where $\boldsymbol{R}_i$ represents the position vector of atom i within the unit cell and the last term in the exponential is known as the *Debye-Waller factor* which accounts for the thermally induced displacements of the atoms around their mean position.

The structure factor is related to the coherent elastic differential cross section via:

$$\left(\frac{d^2\sigma}{d\Omega}\right) = \frac{(2\pi)^3}{V_0}\sum_{\tau}\left|F_N\left(\boldsymbol{q}\right)\right|^2\delta\left(\boldsymbol{q}-\boldsymbol{G}\right) \tag{3.10}$$

where V_0 is the volume of the crystallographic unit cell and $\boldsymbol{G}$ a reciprocal lattice vector. The delta function in the above equation is a restatement of the Bragg condition that diffraction may only occur when the momentum transfer vector equals a reciprocal lattice vector. Of course, in reality a Bragg reflection does not correspond to a delta function. The Bragg peaks are finite in two dimensional space due to factors such as crystal mosaic spread and instrumental resolution (due to an error in the incident neutron wavelength and/or imperfect collimation). In three dimensions, the Bragg reflection is contained within a *resolution ellipsoid*. It is for this reason that the reflection is measured and integrated over an extended range to measure the total intensity of each reflection (I_{hkl}). The structure factors are calculated thus:

$$I_{hkl} = \frac{N_{hkl}\omega}{\Phi_0} = \frac{\lambda^3 V}{V_0^2}\left|F_{hkl}\right|^2 \tag{3.11}$$

where N is the number of diffracted neutrons, V the sample volume and ω the rotational angular velocity. Several corrections need to be made to the data. Firstly, as mentioned above, thermal agitation of the crystal structure is accounted for via the Debye-Waller factor. Secondly, if the sample is highly absorbing a correction for Φ_0 as a function of sample thickness needs to be made. Thirdly an effect known as *extinction* should be accounted for. Primary extinction produces a similar effect to absorption; if a large proportion of the incoming neutrons are diffracted by the first part of a crystal, the incident flux further into the crystal is significantly reduced. Secondary extinction relates to the diffraction of beams by misaligned domains within the crystal. Finally, the Lorentz factor incorporates the effect due to the angular rotation of the crystal. Since the Ewald sphere is centred on the origin of $\boldsymbol{k}_i$ and not the reciprocal lattice, a constant speed of rotation in real space causes different points in reciprocal space to pass through the Ewald sphere with different velocities; each reciprocal lattice point therefore obtains a

different period of time with which to satisfy the Bragg condition leading to an alteration in the measured values of I_{hkl}.

3.11 Least-Squares Structure Refinement

Least-squares refinement techniques applied to crystal structure refinements fit into two main categories. Firstly, the Rietveld technique for the analysis of powder data uses the entire intensity versus 2θ profile function to fit calculated profiles to the observed data points. Secondly, a list of observed structure factors $|F_{hkl}|_O$ are compared to calculated structure factors $|F_{hkl}|_C$, in a similar process using the refinement of parameters in the structural model to minimise the difference between $|F_{hkl}|_O$ and $|F_{hkl}|_C$. This second technique can be used for the analysis of either single crystal or powder samples.

The work presented in chapter 5 of this thesis utilises the Rietveld refinement method. An intensity profile as a function of scattering angle is measured and the peaks in the pattern indexed to a particular space-group, from which an accurate determination of the unit cell parameters can be made. Diffraction patterns from structures with large unit cell volumes and relatively low symmetry contain a large number of reflections, the intensities of which may overlap depending on the diffractometer resolution function and the quality of the sample. In other words, the intensity at any one particular step in 2θ is likely to contain contributions from several Bragg reflections. This, combined with an unknown error in the measured values of 2θ, makes the process of assigning Miller indices to every reflection a difficult task. The Rietveld method overcomes this problem by fitting the diffraction as a whole (I_i), rather than a set of individual (I_{hkl}) reflections, with a least-squares fit to each value of intensity in the pattern carried out simultaneously. A review of Rietveld refinement method can be found in reference [63]; a general overview of the process is presented below.

Let y_{io} be the observed intensity of the i^{th} data point and y_{ic} the intensity

calculated from the structural model. This model is refined by minimising the quantity S_y:

$$S_y = \sum_i w_i \left(y_{io} - y_{ic}\right)^2 \tag{3.12}$$

where $(w_i)^{-1} = \sigma_i^2 = \sigma_{ip}^2 + \sigma_{ib}^2$ is the weighting factor for each intensity, σ_{ip} is the standard deviation associated with the peak value (Poissonian counting statistics) and σ_{ib} is the standard deviation associated with the background measurement. As mentioned above each value of y_{ic} is equal to the sum of contributions from neighbouring Bragg reflections plus a value from the background. The calculated intensities are determined from the $|F_{hkl}|^2$ values obtained from the structural model. Specifically:

$$y_{ic} = s \sum_{hkl} L_{hkl} \left|F_{hkl}\right|^2 G\left(\Delta\theta_i\right) P_{hkl} A + y_{ib} \tag{3.13}$$

where s is a scale factor, L_{hkl} contains the Lorentz, polarisation and multiplicity factors for reflection (hkl), F_{hkl} is the structure factor for reflection (hkl), $\Delta\theta_i$ is the 2θ value corrected for the zero-point shift of the detector, $G\left(\Delta\theta_i\right)$ a reflection profile function, P_{hkl} the preferred orientation function, A an absorption factor and y_{ib} the background intensity at the i^{th} step. The reflection profile function is dependent on many factors including the nature of the source of radiation, the distribution of wavelengths in the incident beam (perhaps due to the finite mosaic spread of a crystal monochromator), the beam collimation and the detector system. As such, Rietveld refinement programs usually contain many different choices of profile function shapes. The correct function, and the values of the refinable parameters within it, should be previously determined by the analysis of a standard sample, usually Si. For the analysis of the data presented in chapter 5, a triple pseudo-Voigt function was used. The pseudo-Voigt function $pV\left(x\right)$ is a linear combination of a Lorentzian $L'\left(x\right)$ and a Gaussian $G'\left(x\right)$ distribution, i.e. $pV\left(x\right) = \eta L'\left(x\right) + \left(1-\eta\right) G'\left(x\right)$ where η is a constant between 0 and 1. The triple pseudo-Voigt profile is defined as:

$$G\left(x\right) = XpV\left(x - D\right) + \left(1 - X - Y\right) pV\left(x\right) + YpV\left(x + D\right) \tag{3.14}$$

where $D = S/d\cos\theta$ and X, Y and S are refinable constants. The full width half maximum (FWHM) of the peaks varies with scattering angle:

$$\begin{aligned}(FWHM)_{G'(x)} &= \left(U\tan\theta^2 + V\tan\theta - W\right)^{1/2} \\ (FWHM)_{L'(x)} &= X\tan\theta + \frac{Y}{\cos\theta}\end{aligned} \tag{3.15}$$

where U and V are also refinable parameters. The background term in equation 3.13 arises from factors such as diffuse scattering, noise in the detector system and insufficient shielding. It is usually refined to a polynomial function:

$$y_{ib} = \sum_n b_n \left(2\theta_i\right)^n \tag{3.16}$$

where b_n are refinable coefficients.

A successful profile refinement relies on the knowledge of a reasonably accurate crystal structure and profile parameters. The second of these two quantities, as mentioned above, may be obtained from the fitting of data from a sample where the crystal structure is already accurately known. If this information is not available the "Le Bail" refinement process may be used, where the calculated intensities are adjusted to fit the observed intensities in order to obtain initial values for the profile parameters, before the refinement of the crystal structure is attempted. The refinable parameters for each phase in the crystal structure include the lattice parameters, the (x_i, y_i, z_i) atomic positions of each site (unless constrained to high symmetry positions), the atomic thermal parameters B_i and the site occupancies n_i. Multiple phases may be refined simultaneously and the whole procedure repeated for patterns taken at different temperatures, magnetic fields and/or pressures in order to characterise the structural (and possibly magnetic) properties of a material across its phase diagram.

There are several measures of the accuracy of the refinement. The most useful of these are the weighted profile $R_{wp} = \left[S_y / \sum_i w_i y_{io}^2\right]^{1/2}$ and the expected profile $R_E = \left[(n-p) / \sum_i w_i y_{io}^2\right]^{1/2}$ (where n and p are the number of data points in the profile and the number of refined parameters respectively).

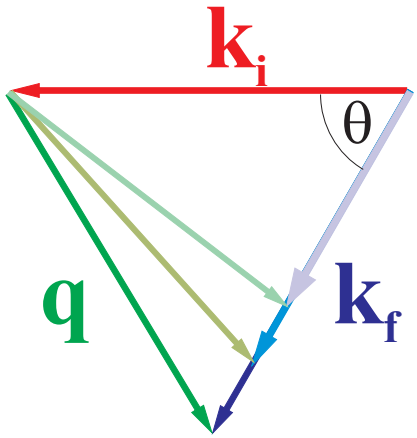

Figure 3.11: The scattering triangle for neutrons with incident and final wavevectors $\boldsymbol{k}_i$ and $\boldsymbol{k}_f$.

The square of the ratio of these two values is equal to the reduced chi-squared value (χ^2). Another useful indication of the goodness of fit is the Bragg factor $R_B = \sum_{hkl} |I_{O\,hkl} - I_{C\,hkl}| \,/\, \sum_{hkl} I_{O\,hkl}$ as this depends on the fit of the structural parameters more than on the fit to the profile.

3.12 Neutron Spectroscopy

Neutron diffraction describes the elastic scattering of a neutron from an atom and provides information for determining the crystal structure. Neutrons are also inelastically scattered from atoms, either losing or gaining energy during the collision. A diffraction experiment counts neutrons that satisfy the Bragg condition of the crystal i.e. when $|\boldsymbol{k}_i| = |\boldsymbol{k}_f|$, the scattering processes when this condition is not met are measured in inelastic neutron spectroscopy (INS) and give information on the time dependence of atomic motions. The scattering vector $\boldsymbol{q}$ is defined as the difference between the incident and final wavevectors $\boldsymbol{q} = \boldsymbol{k}_i - \boldsymbol{k}_f$. Applying the cosine rule to the wavevector configuration (shown in figure 3.11) gives:

$$\boldsymbol{q}^2 = \boldsymbol{k}_i^2 + \boldsymbol{k}_f^2 - 2\,|\boldsymbol{k}_i|\,|\boldsymbol{k}_f| \cos\theta \tag{3.17}$$

Written in terms of the neutron energy:

$$\frac{\hbar^2 \boldsymbol{q}^2}{2m_N} = E_i + E_f - 2\sqrt{E_i E_f}\cos\theta \tag{3.18}$$

The neutron transfers both energy ($\hbar\omega$) and momentum ($\boldsymbol{q}$) to the sample; an inelastic scattering experiment therefore counts neutrons that satisfy equation 3.17 and maps out the scattering function $S(\boldsymbol{q}, \hbar\omega)$. The scattering function at non-zero energy contains both inelastically scattered neutrons and quasielastic scattering - scattering due to non-periodic motions of atoms that results in nearly elastic scattering at $\boldsymbol{q}$ values between Bragg reflections. The coherent part of this scattering is also known as diffuse scattering as mentioned in section 1.3.2, which characterises the deviation of the system from perfect (spatial or temporal) periodic order, and results in a broadening of the elastic line into both positive and negative energy transfer (see figure 3.13).

The techniques for measuring INS are split into two categories, direct and indirect geometry spectrometers. Direct geometry instruments monochromate the incident neutron beam. Aligning the crystal along a direction of interest with the neutron beam defines $\boldsymbol{k}_i$ in terms of the reciprocal lattice of the system under study. The neutron scatters from the sample, changing in both energy and momentum and then $\boldsymbol{k}_f$ is measured. Indirect geometry spectrometers make use of a white beam of neutrons (either by taking the incident beam at a spallation source, or by inserting a chopper into the beam on a steady state reactor source). A crystal analyser then selects the final neutron energy. Further to this, direct geometry spectrometers are divided into two categories, time of flight spectrometers and triple axis spectrometers.

3.12.1 Time-of-Flight Spectroscopy

As described above, the incident neutron energy and direction with respect to the crystal are fixed by the experimenter. The neutron transfers both momentum and energy to the sample and the direction and time of the scattered neutron is then

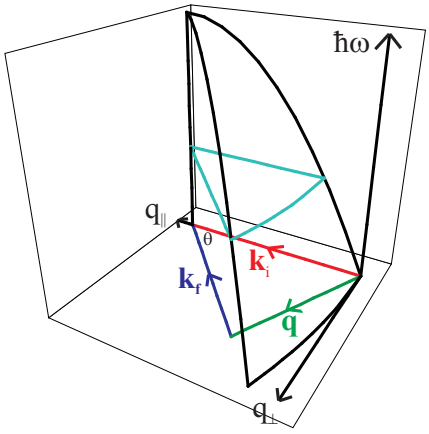

Figure 3.12: The range of $(\boldsymbol{q}, \hbar\omega)$ space available to a set of detectors that lie in an arc with scattering angles between 0 and θ. The plane that describes scattering in all available directions with a constant and finite positive energy transfer is outlined in pale blue.

measured. Consider a detector that is situated at an angle θ to the incoming beam. Expressing equation 3.17 in terms of the scattering vectors gives $\hbar\omega = \frac{\hbar^2}{2m}\left(|\boldsymbol{k}_i|^2 - |\boldsymbol{k}_f|^2\right)$, i.e. the difference of the magnitude of the scattering vectors in quadrature is equal to the energy transferred from neutron to sample. For the given scattering angle θ there exists a set of $\boldsymbol{k}_f$s and $\boldsymbol{q}$s that will close the scattering triangle, the energy transfer corresponding to each set will be parabolic in form, as shown in figure 3.12. A line of such detectors, all at the same distance from the sample, will therefore produce a scattering plane in $(\boldsymbol{q}, \hbar\omega)$ space in the form of a paraboloid. This technique requires judicious choice of $\boldsymbol{q}_\parallel$ and $\boldsymbol{q}_\perp$ when aligning the crystal since the third component of $\boldsymbol{q}$ is integrated over in the measurement.

The energy resolution of a direct geometry TOF instrument is related to the width of the pulse from the moderator (Δt_m) and the opening time of the chopper (Δt_{ch}). The total energy resolution is a summation of the two error terms:

$$\begin{aligned}\left(\frac{\Delta\epsilon}{E_i}\right)^2 &= \left(\frac{\Delta\epsilon_m}{E_i}\right)^2 + \left(\frac{\Delta\epsilon_{ch}}{E_i}\right)^2 \\ \left(\frac{\Delta\epsilon_{m[ch]}}{E_i}\right) &= 2\left(\frac{\Delta t_{m[ch]}}{t_{m[ch]}}\right)\left[1 + \frac{l_{m[ch]}}{l}\left(1 - \frac{\epsilon}{E_i}\right)^{3/2}\right] \end{aligned} \qquad (3.19)$$

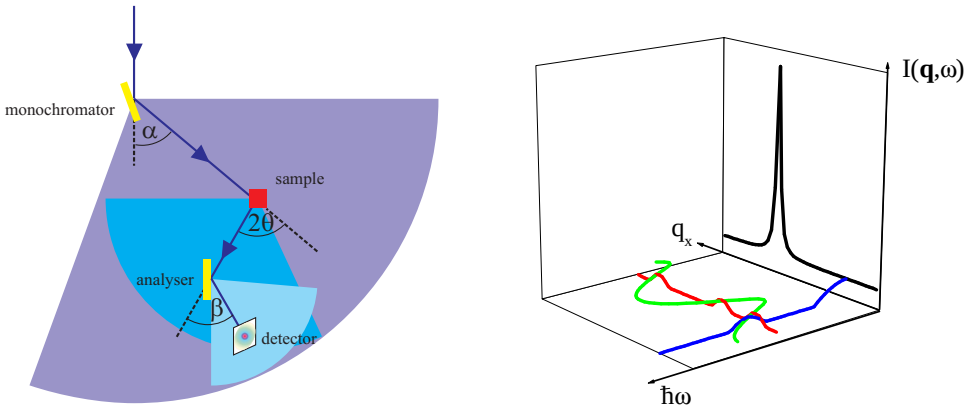

Figure 3.13: The scattering plane in a TAS measurement in real (left) and reciprocal (right) space. The elastic channel (black - not drawn to scale) at $\hbar\omega = 0$ is made up of Bragg reflections, incoherent and diffuse scattering. A magnetic excitation (green) at finite energy transfer is also plotted. The TAS method employs two modes of operation: constant $\boldsymbol{q}$ scans (blue) and constant $\hbar\omega$ scans (red). An excitation is mapped by locating the peaks on both types of scans.

where $\Delta t_{m[ch]}$ is the pulse width from the moderator [opening time of the chopper], $t_{m[ch]}$ is the time-of-flight from the moderator to the chopper [moderator to the sample], $l_{m[ch]}$ is the distance from moderator to the chopper [moderator to sample] and l is the distance from the sample to the detector. The form of these equations dictate that the instrument has its best resolution at highest energy transfers.

3.12.2 Triple Axis Spectroscopy

A TOF spectrometer "sees" an area of reciprocal space during one measurement. In triple axis spectrometry, the instrument is set up to travel through paths of reciprocal space and energy as defined by the experimentalist and therefore requires prior knowledge of the nature of the excitations under study. There are three axes of rotation on the instrument as shown in figure 3.13. The first rotation (α) sets the monochromator crystal to the Bragg angle that selects the $\boldsymbol{k}_i$ required by the user. The second axis (2θ) is centered on the sample itself, which is oriented to the point in $\boldsymbol{q}$ space under study. The final rotation (β) refers to another monochromating crystal, the analyser, which positions the detector at the correct angle to intercept neutrons with the required final energy. Each configuration of

the spectrometer corresponds to a well-defined point in $(\boldsymbol{q}, \hbar\omega)$ space, and there are many possible ways (many possible scattering triangles) to reach a particular $\boldsymbol{q}$ and $\hbar\omega$. The actual values used for α, 2θ and β used will be a compromise between intensity and resolution as well as the physical limitations of the instrument itself. The sample may be placed on a 4-circle Eulerian cradle, allowing full access to the reciprocal space of the crystal, however the use of conventional cryostats is more common, requiring greater thought as to the orientation of the sample. Magnetic neutron scattering cross sections are dependent on a quantity $\boldsymbol{Q}(\boldsymbol{q})$, known as the magnetic interaction vector. It is defined as:

$$\boldsymbol{Q}(\boldsymbol{q}) = \boldsymbol{q} \times \tilde{\boldsymbol{M}}(\boldsymbol{q}) \times \boldsymbol{q} \tag{3.20}$$

where $\tilde{\boldsymbol{M}}(\boldsymbol{q})$ is the magnetic structure factor, the Fourier transform of the spin density function of the magnetic ordering in real space. $\boldsymbol{Q}(\boldsymbol{q})$ therefore projects the magnetic structure factor onto the plane perpendicular to the momentum transfer $\boldsymbol{q}$. As a consequence, only the components of the magnetic moments perpendicular to $\boldsymbol{q}$ contribute to the magnetic scattering cross section and the sample must therefore be oriented with $\boldsymbol{q}$ coplanar to the flight path of the neutron in the instrument and with the magnetic moments perpendicular.

There are two modes of operation in TAS, constant $\boldsymbol{q}$ scans and constant $\hbar\omega$ scans, as illustrated in the right hand side of figure 3.13. A typical TAS experiment will employ both modes of scanning to map the dispersion under study. In constant $\hbar\omega$ scans, the direction in $\boldsymbol{q}$ through which the spectrometer is scanned must be chosen carefully in order to measure the correct line-width of the dispersion. The intensity in an inelastic neutron experiment is not measured at each infinitely small point in reciprocal space, but is a convolution between the scattering function $S(\boldsymbol{q}, \hbar\omega)$ and the resolution volume of the spectrometer. The intensity of neutrons in the detector is given by:

$$I(\boldsymbol{q}, \hbar\omega) = N \int J(\boldsymbol{k}_i, \boldsymbol{k}_f) d\boldsymbol{k}_i d\boldsymbol{k}_f \tag{3.21}$$

where the function $J(\boldsymbol{k}_i, \boldsymbol{k}_f)$ multiplies the scattering function with the spectrum

of the source (i.e. the finite spread of neutron energies in the incoming beam) and the transmission functions of both the monochromator and the analyser. The size and shape of the resolution ellipsoid can be computed with knowledge of the analysing crystal used and the angular divergences of the beam after each collimation; the direction with the best resolution for scanning can then be identified.

Chapter 4

Magnetism in Na_xCoO_2

The properties relating to the two different types of magnetic ordering found in sodium cobaltate are discussed in this chapter. Firstly, in section 4.1, the effects of the spin density wave ordering (found at higher sodium concentrations ($x > 0.65$)) are reported through magnetic susceptibility, heat capacity, transport and pressure measurements. The magnetic anisotropy of the system is discussed. A SDW is antiferromagnetic in nature, with the application of large fields it is possible to force the moments through a metamagnetic transition, discussed in section 4.2. Below $T_{SDW} = 22$ K, there exist significant modifications to the magnetic ordering. At a temperature of ∼10 K, a small ferromagnetic moment is observed, described in section 4.3. At the lowest temperatures, the SDW is pinned to the structural lattice, resulting in a glassy ground state. Evidence for this is presented in section 4.4. Finally, the antiferromagnetic ordering of the $x = \frac{1}{2}$ system, and the metal-insulator transition, is discussed in section 4.5.

4.1 The Spin Density Wave

4.1.1 Magnetic Susceptibility

The dc susceptibility (χ_{dc}) was measured using the SQuID magnetometer between temperatures of 1.8 and 400 K for crystals with varying x. For $x = 0.71$ (figure 4.1) χ_{dc} is anisotropic with the measured value for $H \parallel ab$ typically $\frac{4}{3}$ times larger than

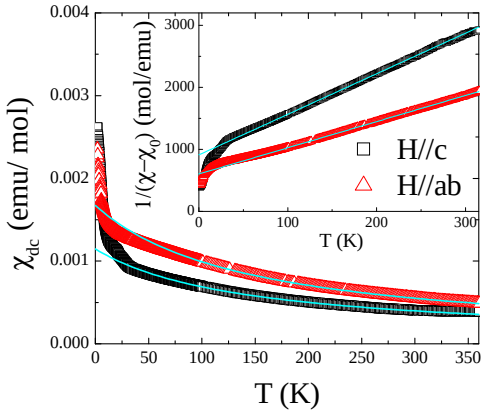

Figure 4.1: The dc susceptibility of $Na_{0.71}CoO_2$ measured in an applied field of 1 kOe. The data are anisotropic with $\chi_{ab} = \frac{4}{3}\ \chi_c$ and exhibit Curie-Weiss behaviour above ∼60 K (fitted solid curves). The inverse χ_{dc} with the constant van Vleck term removed is shown in the inset. The anisotropic gradients are indicative of the anisotropic nature of the g-factor.

that for $H \parallel c$ and a changeover in anisotropy at ∼6 K. The data can be fitted to a Curie-Weiss term plus a constant χ_0 of 5.0(2)×10^{-5} emu mol^{-1} for $H \parallel c$ and 1.1(2)×10^{-5} emu mol^{-1} for $H \parallel ab$. This temperature independent term comprises a small (∼4×10^{-5} emu mol^{-1}) diamagnetic contribution from the localised core electrons[1], a significant contribution from orbital paramagnetism analogous to van Vleck paramagnetic susceptibility plus a Pauli paramagnetic component arising from the s electrons. After subtraction of χ_0, the inverse susceptibilities (inset of figure 4.1) are linear and can be fitted to the standard Curie-Weiss equation:

$$\chi - \chi_0 = \frac{C_{CW}}{T - \theta} \tag{4.1}$$

where the constant C_{CW}, as stated in section 1.1.2, is related to the moment μ on each Co site equalling $n\mu^2/3k_B$ and θ, the Curie-Weiss temperature, represents the magnitude and sign of the coupling between the moments. Assuming an isotropic free electron value of the Landé g-factor, this yields values for the Co^{4+} effective moment of 2.05(5) and 2.56(4) μ_B for $H \parallel c$ and $H \perp c$ respectively.

[1]This is calculated using Pascal's constants: $\chi = \sum_i x_i\chi_i$ where x_i is the number of atoms of type i per formula unit and χ_i the value of Pascal's constant for atom i [64].

Assuming the moments are localised, the ground state of Co^{4+}, which has an electronic configuration of $3d^5$ can be characterised using Hund's rules as stated in section 1.1. The spin angular momentum is maximised by putting one electron in each of the five bands i.e. in the arrangement $t_{2g}^3 e_g^2$. The 3d shell is exactly half full with all spins aligned so that there is no net contribution to the orbital angular momentum. The three angular momentum quantum numbers are therefore $\boldsymbol{S} = \frac{5}{2}$, $\boldsymbol{L} = 0$ and $\boldsymbol{J} = \frac{5}{2}$. The Landé g-factor is then calculated as:

$$g_J = \frac{\boldsymbol{J}(\boldsymbol{J}+1) + \boldsymbol{S}(\boldsymbol{S}+1) - \boldsymbol{L}(\boldsymbol{L}+1)}{2\boldsymbol{J}(\boldsymbol{J}+1)} = 2 \tag{4.2}$$

giving an effective moment of $\mu = g_J \mu_B \sqrt{\boldsymbol{J}(\boldsymbol{J}+1)} = 5.92\ \mu_B$. The application of Hund's rules requires that the two most significant energy terms are the Coulombic and spin-orbit interactions. In the transition metals, the crystal field environment is often much stronger than the spin-orbit coupling leading to a situation in which the system has zero $\boldsymbol{L}$ for all $\boldsymbol{S} = \boldsymbol{J}$. This phenomenon is known as *orbital quenching*. The Landé g-factor is equal to 2 as before and the effective moment is dependent only on the spin angular momentum i.e. $\mu = g_J \mu_B \sqrt{\boldsymbol{S}(\boldsymbol{S}+1)}$. There are now three possible spin arrangements for Co^{4+} with similar energies: $t_{2g}^3 e_g^2$ with $\mu = 5.93\ \mu_B$ as discussed above, $t_{2g}^4 e_g^1$ with $\mu = 3.87\ \mu_B$ and $t_{2g}^5 e_g^0$ with $\mu = 1.73\ \mu_B$ labelled as high spin (HS), medium spin (MS) and low spin (LS) respectively.

The degree of orbital quenching depends on the relative energy of the crystal field and spin-orbit interactions. If the latter cannot be completely disregarded it should be included as a perturbation on the system, which introduces non-zero angular momentum states into the atomic ground state. The crystal field itself is anisotropic, due to trigonal distortion in the CoO_6, resulting in anisotropic values of the g-factor and hence the inequivalent values of the moment μ measured along the two different crystallographic directions. The magnetic susceptibility of a paramagnet can be described by the Brillouin function as described in section 1.1.1, which can be approximated to $\chi \approx n\mu_0\mu^2/3k_BT$ in the limit of small magnetic fields. The moment appears in quadrature and therefore contains the square of

the Landé g-factor. Following the notation adopted by Chou et al. [18], the total magnetic susceptibility can be written as $\chi(T) = \chi_0 + g^2 f(T)$. Resolving along both crystallographic directions and eliminating $f(T)$ we get:

$$\left(\frac{g_{ab}}{g_c}\right)^2 = \frac{\chi_{ab}(T) - \chi_0^{ab}}{\chi_c(T) - \chi_0^c} \tag{4.3}$$

It is not possible to determine both g_{ab} and g_c from the magnetisation measurements alone, however, their ratio can be calculated by plotting χ_{ab} versus χ_c. For this sodium concentration the value of (g_{ab}/g_c) is 1.225(1) which agrees well with the data published in reference [18]. A direct measurement of the g-factors is possible with a technique known as electron spin resonance (ESR). The sample is placed inside a high Q resonant cavity and microwave radiation is fed to the system via a waveguide at a fixed frequency ω. An increasing external field B is then applied, lifting the degeneracy of the spin states via the Zeeman effect. When the field reaches a value where the gap between two energy levels is equal to $\hbar\omega$, transitions between the spin levels are induced by the radiation and a peak is seen in the absorption spectrum. Crystal field splitting and hyperfine coupling complicates the picture somewhat, but to a first approximation the increase in absorption occurs when $\hbar\omega = g_J \mu B$. Measurements with the field aligned along the two different crystallographic directions would define both g_{ab} and g_c. ESR measurements were attempted, however the experiment suffered due to the *skin depth effect*, where the microwave radiation is confined to a small layer at the surface of the sample. The value of the skin depth is calculated as $\delta = \sqrt{\rho/\mu_0\omega}$ where ρ is the electrical resistance in the sample. Sodium cobaltate, at $x = 0.7$, is a good conductor and so the skin depth is estimated to be very small, approximately 10^{-3}cm at a Q range frequency of 30 GHz. Consequently the absorption signal is very weak. The total widths of the absorption bands in both directions were found to be extremely broad, and therefore the measurements (which were taken at a temperature of 15 K) do not provide any useful information in interpreting the magnetic susceptibility.

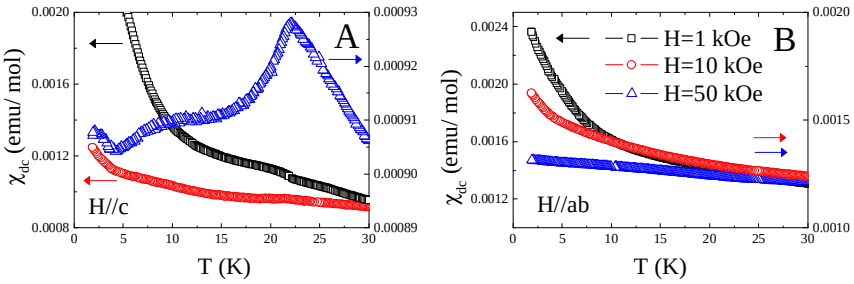

Figure 4.2: Low temperature dc susceptibility versus temperature data for $Na_{0.71}CoO_2$. Panel A: the SDW transition is clearly visible in low fields as a step in χ_{dc} and as a cusp in higher fields with the field oriented along *c*. Panel B: χ_{dc} data collected over the same temperature range with the field oriented along the *ab* planes. No features that can be associated with the SDW are observed.

In low fields at $T_{SDW} = 22$ K, a shoulder in the magnetisation is visible in data measured along the *c*-axis (figure 4.2) with no corresponding feature discernible in the *ab* plane. The susceptibility data can be explained on the basis of the establishment of an antiferromagnetic spin density wave within the cobalt oxide layers whose moments are aligned antiferromagnetically along *c*; in contrast to the case for other published data [22] there is no evidence for a canting of the moments into the *ab* plane. A similar behaviour has also been observed in the related layered cobaltate $Ca_3Co_4O_9$, where the spin density wave can only be distinguished in the *c* plane susceptibility [65]. The step in χ_{dc} at T_{SDW} can be observed even in very low fields of 10 Oe; with an increase in applied magnetic field the step becomes more distinct. At the highest fields the transition is qualitatively different and more reminiscent of an antiferromagnetic cusp, accentuating the fact that the principal magnetic interaction in this system is AFM in nature. Because of the lack of any significant impurity levels in the samples, as measured by powder x-ray diffraction, the upturn in χ_{dc} at low T cannot be attributed to magnetic impurities. The magnitude of the Curie constant in the low temperature data corresponds to the contribution of all of the Co^{4+} spins in the sample; the possibility of a Curie tail arising from free spins at the ends of broken spin chains

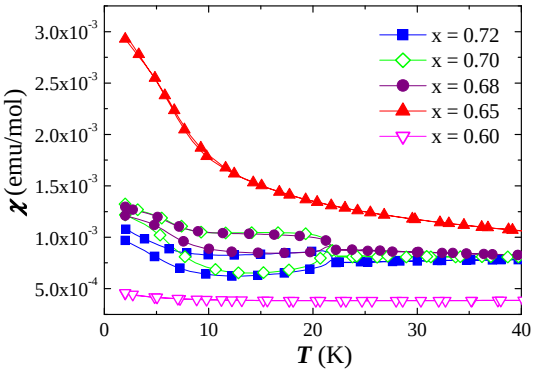

Figure 4.3: Magnetic susceptibility versus temperature of Na_xCoO_2 with the applied field of 1kOe parallel to the *c*-axis. For 0.68$\leq x \leq$0.72 the transition temperature T_{SDW} is invariant with x. The signature of magnetic order disappears altogether at a doping level of x =0.65 and leads to a rapid increase in χ_{dc}, followed by a decrease to an almost T independent susceptibility at x =0.60.

can therefore be ruled out. Although the upturn is suppressed at high fields, this cannot be due to saturation of free moments, since $M(H)$ does not saturate even in fields as high as 120 kOe (see section 4.2). The transition temperature is independent of the applied field and does not display hysteretic behaviour, indicating that it is a second-order magnetic phase transition. Figure 4.3 shows the dc magnetic susceptibility versus temperature dependence with H = 1 kOe applied parallel to the *c*-axis for a sequence of Na_xCoO_2 materials with varying Na content. As the sodium level is reduced, T_{SDW} remains constant. Any signature of magnetic ordering disappears abruptly at x =0.65. The degree of hysteresis between the zero field cooled (ZFC - lower curve) and field cooled (FC - upper curve) data reaches a maximum at x =0.70. The removal of Na and the eventual suppression of magnetic order is accompanied by an increase in the overall magnitude of the magnetic susceptibility. This is due to the increasing number of Co spins that are successively decoupled from the antiferromagnetic SDW; an increase in the paramagnetic signal is consistent with an increase in uncompensated moments. This is followed by a rapid reduction in χ_{dc} to an almost T independent signal for x =0.60.

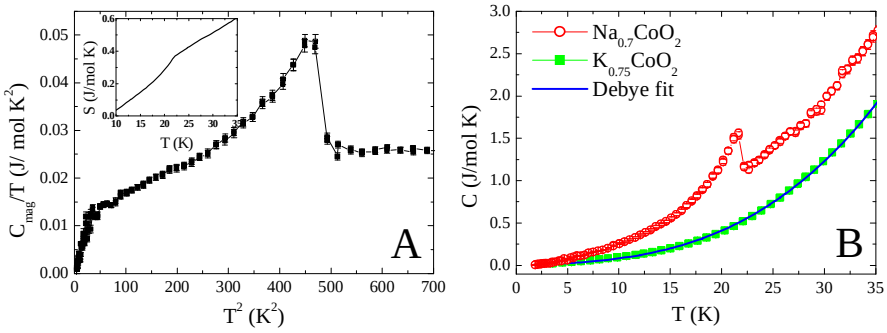

Figure 4.4: The low temperature heat capacity data for a $Na_{0.7}CoO_2$ single crystal. The data in panel A contain just the magnetic and electronic contribution to the specific heat, the phonon contribution having been estimated from the total specific heat of an isostructural non-magnetic compound K_xCoO_2 (shown in panel B).

One of the crystal boules produced by the method described in section 3.3, showed magnetic ordering, identical to that described above at a temperature of 28 K. Deintercalating increasing amounts of sodium from crystals cut from the same boule, it was possible to produce samples with ordering temperatures of both 22 and 20 K, as plotted in figure 2.2. As discussed in chapter 2, the difference is most likely due to the change in Na-O coordination due to the gliding of the CoO_2 layers during the chemical deintercalation process. Such changes in ordering temperature with reduced sodium content has been described by previous authors [66].

4.1.2 Heat Capacity

The specific heat of a substance is defined as the quantity of heat (Q) required to raise a unit mass of the system by a temperature (T) of 1 K:

$$C_i = \left(\frac{dQ}{dT}\right)_i \tag{4.4}$$

where the subscript i denotes the parameter kept constant during the measurement such as pressure, volume or applied magnetic field. The heat capacity at constant

volume (C_V) can be written in terms of the system's entropy:

$$C_V = T\left(\frac{\partial S}{\partial T}\right)_V \tag{4.5}$$

and is described by the Debye approximation to the specific heat. The crystal is defined as an array of quantum oscillators whose vibrations (phonons) are characterised by a frequency spectrum up to a maximum frequency $\omega_D^3 = 6\pi^2\nu^2 N/V$ where ν is the velocity of sound in the crystal, N the number of acoustic phonon modes and V the crystal volume. The specific heat is calculated by differentiating the total phonon energy with respect to temperature and is given as:

$$C_V^D = \frac{3V\hbar^2}{2\pi^2\nu^3 k_B T^2}\int_0^{\omega_D} \frac{\omega^4 e^{\hbar\omega/k_B T}}{\left(e^{\hbar\omega/k_B T}-1\right)^2} d\omega \tag{4.6}$$

The Einstein model treats the same oscillators as having a single, fixed frequency ω_E resulting in an expression for the specific heat that fits well at high temperatures but fails to reproduce the experimentally observed T^3 dependence at low temperatures:

$$C_V^E = Nk_B T\left(\frac{\hbar\omega_E}{k_B T}\right)^2 \frac{e^{\hbar\omega_E/k_B T}}{\left(e^{\hbar\omega_E/k_B T}-1\right)^2} \tag{4.7}$$

The derivations of both theories can be found in any solid state text book such as Kittel [67]. Two characteristic energy scales present themselves in both formulations: θ_D is related to the maximum phonon frequency $\hbar\omega_D/k_B$ and θ_E to the fundamental vibrational frequency $\hbar\omega_E/k_B$. The failure of the Debye model to fit to some experimental data usually indicates that a few atoms in the unit cell are not participating fully in the acoustic vibrations perhaps as a result of a mismatch in atomic masses. In this case, the inclusion of an Einstein mode, which gives a good description of the optical phonons within a system, may correct the problem.

The data collected using the measurement technique described in section 3.8 are the heat capacity at constant pressure. Consider the entropy of one mole of a sample at a temperature T and pressure P:

$$\begin{aligned} dS &= \left(\frac{\partial S}{\partial T}\right)_P dT + \left(\frac{\partial S}{\partial P}\right)_T dP \\ \Rightarrow \left(\frac{\partial S}{\partial T}\right)_V &= \left(\frac{\partial S}{\partial T}\right)_P + \left(\frac{\partial S}{\partial P}\right)_T \left(\frac{\partial P}{\partial T}\right)_V \end{aligned} \tag{4.8}$$

Multiplying both sides of equation 4.8 by T:

$$\begin{aligned} T\left(\frac{\partial S}{\partial T}\right)_V &= T\left(\frac{\partial S}{\partial T}\right)_P + T\left(\frac{\partial S}{\partial P}\right)_T \left(\frac{\partial P}{\partial T}\right)_V \\ \Rightarrow C_V &= C_P + T\left(\frac{\partial S}{\partial P}\right)_T \left(\frac{\partial P}{\partial T}\right)_V \end{aligned} \tag{4.9}$$

Using the Maxwell relation $(\partial S/\partial P)_T = -(\partial V/\partial T)_P$ and a similar argument to that presented in equation 4.8 for a process at constant volume as a function of P and T which leads to the relation $(\partial P/\partial T)_V = -(\partial V/\partial T)_V / (\partial V/\partial P)_T$:

$$C_P - C_V = -T\left(\frac{\partial V}{\partial T}\right)_P^2 \left(\frac{\partial V}{\partial T}\right)_T^{-1} \tag{4.10}$$

The heat capacity at constant pressure, as measured, can therefore be related to the calculated heat capacity at constant volume by two parameters: the temperature coefficient of volume expansion $\beta = V^{-1}(\partial V/\partial T)_P$ and the isothermal compressibility $\kappa_T = -V^{-1}(\partial V/\partial P)_T$:

$$C_P - C_V = \frac{\beta^2}{\kappa_T} VT \tag{4.11}$$

The isothermal compressibility is always positive and so C_P is always the greater of the two quantities. At low temperatures the difference in equation 4.11 is very small and can be neglected when analysing the data. Corrections for higher temperatures are not easily made due to a lack of knowledge of β and κ_T as a function of temperature and are therefore usually ignored.

The specific heat capacity at constant pressure of a $Na_{0.7}CoO_2$ single crystal was measured from 400 mK to 400 K, the low temperature data is plotted in figure 4.4. To analyse the data, both the Debye and Einstein models for heat capacity were used. Over the whole temperature range studied, the $Na_{0.7}CoO_2$ data cannot be fitted using a single Debye expression. A satisfactory fit can be obtained using a combined Debye-Einstein function giving a θ_D of ~410 K and θ_E of ~820 K weighted in the ratio 4:5; the fit is plotted against the data in figure 4.5. This appears to be consistent with a mixture of acoustic and optical modes as expected from a combination of light and heavy elements. The Einstein energy,

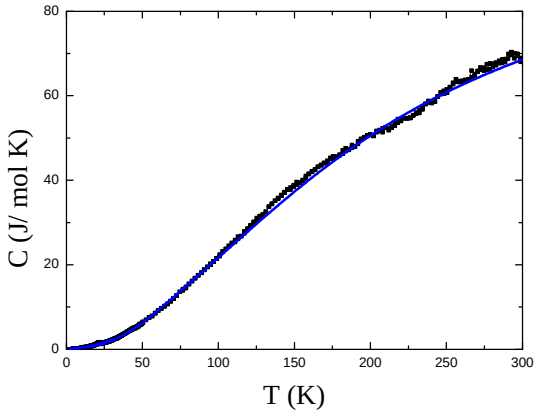

Figure 4.5: The high temperature heat capacity data for a $Na_{0.7}CoO_2$ single crystal (black squares) and the corresponding Debye-Einstein fit (blue line).

when converted into units of reciprocal space equals 571 cm^{-1} which correlates well with the value for the a_{1g} phonon modes, that are related to vibrational modes of the oxygen atoms only, identified by Lemmens et al. [68] using Raman spectroscopy.

In a limited temperature range of 22 - 30 K the data can be explained by assuming that C comprises two terms, an electronic term and a phonon component, which in the low temperature limit can be characterized using the Debye model, giving:

$$C^D_{low\,T} = \gamma T + \beta T^3 \tag{4.12}$$

A linear fit to the data plotted as C/T vs. T^2 gives γ = 30.9(7) mJ mol^{-1} K^{-2} and β = 0.0385(8) mJ mol^{-1} K^{-4}. From this a low temperature value for θ_D can be estimated as:

$$\theta_D = \left[\left(\frac{12}{5}\right)\frac{NR\pi^4}{\beta}\right]^{1/3} \tag{4.13}$$

where N is the number of modes per formula unit and R the molar gas constant. This gives a value of θ_D = 396(3) K in line with the previous estimate even though the number of modes was estimated as 3 $\times$ the number of atoms per formula unit, which only holds true for atoms of similar masses. Using these values we find that above 40 K the experimental data deviate substantially from the Debye theory.

This is consistent with the low T approximation which is only accurate below temperatures of $\sim \theta_D/10$. We find $[C(400K)/NR]_{measured}$ =0.9, the expected ratio as calculated by the Debye theory.

There is a lambda-like anomaly at 22 K indicating the onset of magnetic ordering. The transition is rather broad, extending over at least 7 K, whereas the minimum sample heat pulse used around the transition was 0.1 K. This feature occurs at the same temperature in heating and cooling runs with no discernible hysteresis to within the experimental accuracy of the technique used, again indicating that this is a second-order phase transition[2]. The jump at T_{SDW} is ∼0.4 J mol^{-1} K^{-1} which corresponds to 25% of the signal at this temperature. Using the standard BCS expression $\Delta C/T_{SDW} = 1.43\gamma$ gives $\gamma \approx$ 13 mJ mol^{-1} K^{-1}. This is consistent with the reduction in γ as seen at low temperatures. An extrapolation of the data below T_{SDW} produces a value of 15(1) mJ mol^{-1} K^{-2}. These values agree well with those of Bayrakci et al. [24] who calculated γ for a $x = 0.82$ sample from the data below 22 K. It is interesting that the γ value below the SDW transition also agrees with estimates for γ made for the superconducting material $Na_{\frac{1}{3}}CoO_2 \cdot \frac{4}{3}H_2O$ [33, 60, 69]. Assuming that the γ term arises solely from charge carriers we can use:

$$\gamma = \left(\frac{\pi^2}{3}\right) k_B^2 N\left(E_F\right) \tag{4.14}$$

to calculate the free electron density of states. $N\left(E_F\right)$ is calculated to be 5.3(1)$\times 10^{24}$ eV^{-1} mol^{-1} just above T_{SDW}, reducing to 2.6(2) $\times 10^{24}$ eV^{-1} mol^{-1}. The ratio of γ above and below the transition suggests that 50-60% of the Fermi surface is removed on the opening up of a gap at T_{SDW}.

The entropy associated with this feature can be obtained by subtracting from the total specific heat, C, an estimate of the background specific heat, C', made from the measured specific heat of an isostructural non-magnetic sample. K_xCoO_2 crystallises in the same space group as sodium cobaltate with similar lat-

[2]Note that during both warming and cooling runs, the sample is heated by a certain percentage of the set point for data collection.

tice parameters of $a = 2.85$ Å and $c = 12.42$ Å [70], and can be manufactured in a fashion akin to that described in section 3.1. A powder sample of $x = 0.75$ was produced; x-ray diffraction analysis confirms the crystal structure and the absence of impurities down to a volume fraction of 2%. The magnetic susceptibility was measured in the SQuID magnetometer and is paramagnetic in nature (comprising Pauli and van Vleck contributions [71] and showing no evidence of magnetic impurities). The heat capacity data also show no sign of long ranged magnetic ordering. By adapting the temperature values of the $K_{0.75}CoO_2$ data an estimate of the phonon contribution to the specific heat of sodium cobaltate can be made defining the magnetic contribution to C. In order to correct for the differences in the formula masses the ratio of the Debye temperatures must be considered. The potassium sample was fitted to the same Debye-Einstein function as before (over a temperature range of 2 - 300 K) giving values of $\theta_D \sim 260$ K and $\theta_E \sim 690$ K. The ratio $r = \theta_D^{Na}/\theta_D^K = 1.6$ should map the two specific heat curves onto each other. However, this scaling law applies to systems that fit the Debye approximation to the specific heat. Both Na_xCoO_2 and K_2CoO_2 contain contributions from optical phonon modes that do not fit the scaling law and so a more accurate r must be obtained from the low temperature data only. Fitting the potassium data to equation 4.12 gives $\gamma_K = 9.1(2)$ mJ mol^{-1} K^{-2} and $\beta_K = 0.196(1)$ mJ mol^{-1} K^{-4} (shown in panel B of figure 4.4). As defined in equation 4.13 the ratio r of the Debye temperatures will now be proportional to the inverse of the cubed root of the ratio of the β terms giving $r = 1.72(1)$. The temperature data for the $K_{0.75}CoO_2$ sample were modified by this value of r and a difference curve taken.

The entropy associated with the anomaly alone (i.e. from T = 14 to 22 K) amounts to 0.065 J mol^{-1} K^{-1} and corresponds to only 4% of the magnetic entropy expected for a $x = 0.7$ sample with a Co^{3+} (spin 0)/Co^{4+} (spin $\frac{1}{2}$) system in the ratio of 7:3 i.e. $\left(\frac{3}{10}R\ln(2S+1)\right) = 1.73$ J mol^{-1} K^{-1}. Including the excess entropy down to 0.4 K (the origin of which is discussed in section 4.4), this value rises to 0.16 J mol^{-1} K^{-1}. The value compares well with estimates

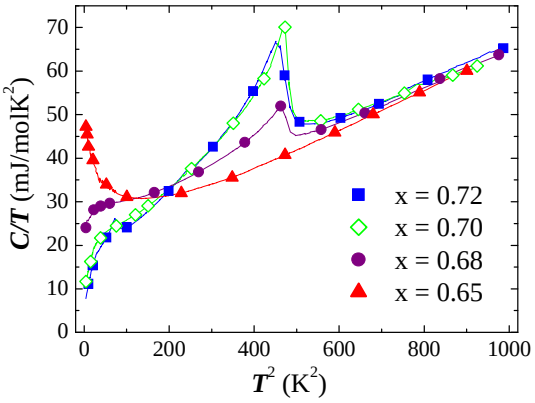

Figure 4.6: C/T versus T^2 curves at different doping levels (without phonon subtraction). The size of the anomaly remains constant for 0.70$\leq x \leq$0.72 and then decreases with decreasing sodium content whilst the transition temperature T_{SDW} remains constant. No transition is evident for $x \leq$0.65.

made in other reports [24, 20] and is consistent with previous reports for SDW compounds (see section 4.6). According to the lattice background subtraction, significant magnetic entropy exists to high temperatures, a subtraction over the whole data range indicates that C_{mag} will tend to zero at around 420 K ($\sim \theta_D^{Na}$). In low dimensional magnetic systems it is not unexpected that the magnetic entropy around the ordering temperature is just a fraction of the total, however the sum of the magnetic entropy up to the highest temperatures measured is $\sim$15 J mol^{-1} K^{-1}, an order of magnitude higher than the value expected (1.73 J mol^{-1} K^{-1}). This is most likely because the scaling factor used for the K_xCoO_2 data was based on an approximation valid only at low temperatures. Above the SDW transition, the subtracted data remain at a constant value of $\sim$27 mJ mol^{-1} K^{-2}, in reasonable agreement with the electronic contribution γ calculated previously.

The dependence of the specific heat on sodium concentration (figure 4.6) agrees well with the observations from the magnetic susceptibility data. The data contain the same lambda-like anomaly at 22 K that is present in all materials down to $x = 0.68$. The magnitude of the anomaly ($\sim$0.4 J mol^{-1} K^{-1}) remains fixed for 0.70$\leq x \leq$0.72, but then gradually diminishes before disappearing at $x = 0.65$.

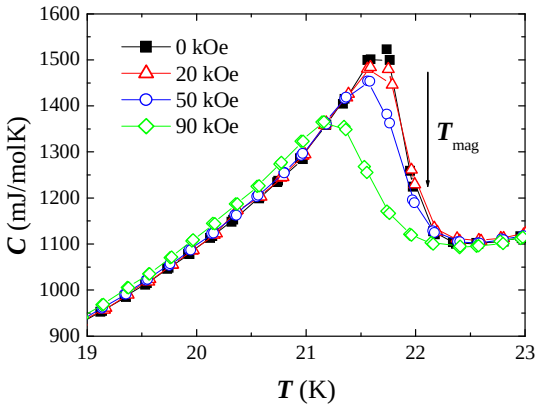

Figure 4.7: Heat capacity of $Na_{0.7}CoO_2$ in various magnetic fields applied parallel to the *c*-axis of the crystal. The temperature of both the peak and the midpoint of the transition are reduced in field indicating a broadening with applied field, however the onset temperature remains constant.

At low T, the temperature dependence of C varies enormously; γ increases from 8 mJ mol^{-1} K^{-2} at $x = 0.72$ to approach 50 mJ mol^{-1} K^{-2} at $x = 0.65$. As mentioned previously, the onset of magnetic ordering is accompanied by the removal of approximately half the Fermi surface. The destruction of this magnetically ordered state for lower x may leave us with a system of highly correlated electrons with an enhanced γ. Alternatively, the increase in C/T versus T at low T for $x = 0.65$ may be the result of a Schottky anomaly [72, 73].

Figure 4.7 shows the specific heat capacity versus temperature data collected for a $x = 0.70$ sample in fields of 0, 20 , 50 and 90 kOe applied parallel to the *c*-axis. The application of an external field leaves the temperature at which the onset of the magnetic ordering is observed unchanged. The transition is progressively broadened and the magnitude of the anomaly around T_{SDW} is considerably reduced as the applied field is increased.

4.1.3 Electronic Transport

The values of the resistivity for a $x = 0.71$ sample at room temperature, in both the *ab* and *c* directions, are of the order of 1-10 mΩ cm (shown in figure 4.8). These

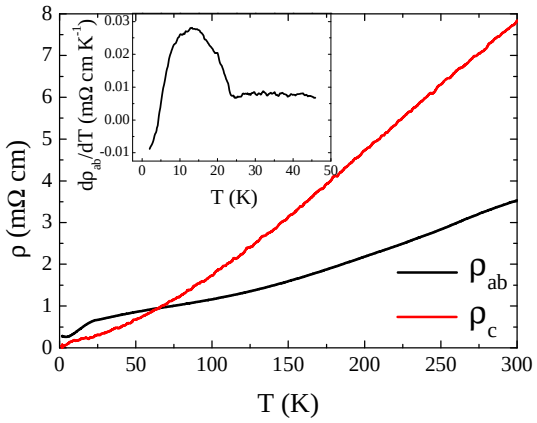

Figure 4.8: The resistivity of $Na_{0.71}CoO_2$ as a function of temperature. No evidence of the SDW transition is visible in the I$\|c$ data, whereas the resistivity is seen to drop in the *ab* plane in the magnetically ordered state. The derivative of the in-plane resistivity is shown in the inset, clearly indicating the transition at 22 K.

values are in reasonable agreement with several other reports of resistivity measurements made on either polycrystalline or single-crystal samples of $Na_{0.7}CoO_2$ in the *ab* plane [6, 20, 24, 25]. At room temperature the resistivity is only slightly anisotropic with $\rho_c \approx 2\rho_{ab}$ and a crossover in anisotropy at ∼60 K. The resistance ratios (R_{300K}/R_{2K}) along *ab* and *c* are 15 and 150 respectively. In both directions the resistivity between 150 K and 300 K varies almost linearly with temperature with $d\rho/dT$ = 13.2(2) and 31.4(2) $\mu\Omega$ cm K^{-1} for the *ab* and *c* directions respectively. A significant reduction in ρ_{ab} below 22 K marks the SDW transition. No corresponding feature is seen in ρ_c. The reduction in ρ suggests that the opening up of a gap associated with the SDW leads to a decrease in the total scattering within the *ab* plane while the conduction along *c* is unaffected.

4.1.4 Modifications to the SDW with Externally Applied Pressure

The structure of Na_xCoO_2, as will be discussed in chapter 5, depends strongly on x, the details of which depend on how the sodium ions are arranged in the charge reservoir layer and how the CoO_2 layers respond structurally to changes in the electron count and the Na ion distribution. As x increases up to ∼0.75, the

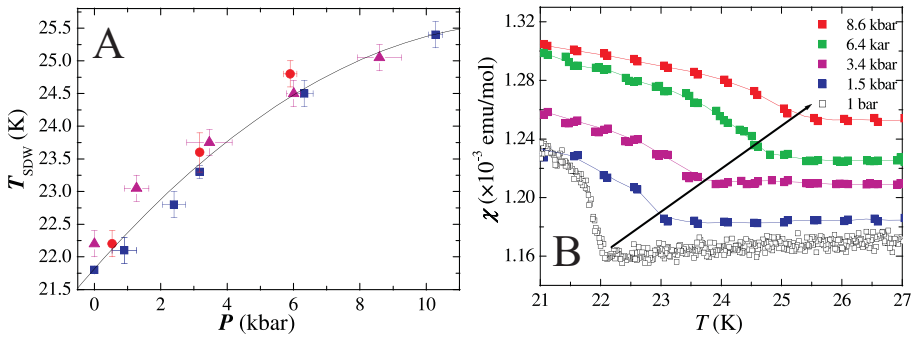

Figure 4.9: Panel A: The variation of T_{SDW} for two $Na_{0.7}CoO_2$ crystals. A clear increase in T_{SDW} is seen with increasing pressure. The solid line is a guide to the eye. Panel B: The raw magnetic susceptibility data showing the variation in T_{SDW} at five different applied pressures. The data are offset vertically from each other by 2×10^{-5} emu mol^{-1} so that the shift of T_{SDW} to higher temperatures (as indicated by the arrow) is visible.

c-axis lattice parameter decreases as a result of a decrease in the thickness of the NaO_2 layer that is not offset by an increase in the CoO_2 layer thickness (and the Co-O bond lengths, which leads to a slight increase in *a*). Above x ~0.75 both *c* and *a* continue to vary as before, although the decrease[increase] with x in the NaO_2[CoO_2] layers is more pronounced. The application of external pressure is known to reduce both the lattice parameters, although the compressibility along *c* is an order of magnitude higher than that along *a* [74]. Since it is *c* that varies the most with Na content, the application of external pressure, to a first approximation, should be equivalent to the chemical pressure achieved by doping. The difference between the two pressures is the variation of the absolute valence state of the Co and will be discussed in section 4.6.

Figure 4.9 shows the pressure dependence on T_{SDW} for two single crystal samples of $x = 0.70$. Data were collected in three separate runs in magnetic fields of 50 kOe with both increasing and decreasing pressure. The raw magnetisation data for one of the crystals is shown in panel B. The signature of magnetic order is seen at $T_{SDW} = 22.0(2)$ K at 1 bar and initially increases at a rate $\partial T_{SDW}/\partial P = +0.44(3)$ K bar^{-1}. This increase begins to saturate at higher pressures with T_{SDW} reaching 25.4(2) K at 10 kbar. For similar measurements on a $x = 0.65$ sample

(i.e. a composition for which there are no features in either the magnetisation or the heat capacity data that can be associated with the onset of the SDW) the application of pressures of up to 10 kbar does not induce any features in the M versus T data that indicate that pressure can restore the magnetic order.

4.2 Observation of the Metamagnetic Transition in High Fields

In magnetic systems exhibiting antiferromagnetic ordering, the application of an external field will alter the orientation of the spins within the two sublattices. If H is applied perpendicular to the magnetic easy axis, the application of the field will slowly rotate the moments along the field as the magnitude of H is increased. If, however, the field applied is parallel to the crystal magnetisation, the total energy of the system can be written as:

$$E = -\mu H \left[\cos(\theta) + \cos(\varphi)\right] + \mathbf{J}_c \mu^2 \cos(\theta + \varphi) - \frac{1}{2} D \left[\cos^2(\theta) + \cos^2(\varphi)\right] \tag{4.15}$$

where the first term describes the interaction of the moments with the field H, the second term relates the exchange between two spins along *c* and the last term includes the magnetic anisotropy which quantifies the preference of the moments (μ) to lie along the *c*-axis. The constants have been labelled according to the definitions in section 6.5 and the angles are defined in figure 4.10. For the AFM system, with spins on each sublattice aligned antiparallel and along the easy axis (i.e. $\theta = 0$ and $\varphi = \pi$), equation 4.15 reduces to $E = -(\mathbf{J}_c \mu^2 + D)$, independent of the applied field. If H becomes large enough, the system will reconfigure the alignment of its spins as shown in panel A of figure 4.10, known as a "spin-flop" transition. Now $\theta = \varphi$ and the total energy is defined as:

$$E = -2\mu H \cos(\theta) + \mathbf{J}_c \mu^2 \cos(2\theta) - D \cos^2(\theta) \tag{4.16}$$

The minimum energy of the spin-flopped system occurs at an angle of $\cos(\theta) =$

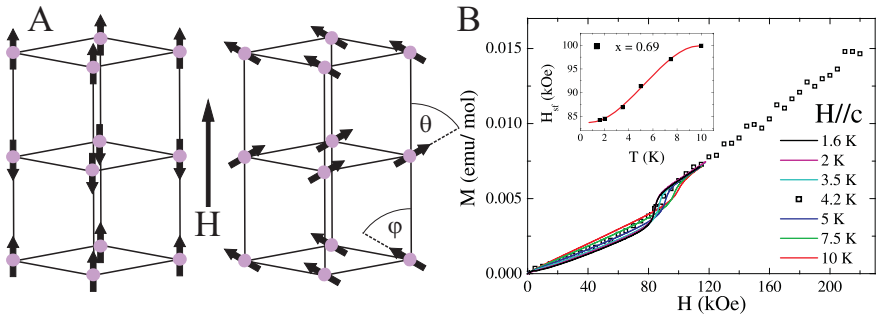

Figure 4.10: Panel A: The application of a field along *c* forces the spins to flip from an antiferromagnetic to a ferrimagnetic arrangement. Panel B: The magnetic susceptibility χ_c as a function of temperature; a sharp increase is observed at the metamagnetic transition .The field H_{sf}, defined as $\frac{\partial^2 M}{\partial H^2}$=0, increases monotonically with temperature as shown in the inset.

$(H_{sf})\,/\,(2\mathbf{J}_c\mu - D/\mu)$, the system will "flop" once the field reaches the critical value as defined by this relation. The magnetisation should show a jump at H_{sf} and saturate once the field has forced all the spins to align with $\theta = 0$. The magnetisation with $H \parallel c$ is shown in panel B of figure 4.10. The measurements were taken using the VSM described in section 3.7.3, except for the data plotted in open squares, which were acquired at the Grenoble High Magnetic Field Laboratory at the CNRS Grenoble. The Bitter magnet used in the study is resistive and requires high volumes of coolant pumped through the system to keep it operational. The magnetometer, which operates with a standard extraction technique as used in the SQuID (described in section 3.7.1), therefore suffers from noise induced from the vibrations of the cooling system and thus has a precision of 10^{-3} emu, four orders of magnitude less than the VSM or SQuID which employ superconducting magnets to apply the external field. Given the small value of the ordered moment in $Na_{0.7}CoO_2$, and the limitation imposed on the sample volume by the diameter of the magnet bore, the measurements obtained were on the limit of instrumental resolution. It is clear however, that even in fields as high as 220 kOe, the magnetisation has not reached saturation. In the spin-flop system, with all the moments aligned perpendicular to H, the expected moment (as calculated in

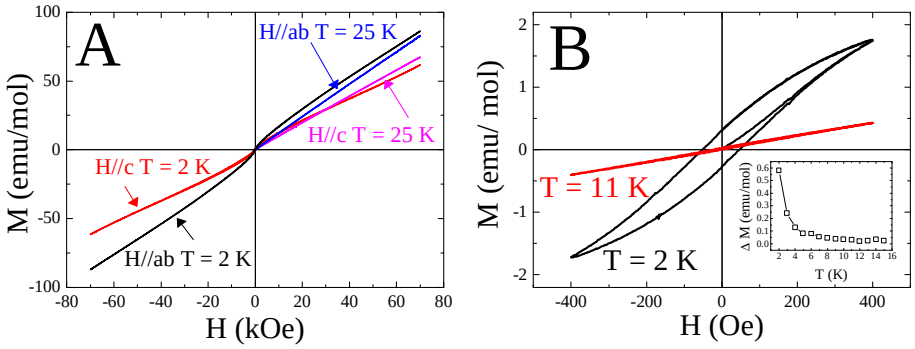

Figure 4.11: Magnetisation versus field measurements for a $Na_{0.71}CoO_2$ crystal. Panel A: High field magnetisation at temperatures above and below the SDW transition and with the field aligned along *c* and *ab*. Panel B: The low field hysteresis as measured with H$\|c$. The remanent magnetisation clearly visible at 2 K has disappeared by 11 K; the magnitude of this ferromagnetic component is plotted as a function of temperature in the inset.

section 4.1 for a system containing 30% spin half cobalt ions) is 0.52 μ_B mol^{-1}. Calculating the molecular weight of $Na_{0.7}CoO_2$ and substituting for the value of one Bohr magneton in electromagnetic units gives a total saturation moment of 27.1 emu g^{-1}. The measured moment at 220 kOe is ∼1.5 emu g^{-1} suggesting the spins are far from aligning collinear to the field, but θ is actually ∼ 87°. Just after the metamagnetic transition θ is calculated to be ∼89 °. This is in excellent agreement with Helme et al. [75] who confirmed the spin arrangement detailed in figure 4.10 by neutron diffraction and calculated θ = 87.8(5) ° at H_{sf} from the exchange constants measured from spin wave dispersions. If M continues to vary linearly with H, a total applied field of 3500(100) kOe will be necessary to obtain ferromagnetically aligned moments.

4.3 Onset of a Low Temperature Ferrimagnetic State

Magnetisation data as a function of applied field were collected above and below T_{SDW} and are shown in figure 4.11. Once again, $M_{ab} > M_c$ and the anisotropy in the highest measured fields is independent of temperature at ∼1.4, which is in line with the χ_{dc} versus T results. At the lowest temperatures the loops ex-

hibit considerable curvature, which disappears above 10 K. At 2 K the value of the magnetisation at 10 kOe corresponds to moments of only ∼0.016 μ_B/Co and ∼0.011 μ_B/Co along *ab* and *c* respectively. At low fields the data have hysteretic behaviour, which disappears above a temperature of ∼10 K. The remanent magnetisation at 2 K is extremely small, corresponding to just 0.0001 μ_B/Co along *c* and an order of magnitude smaller along *ab*. The appearance of this low temperature ferromagnetic component has been noted by previous authors [20] although it was reported to occur below T_{SDW}, whereas these data indicate a lower temperature transition. Anomalies in the magnetic susceptibility data below T_{SDW} have also been observed by Sakurai et al. [21] and attributed to modifications to the magnetic ground state. The transition is also visible in the χ_{dc} data in this study (figure 4.3). The upturn in susceptibility persists in samples with lower sodium concentrations where the SDW transition is absent, suggesting that this magnetic ordering is independent of the SDW. The coexistence of a ferrimagnetic ground state with a SDW state (with different ordering temperatures) has previously been seen in the related material $Ca_3Co_4O_9$ [65] as well as several other SDW systems, e.g. UNi_2Si_2 [76]. In these materials the small ferromagnetic component arose from magnetic anisotropy, from modifications to the geometry of the Fermi surface as a function of temperature below T_{SDW} and from the structure, which leads to differences between the inter-layer and intra-layer coupling. In Na_xCoO_2, the ferrimagnetism may be due to a combination of any of these effects, especially since a structural change in the cobalt oxide octahedra occurs below T_{SDW}, as discussed in chapter 5.

4.3.1 Positive Magnetoresistance Coexisting with the FiM

Magnetoresistance (MR) is defined as the percentage difference between the resistivity at an applied field H and the zero field resistivity, or $(\rho_H - \rho_0)/\rho_0$. The MR effect in metals can easily be explained if two types of charge carriers, with different drift velocities, are present in the material. The application of a trans-

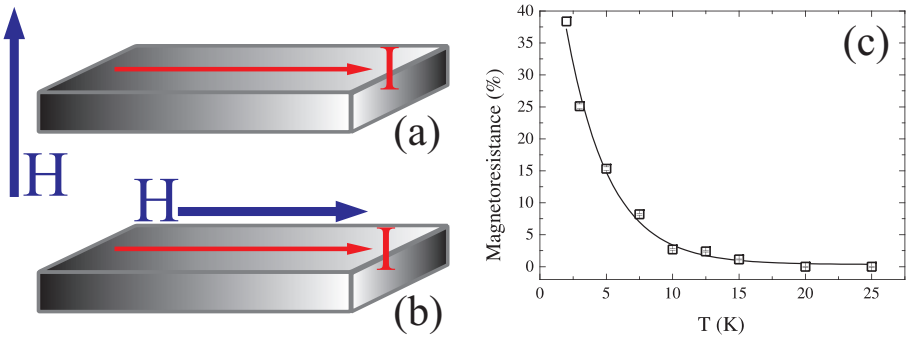

Figure 4.12: The magnetoresistance of a $Na_{0.71}CoO_2$ crystal was measured in both transverse (a) and longitudinal (b) geometries. The magnitude of the MR was comparable in both geometries, the value at 70 kOe is plotted in panel (c).

verse field produces a Hall current for both charge populations. In a normal metal, the transverse Hall field builds up until there is no net transverse current. For the two types of charge carriers, there is no one value of the transverse E field that will satisfy the Hall condition for both charge populations. Combining the effect of the Lorentz force from the external field and the force from the Hall field that overcompensates the Lorentz force for one set of charge carriers and undercompensates for the other, transverse currents are produced in opposite directions for the two charge types. A second Hall effect occurs for the transverse field, turning the current of one type of charge against the original current I and the other along I. The net effect of these additional currents that flow with and against the main current always opposes I, since it is the second charge carrier population with the weaker transverse voltage that flowed in the opposite sense to the conventional Hall current. The magnitude of the transverse Hall field is proportional to the applied field; in this situation two transverse fields are set up, requiring the magnetoresistance to be proportional to H^2. This is known as Kohler's rule, which predicts a quadratic dependence of the MR at low fields, saturating to a constant value with higher applied fields. The MR effect also occurs when the field is applied parallel to the current; transverse components of the velocities cause the electrons to spiral along I, the scattering associated with the spiralling electrons

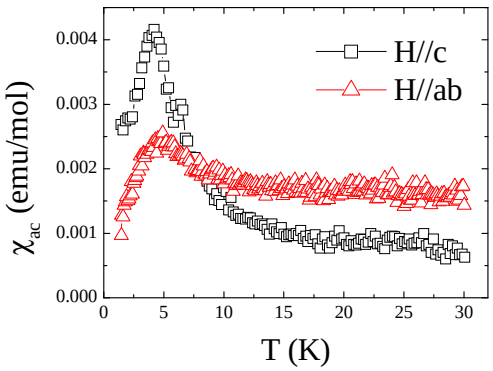

Figure 4.13: Low temperature ac susceptibility of $Na_{0.71}CoO_2$. No feature associated with the spin density wave transition is visible, however, the cusp at 4 K indicates that the break up of the SDW has resulted in a glassy ground state.

creates a resistance that is also proportional to the square of the applied field.

MR was found to exist in the *ab* plane resistivity data, and was absent for $I \parallel c$. The effect (shown in figure 4.12) is large ($\sim$40%) and positive, which classifies the material as having Giant Magnetoresistance (GMR). The resistivity was measured with the field in both transverse and longitudinal geometry and found to be of similar magnitude in both experiments. The MR obeys Kohler's rule (with no indication of saturation up to the maximum measured field of 70 kOe) and is removed by raising the temperature above $\sim$10 K. It is interesting to note that this correlates well with the temperature at which the spontaneous magnetisation present in the $\chi(H)$ data disappears. The onset of the ferrimagnetism may be associated with a change in the morphology of the Fermi surface as mentioned previously. The creation of a second type of charge carrier, with different effective mass and velocity, could originate from such a change in the FS.

4.4 Evidence of a glassy ground state

Low temperature ac susceptibility measurements on a x =0.71 sample were taken with the driving field oriented along the *c*-axis and in the *ab* plane and are shown in

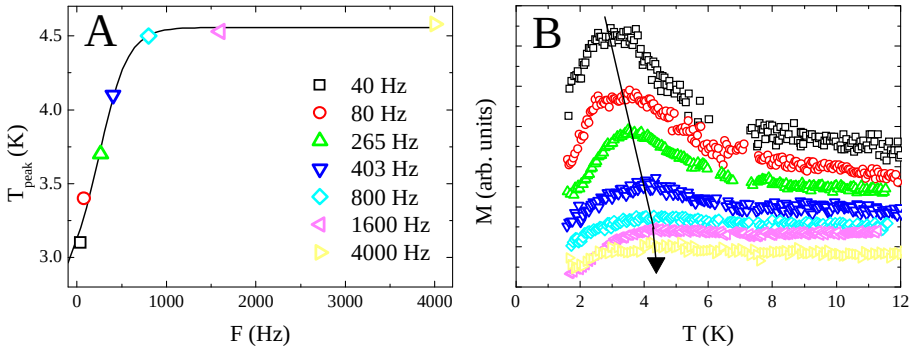

Figure 4.14: Low temperature ac susceptibility of $Na_{0.71}CoO_2$ measured at different driving field frequencies. Panel A: the position of the peak maximum shifts with increasing frequency (the line is a guide to the eye). Panel B: Raw magnetisation data for the seven different frequencies. The data have been offset from each other for clarity.

figure 4.13. χ_{ac} displays the same anisotropy and low temperature crossover as χ_{dc}. Curiously, no magnetic features were visible at T_{SDW}. A peak at 4 K is visible for fields applied along both *ab* and *c*, which has previously been reported [77] and attributed to antiferromagnetic ordering. This low temperature feature is reminiscent of the susceptibility cusps found in spin glasses. Investigations of the frequency dependence show an increase in the cusp temperature with increasing frequency (figure 4.14), which is consistent with the varying dynamic response expected from a glassy ground state. The peak also broadens with increasing frequency and, given the very small magnetic signal, it is difficult to determine the temperature of the onset of the glassy phase at the highest frequencies. The peak temperature, however, appears to saturate at $T_{peak} = 4.5$ K. The origin of this state is likely to be a consequence of the incoherency of the SDW with the periodicity of the lattice. It is plausible that the density wave may become pinned to the underlying Co lattice with decreasing temperature which would result in low T "glassy" behaviour. Other materials in which a spin density wave state has been observed, for example the organic salt $(TMTSF_2)PF_6$ [78], also exhibit low temperature glassy states for this very reason.

The freezing of the SDW on cooling also adds to the magnetic entropy

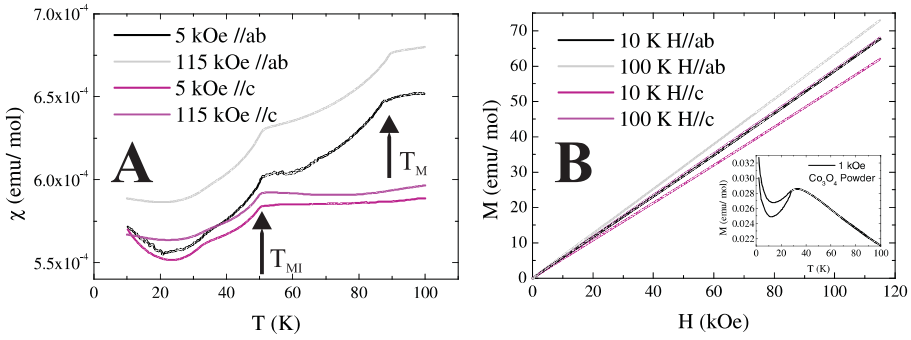

Figure 4.15: Panel A: Magnetic susceptibility of $Na_{\frac{1}{2}}CoO_2$ with the field aligned in different directions at high and low fields. The magnetic transition at T_M is not apparent in the data for $H \parallel c$. Panel B: The magnetisation as a function of field. In contrast to the higher doped system, there is no metamagnetic transition in fields of up to 115 kOe.

of the system and is therefore visible in the heat capacity data. The additional component to C is visible as a broad bump (extending from 4 to 15 K) in panel A of figure 4.4. The low temperature nodule is also consistent with the notion of a glassy state.

4.5 Magnetic Ordering in the Half Doped System

4.5.1 Antiferromagnetism in $Na_{\frac{1}{2}}CoO_2$

The dc magnetic susceptibility at $x = \frac{1}{2}$ is of the same magnitude as that found in the non-magnetically ordered $x = 0.60$ phase, however two transitions are visible as shoulders in the magnetisation at $T_{MI} = 53$ K and $T_M = 88$ K, as shown in figure 4.15. A downturn in susceptibility occurs at both critical temperatures, indicating antiferromagnetic ordering at T_M which is modified at T_{MI}. At the lowest temperatures there is a general upturn in susceptibility, which is suppressed by the application of large fields. The most likely origin of this Curie tail is the presence of a magnetic impurity, namely Co_3O_4. This phase of cobalt oxide magnetically orders at 35 K, the magnetic susceptibility of Co_3O_4 powder is detailed in the inset of panel B. The peak at the ordering temperature is evident in the susceptibility curves in panel A, especially with the field oriented along *c*. From the relative

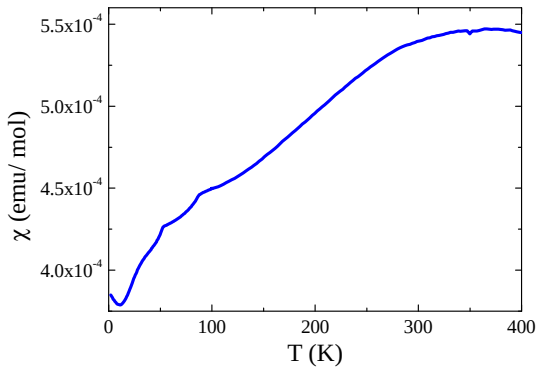

Figure 4.16: The high temperature magnetic susceptibility of a $Na_{\frac{1}{2}}CoO_2$ single crystal with a field of 50 kOe applied along the *ab* planes.

magnitudes of the susceptibilities at the ordering temperature of Co_3O_4 we may infer that the impurity level in this sample is $\sim 2\%$. Co_3O_4 is absent in the parent single crystals and so it has most likely originated during the chemical deintercalation process as described in section 3.5. Curie tails in the low T susceptibiltiy data are a common feature in many $Na_{\frac{1}{2}}CoO_2$ publications [28, 31].

The transition at 88 K, in direct contrast to higher doped system, is visible only with the field aligned in the *ab* plane, indicative of magnetic ordering in which the moments align within the basal planes. Neither transition shifts with applied fields within experimental error ($\sim$0.1 K), however, close examination of the derivative of χ_{ab} reveals that the MI transition is broadened by 1 K in a field of 115 kOe. The magnetisation as a function of field was also investigated and is plotted in panel B. χ is less anisotropic than at $x = 0.7$ with $\chi_{ab} = 1.1\chi_c$. It is interesting to note that χ does not exhibit the Curie-Weiss-like character as seen in the SDW material but increases with increasing temperature reaching a maximum at $\sim$370 K (shown in figure 4.16): there is no signature of charge locality from the macroscopic measurements. No metamagnetic transition is visible in the in-plane data, suggesting that the coupling between spins is much stronger at this doping level. The magnetisation at 120 kOe corresponds to $0.022\mu_B/Co^{4+}$, just 2.5% of the value expected at saturation, assuming an equal population of Co^{3+} and Co^{4+}.

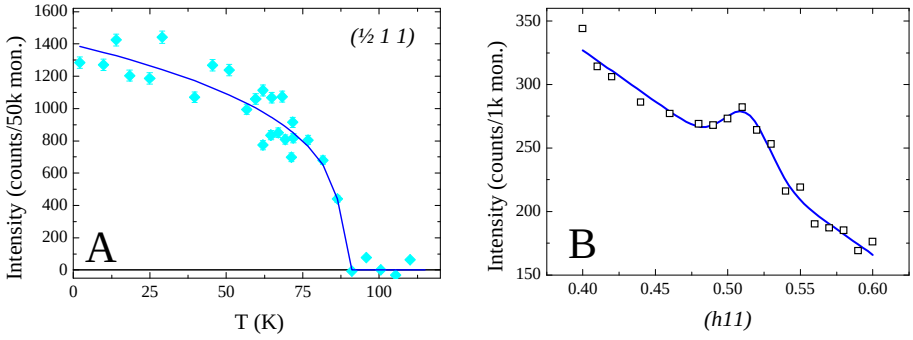

Figure 4.17: Panel A: The diffracted intensity of the magnetic Bragg peak $(\frac{1}{2}11)$ in $Na_{\frac{1}{2}}CoO_2$ measured as a function of temperature. A fit to the magnetic order parameter is shown in dark blue. Panel B: The measured intensity of the magnetic Bragg peak scanning along h. The line is a guide to the eye.

The magnetic ordering in $Na_{\frac{1}{2}}CoO_2$ has been the subject of two neutron diffraction experiments [28, 79]. Both studies found magnetic Bragg peaks occurring at $\left(\frac{1}{2}\,\frac{1}{2}\,l_{odd}\right)$. During the inelastic neutron scattering experiment to measure the magnetic excitations, as described in chapter 6, the crystal was oriented with spectrometer parameters that satisfied the $(\frac{1}{2}11)$ Bragg condition and measurements made as a function of temperature, plotted in figure 4.17. A large background was removed from the data in order to do this analysis (corresponding to the large sloping background in the raw data shown in panel B), in fact the magnitude of the magnetic scattering at base temperature is just 12% of the background signal. The intensity of the magnetic peak increases below the ordering temperature T_M and the data are fitted to $\langle M\rangle^2 \alpha\,(T_M - T)^{\beta}$ with T_M = 88.0(2)K and β = 0.30(4). The value of the critical exponent is in good agreement with that expected for Ising models (D = 3, d = 1 as stated in table 1.1) suggesting the dimensionality of the magnetic ordering is one.

The notion of low dimensional magnetism in this system is further strengthened by the fact that the measured specific heat is continuous at all temperatures: there are no anomalies at either T_M or T_{MI} (shown in figure 4.18). The heat capacity is related to the entropy (S) of the system by $C = T\,(\partial S/\partial T)$, the en-

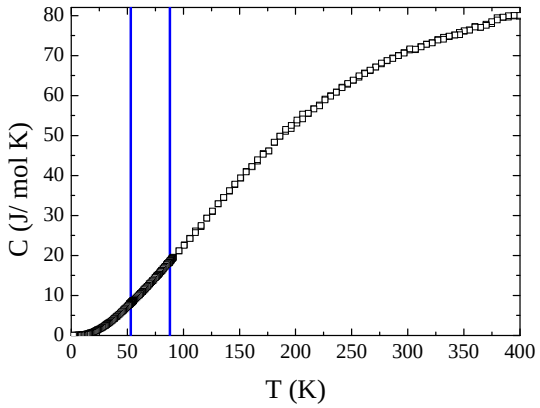

Figure 4.18: The specific heat of a $Na_{\frac{1}{2}}CoO_2$ single crystal in zero applied field. The blue lines mark the temperatures of the two transitions as seen in the magnetic susceptibility; within experimental error, C is continuous through both temperatures.

tropy itself is the negative of the first temperature derivate of the Helmholtz free energy, F. A change of state produces a change in F which is detectable by a discontinuity in S. It should be noted that the "pulse" method of heat capacity measurement as employed in the PPMS is not always suitable for measuring phase transitions that occur over a very small temperature range dT; if the heat pulse applied is larger than dT the expected increase in heat capacity may be missed. However, the density of measurements around each temperature of interest was high (every 0.2 K) with small increases in temperature made at each measurement ($\sim$0.5 K). There are other methods of measuring the heat capacity, in which the system is thermally isolated and small pulses of heat are added to the sample. Heat capacity data in the published literature is notable by its absence, suggesting that no large jumps in C occur at the phase transition temperatures no matter what the experimental method. The absence of observable features around T_M and T_{MI} essentially means that there is little change in magnetic entropy at either transition. It is not uncommon in low dimensional magnetic systems that magnetic correlations may build up faster in one crystallographic direction than another, due to a mismatch in the magnitudes of the magnetic exchange parameters. In this particular case, it may be that in-plane correlations build up slowly with decreas-

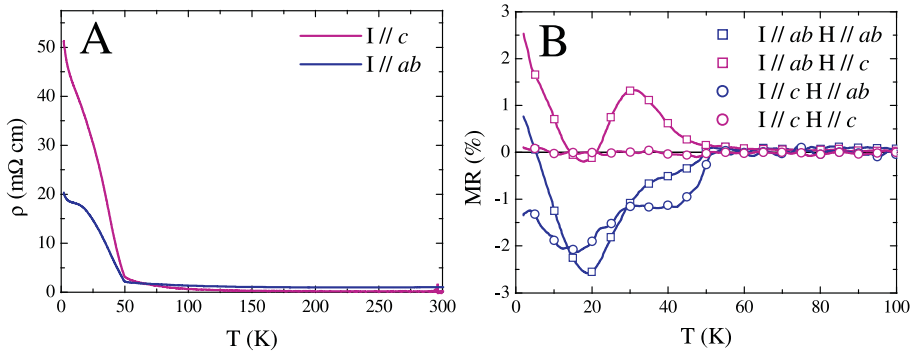

Figure 4.19: Panel A: The zero field resistivity of $Na_{\frac{1}{2}}CoO_2$ with the current parallel to the *ab* and *c* planes. The resistivity is anisotropic with $\rho_c \approx 2.5\rho_{ab}$ at 2 K and a crossover in anisotropy at ∼65 K. The MI transition is clearly visible at 53 K along with a further increase in ρ at ∼20 K. Panel B: The magnetoresistance at 90 kOe in the *ab* and *c* directions with the field oriented both parallel and perpendicular to the current. The magnetic transition at 20 K strongly affects the MR.

ing temperature before locking in-phase along *c* at T_M. A recent NMR study [31] suggested that both transitions could be attributed to spin density waves, i.e. Fermi surface nesting effects, in which case the transition at T_{MI} would involve only modest modifications to the spin order, again producing little measurable magnetic entropy. The neutron diffraction study mentioned above [28], did not measure any large change in the spin order below T_{MI}, citing a maximum reorientation in the spin direction of 10°. They produced a model for the magnetism which involves chains of magnetically ordered Co atoms running along a; provided these chains are sufficiently decoupled along c this model may explain the two dimensionality as suggested by the macroscopic measurements. This is discussed further in chapter 6.

4.5.2 Metal-Insulating Transition

The resistivity was measured with the current flowing through the *ab* plane and along the *c*-axis as a function of temperature and field, as detailed in figure 4.19. The resistivity in zero field is plotted in panel A; both curves increase slowly with decreasing temperature before a rapid upturn at T_{MI}. There is a further

modification to the resistivity at ∼20 K, however there is no feature in the resistivity that can be associated with the magnetic ordering at 88 K. The shape of the resistivity is reminiscent of a standard Mott metal-insulator transition, and the total value of ρ_{ab} increases by a factor of 26 along *c* and 10 along *ab* between T_{MI} and 2 K. The datasets as presented in panel A were retaken in applied fields of 90 kOe in directions both parallel and perpendicular to the current. The resistance contacts were removed and swapped in orientation in order to check the validity of the collected results, which were found to be repeatable except for measurements made around T_{MI} indicating possible hysteretic behaviour. The MR as presented in panel B is connected with the MI transition and is evidently complex: an applied field in the basal planes suppresses the resistance to a maximum value of $\sim 2.5\%$ at 20 K before tending to zero at base temperature. For a perpendicularly applied field, there appears to be no effect with the current aligned with the field, but a small positive MR for currents along *ab* which is suppressed by the 20 K magnetic transition before reappearing once more at lower temperatures.

The absolute values of the in-plane resistivities agree well with other published data however the anisotropy falls far short of other reported values in the range of 200-2500 [29, 80]. It should be noted however, that these references report measurements made from flux grown crystals that typically have plate-like habits and therefore very small dimensions along *c*, an order of magnitude smaller than those produced by the floating zone method. In fact, only reports of ρ_{ab} measurements are available for floating zone crystals [28, 30]. It may be the case that the flux grown crystal provide better measurements of the bulk resistive properties if the floating zone crystals have many dislocations within the basal planes or inclusions of misaligned crystals, as described previously in section 3.3. In the imperfect crystals, a nominal *c*-axis measurement may determine the resistance of paths through the *ab* plane joined by sections of misaligned crystals. Although this explanation readily resolves the contradiction between the magnitudes of ρ_{ab} and ρ_c, the fact that features such as the SDW transition in the $x = 0.7$ samples

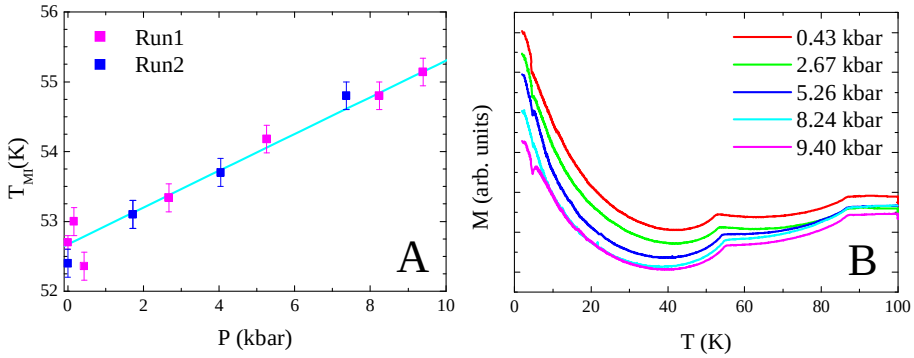

Figure 4.20: Panel A: The increase in T_{MI} as a function of pressure. Panel B: The raw magnetisation data at several pressures. T_M remains unchanged in pressures up to the maximum measured P of 9.5 kbar, however T_{MI} is shifted to higher temperatures along with a general decrease in the magnetisation.

and the anisotropic MR results at both $x = 0.7$ and 0.5 are different with the current aligned along different directions is less well understood. The anisotropy found in the magnetoresistance matches the results of Wang et al. [29] for some directions and not others. Importantly, the results in this reference show only the isothermal MR measurements as a function of field for just temperatures of 2 K and 20 K, the temperature at which the in-plane MR is suppressed for $H//c$ and a maximum for $H//ab$. The authors suggest the magnetic stripe ordering found at this doping level is necessary in order to produce the complicated angular MR dependence.

4.5.3 Modifications to the Magnetic Order Under Pressure

The magnetic susceptibility was investigated as a function of pressure as in section 4.1.4. $M(T)$ measurements were made on two different crystals with $H_{ab} =$ 50 kOe in isostatic pressures up to 9.5 kbar, shown in figure 4.20. The critical temperature of the magnetic ordering T_M was found to be invariant with applied pressures in this range, whereas the MI transition temperature increased linearly from 52.5(2) K to 55.1(2) K at a rate of 0.26(2) K/kbar. The increase in T_{MI} with pressure supports the proposal of Bobroff et al. [31] that this transition is due

to the formation of a SDW state as a consequence of FS nesting effects; as seen at the higher doping level, the application of pressure distorts the FS topology with direct consequences on the magnetic ordering temperature. It is interesting to note that a general decrease in magnetisation is brought about by the increase in pressure; the data in panel B of figure 4.20 have not been offset from each other.

4.6 Discussion

In summary, the magnetic, thermal and electrical properties of Na_xCoO_2 single crystals samples have been measured at a range of different doping levels as a function of temperature T and applied field H, oriented parallel and perpendicular to the stacking planes of the crystal. At higher doping levels, an AFM SDW transition is observed at 22 K. T_{SDW} is independent of both x and H, however may be increased to higher temperatures by the application of external pressure. The pressure measurements were made in order to fully investigate the proposed dome shaped dependence of T_{SDW} with x, as discussed in section 2.2. We must first consider whether there is any equivalence between the pressures applied here and the effects of doping. There are few studies of the pressure dependence of the structure of Na_xCoO_2. Rivadulla et al. [74] have measured the change in the room temperature lattice parameters with pressures up to 45 kbar for a powder sample of x=0.57 crushed from single crystals. The structure remained unchanged, with a first order phase transition at 35 kbar separating a highly compressible low-pressure phase from a high-pressure phase which is less compressible. The *c*-axis initially decreases from 10.99 Å at ambient pressure to 10.88 Å at 10 kbar ($\partial c/\partial P = -0.012$Å/kbar) whilst *a* decreases from 2.8293 to 2.8193 Å ($\partial a/\partial P = -0.001$Å/kbar) over the same pressure range. Assuming a similar behaviour across the Na_xCoO_2 series we can use the data of Huang et al. [10] to estimate that a reduction in x from x=0.71 to x=0.63 brings about a change in *c*[*a*] that could

be induced by the application of a positive[negative] pressure of around 11 kbar[7 kbar]. This suggests that the magnitude of any chemical pressure induced through doping should be comparable with our maximum externally applied hydrostatic pressure of 10 kbar, although doping will also alter the nature of the electronic configurations within the system.

There have been suggestions that over the range of x considered here, Na_xCoO_2 phase segregates into magnetic and non magnetic regions [81]. This may explain the gradual reduction in the magnitude of the jump at T_{SDW} seen in the $C(T)$ data and if there is a non magnetic phase, why the application of pressure is unable to restore the magnetic order. Whether this is the case or not, it is clear that the application of moderate pressure modifies the exchange pathways within the magnetically ordered phase sufficiently to strongly influence the magnetic order. We must therefore consider how this may occur and what consequences this has for our understanding of the nature of the magnetic order in this material. How does the observed behaviour compare with that of well characterised SDW systems? In both the 1D Bechgaard salts [82] and the 2D $(ET)_2X$ organic conductors [83], an almost perfect nesting of the Fermi surface stabilises a SDW state. The application of pressure increases the deviation from perfect nesting and suppresses the SDW. In other words, pressure increases the dimensionality of the system, which destroys the Fermi surface topology necessary to support the SDW ground state. For a perfect nesting case [84], the application of a magnetic field also decreases the SDW transition temperature; in contrast, for imperfect nesting, the SDW ordering temperature increases in an applied field. The behaviour of the magnetic ordering temperatures plotted in figure 4.9 and 4.20 evidently agree with the scenario of imperfect nesting being enhanced by the application of pressure. In order to fully ascertain the link between hydrostatic pressure and the effects of Na doping, detailed measurements of the crystal structure as a function of pressure are necessary. It is known that at room temperature the thickness of the CoO_2 layer and the Co-O distance remain almost constant for $0.7 < x < 0.76$, while the

thickness of the NaO_2 layer increases [10]. If it is principally the thickness of the CoO_2 layer that controls the magnetism, this may explain why T_{SDW} remains constant within this range of x and why the application of pressure leads to an increase in T_{SDW}. However, given that the CoO_2 layer thickness continues to decrease with x for x <0.7 while the signature of magnetic order disappears, we must assume that the thickness of the NaO_2 layer or other factors also play a role. Recent calculations [85] of the exchange pathways within this material suggest that superexchange via direct O-O hopping and/or through intermediate Na atoms (i.e. Co-O-Na-O-Co) are important and that the exchange integrals are rather more two dimensional than suggested by the neutron scattering data [16, 17]. This interplanar Co-Co AFM coupling, whether mediated through the Na orbitals or not, will undoubtedly rely on the Na occupation level. Since superexchange depends more strongly on distance in comparison to the in-plane FM double exchange interactions, a decrease in *c* caused by applying external pressure will result in a marked change in inter-planar hopping distances without altering the number of superexchange pathways.

In the SDW phase, the hysteresis observed in $M(H)$ loops below 10 K indicates that the magnetic order has a small ferromagnetic component. A large, positive magnetoresistance coexists with this FM state. The magnitude of the observed hysteresis along with the nearly linear $M(H)$ behaviour and the peak in $\chi_{dc}(T)$ seen at higher fields, underline the fact that whilst ferromagnetic correlations play a role in this system, the SDW is predominantly antiferromagnetic in nature. At the lowest temperatures both the heat capacity and the χ_{ac} data suggest that a significant portion of the SDW state is pinned, producing a glassy ground state. This is not uncommon among SDW materials.

It is clear that electronic correlations play an important role in the physical properties of sodium cobaltate across the phase diagram. It has been suggested for Na_xCoO_2 that the two sections of the Fermi surface (i.e. the narrow a_{1g} and the broader $a_{1g} + e'_g$) bands play different roles. The magnetic susceptibility, χ,

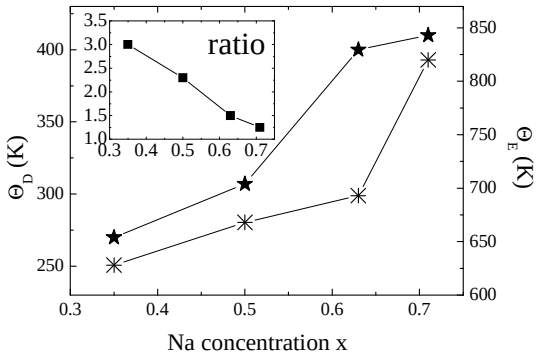

Figure 4.21: The dependence of x on the Debye and Einstein fits to the heat capacity data. Inset: the relative weighting of the Debye and Einstein functions to the total heat capacity where the units represent strength of the Einstein fit compared to a value for the Debye fit of unity.

and the electronic component of the heat capacity, γ , depend (to lowest order) on the density of states which is determined by the large Fermi surface with a_{1g} symmetry. The carriers in the $a_{1g} + e'_g$ band are mobile because the band is spread in the *ab* plane. The a_{1g} band is unstable to the formation of the SDW leading to modifications in χ and γ. The reduction in electron-electron scattering resulting from the formation of the SDW leads to an increase in conductivity along *ab*, despite the expected reduction in the number of charge carriers.

The layered structure of the Na_xCoO_2 system is reflected in the magnetic susceptibility data where both the temperature independent susceptibility and Landé g-factor are anisotropic, a feature common to other cobalt based oxide materials. The transport properties are also anisotropic. This anisotropy appears to increase with decreasing x (towards $x = \frac{1}{2}$). Other features also appear to depend sensitively on doping levels. For instance, both the Debye and Einstein temperatures in the fits to the heat capacity data decrease monotonically with decreasing x, indicating a lowering of acoustic velocities in the system due to the decoupling of CoO_2 layers when sodium is removed. An increase in two dimensionality with reduction in x is also visible in the transport measurements with a general increase in ρ_c as the sodium level is reduced.

Finally, the magnetic ordering in the half doped system has been investigated. The macroscopic measurements quantitatively agree with the proposed AFM ordering at $T_M = 88$ K, where the moments are aligned within the *ab* plane. This is followed at $T_{MI} = 53$ K by a MI transition and complex, angle-dependent MR, that is significantly modified by a yet another transition at approximately 20 K. The origin of the low temperature transition has yet to be identified with claims of magnetic transitions occuring at all three temperatures T_M, T_{MI} and $\sim$20 K in μSR studies [19, 86], disputed by neutron diffraction measurements [28] in which the magnetic order established at T_M is apparently invariant down to the lowest measured temperatures.

Chapter 5

Ionic Ordering in Na_xCoO_2

The macroscopic properties of Na_xCoO_2, as presented in the previous chapter, are clearly intimately linked to the effect of sodium doping on the electronic structure. In order to fully understand the nature of the electronic coupling of the sodium to the cobalt oxide planes, precise knowledge of the crystallographic structure across the phase diagram is necessary. Sodium cobaltate has been the topic of several powder neutron scattering studies [8, 30, 87] and its average crystal structure has been determined at room temperature. The trigonal distortion in the cobalt oxide octahedra is found to depend sensitively on the distribution of the sodium in the charge reservoir layers, and in particular on which crystallographic sites within the structure are occupied or vacant.

Figure 5.1 reproduces the crystal structure presented in figure 2.1 viewed down the *c*-axis, and depicts the crystallographic positions available to the sodium ions. The spheres drawn in the figure have been scaled down by five and a half times; due to its large ionic radius, not all of the sodium sites may be simultaneously occupied. According to the study undertaken by Huang et al.[10], materials with $x <$0.75 have $6h$ and $2b$ sites occupied in a ratio of 1:1.6. Above $x =$ 0.75, one half of the sodium atoms preferentially occupy the higher symmetry $2c$ site whilst the remaining $x - 1/2$ atoms reside on the $2b$ site. It is possible for a sample to contain phase separated combinations of both of these structural arrangements,

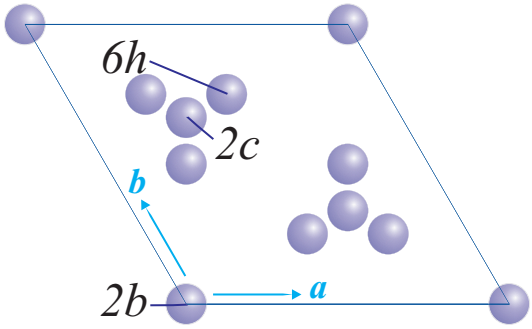

Figure 5.1: The three different crystallographic sites occupied by the sodium atoms.

with the $x = 0.75$ sample in the Huang et al. [10] study comprising a 30% weight fraction of the first phase of partially occupied $6h$ and $2b$ sodium sites, and a 70% fraction of the second phase with the $2c$ and $2b$ atomic sites occupied. These two phases are subsequently labelled $6h$ and $2c$ after the respective Wykoff positions of the first sodium site. The transition between the phases is driven not only by changes in the total sodium content of the sample, but may also be thermally induced [88]. A systematic study of the crystal structure of sodium cobaltate is presented in the following sections, determined as a function of temperature, in order to shed light on the nature of the magnetic, thermal and transport properties. Information describing the unit cell and atomic positions of both phases may be found in the caption of table 5.2.

5.1 Evidence for Sodium Ordering in the Heat Capacity and Resistivity Measurements

Heat capacity and transport measurements were performed on single crystal and powder samples in temperatures up to 400 K (shown in figure 5.2). Several high temperature anomalies are present in both data sets, each exhibiting hysteresis of the order of 1 K. The anomalies are unaffected by the application of fields up to 90 kOe, suggesting the transitions are structural, rather than magnetic, in

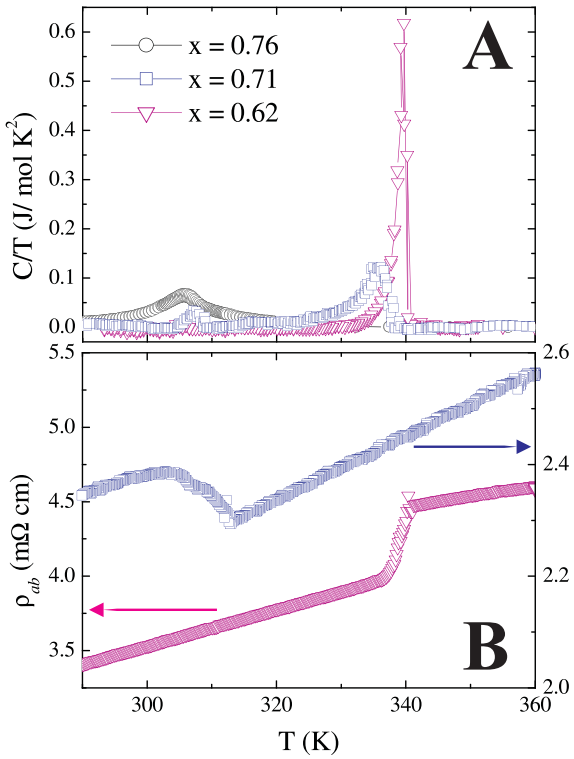

Figure 5.2: Panel A: The high temperature heat capacity data for $x = 0.75$ powder, and $x = 0.71$ and 0.62 crystals. A background of the Debye and Einstein fits were subtracted. Anomalies that evolve with changing sodium content occur at two distinct ordering temperatures of 305 K and 340 K (T_{Na1} and T_{Na2}). No sodium ordering transitions are visible in samples with x <0.6. Panel B: The in-plane resistivities for the two crystals. Anomalies in ρ_{ab} occur at temperatures coincident with the Na ordering temperatures seen in the heat capacity.

origin[1]. At the highest sodium concentrations, a peak is visible in the heat capacity data centered on $T_{Na1} = 305$ K. The peak is rather broad, with the onset of a larger than expected C value occurring at ∼315 K. At lower values of x, a much larger anomaly is seen at $T_{Na2} = 340$ K. With intermediate sodium concentrations, peaks at temperatures within a few degrees of both ordering temperatures may be obtained. After a background subtraction of the Debye-Einstein fits obtained over the temperature range 2 - 400 K, an integration of the C/T versus T plot (as presented in panel A of the figure) will calculate the measured change in entropy at each transition. Assuming the jump in heat capacity occurs due to the transition from a high temperature state, where the Na ions are completely mobile, to an ordered structure in which the Na ions have been "frozen" onto specific sites, the total configurational entropy for the $x = 0.71$ crystal is calculated to be 10.03 J mol^{-1} K^{-1} (see appendix B). The total measured entropy for the $x = 0.75$ powder and the $x = 0.71$ and 0.62 crystals over the entire temperature range presented

[1]It is noted, however, magnetic interactions with an energy scale of ∼350 K = 30 meV would require much larger magnetic fields to manipulate the moments.

in the figure is 1.05, 0.98 and 1.09 J mol^{-1} K^{-1} respectively. This corresponds to just 10.1%, 9.3% and 10.8% of the configurational entropy expected for sodium ordering over the two available sites, using the site occupancies as defined above for the $6h$ and $2c$ structures. This may indicate that considerable Na disorder persists below $T_{Na1[2]}$. The similarity of the measured entropies over the three different doping levels suggests, however, that both transitions are driven by similar events of real space sodium ordering.

Anomalies also occur in the in-plane resistivity measurements, shown in panel B of figure 5.2. Two kinks in the data are visible for the $x = 0.71$ crystal, one at T_{Na1} and another much larger than the first at 315 K, the onset temperature of the jump seen in the $x = 0.75$ powder sample. Ionic conduction between the CoO_2 planes is expected at high temperatures via the direct movement of the sodium ions. The freezing of the Na ions onto well-defined sites at the order-disorder transition could therefore lead to a small increase in ρ. However, ionic conductivities at room temperature are expected to be much lower (10^{-3} S cm^{-1}) than the magnitude of the jump seen here, where $\Delta\rho_{ab} \approx 0.1$ mΩ cm ($= 10^3$ S cm^{-1}). Foo et al. [25] have suggested that there are strong correlations between the Na ions and the charge carriers which, at $x = 1/2$, leads to an insulating state at low T. At $0.6 < x < 0.8$ the effects are expected to be weaker. Nevertheless, the carriers are still likely to be influenced by modulations in the Na layers as the sodium ions order leading to some charge localisation. These effects are much more strongly felt within the CoO_2 layers resulting in the sharp increase in ρ. This is in contrast to the transition seen at T_{Na2} in the $x = 0.62$ sample where a reduction in temperature through the Na ordering transition is accompanied by a large drop in resistivity. The likely origin of the sudden reduction in the resistivity is the decrease in scattering from the more ordered phase. Both decreases [22, 89] at 340 K and increases [90, 91] at lower temperatures have been reported to occur in the resistivity, although most measurements in the literature have been made to a maximum temperature of just 300 K. Without a more complete survey of

sodium ordering transitions as a function of x, the connection between the sodium doping level and whether charge localisation or reduced scattering is the dominant effect cannot be clearly defined.

5.2 The HRPT Diffractometer

The HRPT diffractometer at SINQ (PSI) is a standard thermal neutron powder diffractometer as described in section 3.10. Three samples of x = 0.75, 0.59 and 0.50 (consisting of ∼20 g) were packed into vanadium cans in a He atmosphere and diffraction patterns obtained for temperatures between 1.2 $\leq T \leq$400 K using a cryofurnace. Typical counting times were of the order of one hour for each temperature set point. This enabled data acquisition for small steps around the transition temperatures to be taken within a reasonable time limit for the instrument. The machine was operated in high intensity mode, utilising a Ge monochromator to select a wavelength of 1.155 Å. The crystal structure refinements were carried out using the program $\mathrm{FULLPROF}$ [92]; the neutron scattering lengths for each atomic species were obtained from the program's internal tables. Diffraction data collected around the T_{Na} transitions were measured with both increasing and decreasing temperature in the higher x compound to check for hysteretic behaviour. No magnetic peaks were observed below the magnetic ordering transitions in either the SDW phase or the half doped phase. To date, only two neutron scattering studies have directly observed the antiferromagnetic ordering at $x = 0.82$ [17] and $x = 0.50$ [28]: the single crystal, spin polarized diffraction experiments estimated a total ordered moment of just 0.13(2) and 0.13(1) μ_B per Co respectively. It is therefore not unreasonable to expect that powder averaging in an unpolarized neutron diffraction experiment will lead to a lack of sufficient sensitivity to discern the magnetic scattering.

5.2.1 Coexistence of two Structural Phases in the SDW System

Structural detail relating to the ordering of Na between the CoO_2 planes can however, be ascertained. The crystal structures of $x = 0.75(3)$ and $x = 0.59(2)$ powder samples were refined to contain the two phases as defined above; one in which the first sodium atom is positioned in the centre of the Co triangular lattice and one in which this sodium atom is displaced slightly. This displacement relaxes the energy degeneracy between the two Na sites. Despite the small magnitude of this structural offset, strong correlations between Na-O co-ordination and the charge transfer to the CoO_2 system (which also influences the charge density on the oxygen site by a hybridization between the Co e_g band the O $2p$ states [93]) lead to a change in the CoO_6 octahedra and consequently to a noticeable difference in lattice parameters between the two phases. The two phases are subsequently easily identified in the diffraction data and the relative weight fractions of each can be tracked as a function of temperature.

The diffraction data for the $x = 0.75$ powder were fitted to severals models: a single $2c$ phase, a single $6h$ phase and a linear combination of the two. Below T_{Na1} the system appears to be stable in a mixed phase state with a $6h$ to $2c$ ratio of 3:2 (figure 5.4). Above T_{Na1}, the $2c$ phase disappears and is completely removed at a temperature of 322 K; the structure refinements using the multi-phase model at higher temperatures produce a 1:1 weight ratio for both phases, with lattice parameters that converge to the same values. Further to this, the B factor for the Na(1) atom in the $2c$ phase jumps from 1.5 $Å^2$ to 2 $Å^2$; discontinuities in the thermal factors are unphysical and indicate either a problem with the atomic occupancy (to which the size of the thermal ellipsoid is coupled within the Rietveld procedure) or a change in atomic position, as in the present case. Refinements of the single phase $6h$ material produce the lowest χ^2 values for these high temperature data. The onset of the ionic ordering is accompanied by a lattice expansion (panel B of figure 5.4), driven by the transfer of Na from one atomic site to the other. This is visible in both phases, before *a* and *c* relax to

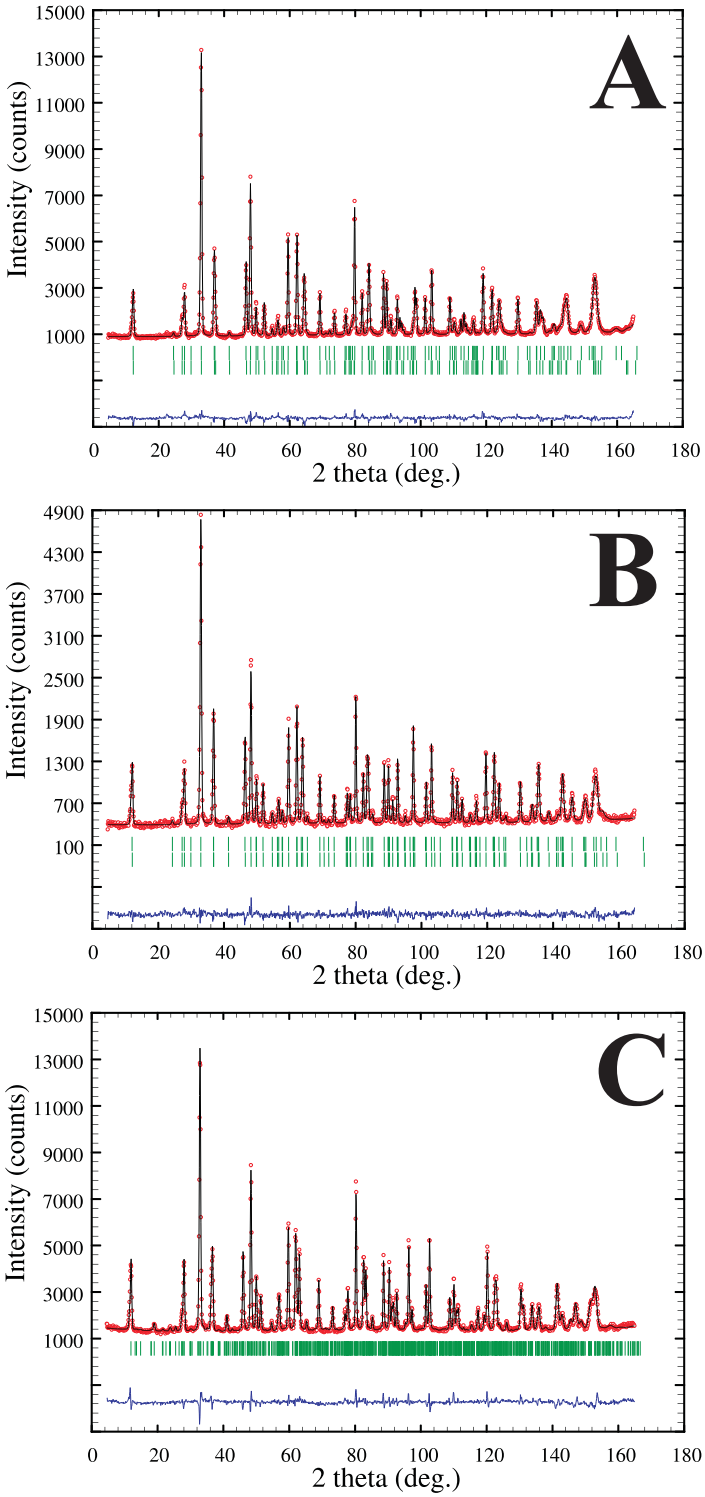

Figure 5.3: Rietveld refinement fits of (A) $Na_{0.75}CoO_2$, (B) $Na_{0.59}CoO_2$ and (C) $Na_{0.50}CoO_2$ at 300 K. The data points are represented by red circles, and the refinement fit as a black line. The two sets of green vertical lines detail the Bragg positions of the reflections belonging to the different phases. The difference between the data and the fit is plotted beneath in blue.

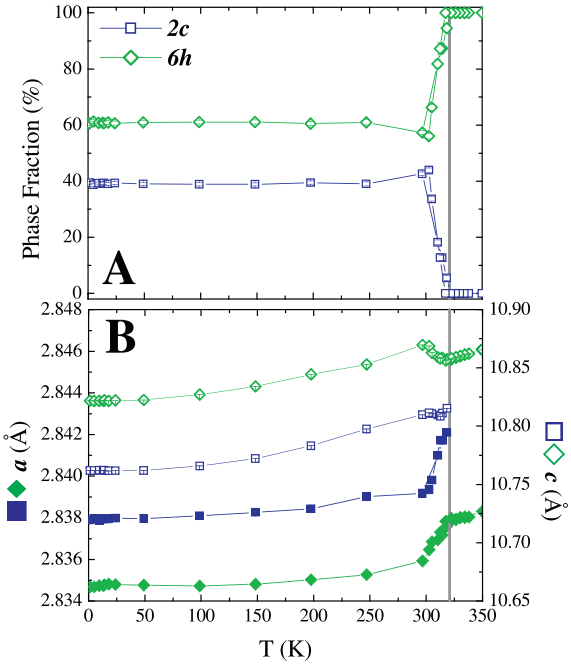

Figure 5.4: Panel A: The $2c$:$6h$ phase ratio as a function of temperature. Reversible phase separation occurs below T_{Na1} = 305 K (denoted by the vertical grey line); the transition shows a hysteresis of ∼2 K. Panel B: The *a* (closed symbols) and *c* (open symbols) lattice parameters for both phases show the lattice deformation that accompanies this transition. Data for the $2c$ phase is plotted in blue, those in green refer to the $6h$ phase.

values between those of the individual phases above T_{Na1}. The transition exhibits a slight hysteresis of ∼2 K most clearly seen in the evolution of the 6*h* lattice parameters (not shown), consistent with previous measurements [94]. The behaviour of $a_{2c[6h]}(T)$ and $c_{2c[6h]}(T)$ agrees well with the measurements of Huang et al. [88] (over the limited temperature range presented by these authors) although the absolute values for the *a* lattice parameter are slightly smaller and, interestingly, the transition occurs at T_{Na1} rather than T_{Na2}. At base temperature, the *a*[*c*]-axis lattice parameter of the $6h$ phase is 0.11%[0.56%] smaller[larger] than that of the $2c$ phase. This corresponds to a difference of 0.33% in the unit cell volumes with the $6h$ phase being the larger of the two. The difference in lattice parameters results in a visible splitting of some of the high angle diffraction peaks, as shown in figure 5.5.

The resulting high temperature single phase material has fractional Na occupancies of 0.35(2) and 0.41(1) at the $6h$ and $2b$ sites respectively. On cooling through the Na ordering transition, the sodium ions are redistributed between the phases. The $6h$ phase has average $6h$ and $2b$ sites with fractional occupancies of 0.33(1) and 0.37(1), whereas the $2c$ phase consists of $2c$ and $2b$ sites occupied at

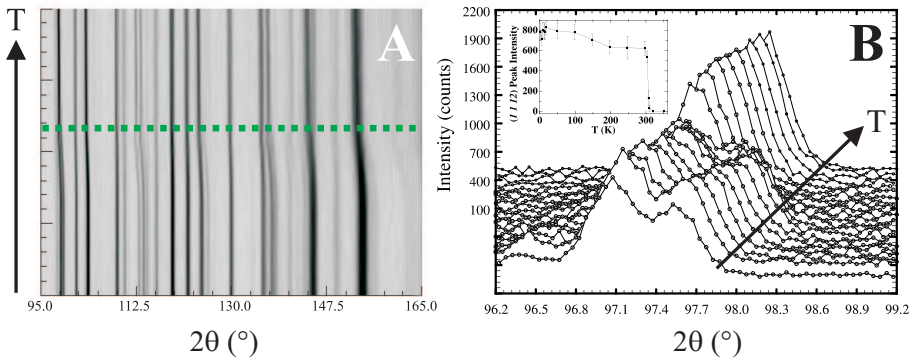

Figure 5.5: Panel A: A 2D interpolated line plot of the high angle diffraction peaks (Note: the datasets are plotted at equal intervals along the y axis which therefore does not represent a linear temperature scale). Differences in the lattice parameters between the $2c$ and $6h$ phase lead to a splitting of peaks below the ionic ordering temperature T_{Na1} (indicated by the dashed green line). Panel B: An intensity vs. 2θ plot detailing the temperature dependence of the $(1\,1\,12)$ reflection (the data sets have been offset for clarity). The integrated intensity of the $2c$ (right hand) peak as a function of temperature is shown in the inset.

0.56(1) and 0.25(1), although the values for the Na n (occupation values) tend to increase[decrease] in the $6h$[$2c$] phase with decreasing temperature. Consequently the x values for both individual phases (calculated by the simple addition of the site fractions) are not static, and vary with temperature as depicted in panel A of figure 5.6 (the individual site occupancies are presented in panel B). The combined phase sodium level is, however, invariant with temperature. In order to check these data, the refinements were repeated at each temperature with the same starting values for the sodium occupancies. The fits converged to the same values for each data set and are therefore considered to be a true representation of the transfer of sodium between the two phases as the temperature is changed, and not just an artifact of the fitting procedure where a false local minimum is found from a starting model based on the output from the preceding fit. The distribution of sodium in the $2c$ phase corresponds well with the values reported by Huang et al. [10], but not for the $6h$ phase for which the authors consistently measure a higher occupancy on the $2b$ site. This site is higher in energy than those found at the centre of the triangular lattice due to the increased Coulomb repulsion resulting

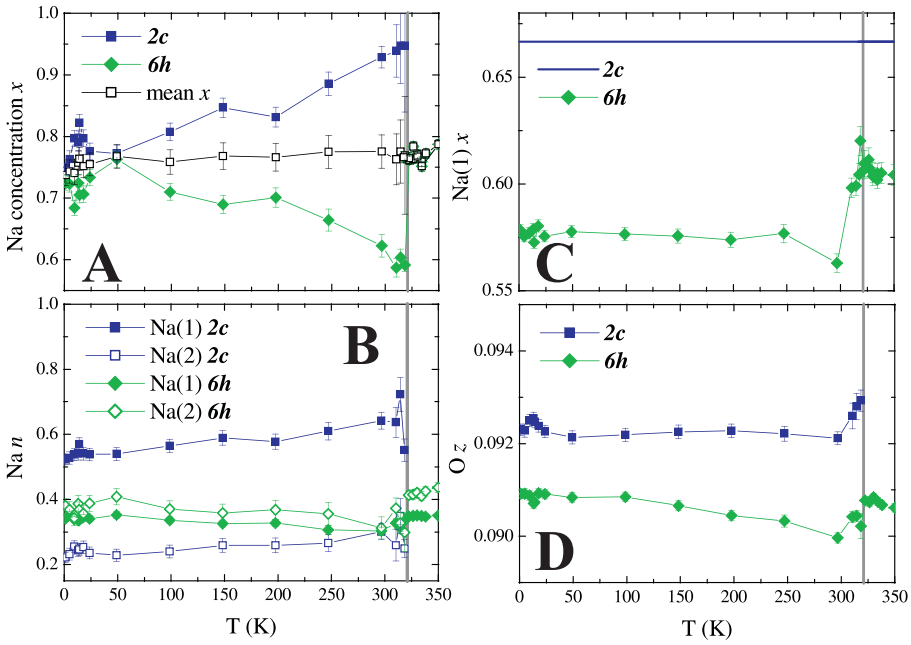

Figure 5.6: Panel A: The total sodium concentration of each phase is variable with temperature whilst the average x remains constant. Panel B: the occupancies of each type of Na atom from which the total concentration is calculated. Panel C: The position of the Na(1) atom in the $6h$ phase jumps to a position slightly closer to the ideal $2c$ position (blue line) above T_{Na1}. Panel D: The z position of the oxygen atoms predicts the $6h$ phase to be more distorted than those in the $2c$ phase. A possible structural distortion of the octahedra around 10-15 K is also visible.

from the smaller Co-Na(2) bond length. The results found in this study, with more or less equal occupancies over both sites, suggest a more realistic structure. The other refinable parameters, namely the positions of the Na(1) atom in the $6h$ phase (which moves slightly closer to the ideal $2c$ position above T_{Na1}), and the height of the oxygen atoms above the cobalt planes were found to vary only a little with T, as shown in panels C and D of figure 5.6.

The bond-lengths and angles presented in figure 5.7 were calculated from the Rietveld refinements using the program Bond_Str, which is part of the Fullprof WinPLOTR suite [95]. Details of the cobalt-oxygen coordination are plotted in panels A and B. The small structural distortion seen in the O z parameter is naturally visible in these data, however the higher temperature data reveal a general increase[decrease] in the $2c$[$6h$] phase that mirrors the change in total sodium con-

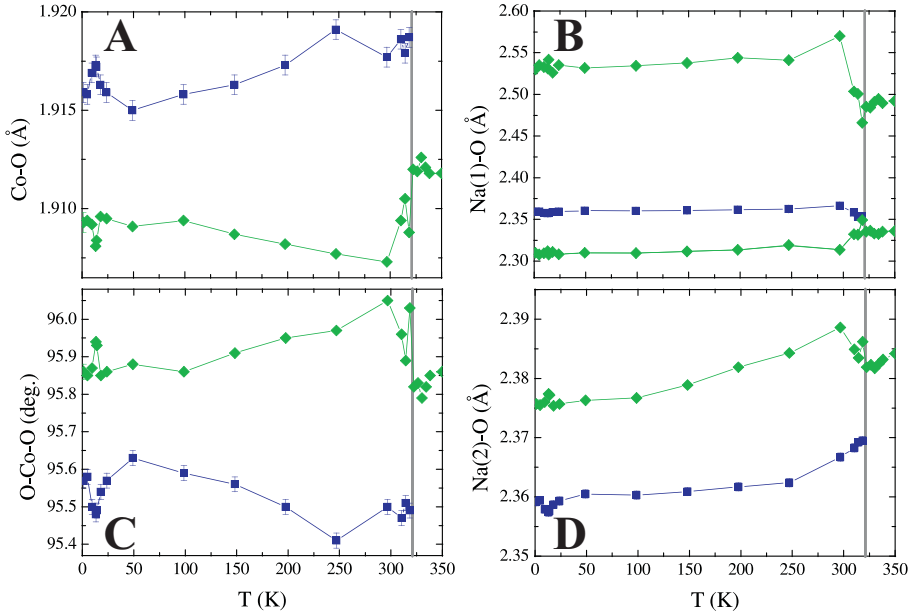

Figure 5.7: Selected bond lengths and angles in $Na_{0.75}CoO_2$ presented as a function of temperature. Panel A: The Co-O distance shows both the low temperature distortion and a general increase[decrease] in the $2c$[$6h$] phase that mirrors the change in total sodium concentration between the two phases. Panel B: The O-Co-O bond angle shows the distortion of the octahedra (i.e. from 90°) in both phases. Panel C: The Na(1)-O bond distances do not change substantially at lower temperatures. The discontinuity seen at T_{Na1} is an effect of the change in the *c*-axis lattice parameter. Panel D: The distance between the oxygen atoms and the Na ions at the $2b$ sites increases monotonically in both phases, again as a consequence of the lattice thermal expansion.

centration between the two phases, suggesting that both the occupation fraction and position of the sodium atoms directly affects the crystal field splitting of the cobalt t_{2g} energy levels. The diffraction data therefore provide the experimental evidence of the role of sodium doping on the magnetic characteristics. Panels C and D show the temperature dependence of the sodium-oxygen distances on the Na(1) ($2c$ or $6h$) and Na(2) ($2b$) sites. The former varies very little with T, whilst the latter shows a general increase in both the phases as a consequence of the thermal expansion of the *c*-axis lattice parameter.

5.2.2 Phase Separation in $Na_{0.59}CoO_2$

The second sample in this study exists in the paramagnetic regime between the SDW magnetic phase at x ∼0.75 and the insulating x = 0.5 system. As such, no noteworthy features in the macroscopic (magnetization or heat capacity) low temperature measurements are observed. The neutron diffraction data do however, show interesting Na ordering effects similar to the magnetic phase discussed in section 5.2.1. The diffraction data were refined to exactly the same models as above: the best fits at low temperature were obtained with a mixed $2c$:$6h$ system in a weight ratio of approximately 1:9, as shown in figure 5.8. The temperature dependence of the lattice parameters also differ; the expansion of *c* in the $6h$ phase is larger than expected, whilst the magnitude of the Co-Co distance (equivalent to the *a*-axis lattice parameter) goes through a minimum at T^* ∼200 K, where the phase segregation occurs with decreasing temperature. Comparisons of the lattice parameters between the two phases follow relations in opposition to those described above, with base temperature values of *a*[*c*] 0.06%[0.50%] smaller[larger] in the $2c$ phase than at room temperature, indicating that the x dependence of the lattice parameters is more complicated than the results presented by Huang et al. [10], who predict the mixed phase to exist only at $x = 0.75$ and not at lower stoichiometries.

The change from a negative to positive lattice expansion in the *a*-axis lattice parameter of the $6h$ phase at T^*, whilst the *c*-axis lattice parameter increases monotonically with increasing temperature, produces a temperature shift of the Bragg peaks that is (hkl) dependent. Consequently, some reflections appear to merge due to an increased translation in 2θ of some peaks in comparison to others. This is most clearly seen in the plots presented in figure 5.9. Whilst the overall result appears similar to the effect of phase separation seen in the $x = 0.75$ sample, all of the reflections plotted in panel B of the figure belong to the $6h$ phase only (the small weight fraction of the $2c$ phase at low temperature ensures the intensity from the Bragg peaks of this phase are not clearly visible in the diffraction pattern

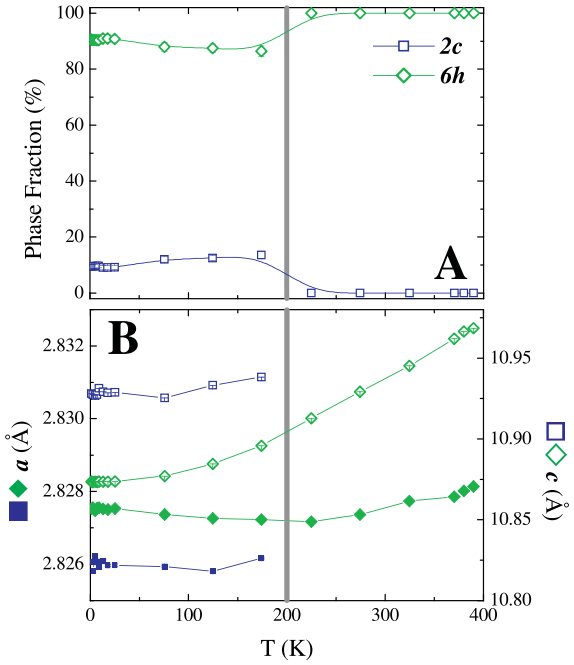

Figure 5.8: Phase fractions (panel A) and lattice parameters (panel B) of $Na_{0.59}CoO_2$. A mixed phase state exists below T^* ~200 K, separating to a single $6h$ phase at higher temperatures. The lattice expansion in the $2c$ phase is less than observed at higher doping and a minimum in the $6h$ *a* lattice parameter coincides with T^*.

as a whole).

The occupancy of the sodium sites of the $2c$ phase mirror that of the higher doped material, with preference of the $2c$ over the $2b$ site leading to a total average sodium concentration of 0.57(4). Once again in the $6h$ phase the sodium ions are distributed almost evenly between the $6h$ and $2b$ sites, giving a calculated average sodium concentration is 0.64(2). The structural parameters obtained in the refinements are plotted in figure 5.10. Due to the small fraction of the $2c$ phase present in the system, the fitted parameters and their evolution with temperature are on the limits of experimental resolution, therefore producing larger errors in the data than seen in the first sample. It is evident, however, that the sodium occupancies and consequently the total sodium concentration of the two phases (panels A and B) do not change with temperature in this sample. The fits also reveal an increased difference in the distortion of the CoO_6 octahedra in the two phases than found in the SDW system (panel D), generated from the increased deviation of the $6h$ Na atom from the high symmetry position (panel C).

The bond lengths and angles were calculated once again and are plotted in figure 5.11. The relations between the bond lengths in the two phases are similar

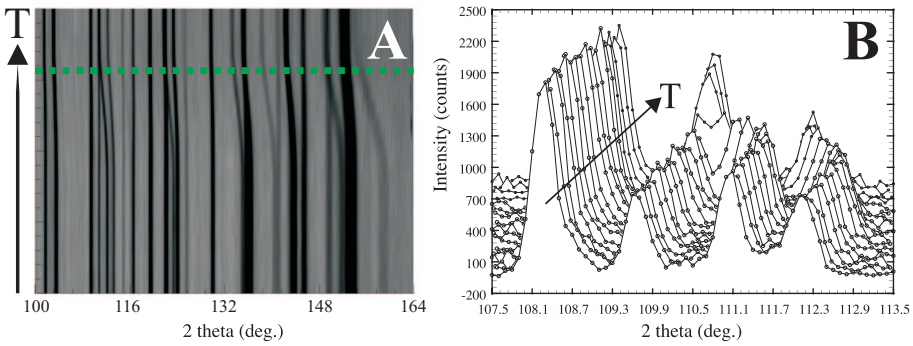

Figure 5.9: Panel A: An interpolated line plot of the high angle diffraction peaks, plotted with a non-linear temperature scale for clarity. A negative lattice expansion in the *a* lattice parameter below T^*, whilst *c* continues to decrease, results in a novel translation of the Bragg peaks with temperature that is (hkl) dependent. Panel B: The temperature evolution of the (220),(222),$(1\,0\,15)$ and $(2\,0\,13)$ (left to right) reflections are detailed in this panel.

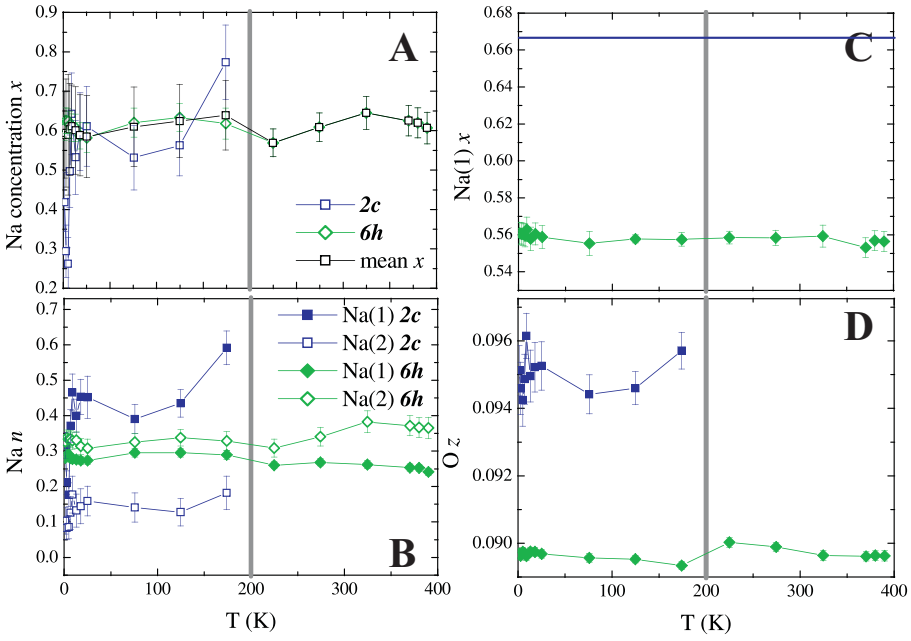

Figure 5.10: Panels A and B: The individual sodium site occupancies and the total sodium concentrations are independent of temperature. Panels C and D: Neither the sodium nor oxygen positions are seen to vary with T, however the absolute values of both present an increase the distortion from the ideal $2c$ and CoO_6 octahedral shape than seen in the previous sample.

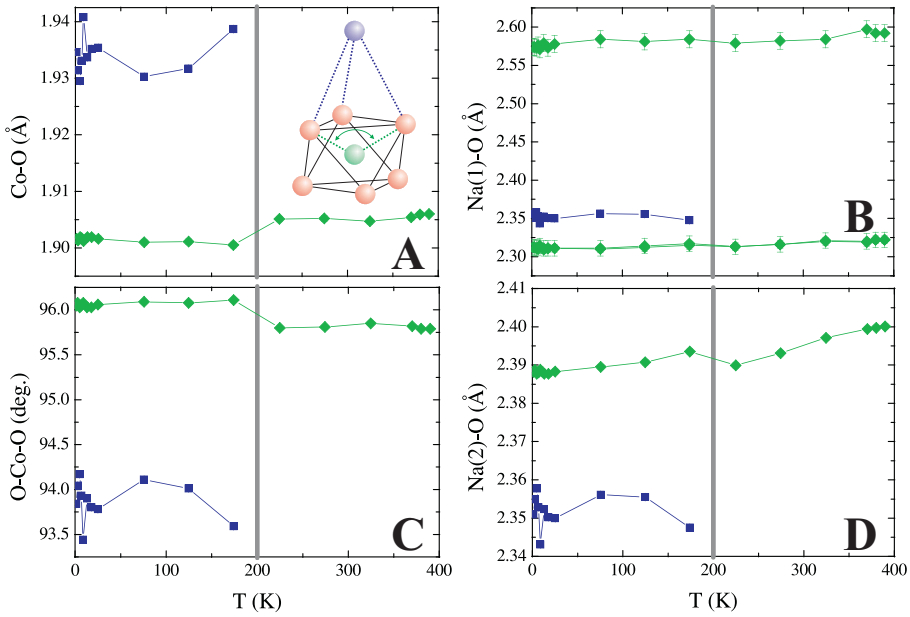

Figure 5.11: Selected bond lengths and angles in $Na_{0.59}CoO_2$ presented as a function of temperature. Panel A: The temperature dependence of the Co-O bond distance mirrors that seen in the $x = 0.76$ sample, although the difference between the two phases is exaggerated by the increased distance of the O z positions. Inset: The partial structure of Na_xCoO_2 showing one CoO_6 octahedron and one Na(2) atom (not to scale). The Co[Na(2)]-O bonds are indicated by green[blue] dashed lines and the O-Co-O angle by the green arrows. Panel B: The distortion of the CoO_6 octahedra is further amplified in the $6h$ phase with a increase in the bond angle observed on passing through the sodium reordering transition. Panel C: The Na(1)-O bond distances follow the same temperature independent relations as found previously. Panel D: The increase in Na(2)-O with temperature is less than expected due to the anomalous values of $a_{6h}(T)$. The colour scheme used in all four panels follows the convention used in the previous figures.

to those of the $x = 0.75$ sample. However, it is the decreased value of the O-Co-O bond angle in the $2c$ phase, combined with the increase in the difference in the Co-O bond lengths between the two phases, that results in the *c*-axis lattice parameter being larger than that of the $6h$ phase, as confirmed by a calculation of the Co-Na(2) bond lengths which are equal to one quarter of the total lattice parameter. A diagram of the partial structure of Na_xCoO_2 explaining the atomic coordination is shown in the inset of panel A in figure 5.11. The data at low temperature do not present any evidence of a lattice distortion, complementing the fact that no magnetic anomalies are present in this system.

5.2.3 Supercell Ordering in $Na_{\frac{1}{2}}CoO_2$

The half doped system was studied between temperatures of 1.2 K and 300 K, with smaller temperature steps taken around each of the three transitions of interest (T_M, T_{MI} and the 20 K magnetic transition). A Rietveld refinement of the 300 K data is shown in panel C of figure 5.3; the structural model previously proposed by Huang et al. [30] was used with an orthorhombic supercell of ($2a \times \sqrt{3}a \times c$). The positions of the atoms within the new unit cell were written down and compared to the available atomic sites for the spacegroup P*mmn*. It was confirmed to be the correct choice of spacegroup and the second origin choice setting was chosen to model the orthorhombic unit cell. The "ideal" atomic positions based on the hexagonal unit cell are listed in table 5.1, and the two origin choices for the new unit cell are indicated in figure 5.12. In order to compare the high symmetry atomic positions with the Wykoff positions listed for this particular spacegroup, the axes were permuted $(x, y, z) \rightarrow (z, x, y)$ and the *a*- and *b*-axes of the orthorhombic cell were interchanged so that $a_{orth} = 2a_{hex}$ and $b_{orth} = \sqrt{3}b_{hex}$ in keeping with the new unit cell cited by previous authors [30]. The Wykoff positions written in the table incorporate these changes and hence are different to those listed in the International Tables of Crystallography.

As in the more recent structural study performed by Williams et al. [32], the positions of atoms not at special crystallographic sites were not constrained, producing several interesting observations. Firstly, as seen in panel A of figure 5.13, the lattice parameters *a* and *b* deviate from their ideal values of $2a$ and $\sqrt{3}a$ below room temperature. This orthorhombic distortion of the CoO_2 planes reaches a maximum of 0.05% at 200 K, remaining constant down to temperatures of 1.2 K, and is accompanied by the diagonal distortion of the CoO_6 octahedra as the second and third oxygen atoms move away from their symmetric position in the centre of the Co triangular lattice. This distortion is also seen in the deviation of the two Co(1) atoms from the $y = 0$ plane (as shown in figure 5.12); the magnitude of this twisting increases by a value of one third around T_{MI}, shown in figure 5.14. At

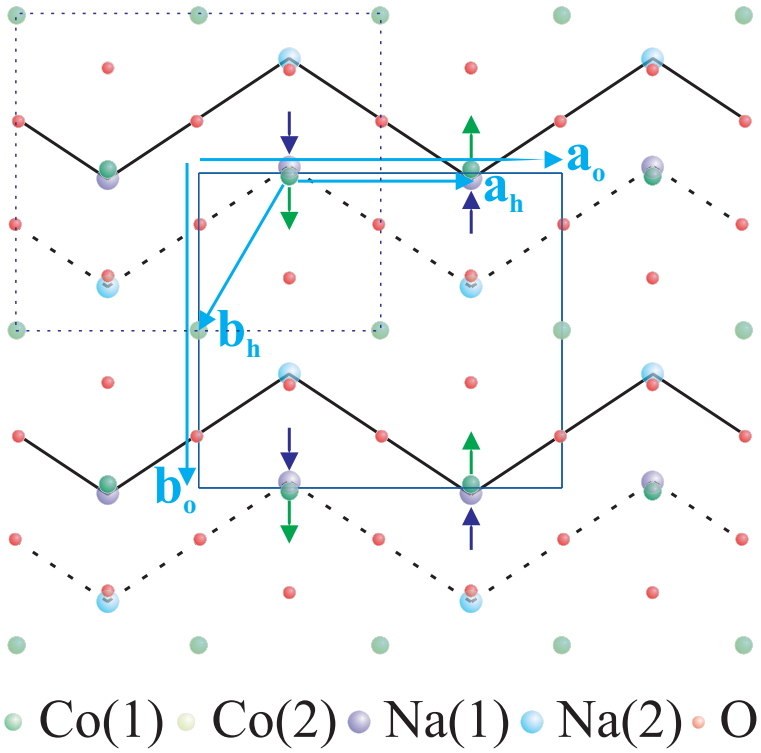

Figure 5.12: The crystal structure of $Na_{\frac{1}{2}}CoO_2$ as viewed down the *c*-axis. The dashed blue and solid blue rectangles represent the first and second choice of unit cell in the new orthorhombic setting. Zig-zag chains of two sodium sites (which are fully occupied in this crystal structure) form along the *b*-axis and are indicated in the figure by solid and dashed black lines (representing chains at $z = \frac{1}{4}$ and $z = \frac{3}{4}$ respectively). With the exception of Co(2), all the atoms deviate from their ideal positions as illustrated by the fact the Co(1) and Na(1) atoms do not lie directly on top of one another. The arrows at these atoms represent the direction in which the atoms move during the extra lattice distortion that occurs around T_{MI}.

	Co(1)	Co(2)	Na(1)	Na(2)	O(1)	O(2)	O(3)
x	1/4	0	1/4	3/4	1/4	3/4	0
y	0	1/2	0	1/3	1/3	1/3	-1/6
z	0	0	3/4	3/4	z	z	z
Wykoff letter	$4e$	$4d$	$2b$	$2a$	$4e$	$4e$	$8g$
Wykoff position	$\frac{1}{4}, y, z$	$0, \frac{1}{2}, 0$	$\frac{1}{4}, y, \frac{3}{4}$	$\frac{3}{4}, y, \frac{3}{4}$	$\frac{1}{4}, y, z$	$\frac{1}{4}, y, z$	x, y, z

Table 5.1: The ideal atomic positions of $Na_{\frac{1}{2}}CoO_2$ in the orthorhombic cell, based on the atomic coordinates of the parent hexagonal cell. The Wykoff letter of each site is labelled on the bottom row (note the change in the coordinate system as described in the text). The coordinates not at high symmetry positions are shaded in grey.

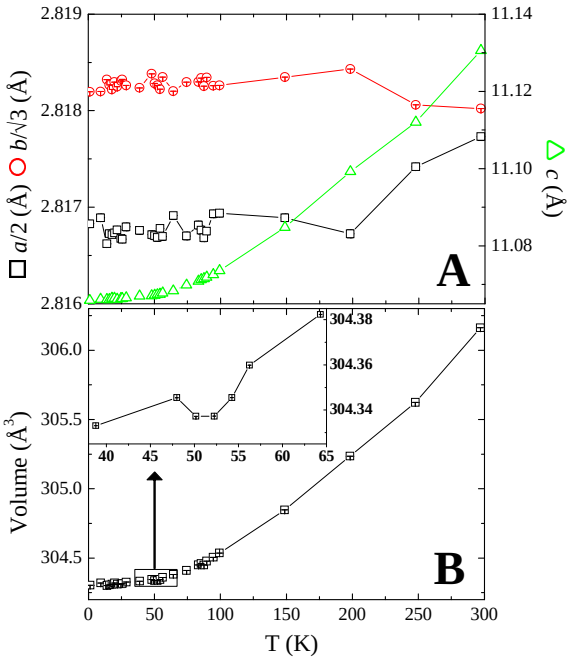

Figure 5.13: Panel A: The lattice parameters of $Na_{0.50}CoO_2$ plotted as a function of temperature. The *a* and *c* axes deviate from their ideal hexagonal cell values below ∼300 K, remaining fairly constant a lower temperatures. Panel B: The variation of the unit cell volume as a function of temperature. The inset shows the lattice contraction around the 53 K transition.

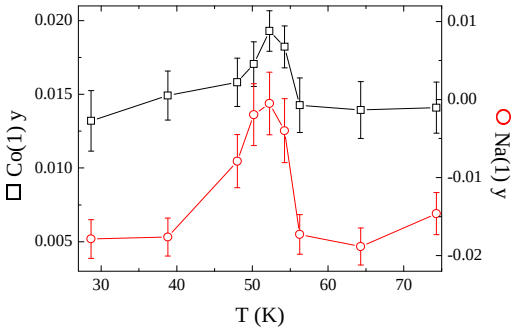

Figure 5.14: Details of the distortion of the Co(1)-Na(1) chains around the 53 K transition.

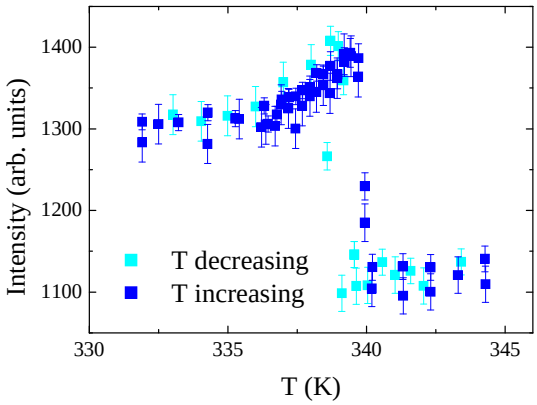

Figure 5.15: Neutron diffraction data in a x ~0.75 single crystal. The integrated intensity of the $2c$ (107) Bragg peak is plotted as a function of temperature.

the same temperature, the y position of the Na(1) atom which sits almost directly below[above] the first[second] Co(1) atom moves from its distorted atomic position to the ideal position in the hexagonal unit cell and back. The second Na atom, whilst also slightly shifted from its ideal ($2c$) position, shows no movement around T_{MI}. This movement of Na and Co along the y axis results in a small contraction in the total unit cell volume around T_{MI} as shown in the inset of figure 5.13 panel B.

Table 5.2: Structural refinement parameters of Na_xCoO_2 at 1.2 K. Samples 1 and 2 were refined in space group *P6$_3$/mmc* with the following atomic positions: Co [$2a$] (0,0,0), O [$4f$] (1/3,2/3,*z*), Na(1) [$6h$] (2*x*,*x*,1/4) and Na(2) [$2b$] (0,0,1/4). Sample 3 was refined in the orthorhombic spacegroup *Pmmn* in the second origin setting, with the following atomic positions: Co(1) [$4e$] (1/4,*y*,*z*), Co(2) [$4d$] (0,1/2,0), O(1,2) [$4e$] (1/4,*y*,*z*) O(3) [$8g$] (*x*,*y*,*z*), Na(1) [2*b*] (1/4,*y*,3/4) and Na(2) [2*a*] (1/4,*y*,1/4).

	$1.\ x = 0.75(2)$		$2.\ x = 0.59(2)$		$3.\ x = 0.50$
	2*c*	6*h*	2*c*	6*h*	
a (Å)	2.837990(4)	2.834620(3)	2.82606(3)	2.827530(3)	4.88131(4)
b (Å)					5.63364(6)
c (Å)	10.761621(3)	10.821926(2)	10.928080(2)	10.873570(3)	11.06592(12)
V (Å^3)	75.07363(2)	75.30514(2)	75.585(1)	75.2864(2)	304.30754(2)
Co(1) y					0.012(2)
Co(1) z					0.0110(6)
Co B (Å^2)	0.04(1)		0.10(1)		0.23(2)
O(1) y					0.334(1)
O(1) z	0.0923(1)	0.09092(9)	0.0951(7)	0.0897(1)	0.0862(3)
O(2) y					0.327(1)
O(2) z					0.0835(2)
O(3) x					-0.0047(8)
O(3) y					-0.1605(8)
O(3) z					0.0902(1)
O B (Å^2)	0.22(5)		0.09(1)		0.07(1)
Na(1) x	2/3	0.578(2)	2/3	0.561(6)	
Na(1) y					-0.021(2)
Na(1) *n*	0.53(1)	0.351(8)	0.32(3)	0.28(2)	
Na(2) y					0.361(2)
Na(2) *n*	0.23(1)	0.39(2)	0.10(3)	0.33(1)	
Na B (Å^2)	0.44(5)	0.50(5)	0.85(23)	0.88(11)	0.06(2)
x	0.760(1)	0.74(2)	0.42(4)	0.61(2)	
R_p	5.63	5.51	5.80	5.11	5.31
R_{wp}	3.99	3.76	4.56	3.41	4.21
χ^2	1.98		1.70		3.54

5.3 Discussion

The refined structural parameters of all three samples at 1.2 K are listed in table 5.2. The powder diffraction data show evidence of a structural change at T_{Na1} for $x = 0.75$, unexpected ionic ordering above 200 K in the $x = 0.59$ sample, and clear evidence of the orthorhombic superstructure in $x = 0.50$ along with the first experimental evidence of a structural distortion around the MI transition temperature. The observation of a transition from a high temperature $6h$ phase into a mixed phased state below 305 K, and the associated changes in lattice parameters and bond lengths, agrees well with the findings of Huang et al. [88]. It must be noted, however, that their change in phase fractions occurred at the higher Na ordering temperature T_{Na2} of 340 K, with a prevalence of the $2c$ phase (with a total weight fraction of 70%) at base temperature. Such a transition was observed, however, in a $x \sim 0.75$ single crystal on the D10 diffractometer at the ILL (details of the instrument are given in chapter 7). The diffractometer was positioned in order to satisfy the Bragg condition of the (107) reflection in the $2c$ phase. The temperature was increased and decreased through T_{Na2}, and the summed intensity calculated for each temperature set point. The disappearance of the $2c$ phase at this temperature is clearly seen as a sharp drop in the scattered neutron intensity, although a large background remains, most likely due to the fact the crystal had a significantly large mosaic spread in the *ab* plane. The transition is hysteretic with a width of $\sim$1 K, again in good agreement with the macroscopic measurements. Although this sample shows the same phase ordering as that seen by Huang et al. [88], some significant differences are apparent. Firstly, the transition in their publication occurs over $\sim$30 K in both warming and cooling runs, an order of magnitude larger than the width of the transition seen in this single crystal experiment. This is perhaps due to Na inhomogeneity in the powder sample. Secondly, the hysteresis is slightly larger at a value of 5 K, although no heat capacity measurements were presented in the paper to check this value.

x = 0.75			x = 0.59			x = 0.50	
$2c$	*a*	14	$2c$	*a*	17	*a*	-5
	c	1730		*c*	1340	*b*	1
$6h$	*a*	13	$6h$	*a*	6	*c*	2420
	c	1750		*c*	2570		

Table 5.3: The lattice thermal expansion parameters of the three powder samples, listed for all phases in units of ppm.

The thermal expansion of the lattice parameters in all three samples, defined as the fractional difference between the lattice parameters at room and base temperatures, are listed in table 5.3 (Note: the calculated values for the $2c$ phase in the x = 0.59 sample are based on the room temperature lattice parameters of the $6h$ phase). The expansivity is highly anisotropic with coefficients differing along the different crystallographic directions by two orders of magnitude. This reflects the nature of the layered structure and agrees with the evolution of the lattice parameters under externally applied pressure [74], which differ by an order of magnitude. The thermal expansion of the *c*-axis in the $6h$ phase of the x = 0.59 sample is almost a factor of two larger than expected. The *c*-axis expansion is a reflection of the high thermal expansivity found in the NaO_2 layers [32] and so the larger value of 2570 ppm is attributed to the distortion of the NaO_6 octahedra that occurs with the decreased value of the Na(1) x position (as described in section 5.2.2). The deviation of the Na(1) site further from the centre of the triangular lattice produces average Na-O distances similar to those found in the x = 0.50 phase, which has a similarly high *c*-axis lattice expansion parameter. The sodium-oxygen coordination is therefore strongly coupled to the structural parameters.

The data presented in this chapter complete the ionic ordering phase diagram proposed by Huang et al. [10] who performed measurements at room temperature only. The mixed $2c$ and $6h$ solid state solution occurs not only at x = 0.75, but exists at lower temperatures with lower sodium concentrations. The

phase fraction of the $2c$ phase at base temperature also decreases with decreasing x, with a measured value of 70% in the $x = 0.75$ data of Huang et al. [88], decreasing to 40% and 10% in the two samples in this study. Plotting the Na ordering temperatures versus the x value of the $6h$ phase suggests that the $2c$ phase extends down to a value of $x = \frac{1}{2}$, where the new ionic ordering pattern occurs; the many different temperatures at which anomalies occur in the published resistivity data may be explained within the framework of this new sodium ordering phase diagram. These data also add weight to the idea proposed in section 4.6, that the material is phase segregated into magnetic and non-magnetic constituents, the relative proportions of both in any particular sample controlling the size of the measured magnetic moment and the jump in the heat capacity at T_{SDW}. Recent NMR and electron paramagnetic resonance (EPR) measurements [81, 96] have verified the presence of mesoscopic phase separation in samples with $0.65 \geq x \geq 0.75$, below temperatures in the range of 220 - 270 K, consistent with the results of this work. The hypothesis is congruous with the measured magnetic properties, given that only the $2c$ phase may exhibit magnetic ordering. A spin density wave results from a nesting instability in Fermi surfaces with high symmetry. Further investigation into the electronic structure of Na_xCoO_2 is necessary in order to confirm whether the movement of the sodium from the high symmetry $2c$ position is enough to significantly alter the Fermi surface topology and suppress the magnetic ordering.

What is the driving mechanism for the different types of sodium ordering? The most popular Na ordering theories rely on the formation of sodium superstructures leading to charge localisation on the cobalt lattice, which is similarly ordered due to the influence of the charge modulations in the Na layers. A large array of different ordered structures have been proposed by density functional theory [97] and Monte-Carlo simulations [98], many of which have been seen in electron diffraction studies [77, 99]. As of yet, only two bulk structure measurements have revealed any superstructure ordering for the SDW material [98, 100], the first a

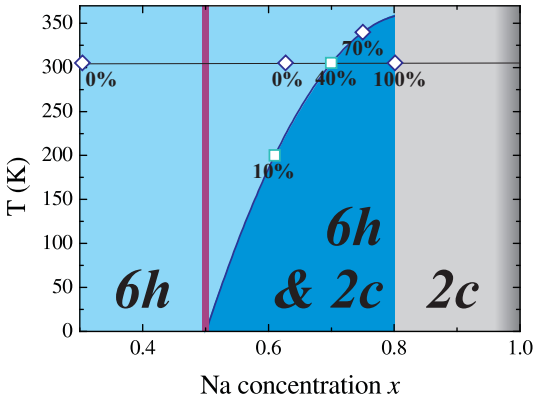

Figure 5.16: The ionic ordering phase diagram of Na_xCoO_2, after this work (data points plotted in light blue squares) and references [10] and [88] (dark blue diamonds). Above half doping, at which the long-ranged orthorhombic supercell ordering occurs (purple line), the transition between the mixed $2c$ and $6h$ phases (dark blue) and the pure $6h$ phase (light blue) occurs at higher temperatures with increasing sodium content. Above $x \sim 0.8$, only the $2c$ phase (grey) is present. At $x = 1$ the $2c$ sites are fully occupied (dark grey). The number beneath each data point represents the weight fraction of the $2c$ phase at base temperature.

high intensity neutron Laue single crystal experiment and the second a high energy x-ray single crystal diffraction study, finding superstructures based on clusters of Na vacancies and Na density stripes respectively. No sign of any Na superstructures were visible in the neutron diffraction patterns for the $x = 0.75$ or $x = 0.59$ samples in this study, although due to the high density of reflections and limited experimental resolution the presence of weak superstructure modulations cannot be definitively ruled out. What is clear, is that the ordering is extremely sensitive to x and in many cases, apparently sample dependent, with more than one kind of superstructure order seen in the same sample in some of the transmission electron microscopy (TEM) experiments. The degree of coupling between the cobaltate layer and the Na ions is expected to be weak, however the charge and magnetic ordering in this material occur at low energies indicating the physics of the CoO_2 layers may still be affected by the nature of the ionic ordering in intermediate charge reservoir layers.

Evidence for charge localisation as a result of Na ordering has not yet ap-

peared. IR conductivity measurements [101] see a far infrared peak (FIP) with an optical gap at $x = 0.5$, a feature common to the conductivity of many charge ordered materials. At higher sodium doping, the FIP remains whilst the gap is closed, to which they attribute a coexistence of localised and itinerant charge carriers. Even in the half doped system, proof of a completely charge ordered (CO) cobalt system with full charge disproportionation into Co^{3+} and Co^{4+} remains elusive. The bond valence sum method was used to calculate the formal cobalt valence on each site in the $x = 0.50$ sample using the fitted crystal structures over the entire temperature range measured. The results agree well with those of Williams et al. [32]. The convergence of the crystal structure at high temperatures to the "ideal" hexagonal structure leads to an identical Co-O hybridisation on both sites and equal values for the valence of $+3.35$. The orthorhombic distortion that presents itself at lower temperatures lifts the degeneracy on the two sites resulting in a slightly charge disproportionated state with formal valencies of $+3.45$ and $+3.32$ on the first and second cobalt sites respectively. Each measurement is less than the value of $+3.5$ expected from the simple ionic picture as described in section 2.2. It is clear, however, that a fully charge ordered state never appears in $Na_{\frac{1}{2}}CoO_2$, even during the further orthorhombic distortions seen around the T_{MI} transition. As the material passes through this transition careful examination of the bond lengths as a function of temperature reveal that the increase in one Co-O bond length is balanced by the decrease in another, leading to a temperature independent value of the Co valence. In the absence of charge ordering, a viable explanation for the lattice expansion anomaly has yet to be found. The modification of the magnetism already present in both the $x = 0.75$ and $x = 0.5$ samples at $\sim$10 K and T_{MI} respectively, appears to exhibit sufficient magnetoelastic coupling to induce a mechanical stress within the crystal structure, producing the measured distortions within the crystal structure. Suggestions that the ordering in the Na layers is largely driven by intraplanar electrostatic interactions [98] do not account for the one superstructure on which more than one set of authors agree

to exist, namely the zig-zag stripes of the Na orthorhombic supercell at $x = 0.5$, since this type of ordering does not maximise the average Na-Na distance as would be required for simple electrostatic repulsion. This strongly indicates the driving force for Na ordering in sodium cobaltate is more complicated and may result from band structure effects originating in the electronically active cobalt oxide planes, in opposition to the previously assumed model in which ionic ordering was the cause of such electronic effects.

Chapter 6

Magnetic Excitations in $Na_{\frac{1}{2}}CoO_2$

6.1 The MAPS Spectrometer

The MAPS spectrometer at ISIS (RAL) is a time-of-flight inelastic neutron spectrometer that operates in direct geometry, i.e. the neutrons incident on the sample are monochromated by the use of a chopper, a mechanical rotating device that selects neutrons of a defined wavelength, as described in section 3.12.1. The scattered neutrons are incident on a 16 m^2 array of detector banks consisting of 40,000 detector elements covering a large area in reciprocal space. The final energy of the neutrons is determined by the time-of-flight from the moderator to the detector and measured at every pulse in 2500 time channels. Each data set therefore consists of 10^8 pixels of data, approximately 0.4 GB. In contrast to the experimental description in section 3.12.1, where a line of detectors measured an area of reciprocal space as a function of energy, the area detectors in MAPS measure a reciprocal space volume, again as a function of energy. The scattering function therefore exists in four dimensional reciprocal space, however, of the three components of $\boldsymbol{q}$ and the energy, only three are independent as they are all correlated to the three components of $\boldsymbol{k}_f$. After the measurements are made, the data are converted into an absolute cross-section by a comparison to scattering from vanadium and the data normalised per formula unit of sample. After the decision of how to align the crystal (i.e in which plane to look for excitations) and which incident energy

to use (how much of reciprocal space is to be viewed and at what resolution) is made, MAPS simply collects data in all of the available scattering volume. The data is reconstructed after the experiment, from which cuts or curved trajectories through planes, and slices through volumes can be evaluated. Because the data in a TOF experiment are collected simultaneously for a large range of $\boldsymbol{q}$ values (even those that are not of interest), the data collection is significantly faster than the TAS technique, however the incident flux is much lower ($\sim 10^3$ n cm^{-2} s^{-1} though this is E_i and collimation dependent) and the energy resolution is worse, especially at low energy transfers.

6.2 The 2T1 Triple-Axis Spectrometer

The Orphée reactor at LLB (Saclay) provides a flux of 3×10^{14} neutrons cm^{-2}s^{-1} that are thermalised in a heavy water moderator around the reactor core. Guide tubes, tangential to the core, direct the neutron beam to the instrument. The 2T1 triple axis spectrometer (TAS) has its guide tube situated in the moderator near the core, where the flux of thermalised neutrons is at a maximum; the total flux at the sample, as in the TOF spectrometers, is strongly dependent on collimation and incident energy but is of the order of 10^6 n cm^{-2} s^{-1}. The spectrometer itself works as described in section 3.12.2. The first axis corresponds to the angle of the crystal monochromator used to select the energy of the incident neutrons. The second axis relates to the orientation of the sample. The third axis contains a pyrolytic graphite (PG) analyzer used to select neutrons of a given final energy, the number of which are measured by a ^{3}He detector.

6.3 Observation of Magnons in the Supercell Lattice

For the measurements made on MAPS, a mosaic of six crystals, each of mass $\sim$0.5 g, was mounted onto an Al sample holder, placed inside a vanadium can and cooled to 10 K in a closed-cycle refrigerator (CCR). The can contained an

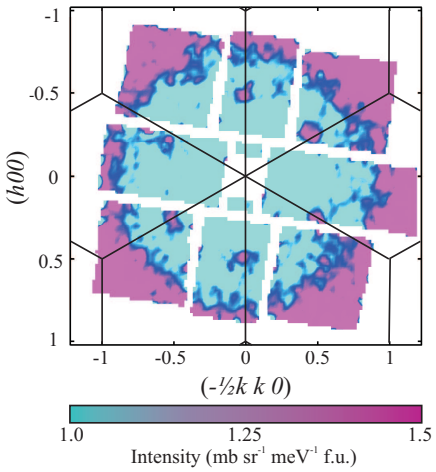

Figure 6.1: Inelastic scattering in the $(hk0)$ plane summed over energy transfers of 10-20 meV. Scattering is visible at points corresponding to (100) in the orthorhombic supercell, although twinning reproduces the hexagonal symmetry. An overlay of the parent hexagonal reciprocal lattice is shown.

atmosphere of He to allow efficient heat exchange between the cold head of the CCR and the crystals. An initial survey of the six crystals using the neutron Laue facility (ALF) at ISIS revealed that the (100) direction had been seeded in the crystal at an angle of 10 ° to the growth direction; this had continued through the entire crystal boule. The six crystals used in this experiment originated from three slices of the crystal boule that were split down the growth axis (in order to produce a larger surface area) and consequently three were crystallographic mirror images of the other three. The two mirror sets had to be identified and mounted on opposite sides of the sample holder. Despite the experimental difficulty involved, the final mounted crystal set had a mosaic spread of $\sim$10°, small enough to make an initial survey of the inelastic excitations. The spectrometer was configured with the incident neutron beam parallel to the *c*-axis of the crystals so that the scattering in the *ab* plane would be measured. An incident neutron energy of 100 meV was selected and long counting times (typically 48 hours) were adopted to build up sufficient statistics in ($\boldsymbol{q}$,$\hbar\omega$) space over the range of interest ($-1 \leq \boldsymbol{q} \leq 1$, $\hbar\omega \leq$25 meV). The data were analysed using mslice [102], a Matlab data analysis

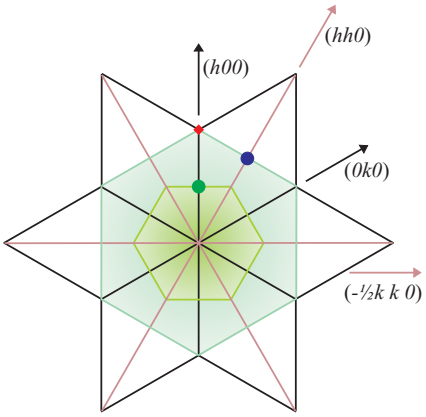

Figure 6.2: The two dimensional reciprocal lattice of Na_xCoO_2. The hexagonal unit cell is outlined in black with the (100) and (010) directions also marked in black. The first Brillouin Zone (BZ) is constructed by marking the perpendicular bisectors of the six reciprocal lattice vectors $\underline{G}_{hk} = h\underline{a}^* + k\underline{b}^*$ $(h = k = 1)$ and is filled in green. The zone centre of the magnon (the green circle) corresponds with the zone boundary of the BZ. The second BZ (filled in pale blue) is constructed in a similar fashion, by bisecting the reciprocal lattice vectors that cross only the first BZ (i.e. along $(hh0)$, marked in pink). The zone centre of the observed phonon is identified by a red diamond.

programme for time-of-flight neutron spectrometers. To plot the data correctly, the coordinates must first be written in terms of orthogonal viewing axes $\underline{\boldsymbol{u}}_1$ and $\underline{\boldsymbol{u}}_2$, i.e. the direction perpendicular to *a** must be written as a projection of the hexagonal direction *b**. The matter is further complicated by the fact that the crystals were mounted with *a** vertically offset and so the actual viewing axes are the product of the orthogonal projection of the hexagonal cell and an anticlockwise rotation of $\varphi = 10°$:

$$\begin{pmatrix} u_{1x} & u_{1y} \\ u_{2x} & u_{2y} \end{pmatrix} = \begin{pmatrix} -\frac{1}{2} & 1 \\ 1 & 0 \end{pmatrix} \bullet \begin{pmatrix} \cos\varphi & \sin\varphi \\ -\sin\varphi & \cos\varphi \end{pmatrix} \tag{6.1}$$

In figure 6.1 inelastic scattering is clearly visible at points relating to (100) in the orthorhombic notation, or $\left(\frac{1}{2}00\right)$ in the parent hexagonal lattice (Note: all (hkl) notation from this point refers to the hexagonal structure). All six peaks are also visible in the elastic channel, which is at odds with a true long-ranged orthorhombic superstructure, where there should only be two. However,

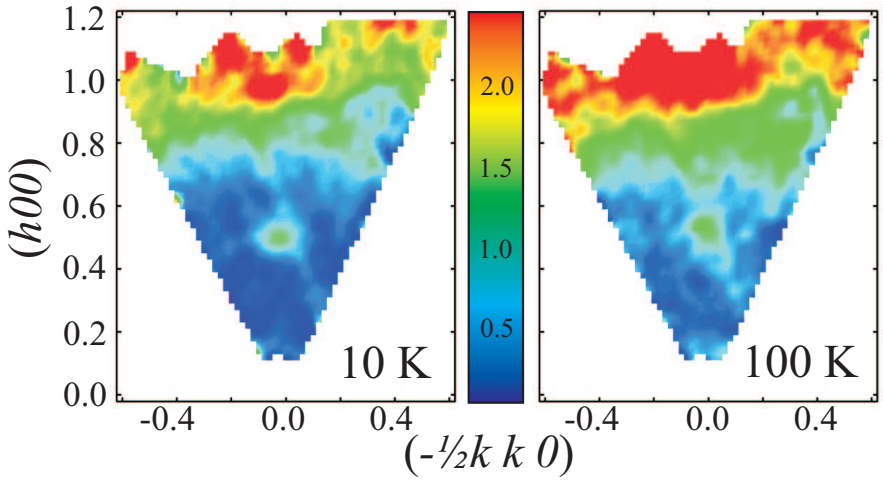

Figure 6.3: $\boldsymbol{q}$-data maps summed over an energy transfer of 10$\leq \hbar\omega \leq$20 meV at temperatures above and below T_M plotted in units of mb sr^{-1} meV^{-1} per formula unit. The scattering related to the magnon at $\left(\frac{1}{2}00\right)$ is still visible at 100 K although broader.

the integrated intensity of pairs of peaks diametrically opposite each other match, suggesting that either the six crystals had been aligned along different equivalent direction choices of (100) or the crystals exhibit structural twinning (or more correctly - tripling) in the basal planes which, as measured by Gašparović et al. [28], is directly proportional in magnitude to the tripling of the magnetic domains. The latter scenario is more likely since the six crystals were all mounted with the original crystal growth axis vertical. The relative populations of each of the three domains should not necessarily be assumed an invariable characteristic of each crystal; as described in section 2.1, the layered structure of Na_xCoO_2 permits ionic conduction of Na through the crystal and persistent temperature cycling could potentially make quantitative analysis on single crystal experiments meaningless. In order to maximise the signal in this experiment however, the data were folded onto one 60° segment, thus combining all three crystal domains. A schematic diagram of the reciprocal unit cell illustrating the geometry is shown in figure 6.2.

$\boldsymbol{q}$-data maps were produced by slicing the data across different energy transfer levels (the data in figure 6.1 shows a slice with 10$\leq \hbar\omega \leq$20 meV) and then

folding the datasets through successive 60° segments. For a G-type antiferromagnetically ordered system, spin excitations should be visible as a cone of scattered neutron intensity around the magnetic zone center. Slicing the data across $\boldsymbol{q}$ over finite energy ranges will therefore produce a set of rings. However, it should be noted that there is no magnetic scattering in the $(hk0)$ plane. Nevertheless, taking a cut through the data along $(h00)$ (figure 6.4) reveals several interesting features. Firstly, the prominent peak visible at $(\frac{1}{2}00)$ at 10 K, has broadened and decreased in intensity at 100 K and is no longer apparent against the background in the one-dimensional slice of the data. Secondly, there exists a sharper peak at (100) which increases in magnitude when the temperature is increased and can therefore be attributed to a phonon mode.[1] Thirdly, an isotropic increase in scattering intensity is visible at $|\boldsymbol{q}|$ ∼0.8 in reciprocal lattice coordinates. There are two possible causes for this background. The first is due to elastic scattering from the sample environment which, having taken a different path through the instrument, arrives at the detectors in the time channels corresponding to this level of energy transfer. A slice through the elastic channel of the data produces two concentric rings of intensity at $h = 1.05$ and 1.20. These values, when converted to inverse ångströms correspond exactly to the $|\boldsymbol{q}|$ values of the two highest d spacings for aluminium, d_{111} and d_{200}. Although the measured scattering function was corrected by taking a background from vanadium, scattering from the sample environment, including the aluminium to which the crystals were attached, will be present in these data. The second explanation refers to the size of the resolution ellipsoid of the instrument. A cut through the data, analogous to a constant $\boldsymbol{q}$ scan in a TAS measurement (panel B of figure 6.4) reveals the quasielastic scattering extends to and energy transfer of almost 10 meV. This originates from the convolution of real quasielastic scattering (perhaps from hydrogen within the sample or the sample environment) and the finite spectrum of neutron energies within the "monochro-

[1] It should be noted that due to the orientation of the sample with respect to the MAPS detector array, data was collected only at the (010) and $(0\bar{1}0)$ reciprocal lattice points and the four other positions in the two equivalent directions were absent. The integrated intensity of this peak will therefore not be representative of the size of the phonon involved.

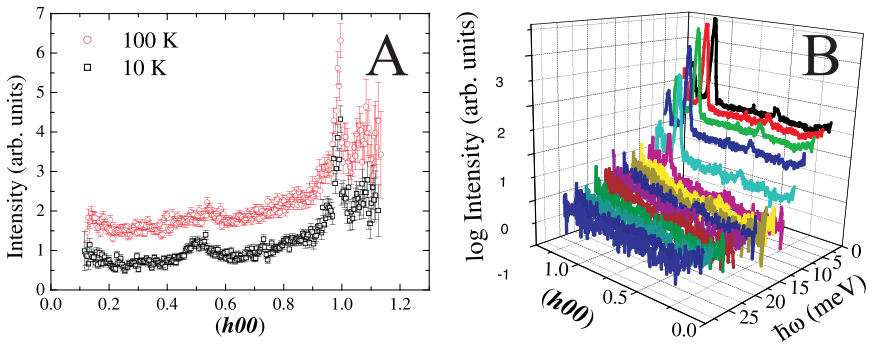

Figure 6.4: Panel A: A cut through the data in figure 6.3, the 100 K data have been offset vertically by 0.75 for clarity. The excitation at $\left(\frac{1}{2}00\right)$ has softened with increasing temperature and is almost invisible against the background in this one-dimensional plot. The sharper peak at (100) has increased with temperature, indicating it is a phonon mode. Panel B: Cuts along the same direction with smaller widths in energy transfer ($\pm$1 meV); as a consequence of binning the data into smaller regions the detail seen in panel A is lost. However, the extent of the quasielastic scattering (up to $\sim$10 meV) at this incident neutron energy and chopper setting is visible (the intensity is plotted on a log scale).

mated" incident beam. The data in figure 6.3 will naturally include some of the scattering from below 10 meV; a resolution ellipsoid which is $|\boldsymbol{q}|$ dependent will sum over larger portions of the background as it moves away from the origin of reciprocal space. The evidence for this is visible in panel B of figure 6.4 where the cuts nearest the boundary of the diffuse scattering carry more spectral weight at higher $\boldsymbol{q}$.

To follow on from these observations and take more precise measurements of the magnetic excitations, measurements were undertaken on the 2T1 TAS. Just one of the crystals was selected for the triple axis measurement in order to reduce the overall mosaic spread and optimise resolution. The crystal was cooled in an orange cryostat with the *c*-axis aligned vertically so that the Co moments were in the scattering plane. The tripling of the orthorhombic structure ensures that a component of the spin direction is always perpendicular to the scattered wave-vector, no matter the orientation of the crystal in this plane. Measurements

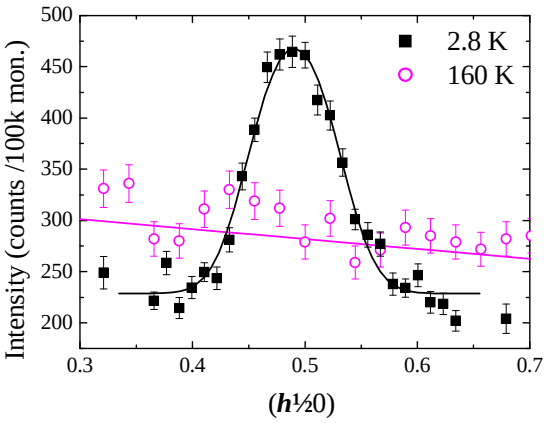

Figure 6.5: Constant energy scans through $\left(\frac{1}{2}\frac{1}{2}0\right)$ at an energy transfer of 15 meV. Whilst the peak in the elastic line remains at high temperatures, the inelastic signal has disappeared at twice the ordering temperature T_M, with an increase in the background corresponding to an increase in diffuse scattering.

were taken both at constant energy transfer through a crystallographic direction of interest and also at constant $\boldsymbol{q}$ with increasing $\hbar\omega$. At a temperature of 2.8 K, a clear peak is identifiable in both the inelastic and elastic channels at $\boldsymbol{q} = \left(\frac{1}{2}00\right)$ as expected. In order to access high enough energy transfers to examine the dispersion, it was necessary to move to the next Brillouin zone and take measurements at $\left(\frac{1}{2}\frac{1}{2}0\right)$ (see figure 6.2). The magnitude of the change in intensity between the two sites is 18%, comparable to that expected (15%) from the decrease in the magnetic form factor of Co^{4+} with an increase $|\boldsymbol{q}|$ from 1.28 $Å^{-1}$ to 2.22 $Å^{-1}$. A further indication that the signal is magnetic in origin is that the peak is destroyed by increasing the temperature to $\sim 2T_M$ (figure 6.5). Similar sets of $\boldsymbol{q}$-scans were made at increasing energy transfers and are shown in figure 6.6. Two interesting features arise. Firstly, the excitation is gapped; no scattering is seen below 11.5 meV. Secondly, the peaks are overly damped, increasing in width with increasing energy, whilst the overall dispersion is very steep. The dispersion is qualitatively similar to that seen in the SDW phase [16, 17] in the *ab* plane, although the intraplanar exchange interactions are antiferromagnetic at this doping level and the spin wave gap is an order of magnitude larger.

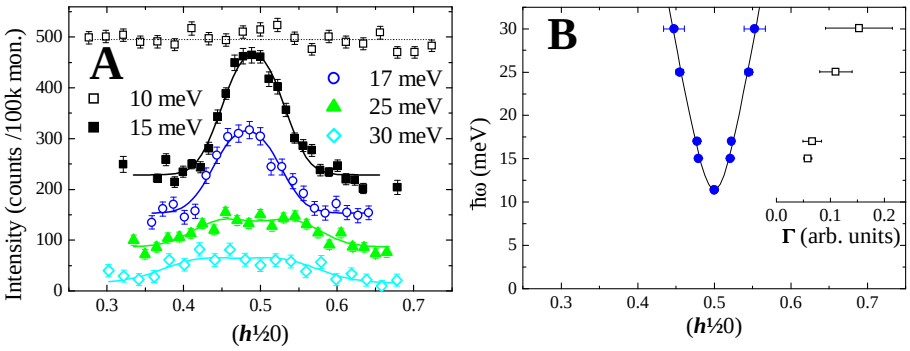

Figure 6.6: Panel A: Constant energy transfer scans at $\left(\frac{1}{2}\frac{1}{2}0\right)$ taken along the (100) direction at 2.8 K, fitted to two gaussian peaks. The 10 meV dataset has been offset by $+350$ counts, whilst the last three datasets were offset by -150, -200 and -250 counts respectively for increasing energy transfer cuts. Panel B: The measured spin wave dispersion along $\left(h\frac{1}{2}0\right)$ at 2.8 K; the spin wave gap closes at $\sim$11.5 meV. Inset: the width of the peaks (Γ) increases with increasing energy transfer.

6.4 The Nature of the Excitation Gap

To examine the spin gap further, scans of constant $\boldsymbol{q}$ were made through increasing energy transfer. The gap was observed at both $\left(\frac{1}{2}00\right)$ and $\left(\frac{1}{2}\frac{1}{2}0\right)$ (figure 6.7) at $\mathrm{E}_g \cong$ 11.5 meV. The onset of scattering is sharp, and decays with increasing $\hbar\omega$ as expected. As seen at the higher doping levels, there exists an optical phonon at $\sim$20 meV which dominated the signal in the $\boldsymbol{q}$-scans at that energy transfer. Fortunately, since optical phonon modes are relatively flat, it was therefore possible to pick up the signal from the magnetic excitation once more at higher $\hbar\omega$. In order to correct for the additional phonon component to the scattering, another energy scan was taken at an offset position from the excitation of (0.594 0.4 0), the exact values of $(hk0)$ chosen to set the analyzer at the same 2θ position as the previous scan. The difference curve then removes the diffuse[phonon] scattering below[above] the gap.

Finally, the sample was tilted slightly into the (100)-(001) scattering plane and the same energy scan repeated for $\boldsymbol{q}$=$\left(\frac{1}{2}0\frac{1}{2}\right)$ (not shown). The value of E_g is shifted to $\sim$9 meV, a decrease of 25%. Such a modification to the gap

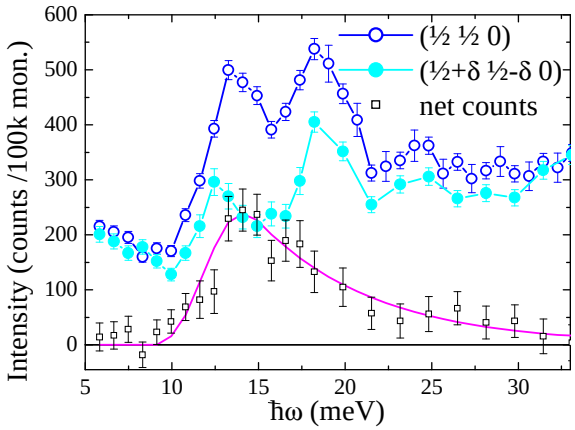

Figure 6.7: Constant $\boldsymbol{q}$-scans at $\left(\frac{1}{2}\frac{1}{2}0\right)$. A background was taken in an offset position of $(\frac{1}{2}+\delta\,\frac{1}{2}-\delta\;0)$ where $\delta \sim 0.1$ was chosen so that the spectrometer was aligned with the same 2θ positions as the on-peak measurements. The subtracted data (black open squares) is plotted; the line corresponds to the convolution of the experimental resolution ellipsoid and the intensity expected for an ideal gapped system ($E_g = 11.5$ meV).

suggests that either the dispersion along c is significantly large, or that the gap at the magnetic zone centres $\left(\frac{1}{2}0l_{odd}\right)$ is much less than the E_g measured here, and merits further investigation.

6.5 Discussion

It is clear from these measurements that the magnetic excitations are sensitive to the amount of sodium in the system, with a large excitation gap appearing at this doping level, and are strongly correlated with the arrangement of the ionic ordering, with the zone centres of the intra-planar excitations in $Na_{\frac{1}{2}}CoO_2$ coinciding with the supercell Bragg peaks as described in section 5.2.3. The magnetic excitations in the SDW system have been characterised by neutron spectroscopy and the structure confirmed as A-type antiferromagnetic ordering [16, 17]. Bayrakci et al. [17] managed to resolve magnetic Bragg peaks at $(1\,0\,l_{odd})$ and $(1\,1\,l_{odd})$ using polarized neutrons on the 4F1 spectrometer at LLB. They extracted a total moment of just 0.13(2) μ_B per Co. For an isolated Co^{4+} ion in the low spin state

the magnitude of its spin angular momentum is given by:

$$\mu = 2\sqrt{S(S+1)} = 1.73\,\mu_B \text{ per Co} \tag{6.2}$$

At a doping level of x = 0.75 only one quarter of the cobalt sites carry spin half, so that the total moment expected from the neutron diffraction measurement should be $\sim 0.4\ \mu_B$ per Co. It should be noted that the crystal field environment may alter the moment of the Co so that these calculations may give just an approximation to the total moment measured. The static magnetic order of $Na_{\frac{1}{2}}CoO_2$ has also been confirmed by neutron diffraction [28] and again, the measured moment of 0.13(1) μ_B per Co is less than expected. The easy axis was found to have changed from *c* to *a*. The symmetry breaking imposed by the orthorhombic supercell produces two separate Co sites, one of which, according to the simple ionic model, is magnetically ordered (Co^{4+}) and the other nonmagnetic (Co^{3+}), leading to alternating rows of spin half and zero spin cobalt atoms that run along *a*. In terms of the new unit cell, the system can be thought of as a simple G-type antiferromagnet with a magnetic propagation vector of $\left(1\frac{1}{2}1\right)$. The magnetic structures for the two different doping levels are presented in figure 6.8. An important difference between the two magnetic structures is that, whilst the inter-planar interactions are both antiferromagnetic, the intra-planar magnetic coupling constant has changed sign. At x = $\frac{3}{4}$ the interaction between spins in the basal plane is ferromagnetic, corresponding to a two dimensional magnetic ordering vector (00). This had been previously observed on the MAPS spectrometer as a peak of scattered intensity centered on the origin [40]. In the experimental geometry used (identical to the experiment described above) the origin of the reciprocal lattice would coincide with the axis of the incident neutron beam, which is not covered by detectors for obvious reasons. In order to access that region of reciprocal space, the crystal was rotated along the axis perpendicular to the incident beam by 30°. During the MAPS experiment in this study, the same procedure as adopted by Boothroyd et al. [40] was used to verify that in-plane

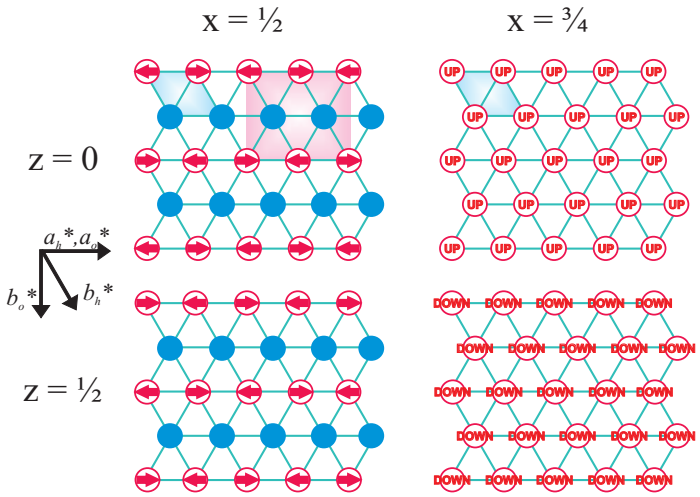

Figure 6.8: The magnetic structures of $Na_{\frac{1}{2}}CoO_2$ (G-type AFM) and $Na_{\frac{3}{4}}CoO_2$ (A-type AFM). The hexagonal unit cell is shaded blue in both systems, and the orthorhombic supercell shaded pink in the x = $\frac{1}{2}$ structure. The magnetic ordering vectors for the two doping levels are $\left(1\frac{1}{2}1\right)$ and (001) respectively.

FM coupling really is absent in the x = $\frac{1}{2}$ system. The results are shown in figure 6.9. In the experiment of Boothroyd et al. [40] the crystal was aligned with the (100) direction horizontal. Adding the extra rotation angle φ, the x = $\frac{1}{2}$ data must be rotated by 100°, and hence the gaps between detectors are seen to be rotationally offset between the two datasets. The data in the x = $\frac{3}{4}$ experiment was also taken with a slightly higher incident neutron energy of 60 meV compared to 50 meV as used in this particular measurement[2]. Consequently, the detectors in the dataset on the right hand side cover slightly more reciprocal space. Despite these experimental differences, it is clear to see that no in-plane ferromagnetic excitations exist in the $Na_{\frac{1}{2}}CoO_2$ sample. The data were summed over energy transfer values of 8$\leq \hbar\omega \leq$12 meV and so little scattering is expected at $\left(\frac{1}{2}00\right)$ (actually $\left(0\frac{1}{2}0\right)$ in this figure since the basis vector set has been rotated to match

[2]This incident energy was the original choice of experimental setting used. After performing this particular measurement, the sample was rotated back to $\mathbf{k}_i \parallel c$. The scattering at $\left(\frac{1}{2}00\right)$ was then observed towards the outside edges of the detectors where the resolution is worse. As a result, a new E_i of 100 meV was adopted for the measurements presented in figure 6.1.

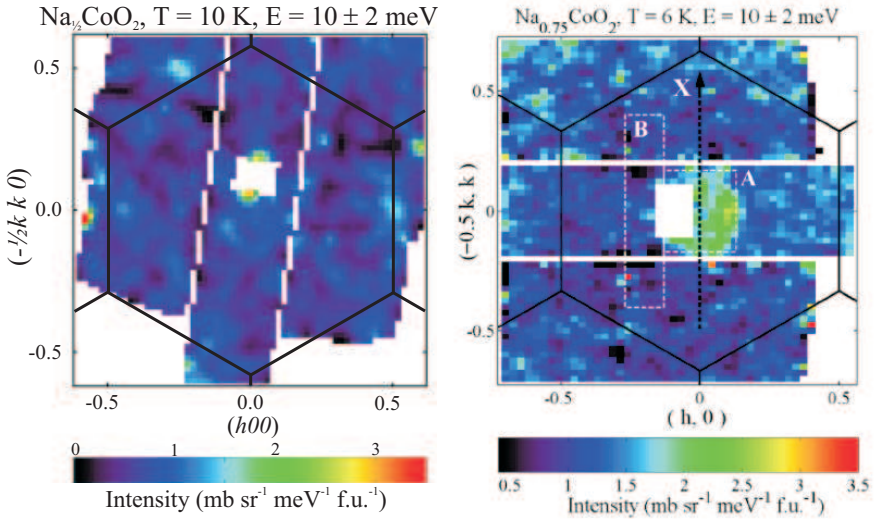

Figure 6.9: Neutron inelastic scattering of $Na_{\frac{1}{2}}CoO_2$ (left) and $Na_{\frac{3}{4}}CoO_2$ (right) in the $(hk0)$ plane averaged over neutron energy transfers of $8 \leq \hbar\omega \leq 12$ meV. Scattered intensity at the origin indicates ferromagnetic interaction between the spins within the (hk) plane, absent at x=$\frac{1}{2}$ and present at x=$\frac{3}{4}$. The x=$\frac{3}{4}$ data is reproduced from reference [40].

the orientation employed by Boothroyd et al. [40]), however the finite resolution ellipsoid ensures that some of the intensity from above the gap is summed over and a faint signal of the scattering seen in figure 6.1 is visible.

Both Helme et al. [16] and Bayrakci et al. [17] fitted their dispersion data using a spin Hamiltonian assuming nearest neighbour interactions of the form:

$$H = -2\mathbf{J}_{ab} \sum_{<ij>} \mathbf{S}_i.\mathbf{S}_j - 2\mathbf{J}_c \sum_{<ij>} \mathbf{S}_i.\mathbf{S}_j - D\sum_i \mathbf{S}_{iz}^2 \qquad (6.3)$$

where the first summation refers to nearest neighbour spins in the basal plane and second summation to spins between planes. The last term in equation 6.3 characterises the exchange anisotropy and the tendency of the spins to align perpendicular to the *ab* planes. The excitation dispersion is calculated as described in section 1.1.4. Using the formalism set out in appendix A, the coefficients of the Fourier transformed Hamiltonian are:

$$a_1 = b_1 \quad = \quad -2\mathbf{J}_{ab}S\left(\sum_{\uparrow\uparrow} e^{iq.\boldsymbol{\delta}_{\uparrow\uparrow}} - z_{\uparrow\downarrow} - z_{\uparrow\uparrow}\right)$$

$$
\begin{aligned}
&= -2\mathbf{J}_{ab}S\left(\sum_{\uparrow\uparrow} e^{iq.\boldsymbol{\delta}_{\uparrow\uparrow}} - 0 - 6\right) \\
c_1 = d_1 &= -2\mathbf{J}_{ab}S\sum_{\uparrow\downarrow} e^{iq.\boldsymbol{\delta}_{\uparrow\downarrow}} = 0 \\
a_2 = b_2 &= -2\mathbf{J}_{c}S\left(\sum_{\uparrow\uparrow} e^{iq.\boldsymbol{\delta}_{\uparrow\uparrow}} - z_{\uparrow\downarrow} - z_{\uparrow\uparrow}\right) \\
&= -2\mathbf{J}_{c}S\left(0 - 2 - 0\right) = 4\mathbf{J}_{c}S \\
c_2 = d_2 &= -2\mathbf{J}_{c}S\sum_{\uparrow\downarrow} e^{iq.\boldsymbol{\delta}_{\uparrow\downarrow}} \\
a_3 = b_3 &= 2DS \\
c_3 = d_3 &= 0
\end{aligned} \tag{6.4}
$$

The nearest neighbour $\boldsymbol{\delta}$ vectors are written in terms of the reciprocal unit lattice vectors $\mathbf{G} = h\mathbf{a}^* + k\mathbf{b}^* + l\mathbf{c}^*$. For the in-plane interactions (term number 1 in the Hamiltonian):

$$
\begin{aligned}
\sum_{\uparrow\uparrow} e^{iq.\boldsymbol{\delta}_{\uparrow\uparrow}} &= \sum \cos\left(2\pi h\right) + \cos\left(2\pi k\right) + \cos\left(2\pi\left(h+k\right)\right) \\
&= 2\left[\cos\left(2\pi h\right) + \cos\left(2\pi k\right) + \cos\left(2\pi\left(h+k\right)\right)\right]
\end{aligned} \tag{6.5}
$$

There are no intraplanar nearest neighbours with antiparallel spin and so the sums in c_1 and d_1 are zero. For the out of plane interaction (term 2), there are no parallel nearest neighbours, and the sums in c_2 and d_2 are:

$$
\sum_{\uparrow\downarrow} e^{iq.\boldsymbol{\delta}_{\uparrow\downarrow}} = 2\cos\left(\pi l\right) \tag{6.6}
$$

Including the interaction coupling constants, we define:

$$
\mathbf{J}_{ab}\left(\mathbf{q}\right) = 2\mathbf{J}_{ab}\left[\cos\left(2\pi h\right) + \cos\left(2\pi k\right) + \cos\left(2\pi\left(h+k\right)\right)\right] \tag{6.7}
$$

$$
\mathbf{J}_{c}\left(\mathbf{q}\right) = 2\mathbf{J}_{c}\cos\left(\pi l\right) \tag{6.8}
$$

The coefficients are added and the dispersion calculated from equation A.33 giving:

$$
\hbar\omega = 2S\sqrt{\left\{\mathbf{J}_{c}\left(0\right) - \left[\mathbf{J}_{ab}\left(\mathbf{q}\right) - \mathbf{J}_{ab}\left(0\right)\right] + D\right\}^2 - \left\{\mathbf{J}_{c}\left(\mathbf{q}\right)\right\}^2} \tag{6.9}
$$

The exchange constants fitted by both experimental teams gave vales of $\mathbf{J}_{ab}$ = 4.5(3) meV [3(1) meV], $\mathbf{J}_{c}$ = -3.3(3) meV [-6.10(25) meV] and $|D|$ = 0.05(5)

meV [0.0430(25) meV] where the values calculated by Bayrakci et al. [17] [Helme et al. [16]] were measured on a sample with x = 0.82 [x = 0.75]. Helme et al. [75] analysed the data further by adding a second, in-plane anisotropy and were able to discern two spin-gaps of 0.95(15) meV and 1.95(15) meV for the out-of-plane and in-plane dispersions respectively. Bayrakci et al. [17] on the other hand were not able to refine a sufficiently accurate value for D and could not ascertain whether or not a gap was present at the zone centre.

The two studies produced similar results except for a factor of two difference in the measured values of $\mathbf{J}_c$ which is not surprising given that the inter-plane interactions are most likely governed by super-exchange via the Na sp^2 orbitals [85] and therefore highly sensitive to the exact stoichiometry of the sample. What is surprising however, is the relative isotropy of the two coupling constants, in a system that exhibits two dimensionality in its macroscopic properties. More specifically, comparisons to other layered magnets like $YBa_2Cu_3O_6$ [103], that have exchange anisotropy of several orders of magnitude may no longer be applicable. In the light of such results we must consider the validity of spin wave model used to fit the data.

The first point of note is the false assumption made in the Hamiltonian itself. Equation 6.3 refers to the spin arrangement for $Na_{\frac{3}{4}}CoO_2$ as detailed in figure 6.8 that requires in-plane ferromagnetic coupling between each hexagonal lattice site. Of course, only one quarter of the Co atoms carry spin. In order for the Hamiltonian to accurately describe the magnetism, the system must be phase separated into areas of non-magnetic Co^{3+} and magnetically dense regions of Co^{4+}. Both studies found the spin-modes to be quite sharp and resolution limited, indicating long-ranged ordering both in- and out-of-plane. Phase segregation was discussed in section 5.2.1, in which a fully magnetic $x = 0$ phase was not observed; whilst it would explain the nature of the spin-modes it is not clear how the system would overcome the Coulomb penalty associated with such clustering of spins. A second model, in which the spin-half ions are distributed evenly on

every fourth lattice site resulting in a triangular supercell with sides equal to 2*a* was discounted by Boothroyd et al. [40] due to the absence of magnetic excitations at half reciprocal-lattice spacings within the plane that would result from a doubling of the real-space lattice. In consideration of these points it may be more appropriate to consider an itinerant model for the magnetism.

Now let us consider the data collected for the system under study in this experiment, $Na\frac{1}{2}CoO_2$. The excitation in AFM systems depends on a $\cos(\pi h)$ term around the zone centre. The data in figure 6.6 were therefore fitted to a the function $\hbar\omega = \sqrt{\Delta^2 + (D\boldsymbol{q})^2}$ where Δ is the value of the energy gap and D is the stiffness constant, more commonly referred to as the spin wave velocity in AFM systems. A fit to the data gives values of $\Delta = 11.5(5)$ meV and $D = 514(22)$ meV Å and is plotted as the solid line in panel B of figure 6.6. Normalising the measured data at low $\boldsymbol{q}$ to the expected $\cos(\pi h)$ $\boldsymbol{k}$ dependence would give a highest value for the energy transfer at the zone boundary of ∼112 meV, even though experimental the signal of the dispersion is lost above ∼30 meV.

The theory of spin waves in itinerant ferromagnetic systems is well understood and can be modeled by including the Hubbard Hamiltonian that takes the Coulomb interaction between the itinerant electrons into account [5]. The resulting spin-wave modes resembles those of localised systems at low energy transfers; at higher energies single-electron modes know as Stoner excitations become important so that the original spin-wave dispersion is damped, decreasing in intensity as the excitations decay into electron-hole pairs. A highly damped spin wave is therefore a signal of intinerancy. The theory of spin-waves in itinerant antiferromagnets is not nearly as developed. In fact, due to zero-point motion, a system with two interpenetrating antiparallel spin lattices is not even an eigenstate of the localised spin Hamiltonian and so AFM spin wave theory is based on a perturbation of the mean-field Néel state [104]. The magnetic excitations of some itinerant antiferromagnets have been measured. For example, both Cr [105] and Mn_3Si [106] have excitations emanating from magnetic Bragg peaks (although the

magnetism in Mn_3Si is incommensurate in structure and therefore the excitations emerge from the magnetic satellite peaks that combine at higher energies) that are very steep in energy and highly damped. If manganese silicide is doped with iron, the magnetic ordering becomes commensurate and it is possible to follow the spin waves to higher energies [106]. The dispersion is seen to vary linearly in $\boldsymbol{q}$ up to energies of $\sim$2 $k_B T_N$ above which it rises vertically and is described as a "chimney" of scattering. That behaviour is not seen in $Na_{\frac{1}{2}}CoO_2$; the dispersion, as plotted in figure 6.6, is linear until the signal disappears at $\sim$4 $k_B T_M$.

The most obvious method for determining the proportion of localised to itinerant spins in a ferromagnetic material is to calculate the ratio of the moment determined from the Curie-Weiss magnetic susceptibility above T_C (as described in section 4.1) and the low temperature saturated moment, equal to one in completely localised magnetic systems and greater than one for itinerant materials. This technique is naturally not applicable in an antiferromagnet. A different technique proposed by Mook [110], relates the spin-wave stiffness (or velocity) to the ordering temperature T_C (or T_N): low ratios of the two numbers indicate localised systems and higher numbers itinerary, where excitations due to misalignments of individual spins would not account for the magnitude of the observed values of spin wave energy. The values for several magnetic systems are listed in table 6.1 and it is clear to see that sodium cobaltate, with a value of 5.90 for the spin velocity to ordering temperature ratio, falls in the category of itinerant systems. For a localised spin system, whether FM or AFM, the energy of the excitation at the zone boundary should be of the order of $k_B T_{C[N]}$. An extrapolation of the data collected in this study predicts these two energies to be different by an order of magnitude. If the system exhibits low dimensionality, as suggested in section 4.5.1, the energy scale characterising the excitation will relate to the strength of interactions along the spin chains, thus underestimating $k_B T_{C[N]}$. However the loss of the excitation into a broadened continuum of decay modes, as witnessed here, indicates strongly that the material is itinerant in character.

	T_C (K)	T_N (K)	D (meVÅ^2)	D (meVÅ)	D/T_C (meVÅ^{2}K^{-1})	D/T_N (meVÅK^{-1})	System			Reference
EuS	17		2.6		0.15		Localised	FM		[107]
EuO	69		12		0.18		Localised	FM		[108]
Mn_3Si		26		37		1.43	Itinerant		AFM	[106]
Cr		300		500		1.67	Itinerant		AFM	[105]
Ni_3Al	41		85		2.07		Itinerant	FM		[109]
$Na_{\frac{1}{2}}CoO_2$		88		514		5.84	?		AFM	This work.

Table 6.1: Spin-wave velocities and transition temperatures for a variety of magnetically ordered materials.

If this is the case, what is the origin of the localised behaviour that is exhibited across the phase diagram? In the SDW system, the magnetic susceptibility displays Curie-Weiss characteristics and at half doping there exists a metal to insulator transition at 53 K. Both these features may originate from Fermi surface nesting effects. The phase diagram of sodium cobaltate is characterised by the effects of strong electron correlations. At $x > 0.5$, some of the Co states may be localised by these interactions causing the Curie-Weiss-like magnetic behaviour and spin wave excitations, whilst the material retains metallic conductivity. Below half doping the electron correlation effects are weaker and the system is Pauli paramagnetic. At $x = 0.5$ a scenario in which the magnetism is largely described by the itinerant electron picture but electron correlation effects play a role in the formation of the MIT appears most appropriate. It should be noted that the insulating transition is anisotropic; the resistivity at low temperatures along *c* is 25 Ωcm and just 15 mΩcm along *ab* [29], a value comparable to that of the "metallic" SDW system [94], and whilst $Na_{\frac{1}{2}}CoO_2$ is considered a low temperature insulator in dc, optical conductivity measurements [111] reveal the MIT is only visible in the low frequency data. The mechanism that drives the MIT is clearly not yet understood and further investigation into the electronic band structure at this doping level is needed. The fact that the magnetic ordering and the insulating transition occur at ordering temperatures that differ by 30 K suggest that the two phenomena are unconnected, as opposed to a more traditional scenario of a Mott insulating transition where electrons are frozen onto lattice sites at one ordering temperature. We can therefore assume that the transport carriers reside mainly on the second Co sites that are not involved in the spin ordering transition at 88 K. The opening of a gap on the part of the FS related to band containing these carriers would readily explain the onset of the insulating transition. An alternative scenario, in which the insulating transition is caused by charge ordering on the cobalt sites can be dismissed for several reasons. Firstly, this type of ordering would be associated with charge modulation in the Na layers. Na superstructure ordering exists to high tem-

peratures whereas both the magnetic ordering and the insulating transition occur at much lower temperatures. Secondly, there does not exist sufficient difference between the Co-O orbital ordering on the two sites that would merit a high level of charge disproportionation into Co^{3+} and Co^{4+}. As detailed in section 5.2.3, valence-bond calculations for both Co sites do not yield any appreciable difference in charge. Thirdly, recent NMR studies [31] did not measure any differences or changes in charge on the two sites at either the magnetic or MI transition. Finally, the excitation modes measured in this study indicate that the system is at least partially itinerant and that a model containing zero spin Co^{3+} and spin-half Co^{4+} is not appropriate anyway.

In summary, the intra-planar magnetic excitations of $Na_{\frac{1}{2}}CoO_2$ have been measured using both time-of-flight and triple-axis neutron spectroscopy. Excitations whose zone centres coexist with the structural supercell ordering Bragg reflections have been studied. The excitation has a gap of 11.5(5) meV. The magnitude of the scattered intensity correlates well with the magnetic form factor expected for Co^{4+} and the excitation is destroyed by increasing the temperature confirming the magnetic origin of the dispersion. A localised moment picture does not provide physically realistic values for the magnon velocity or the energy transfer at the zone boundary and is not consistent with the broadening and diminishing scattering more reminiscent to the transformation between spin wave and Stoner excitations as seen in the itinerant ferromagnets. A more itinerant analysis with a small charge disproportionation is therefore considered appropriate for this magnetic system.

Chapter 7

Superconductivity in $Na_{\frac{1}{3}}CoO_2 \cdot \frac{4}{3}D_2O$

Single crystal and powder samples of $Na_{\frac{1}{3}}CoO_2 \cdot \frac{4}{3}D_2O$ were obtained by a two stage reaction process, with the deintercalation of sodium from the anhydrous higher doped samples followed by the chemical intercalation of water or deuterium oxide, by reaction with either vapour or liquid. It is known, however, that high levels ($>75\%$) of relative humidity [112] are necessary to obtain a fully hydrated phase. The crystals are extremely unstable to the loss of hydration, forming the non-superconducting $y = 0.6$ phase at a temperature of just 35 °C or with exposure to dry atmosphere after ∼30 minutes [12]. The production of the correct level of water vapour in a sealed chamber, as used in some previous studies, requires heating to temperatures around which the decomposition of the $y = 1.4$ phase occurs. The superconductivity of samples produced in this way is highly unstable. The single crystal samples used in this study, were therefore deuterated by submersion in liquid D_2O for a total of three months [60].

The following chapter describes magnetisation and heat capacity measurements in which the nature of the superconductivity is probed, followed by a neutron diffraction investigation into the role of water doping within the superconducting system. Heavy water was chosen over normal water due to the high incoherent

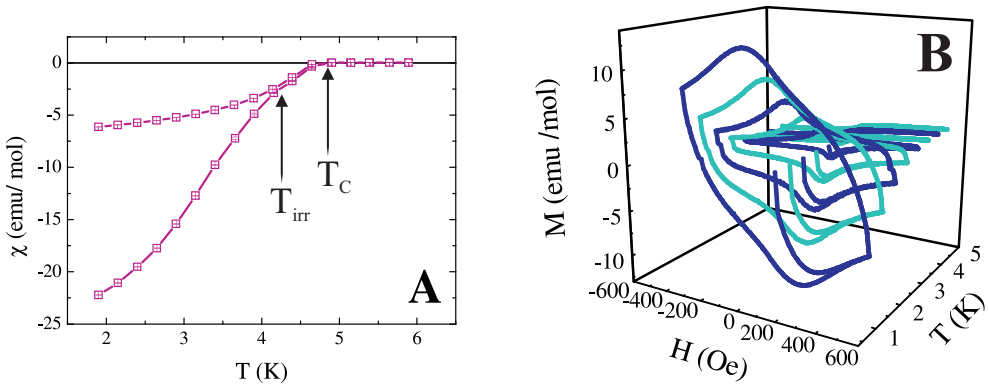

Figure 7.1: Panel A: Magnetic susceptibility of a powder sample in an applied field of 10 Oe, with a critical temperature of 4.8(1) K. The large difference between the field cooled (top) and zero field cooled (bottom) curves show significant pinning effects and a possible irreversibility temperature T_{irr} at ∼4.3 K. Panel B: The magnetisation of a single crystal sample measured as a function of field in different temperatures. T_C is similar to that of the powder, however the superconducting volume fraction is seven times smaller. Deviation from perfect diagmagnetism occurs above 28 Oe.

scattering cross section of hydrogen, which would add a large background and multiple scattering problem to the results of the neutron scattering study described in section 7.4.

7.1 Magnetisation Measurements of the Superconducting Transition

The magnetisation data were collected between temperatures of 1.5 and 10 K as a function of temperature and field using both the SQuID magnetometer and VSM. The superconducting transition is indicated by the onset of negative susceptibility at the critical temperature. Many single crystal and powder samples were measured and superconducting temperatures were found in the range of 2 - 5 K, although a clear correlation between T_C and the sodium doping level (as measured by the time scale of the deintercalation process detailed in section 3.5) was not obtained due to the inability to control the water (and therefore oxonium) content within each sample. In that respect, the $T_C\,(x)$ results mirror those of Chen et al. [38].

Magnetic susceptibility data collected as a function of temperature, and the isothermal magnetisation data plotted as a function of field for a powder and single crystal sample are detailed in figure 7.1. The powder sample (plotted in panel A) has a critical temperature of 4.8(1) K and shows considerable hysteresis between the field cooled and zero field cooled curves, indicating that either flux pinning or weak link effects are important in this system. The value of the magnetisation at 1.8 K corresponds to a Meissner fraction of 45%, although it is apparent the superconducting transition is not yet complete at this temperature. At ∼4.3 K, the FC and ZFC curves appear to merge, indicative of the presence of an *irreversibility line*. Irreversibility effects occur in highly anisoptric systems, such as the HTSCs, in which weak coupling bewteen the transport carrier planes may result in a break up of the 3D line vortices into 2D "pancake" vortices under an applied magnetic field. The line of irreversibility in the $H(T)$ phase diagram roughly follows a power law behaviour with $H_{irr} \sim (1 - T_{irr}/T_C)^n$ where n varies between values of 1 and 5.5 for most HTSC systems [113]. Using the parameters for T_{irr} and T_C as measured above, we obtain a value for n of 3.

Magnetisation data collected on a single crystal sample (with H applied parallel to the *ab* planes) as a function of applied field are plotted in panel B. The critical temperature is measured as 4.5(1) K, however the Meissner fraction in this sample is just 6%, perhaps as a result of the difficulty in hydrating single crystals in comparison to powder samples which have a much greater surface area. Partial Meissner fractions are indicative of poor sample quality, where in this case not all of the material may exist in the $y = 1.4$ phase, or that the superconductor itself is non-BCS. The variety of measured Meissner fractions in both this study and presented in the literature indicate that both such scenarios are likely. The magnetisation at the lowest measured temperature was replotted in S.I. units of A m^{-1} along with a plot for an ideal diamagnet with $M = -(1/4\pi)\,H$ scaled to a superconducting fraction of 6%. The virgin curve was seen to deviate from perfect diamagnetism at a field (H_{C1}) of just 28 Oe; the point at which M turns around

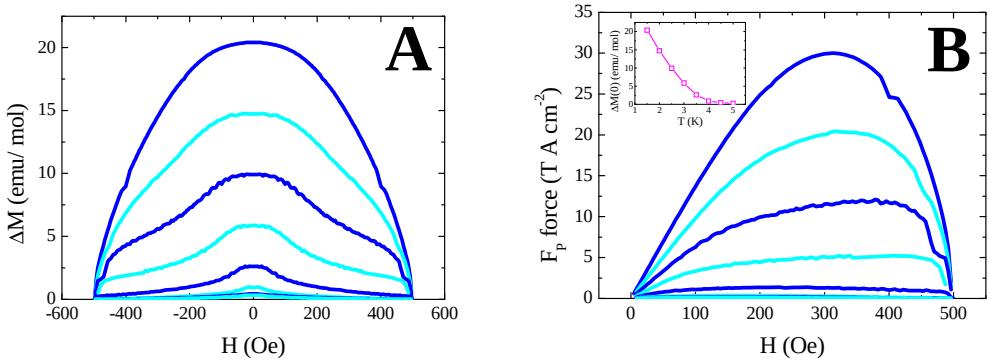

Figure 7.2: Panel A: The width of the hysteretic magnetisation loops as presented in panel B of figure 7.1, plotted in 0.5 K steps between 1.5 and 5 K. Panel B: The flux pinning force for the same temperature datasets are presented in panel A; the maximum in F_P occurs at 320 Oe. Inset: The width of the $M(H)$ curves shown in panel A at zero applied field plotted as a function of temperature.

to have positive susceptibility was measured to be 220 Oe. Using the relation $H_{C1}(T) = H_{C1}(0)\left[1-(T/T_C)^2\right]$, $H_{C1}(0)$ is calculated to be 31.5 Oe.

Information on the pinning force per unit volume of a type two superconductor may be obtained from the hysteresis of the magnetisation curve between the increasing and decreasing field sweeps (ΔM), since the degree of hysteresis depends on the effectiveness of the sample (through defects or sample inhomogeneities) in obstructing the movement of flux vortices through the sample. The pinning force per unit volume is defined as $\boldsymbol{F}_P = \boldsymbol{J}_C \times \boldsymbol{H}$ and is derived from the Lorentz force that acts on the flux line lattice. $\boldsymbol{J}_C$ is the critical current density of the superconductor and is written as $\boldsymbol{J}_C = 2\Delta\boldsymbol{M}/d$ for polycrystalline samples, where d is the average grain size. For single crystal samples, the critical current density is defined in the extended Bean critical model as:

$$\boldsymbol{J}_C = \frac{20\Delta\boldsymbol{M}}{a\left(1-\frac{a}{3b}\right)} \tag{7.1}$$

where a and b are the cross-sectional dimensions of the sample in the directions perpendicular to the applied field and a is the lesser of the two quantities. The hysteresis in the magnetisation loops and the corresponding values for the flux pinning force at temperatures between 1.5 and 5 K (calculated assuming $\boldsymbol{J}_C$ and

$\boldsymbol{H}$ were perpendicular) are plotted in panels A and B of figure 7.2. The hysteresis width at the lowest measured temperature and zero field corresponds to a critical current density of ∼1400 A cm^{-2}, an order of magnitude less than typical $\boldsymbol{J}_C$ values in most HTSCs, although this may be due to the small superconducting fraction (scaling the value to a full Meissner fraction gives $\boldsymbol{J}_C$ ∼23000 A cm^{-2}). The calculated values for the flux pinning force are very small indeed, as can be expected from the morphology of the $M(H)$ loops: the magnetisation does not immediately change sign upon reversal of the applied field.

7.2 Mapping the Field-Temperature Phase Diagram

Heat capacity measurements were made on single crystal $Na_{\frac{1}{3}}CoO_2 \cdot \frac{4}{3}D_2O$ in fields of up to 90 kOe in the temperature range 0.4 to 10 K; the data is plotted in figure 7.3. The data were fitted above T_C to an electronic ($\gamma_N T$), phonon and anharmonic coupling term ($\beta_3 T^3 + \beta_5 T^5$), with γ_N = 13.9(3) mJ mol^{-1} K^{-2}, β_3 = 0.32(1) mJ mol^{-1} K^{-4} and β_5 = 0.9(1) μJ mol^{-1} K^{-6}. This is a substantial reduction on the values obtained for the anhydrous materials and reflects a significant change in the response of the lattice at low T. A large upturn at low temperatures was visible in the majority of the datasets and attributed to a Schottky anomaly. Such a feature is not uncommon among many of the published heat capacity studies [60, 45, 46]. It was fitted to a function of the form:

$$\frac{C_{Sch}}{T} = N k_B \left(\frac{\epsilon}{k_B}\right)^2 \frac{e^{\epsilon/k_B T}}{T^3 \left(1 + e^{\epsilon/k_B T}\right)^2} \tag{7.2}$$

where N represents the number of magnetic, spin-half atoms in the system and ϵ is a characteristic energy scale of the field induced splitting of the spin half levels. Both the high temperature Debye fit and the low temperature Schottky fit for a sample dataset are shown in panel A. Both were removed in all the available datasets in order to produce a plot of the electronic specific heat due to the superconducting transition, as shown for the zero field data in panel B. The size of the superconducting jump is estimated by placing a vertical line at the tem-

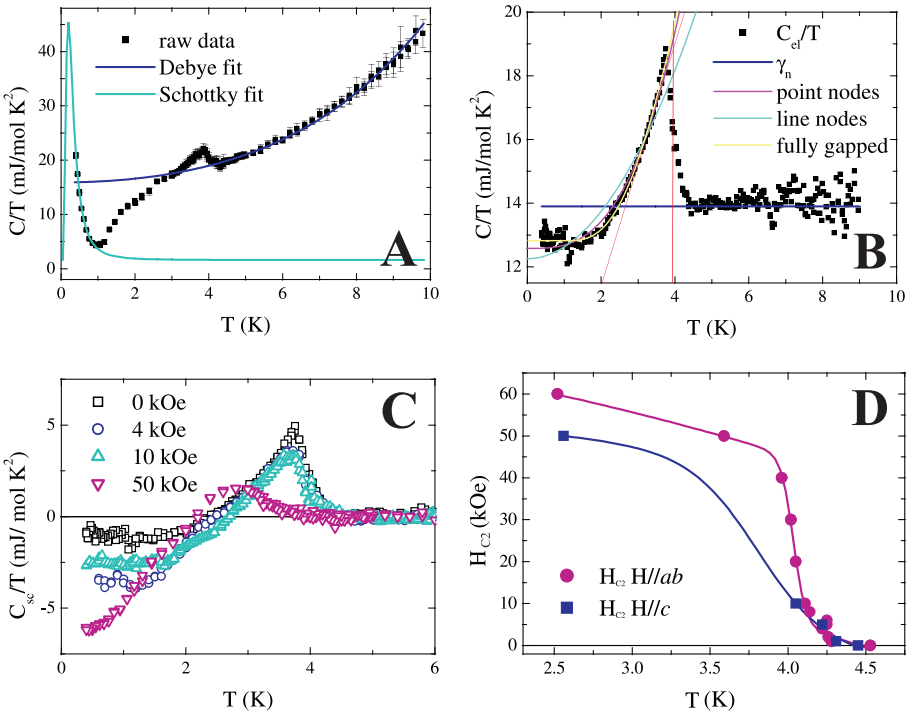

Figure 7.3: Panel A: The raw specific heat data for a single crystal sample with an applied field of 1 kOe parallel to the *ab* planes. The Debye fit (containing the normal state electronic and lattice contributions) made above T_C is plotted in blue, and the low temperature Schottky fit is plotted in cyan. Panel B: The zero field data after the subtraction of the fits detailed in panel A. The red lines indicate the value of T at half the jump and the linear electronic fit below T_C from which an estimate of $\Delta C/T_C$ is made, whilst the normal state electronic term is shown in blue. Several models of the low temperature heat capacity data are also plotted. Panel C: Several datasets of the heat capacity as plotted in panel B with applied fields parallel to the *ab* planes. The suppression of the superconducting jump and critical temperature under magnetic fields is evident. Panel D: The H_{C2} versus T phase diagram. Little anisotropy is observed at low fields.

perature midway between the onset and the peak of the superconducting jump, and measuring the point at which it bisects the linear fit to the data below T_C, which defines the superconducting electronic term to the specific heat, $\gamma_S = 3.8$ mJ mol^{-1} K^{-2} found by an extrapolation to zero temperature. The size of the jump at the superconducting transition, as plotted in panel B, is measured to be $\Delta C_{el}/T_C = 4.9$ mJ mol^{-1} K^{-2} producing a value for $\Delta C/\gamma_N T_C$ of 0.35, just 25% of the expected BCS value of 1.43. This correlates well with the superconducting fraction estimated from the ratio of the superconducting and normal state electronic components with $\gamma_S/\gamma_N = 3.8/13.9 = 27\%$. The size of the superconducting fraction is in line with previous reports [7, 33, 35, 45, 46, 47, 60], indicating either the samples are partially dehyrdrated and the superconducting fraction is an indication of the volume fraction of the $y = 1.4$ phase, or the presence of non-conventional superconductivity. The superconducting transition is a second order phase transition, and consideration of the thermodynamics above and below T_C state that the entropies of the normal and superconducting states must be equal at the transition temperature, i.e.:

$$\frac{d}{dH}\int_0^{T_C} \frac{C\left(T,H\right)}{T} dT = 0 \tag{7.3}$$

Examination of the positive and negative areas of the graph in panel B show that the areas contained above and below γ_N (3.74 and 2.28 mJ mol^{-1} K^{-1} including the extrapolation down to 0 K) are not equal. Furthermore, the positive and negative entropies vary between datasets in different applied fields. Non-conservation of entropy may indicate a change in the nature of the vortex state at higher H, the onset of an additional magnetic phase transition below T$_C$, or two superconducting order parameters with different field dependences. Another problem becomes evident upon examination of the low temperature data, since they never extrapolate to zero specific heat at zero temperature. This may be further evidence of a superconducting fraction of less than 100%, or may indicate an insufficient subtraction of the addenda from the experimental data, which varied

	T dependence	Gap topology
$C_{es}(T)$	$\alpha \exp(-t)$	Fully gapped
$C_{es}(T)$	αt^3	Point nodes
$C_{es}(T)$	αt^2	Line nodes
$C_{es}(T)$	αt	No gap

Table 7.1: Low temperature dependence of the electronic specific heat for different models of the superconducting order parameter. t represents the reduced temperature parameter, equal to T/T_C.

between one and two thirds of the total measured heat capacity due to the small size of the sample used.

The data at low temperatures were fitted to several models in order to elucidate the nature of the pairing mechanism. A fully gapped state is characterised by an exponential dependence of the electronic heat capacity, whereas nodal structures for the gap topology are defined by different power law behaviours. The temperature dependences of the different models are listed in table 7.1 and the first three are plotted with the experimental data in panel B. Satisfactory fits are obtained for a superconducting order parameter with either point nodes or a fully gapped state, in agreement with the data of Cao et al. [33] but not those of references [35, 45, 46].

Measurements were repeated with different applied fields both parallel and perpendicular to the basal planes of the material. A few datasets for the $H//ab$ data are plotted in panel C. The size of the jump in the heat capacity is suppressed in applied fields along with T_C. A summary of the critical fields versus temperature is given in panel D. The values for $H//ab$ are in agreement with other published data, however the anisotropy is surprisingly small in comparison to that measured by Chou et al. [60]. A change in slope of $\partial H_{C2}/\partial T|_{T_C}$ at 5 kOe is visible in the $H//ab$ data, which had been reported in two previous heat capacity studies on

powder samples [46, 114] and attributed to either a field induced transition from singlet to triplet pairing, or the presence of two competing superconducting order parameters with identical critical temperatures that exhibit different responses to an applied magnetic field. The reported discovery of the existence of two superconducting phases in sodium cobaltate oxyhydrate that are separated by another AFM phase by Sakurai et al. [115] supports the latter suggestion.

Using all of the available data, the measurements were used to characterise the material using the Ginzburg-Landau (GL) relations, which are written in c.g.s. units as:

$$H_{C1}(0) = \frac{H_C(0)}{\sqrt{2}\kappa} = \frac{\Phi_0}{4\pi\lambda^2}\ln\kappa \tag{7.4}$$

$$H_{C2}(0) = \sqrt{2}\kappa H_C(0) = \frac{\Phi_0}{2\pi\xi^2} \tag{7.5}$$

where, $H_C(0)$ is the thermodynamic critical field, κ is the ratio between the penetration depth λ and the coherence length ξ, and Φ_0 is the magnetic flux quantum, equal to $h/2e$ or 2.07×10^{-7} G cm^2. The value for $H_{C1}(0)$ was defined by the magnetisation data and gives values for the superconducting penetration depths of λ_{ab} = 5900(600) Å and λ_c = 4900(500) Å. The average of these two values is in agreement with the data of Sakurai et al. [34], slightly smaller than the powder average value of 7900 Å measured by Cao et al. [33] and almost a factor of two smaller than the penetration depth measured by Kanigel et al. [116] by μSR. $H_{C2}(0)$ may be evaluated from the data presented in panel D, using the Wertham-Helfand-Hohenberg (WHH) formula (in the dirty limit) which relates the upper critical field to the initial slope of the H_{C2} versus T_C data:

$$H_{C2}(0) = -0.693\left(\left.\frac{\partial H_{C2}}{\partial T}\right|_{T_C}\right)T_C \tag{7.6}$$

The initial slopes of the data presented in panel B are isotropic at -26(5) kOe K^{-1} below an applied field of 5 kOe, above which data taken with $H//ab$ rises dramatically at a value of 180(20) kOe K^{-1} before being suppressed at fields above 50 kOe. These values correspond to anisotropic upper critical fields of

80(10) kOe along *c* and 560(60) kOe along *ab*. The extrapolation of the data to zero temperature gives a value for the upper critical field much lower than the calculated values. Spin singlet paired systems usually exhibit such suppressions of H_{C2} due to pair breaking effects from the energy splitting induced by the Zeeman effect. The critical field limit in these cases is called the *Pauli paramagnetic* or *Clogston-Chandrasekher limit* and is calculated as $H_P = 18.4T_C \cong 83$ kOe. An extrapolation of the high field $H//ab$ data to zero temperature gives a value of $H_{C2}^{ab} = 83.5(5)$ kOe in excellent agreement with the calculated value.

The superconducting coherence lengths are calculated by combining the WHH formula with equation 7.5:

$$\left.\frac{\partial H_{C2}^{i}}{\partial T}\right|_{T_C} = -\frac{1}{T_C}\frac{\Phi_0}{2\pi\xi_j\xi_k} \tag{7.7}$$

where i, j and k are cyclic permutations of the crystallographic directions. In the present case ξ_i and ξ_j are both equal to ξ_{ab} and $\xi_k = \xi_c$. These values correspond to anisotropic coherence lengths (above 0.5 T) of $\xi_{ab} = 53(5)$ Å and $\xi_c = 7.7(9)$ Å. The fact that the *c*-axis coherence length is less than the interlayer spacing indicates that the system may be a weak link superconductor, as suggested by Cao et al. [33]. The isotropic average coherence length is calculated to be 20(1) Å, which agrees with the results of Sakurai et al. [34] but is slightly smaller than most values reported for powder samples [33, 69].

Finally, the GL parameter κ may be evaluated from the above measurements. κ defines the type of superconductor, since parameters of less than $1/\sqrt{2}$ describe type I materials and vice versa, because near the upper critical field the distance between vortices approaches the size of the coherence length, and a penetration depth larger than ξ will not support the formation of flux lines. The anisotropic parameters are calculated as $\kappa_{ab} = 115(15)$ and $\kappa_c = 650(100)$ which define sodium cobaltate oxyhydrate as an extreme type II superconductor. Other estimates for the GL parameter fall into the range of 100-250 [33, 34]. Typical GL parameters for the HTSCs are of the order of 100 [3].

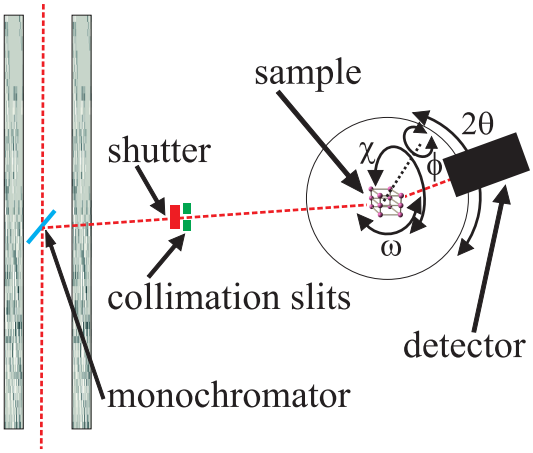

Figure 7.4: The experimental set up of the D10 diffractometer. A single energy incident neutron beam is selected with a PG monochromator and then collimated to reduce the background signal and decrease the beam divergence. The detector is positioned at the correct 2θ to satisfy the Bragg condition for a particular d-spacing, and the crystal oriented (ω, χ and ϕ varied) so that the desired crystallographic direction bisects the incident and final neutron directions.

7.3 The D10 Diffractometer

The D10 instrument (shown schematically in figure 7.4) is a four circle diffractometer. The incident neutron beam is monochromated with pyrolytic graphite (PG) and has a flux of 5 $\times$ 10^6 n cm^{-2} s^{-1}. The sample is fixed to an Al pin inside a CCR mounted on an Eulerian cradle. The cradle has three independent axes of rotation. ω and χ rotations circumscribe the base of the CCR on a sphere whilst the sample mounting is set at the correct length so that the crystal is always coincident with the neutron beam. Rotation around the axis of the mounting pin (ϕ) completes the three axes of rotation needed to orient the crystal in any direction. Finally, the detector moves in an arc around the sample table at an angle 2θ in order to satisfy the Bragg condition for a particular (hkl). The detector is a 80$\times$80 mm^2 two dimensional microstrip detector, which measures two dimensional slices through the three dimensional reflection ellipsoid. For the measurements in this study, the crystal was rotated through a reflection so the detector scanned a direction of interest in **q** space, and the intensity over a defined area of the detector summed at each step. The procedure results in a plot of intensity versus **q**, from which the peaks are fitted to a Gaussian curve in order to calculate the square of the structure factor for each reflection.

7.4 Supercell Ordering and Water Co-ordination

To date, three powder neutron diffraction studies have been performed on $Na_xCoO_2 \cdot yH_2O$ [8, 13, 87], with the intention of determining the coordination of the water to the crystal structure. Hydrogen has a high incoherent neutron scattering cross section (80.26 barns in comparison with the coherent cross section of just 1.76 barns) which is detrimental in collecting high resolution diffraction patterns and so the polycrystalline samples used in these studies were intercalated with heavy water (deuterium has a σ_{inc} of just 2.05 barns). Both Lynn et al. [87] and Jorgensen et al. [8] refined the crystal structure in the same spacegroup as the unhydrated structure, but determined two different structures for the orientation of the water molecules. The two models (with the D_2O molecules structured similarly to ice and D_2O hydration shells around the Na atoms, respectively) are mutually incompatible, moreover examination of the diffraction patterns in both studies reveal Bragg peaks that are undefined. In particular, there exist two broad reflections at d spacings of 2.6 and 2.8 Å. Jorgensen et al. [8] commented that for all of the D_2O molecular positions that their model makes possible, there are only a few feasible atomic structures for the correct fractional occupancies. D-Na repulsion must be minimised by orienting the water with its deuterium atoms pointing away from the Na ion and it is clear to see that several oxygen sites cannot be simultaneously occupied if they are too close to one another. The atomic structure with all possible atomic sites occupied (equating to a composition of $NaCoO_2 \cdot 12D_2O$) is shown in the top half of figure 7.5. Below are two possible superstructures. Firstly, a $(2a \times 2a)$ structure is defined; if the entire sample has this structure the chemical composition will be $Na_{\frac{1}{4}}CoO_2 \cdot \frac{4}{3}D_2O$. Since the fractional occupancies of the sodium and D_2O in their Rietveld refinement did not match this composition, Jorgensen et al. [8] opted for a second supercell ordering with an orthorhombic cell of dimensions $(3a \times \sqrt{3}a)$. This atomic arrangement results in zig-zag D-O chains running parallel to $\sqrt{3}a$ side of the cell. They argue that there are three

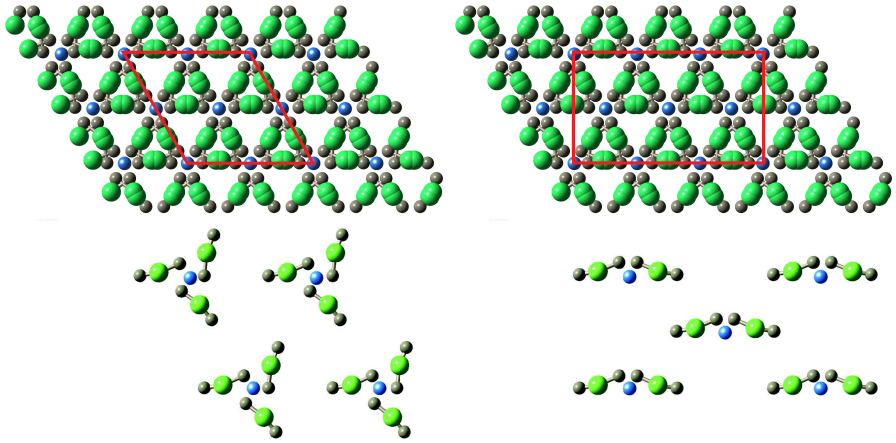

Figure 7.5: Supercell ordering, looking down the *c*-axis. A slice of the atomic structure showing just one layer of Na atoms (blue) and D_2O molecules (green-grey) is shown with all the possible atomic positions occupied (top). Two atomic supercells are shown beneath: a $(2a \times 2a)$ hexagonal cell has a composition of $Na_{\frac{1}{4}}CoO_2 \cdot \frac{4}{3}D_2O$ (left) and a $(3a \times \sqrt{3}a)$ orthorhombic cell exists with a composition $Na_{\frac{1}{3}}CoO_2 \cdot \frac{4}{3}D_2O$ (right).

possible orientations for the D-O chains with equal probabilities of occurrence and hence it is likely that the chains may exhibit ordering in stacking sequences along the *c*-axis. In this case the new unit cell is also tripled along *c*. Despite identifying the supercell ordering, the authors did not attempt to refine the structure in terms of the new atomic cell, but merely commented that the 2.6 Å peak was centred at $(309)_{orth}$ and the 2.8 Å peak at $(303)_{orth}$.

In the third study by Argyriou et al. [13], the positions of the oxygen atoms in the water were first identified by the refinement of the structure of a sample that had been hydrated in a H_2O/D_2O mixture, the exact H:D ratio determined so that their neutron scattering lengths (-3.74 fm and 6.67 fm for H and D respectively) cancel. In this scenario, only the sodium, cobalt and oxygen atoms contribute to the diffraction pattern. The final structure identified by the authors was the $(2a \times 2a)$ supercell with a prismatic water coordination as drawn in figure 7.5. The only difference between the models identified by Jorgensen et al. [8] and refined by Argyriou et al. [13] was that in the latter, the Na occupancy was shared between the $2c$ and $6h$ sites as for the higher doped, anhydrous structures (see

chapter 5). With this structure, the 2.8 Å reflection can be assigned to either the $\left(\frac{1}{2}\frac{1}{2}1\right)$ reflection, or an unresolved reflection from both the $\left(\frac{1}{2}\frac{1}{2}0\right)$ and $\left(\frac{1}{2}\frac{1}{2}1\right)$ Bragg peaks.

At first sight, it appears that the structure of $Na_xCoO_2{\cdot}yD_2O$ has been solved. However, upon close examination of the published diffraction pattern, the broad reflections at 2.6 Å and 2.8 Å reflections have been included into the background function. It is a much sharper peak at 2.8 Å on top of the broad reflection that has been fitted. Most notably, this reflection does not exist in the data of either of the other two publications. Argyriou et al. [13] acknowledge that electron diffraction patterns from different areas of the sample produce different superstructure reflections, and that because of the complex sample fabrication technique (the deintercalation of Na and the subsequent intercalation of D_2O) many possible Na-D_2O coordinations may coexist in the same sample. The fact that the 2.6 Å and 2.8 Å reflections are so much broader than the overlying Bragg peaks suggest that they have a different origin; whilst the reflections in Argyriou et al. [13] diffraction pattern can be assigned to a $(2a \times 2a)$ supercell defined by the Na ordering, the broad reflections must relate to short-ranged correlations of the water. In any case, the 2.6 Å reflection can be assigned to the $\left\{\frac{1}{2}\frac{1}{2}3\right\}$ family of directions and the 2.8 Å peak to reflections with $\left\{\frac{1}{2}\frac{1}{2}1\right\}$ (i.e. those positions in reciprocal space that lie on the circle in figure 7.8). Intensity from the higher l reflections is lost under the stronger Bragg reflections from the Na_xCoO_2 diffraction pattern.

The structure of $Na_xCoO_2{\cdot}yD_2O$ is complicated, with many overlapping Bragg reflections contributing to the powder diffraction pattern. Single crystal diffraction is a more powerful structure determination technique, since reflections with the same d-spacing but different **q** may be investigated independently. Three dimensional reciprocal space requires a longer time for investigation and prior knowledge of which crystallographic directions to probe. At the time of the experiment the third study by Argyriou et al. [13] had not been published and so the

aim of the experiment was to confirm the $(3a \times \sqrt{3}a)$ superstructure as proposed by Jorgensen et al. [8]. A crystal of dimensions 2×2×0.5 mm^3 with a superconducting T_C of 3.8 K, fabricated with the techniques described above, was used. The ambient room temperature was ∼30°C, close to the temperature identified by Foo et al. [12] where spontaneous decomposition to the non-superconducting $y = 0.6$ phase occurs, and so precautionary measures were needed to ensure the water remained in the crystal during the experimental setup. The crystal was glued to an Al pin inside a refrigerated room at ∼5°C before being transported to the instrument packed in dry ice. Once mounted, the CCR was attached and cooled to below 0°C as quickly as possible. Finally, the crystal was oriented using an incident neutron wavelength of 2.36 Å.

In order to determine the quality of the sample (the mosaic spread) and whether any of the lower hydrate phases were present (as described in section 2.1) a scan was made along the $(00l)$ direction. The different hydrate phases ($y =$ 0, 0.3 0.6 and 1.4) have lattice parameters that differ only along the *c*-axis and have been identified using x-ray diffraction [12]. Assuming these different phases are collinear along *c* (as the layered crystal structure ensures) it is a simple matter to calculate the $\boldsymbol{q}$ values for different hydrate reflections. The scan along $(00l)$ is shown in figure 7.6. The peaks were fitted to pseudo-Voigt functions and their integrated intensities compared. The peaks highlighted grey in the plot correspond to the fully-hydrated $y = 1.4$ phase ($c = 19.56$ Å). Two other phases were also identified: the $y = 0.6$ hydrate, highlighted pink, has a *c*-value of 13.69 Å and the $y = 0$ parent phase, highlighted yellow, has *c* equal to 11.12 Å (suggesting a sodium concentration of ∼0.5). Reflections corresponding to the $y = 0.3$ phase were not identified. The relative intensities of each type of reflection give a $y =$ 1.4 : $y = 0.6$: $y = 0$ ratio of $18.0(4) : 1.0(2) : 1.0(2)$.

Given that the double-layer hydrate is the predominant phase in the sample, a range of scans were performed to investigate the supercell ordering. Surprisingly, no reflections corresponding to the $(3a \times \sqrt{3}a)$ supercell were identified.

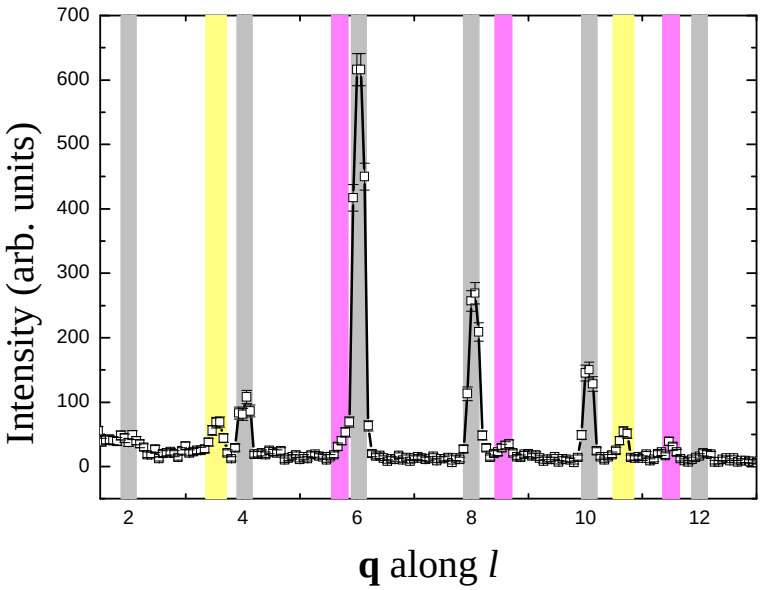

Figure 7.6: Diffracted neutron intensity, scanning along $(00l)$. The reflections belonging to the fully hydrated y = 1.4 phase are highlighted grey. Reflections from other partially hydrated phases occur at non-integer l values and are highlight pink (y = 0.6) and yellow (y = 0).

The following directions were scanned with no reflections observable above the instrumental background intensity: $(10l)_{orth} = \left(\frac{1}{3}\frac{\overline{1}}{6}l\right)_{hex}$, $(20l)_{orth} = \left(\frac{2}{3}\frac{\overline{1}}{3}l\right)_{hex}$, $(11l)_{orth} = \left(\frac{1}{3}\frac{1}{3}l\right)_{hex}$ and $(21l)_{orth} = \left(\frac{2}{3}\frac{1}{6}l\right)_{hex}$. The orthorhombic supercell ordering is therefore not present in this sample. The second choice of supercell was then investigated. Reflections, of the same order of magnitude as the $(a \times a)$ parent cell reflections were observed at half-integer h and k values corresponding to the $(2a \times 2a)$ superstructure. The collected data are plotted in figure 7.7, with blue lines for the $(a \times a)$ cell and green for the $(2a \times 2a)$ supercell reflections. Interestingly, the parent cell reflections only occur at even l (in accordance with the extinction rules for the $P6_3/mmc$ space group) whereas, with the exception of the $(10l)$ reflections, the supercell Bragg peaks occur at odd l. The supercell reflections are also, on average, twice as wide as the parent cell Bragg peaks, indicating short ranged correlations and explaining the origin of the broad reflections seen in the powder diffraction experiments. A summary of directions along which

Bragg peaks were measured is shown in figure 7.8, with the same colour code as used in figure 7.7. The reciprocal unit cells of the $(2a \times 2a)$ and $(3a \times \sqrt{3}a)$ superstructures are indicated by the black and pink dashed lines respectively. The nature of the relative sizes and orientations of the reciprocal unit cells are outlined in appendix C.

In summary, the single crystal diffraction data definitively excludes the possibility of the orthorhombic supercell occurring in the sample in this study. In order to model the validity of the structure of Argyriou et al. [13], the calculated peak intensities were produced using $\mathrm{FULLPROF}$ and compared to the integrated intensities fitted from the data in figure 7.7. The correlation of the calculated and measured intensities (plotted in figure 7.9) is not good; the line of best fit has a correlation coefficient R of just 0.62. Due to experimental difficulties, the amount of measured reflections is relatively low, and attempted single crystal refinements using the program GSAS [117] were not successful due to the small number of independent (hkl) reflections in comparison to the number of degrees of freedom within the crystal structure, which has many atoms within the unit cell and relatively little symmetry. Important conclusions from the data may still be drawn. Firstly, although broader than the Bragg reflections of the parent structure, the reflections were measured as peaks along l in three dimensional reciprocal space and therefore correspond to ordering within the *ab* planes in real space, however, information on the inter-planar correlations cannot be extracted from these measurements. The convolution of the instrumental resolution and the finite mosaic spread was estimated by fitting the $(00l)$ peaks to pseudo-Voigt functions: the average width was found to be 0.21(1) Å^{-1}. The widths of the superstructure peaks were also fitted to pseudo-Voigt functions, and the total fitted width assumed to comprise the above instrumental width and a peak broadening term due to short range correlations, added in quadrature i.e. $2\omega_{total} = \sqrt{2\omega_{res}^2 + 2\omega_{SRO}^2}$, where 2ω represents the full-width-half-maximum of the reflections for the components denoted by the subscripts. An average correlation length for the SRO was found

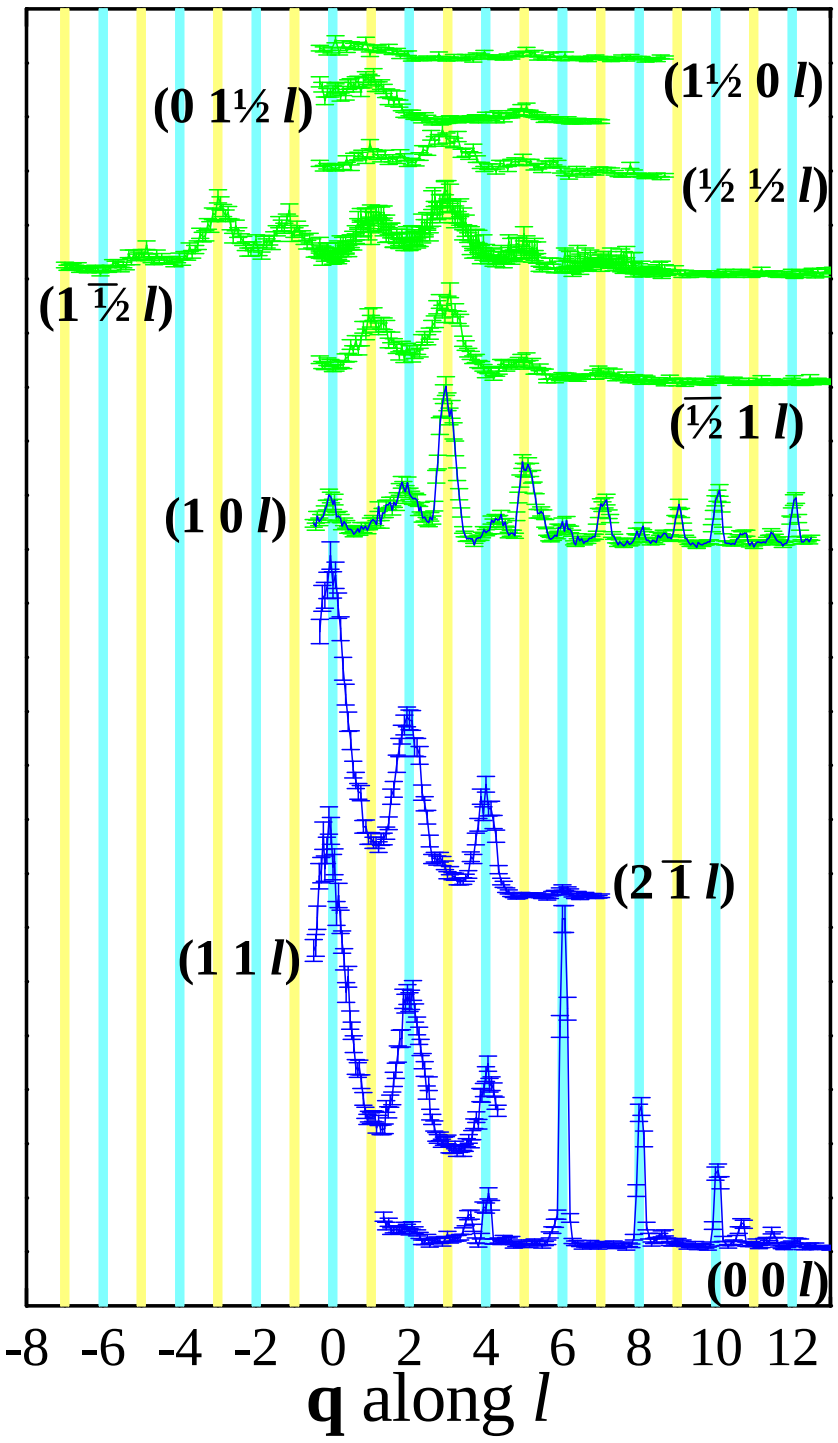

Figure 7.7: $\boldsymbol{q}$ scans along l. The reflections from the parent hexagonal cell are plotted in blue, the supercell reflections in green. The measured reflections from the parent hexagonal cell appear to obey $l = 2n$ extinction rules, whereas the supercell reflections obey $l = 2n$-1, with the exception of the $(10l)$ reflections in which both even and odd reflections are present.

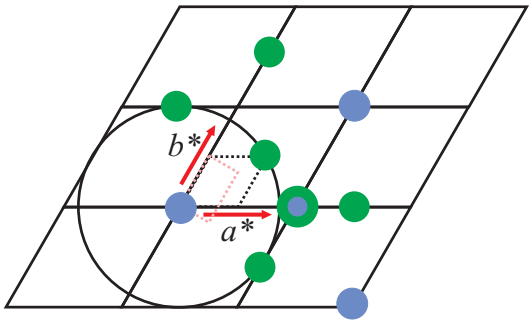

Figure 7.8: Directions in reciprocal space where Bragg reflections were observed are marked with green/blue circles (see figure 7.7). The reciprocal lattices of the orthorhombic and hexagonal supercells are also marked.

by the Scherrer method, showing that the water ordering extends over at least 14 Å, corresponding to ∼5 unit cells. Secondly, definite proof of the existence of the $(2a \times 2a)$ supercell in a single crystal sample has been presented for the first time. Despite the immense interest in the physics of this system, no reports of neutron diffraction performed single crystal samples have been published, presumably due to the difficulty of manufacturing high quality samples.

7.5 Discussion

The physics of Na_xCoO_2 samples with reduced sodium content is influenced by the layered nature of the crystal structure that has a reduced number of Na octahedra with which to bond the cobalt oxide layers together. Measurements of the *c*-axis resistivity on an anhydrous $x = 0.3$ crystal is plotted in figure 7.10 alongside the data for the $x = 0.71$ crystal as presented in section 4.1.3. The overall behaviour as a function of temperature is sample independent, however, the absolute value of the resistivity along *c* for $x = 0.3$ is an order of magnitude larger than that found in the higher doped crystal. The basal plane resistivity on the other hand, remains in the range of 0-3 mΩ cm over all measured sodium concentrations. The anisotropy in the resistivity measurements at $x = 0.3$ is roughly temperature independent at a value of $\rho_c/\rho_{ab} = 90$.

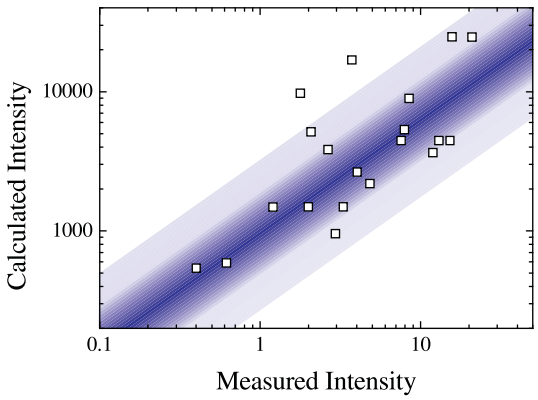

Figure 7.9: A comparison of the measured $Na_{\frac{1}{3}}CoO_2 \cdot \frac{4}{3}D_2O$ diffraction data to the calculated intensities based on the structure of Argyriou et al. [13]. Both sets of data are plotted in arbitrary units.

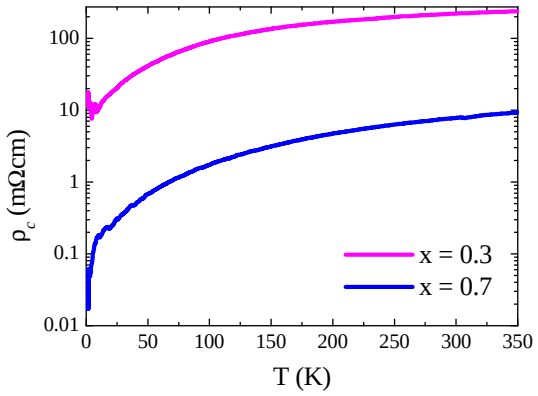

Figure 7.10: Resistivity measurements made with the current along the *c*-axis in $x = 0.3$ and 0.7 crystals. Over the entire temperature range, the former measurements are an order of magnitude larger than the latter. Resistivity in the *ab* planes remains unchanged after the sodium deintercalation process.

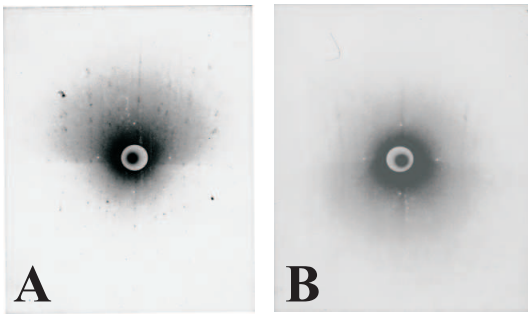

Figure 7.11: X-ray Laue images of x = 0.7 (panel A) and 0.3 (panel B) crystals with the camera aligned along the (100) direction (the $[10l]$ zone therefore runs vertically through the centre of the image). Correlation between the *ab* planes is lost after the sodium deintercalation process transforming the spots into lines of scattering.

The large increase in the *c*-axis resistivity as the sodium is removed is a consequence of decoupling of the CoO_2 planes as the number of exchange pathways along *c* is reduced, which indicates the existence of different scattering mechanisms for the in- and out-of-plane charge transport as expected from the anisotropy of the underlying crystalline structure. This increase in incoherency is also visible in the appearance of diffuse scattering in x-ray Laue experiments, shown in figure 7.11. The two images present the x-ray scattering from a $x = 0.7$ crystal (panel A) and a $x = 0.3$ crystal (panel B) with the (100) direction oriented down the x-ray beam and the (001) direction perpendicular, collinear with the vertical camera axis. The three most clearly visible zones in both images correspond to the $[10l]$ zone running vertically through the centre of the photograph and the $[21l]$ and $[3\bar{1}l]$ curved zones to the left and right, respectively. The sodium deintercalation process evidently removes the correlations between the *ab* planes in different crystallographic layers, transforming the spots seen in panel A into lines of scattering along the directions in which l is varied.

It is undoubtedly this reduced correlation length, coupled with the increased distance between the cobalt oxide planes that produces the two-dimensionality on which the superconductivity in the hydrated compound is said to depend. Due to the highly unstable nature of the superconducting crystals, neither Laue nor

resistivity measurements were made on the hydrated compound in order to make a comparison to the properties of the anhydrated $x = 0.3$ parent compound. Few resistivity studies on the superconducting material have been reported, due to the experimental difficulties involved in attaching the sample contacts without a loss in water concentration. Those few experimental reports [29, 60, 69] do not measure a zero value for the resistance below the superconducting transition indicating the presence of non-superconducting phases.

Evidence for the presence of the normal state coexisting with the superconducting phase was presented in sections 7.1 and 7.2. However, the amount of non-superconducting material within the samples may not be quantified by these measurements alone and it should be noted that the relative amounts of the $y = 1.4$ and $y = 0.6$ - 0 phases in any one sample may change between experiments depending on the environmental and sample handling conditions. The fraction of superconducting and non-superconducting material as found by the $(00l)$ scans in the D10 experiment showed that, even under the least ideal experimental conditions a crystal may retain a high proportion of its water content and that the system is, in general, more resilient than other reports may have led us to believe [12]. It can therefore be said with certainty, that the low Meissner fractions presented in the literature, and in this work, are most likely due to weak link nature of this layered system, which does not exhibit conventional BCS superconductivity.

As previously discussed in section 2.2.1, the superconducting pairing mechanism has not yet been identified, with experimental evidence and theoretical speculation producing many conflicting ideas. The debate centres on the question of whether superconductivity occurs in the spin singlet or spin triplet channels, with different Co NMR and NQR experiments indicating both isotropic [44] and non-s-wave pairing [118]. At the same time, the time reversal symmetry breaking predicted by calculations in the $t - J$ model [119] was disputed by recent μSR experiments [120]. Most of the theoretically predicted pairing states are dependent on the exact model used, the majority of which assumed single band models on

the basis that the e'_g orbitals were predicted to lie below the Fermi level from the numerous ARPES measurements [52, 53, 54, 55]. The latest multi-band models produce spin-triplet f-wave pairing supported by in-plane ferromagnetic fluctuations, as predicted for the anhydrous material with the same cobalt valence, at $x \sim$0.7 [40]. In order to elucidate the fundamental properties of the superconducting state, the exact chemical composition of the sample under investigation must be identified in all future experimental studies, ideally *in situ* since the hydration process and therefore the setting of y and z is a dynamic process, susceptible to change with repeated temperature cycling and on exposure to atmosphere. In the light of the most recent studies, that have identified the presence of two different superconducting phases which exist with the same average cobalt valence [115], but differing ratios of sodium to oxonium, the need for such careful sample identification becomes essential. If the superconducting pairing mechanism is actually dependent on the magnetic interactions within the system, the possibility arises that the previous conflicting reports may mirror the change in oxonium content from sample to sample, which governs the magnetism in the system by tuning the cobalt valency.

Further research into the chemical structure of sodium cobaltate oxyhydrate is therefore needed, in order to advance our understanding of the role of oxonium doping within this material. The neutron diffraction data presented in section 7.4 provides the first evidence of short range ordered water co-ordination in a single crystal sample, however not enough data were collected in order to complete a crystal structure refinement. The exact nature of the water ordering and even the position of the oxonium molecules within the unit cell are currently unknown, with structural [121] and redox titration [36] studies predicting the addition of oxonium onto the Na vacancy sites and another neutron powder diffraction study [13] concluding that the intercalated H_3O^+ resides within the hydrate layer. Since superconductivity is essentially an instability at the Fermi surface, detailed knowledge of the crystal structure as a function of x, y and the oxonium content

z must be ascertained before conclusions can be drawn from the predicted band structure calculations, which are currently in their infancy. It is clear however, the presence and topology of the elliptical hole pockets at the K points discussed in section 2.3, vital to the existence of superconductivity in many theories [49], is extremely sensitive to the overall chemical structure.

Chapter 8

Summary and Conclusions

Sodium cobalt oxyhydrate, $Na_xCoO_2 \cdot yH_2O$, exhibits a rich phase diagram, manifesting intriguing magnetic ordering that is highly dependent on the sodium concentration. The work in this thesis has illustrated the three key areas of the phase diagram that are of interest, namely the spin density wave magnetic ordering at $x \sim 0.75$, the static and dynamic magnetic behaviour of the $x = 0.5$ system and the properties of the superconductivity found in the hydrated samples with $x \sim 0.3$.

At each stage of the analysis, it was clear that an explicit identification of the x value for each sample was needed in order to draw significant conclusions from the experimental data. The research that was carried out into sample preparation and doping level monitoring techniques, fundamental to the work presented in subsequent chapters, was outlined in chapter 3. It was found that, at the reaction temperatures used during the polycrystalline sample preparation, the P3 'γ' growth phase was stable only for stoichiometries of $0.60 < x < 0.8$, with no detectable cobalt oxide impurities if, and only if, oxygen was flowing through the furnace during the reaction procedure. Single crystal samples were subsequently manufactured from powder samples within this x range by the floating zone method. The loss of sodium during the crystal formation was carefully monitored, and found to occur during the melting of the polycrystalline seed rod, and

not as a function of time within the furnace. Crystals with fewer stacking faults were therefore produced by a two stage melting procedure, with the second growth carried out at much slower speeds than recommended in the literature [122]. The deintercalation process using iodine as a oxidising agent was investigated as a function of time and solution strength; an absolute change in sodium concentration was observed to saturate at a value of $(x - y) = 0.2$ after a time of 1 week for the largest single crystals and less than one day in powder samples, using a 1:1 mass ratio of Na_xCoO_2 and I_2. Other changes in x may be performed by directly scaling the above empirical relation. The most accurate, and viable laboratory techniques used to monitor changes in sodium concentrations were identified by simply monitoring the change in sample mass throughout the deintercalation process, coupled with measurements of the *c*-axis lattice parameters made using x-ray diffraction.

In chapter 4 the magnetic, thermal and transport properties of the anhydrous Na_xCoO_2 materials were investigated over the range of $0.5 < x < 0.72$. An anomaly in the magnetic susceptibility of samples in the range of $0.68 < x < 0.72$ was seen at 22 K, and ascribed to long-ranged antiferromagnetic ordering with the moments oriented along the *c*-axis. The values of the high temperature magnetic susceptibility in this doping regime are anisotropic, and Curie-Weiss fits to the data indicate the magnetism has moments interposed between the values expected for low and intermediate spin cobalt ions. The same anomaly is also present in the heat capacity data, although the size of the jump is just a small fraction of that expected for the magnetic ordering of $(1 - x)$ low spin Co^{4+} atoms. The magnetic ordering is additionally identified by a sharp downturn in the electronic transport measured in the *ab* plane. The reduction in ρ suggests that the opening up of a gap associated with the SDW leads to a decrease in the total scattering within the *ab* plane while the conduction along *c* is unaffected. This was initially assigned to the removal of the e'_g hole pockets at the FS, although the evidence presented in section 2.3 and predicted in references [50, 51] now suggests this band lies below the Fermi level at this doping level. It is therefore the reduction

in electron-electron scattering within the *ab* plane with the formation of the SDW that determines the transport properties. The overall behaviour of the magnetic and thermal properties, as presented in sections 4.1.1 and 4.1.2, strongly indicates the material is phase separated into magnetic and non-magnetic systems and that changing the total stoichiometry produces a change in weight fractions of the two. No indication of a change in T_{SDW} was observed as a function of x, however materials with higher and lower ordering temperatures were manufactured with smaller and larger sodium concentrations, respectively. These materials are believed to belong to different allotropes of the Na_xCoO_2 family, a study of which is beyond the scope of this thesis. Finally, the pressure dependence of the SDW magnetic ordering suggests the magnetism at atmospheric pressure is supported by imperfect nesting within the FS, the topology of which is changed by the application of pressure. Powder neutron diffraction measurements made under externally applied pressure are scheduled for the near future, in order to monitor the morphology of the CoO_6 octahedra and the Co-O-Na-O-Co exchange pathways as a function of P.

Further modifications to the magnetic ordering are seen with the application of high magnetic fields and an additional reduction in temperature. A metamagnetic transition was visible in the *c*-axis magnetic susceptibility at an applied field of $\sim$80 kOe. The absolute jump in χ represented an adjustment in the reorientation of the magnetic moments a few degrees from the *ab* plane, in agreement with recent neutron diffraction results [75]. At low fields, a separate alteration to the magnetic state was identified as the onset of a small ferromagnetic component oriented along *c* at a temperature of 10 K. A large positive magnetoresistance of $\sim$40% at 2 K accompanies the entrance of this new magnetic state, which is attributed to a temperature induced change in the FS morphology which supports the increase in polarisation of one of the magnetic subsets in the SDW. Finally, at temperatures of just 4 K, a broad peak in the heat capacity and a large peak in χ_{ac} indicates the onset of a low temperature *glassy ground state*, most likely

originating from the mismatch between the lattice periodicity and the wavelength of the SDW, the magnitude of which is controlled by the size of the FS nesting vector that created the magnetic instability.

The latter part of the chapter concentrates on the properties of the half-doped material, on which fewer facts about the magnetic ordering, and its origin, are known. An antiferromagnetic transition at $T_M = 88$ K and a modification to the magnetic ordering at $T_{MI} = 53$ K are visible in the magnetic susceptibility, which increases with increasing temperature, contrary to that expected from a localised moment, Curie-Weiss system. The latter ordering temperature is seen to increase with increasing pressure, as found for the SDW phase, indicating the two types of magnetic ordering to have similar origins. The temperature dependence of the magnetic order parameter was mapped using neutron diffraction, an analysis of which indicated the system to exhibit low dimensionality, in accordance with the chains of magnetic ordering identified by previous neutron diffraction studies [28]. The notion of low dimensionality was further supported by a lack of observable anomalies in the heat capacity data. Finally, the transport properties were measured as a function of temperature and field. The system appears to exhibit a weak metal-insulator transition at T_{MI} and a small magnetoresistance that varies with both the direction of the applied field and current, that occurs below T_{MI} and is strongly modified at a lower temperature of $\sim$20 K where a hitherto unidentified change in the magnetism is believed to exist [30].

In chapter 5, the structural properties of Na_xCoO_2 were investigated as a function of temperature and sodium doping using powder neutron diffraction. Materials above half doping were found to be intrinsically phase separated, the heterogeneity of the two phases defined by the position of one of the two sodium atoms that exist within the unit cell. The resulting phases were labelled as $2c$ and $6h$ after the respective sodium Wyckoff positions, the latter showing the lower symmetry. The transfer of sodium from one phase to another was tracked and found to occur at temperatures at which anomalies are present in both the heat

capacity and transport measurements, T_{Na1} = 305 K and T_{Na2} = 340 K, and a further, unexpected phase mixing temperature of ∼200 K in the $x = 0.59$ sample. These results indicate that the $2c$ phase persists at lower sodium concentrations and temperatures than predicted in the literature [10]. Finally, the presence of the orthorhombic supercell was identified in the half doped $x = \frac{1}{2}$ system, and a lattice contraction around the metal-insulator transition at T_{MI} = 53 K was observed. Bond valence calculations revealed that the orthorhombic ordering of the Na ions did not result in a significant charge disproportionation on the two cobalt sites, in agreement with other recent neutron diffraction studies [32]; static charge ordering can therefore be ruled out as the origin of the insulating transition.

Chapter 6 details a study into the intra-planar magnetic excitations at $x = \frac{1}{2}$ utilising inelastic neutron scattering on both a time-of-flight and triple-axis machine. Dispersive excitations at points above an energy gap E_g = 11.5(5) meV were observed at the superstructural Bragg reflections. The excitations are highly damped, broadening with increasing energy, and disappear at $\hbar\omega \approx$ 35 meV, an indication that the magnetism is itinerant. Tilting into the *ac* plane reduces the value of E_g by 25%. Further experiments to measure the magnetic excitations along the *c*-axis are also scheduled in the near future, after which the model cacculated using linear spin wave theory may be tested and a full fit to the data will be carried out in order to determine accurate values for the magnetic exchange parameters and identify any spin gaps at the magnetic zone centres.

The final chapter investigates the superconducting material produced by intercalating a sodium deficient sample with water. The magnetic and thermal measurements reveal the onset of superconductivity to occur at a maximum temperature of around 4.5 K, although T_C proved to be sample dependent. The critical temperature was shown to be independent of the sodium doping level, in contrast to some publications, however the most recent reports [36, 39] indicate the superconducting properties rely on three independent parameters of the sodium, water and oxonium content within the sample, the details of which cannot be disen-

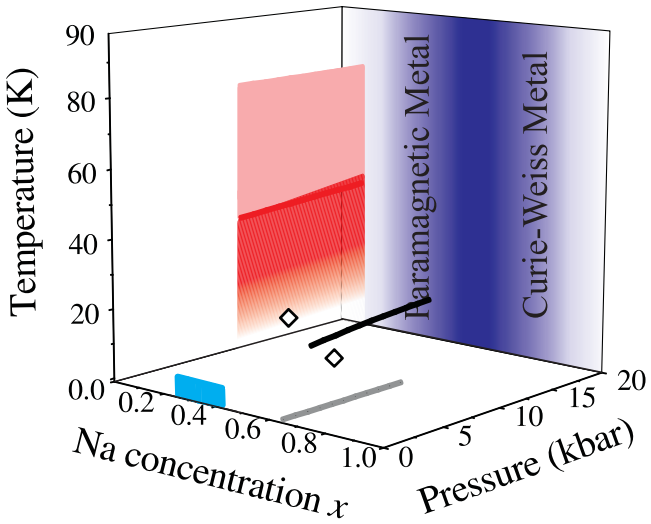

Figure 8.1: The data collected in this thesis work have been summarised in the above phase diagram, which is plotted as a function of temperature and pressure. The invariant $T_C(x)$ in the superconducting material is depicted by the blue rectangle. The two types of magnetic ordering at $x = \frac{1}{2}$ are indicated by the red and pink areas and the spin density wave ordering boundary is represented by a black line. The two other T_{SDW} ordering temperatures are plotted as black diamonds.

tangled from just one measurement of $T_C\,(x)$. The macroscopic properties are indicative of unconventional superconductivity, with a large value of the Ginzburg-Landau parameter, but very low flux pinning properties, in contrast to the HTSC cuprates. The low temperature heat capacity data can be plausibly fitted to both a fully gapped s-wave state, or spin-triplet superconductivity with a superconducting order parameter exhibiting point nodes. Finally, the presence of supercell ordering due to short-ranged correlations of the water molecules was investigated using single crystal neutron diffraction. A previously proposed orthorhombic supercell based on broad peaks witnessed in neutron powder diffraction experiments [8] was disproved, whilst a supercell based on a doubling of the parent hexagonal cell was proven to exist. The width of the superstructural Bragg peaks confirmed the water ordering existed within the basal planes over a distance of at least 5 unit cells.

The work presented in this thesis has furthered the existing knowledge of the magnetic and superconducting phase diagram of $Na_xCoO_2 \cdot yH_2O$, presented in

figure 8.1, and yet has simultaneously highlighted the need for further experimental and theoretical investigation. Work into the magnetic properties as a function of applied pressure has revealed some interesting results, atypical of most SDW systems that merit further investigation. The results of the future powder neutron diffraction experiment are of interest not only in understanding the strengthening of the magnetic response with P, but to how the structure affects the magnetic behaviour as the sodium doping level is changed. In order to verify the analysis used in the inelastic neutron scattering results presented both in this thesis, and by other authors [16, 17], detailed knowledge of the magnetic exchange pathways in the crystal structure are needed. Secondly, investigation into the magnetic properties of the other Na_xCoO_2 structures is very much in its infancy; detailed temperature, pressure and doping investigations into the magnetic states of these materials are needed to complete the sodium cobaltate phase diagram. Finally, throughout the work presented here, the greatest attention to detail has been paid when reporting on experimental results as a function of doping, a feature sadly lacking in many experimental reports that have been published to date, leading to inconsistencies in the reported phase diagram morphologies, namely the non-existent dome shaped SDW ordering. The same lack of clarity of the sample content was acknowledged to exist in the superconducting material in the final chapter. The presence of different types of pairing mechanisms in different areas of the sodium/water/oxonium phase diagram is evidently the origin of the contradictory experimental results presented so far; a clear understanding of the role of each dopant (the latter of which has only recently been identified) on the superconductivity doubtlessly requires further investigation.

Appendix A

Linear Spin Wave Theory

The following work, which describes the derivation of the spin wave equations used to model the excitations measured in chapter 6, was completed in collaboration with Dr. Jim Hague [private communication]. His derivations are presented below using my own notation.

Equation 1.8 may be expanded into components along the three base vectors of the crystallographic unit cell:

$$\begin{aligned} H = & \\ & -2\mathbf{J}\sum_{<ij>}^{nn}\left[S_{ix}S_{jx}+S_{iy}S_{jy}+S_{iz}S_{jz}\right] \\ & -2\mathbf{J}\alpha\sum_{<ij>}^{nnn}\left[S_{ix}S_{jx}+S_{iy}S_{jy}+S_{iz}S_{jz}\right] \\ & -D\sum_{i}(S_{iz})^2 \end{aligned} \tag{A.1}$$

An excitation in a magnetically ordered state, in the classical picture, involves the flipping of individual spins. It is therefore useful to introduce the spin raising and lowering operators:

$$S_+ = S_x + iS_y \tag{A.2}$$

$$S_- = S_x - iS_y \tag{A.3}$$

Using these new operators, the first two terms of the sum in equation A.1 may be

written as:

$$S_{ix}S_{jx} + S_{iy}S_{jy} = \frac{1}{2}\left[S_{i-}S_{j+} + S_{i+}S_{j-}\right] \tag{A.4}$$

The problem was first addressed in 1940 by Holstein and Primakov [123] who introduced new spin wave operators $a_i^\dagger$, which creates a spin wave excitation at site i and a_i, the corresponding annihilation operator.

$$S_{i-} = (2S)^{1/2} a_i^\dagger \left(1 - \frac{a_i^\dagger a_i}{2S}\right)^{1/2} \approx (2S)^{1/2} a_i^\dagger \left(1 - \frac{a_i^\dagger a_i}{4S}\right) \tag{A.5}$$

$$S_{i+} = (2S)^{1/2} \left(1 - \frac{a_i^\dagger a_i}{2S}\right)^{1/2} a_i \approx (2S)^{1/2} \left(1 - \frac{a_i^\dagger a_i}{4S}\right) a_i \tag{A.6}$$

$$S_{iz} = S - a_i^\dagger a_i \tag{A.7}$$

An antiferromagnet can be thought of as two geometrically interpenetrating sublattices of ferromagnetic spins. It is therefore necessary to define the Holstein-Primakov creation and annihilation operators for the second, antiparallel spin population:

$$S_{j+} \approx (2S)^{1/2} b_j^\dagger \left(1 - \frac{b_j^\dagger b_j}{4S}\right) \tag{A.8}$$

$$S_{j-} \approx (2S)^{1/2} \left(1 - \frac{b_j^\dagger b_j}{4S}\right) b_j \tag{A.9}$$

$$S_{jz} = b_j^\dagger b_j - S \tag{A.10}$$

The approximation in $S_{i[j]+}$ and $S_{i[j]-}$ made by taking just the first two terms of the binomial expansion of $\sqrt{1-x}$ is the feature that gives its name to linear spin wave theory. It is important to note that this approximation becomes less valid as x increases, i.e. as S decreases. In the case of spin half systems, Heisenberg Hamiltonians containing the Holstein-Primakov approximation can provide a decent fit to experimental data, however in these cases higher order terms in the expansion also contribute to the spin operators and the spin waves appear with finite lifetimes. In an inelastic neutron scattering experiment the excitation lifetime exhibits itself as a Lorentzian broadening of the spin wave peak.

The next step in the spin wave analysis is to write each term of the Hamiltonian in equation A.1 in terms of the new creation and annihilation operators.

For the easy axis anisotropy term we have:

$$\begin{aligned}
-D\sum_i S_{iz}^2 &= -D\sum_i \left(S - a_i^\dagger a_i\right)\left(S - a_i^\dagger a_i\right) \\
&= -D\sum_i \left(S^2 - 2Sa_i^\dagger a_i + a_i^\dagger a_i a_i^\dagger a_i\right) \\
&= -D\sum_i \left(S^2 - 2Sa_i^\dagger a_i + a_i^\dagger \left(1 + a_i^\dagger a_i\right) a_i\right) \\
&= -D\sum_i \left(S^2 - 2Sa_i^\dagger a_i + a_i^\dagger a_i + a_i^\dagger a_i^\dagger a_i a_i\right) \\
&\approx -D\sum_i \left(S^2 - (2S-1)\, a_i^\dagger a_i\right) \qquad \text{(A.11)}
\end{aligned}$$

where the interaction terms have been neglected for the same reasons as in the approximation made above. Similarly, for the second magnetic sublattice:

$$-D\sum_j S_{jz}^2 \approx -D\sum_i \left(S^2 - (2S-1)\, b_j^\dagger b_j\right) \qquad \text{(A.12)}$$

For the rest of the formulation, only the term in the Hamiltonian relating to the interaction between nearest neighbours is considered, as the mathematics for the next nearest neighbour interactions are identical. It is expanded as before:

$$\begin{aligned}
H_{nn} &= -2\mathbf{J}\sum_{<ij>} \boldsymbol{S}_i.\boldsymbol{S}_j \\
&= -2\mathbf{J}\sum_{<ij>} \left[\frac{1}{2}\left(S_{i-}S_{j+} + S_{i+}S_{j-}\right) + S_{iz}S_{jz}\right] \\
&= -\mathbf{J}\sum_{<ij>} S_{i-}S_{j+} - J\sum_{<ij>} S_{i+}S_{j-} - 2J\sum_{<ij>} S_{iz}S_{jz} \qquad \text{(A.13)}
\end{aligned}$$

In order to express equation A.13 in terms of the Holstein-Primakov formalism, it is useful to break the sum into bonds with neighbours of the same spin orientation (denoted with $\uparrow\uparrow$) and those of opposite spins ($\uparrow\downarrow$).

$$\begin{aligned}
H_{nn} = \\
&-2\mathbf{J}S \sum_{\uparrow\downarrow} a_i^\dagger \left(1 - \frac{a_i^\dagger a_i}{4S}\right) b_j^\dagger \left(1 - \frac{b_j^\dagger b_j}{4S}\right) \\
&-2\mathbf{J}S \sum_{\uparrow\uparrow} a_i^\dagger \left(1 - \frac{a_i^\dagger a_i}{4S}\right) \left(1 - \frac{a_j^\dagger a_j}{4S}\right) a_j \\
&-2\mathbf{J}S \sum_{\uparrow\downarrow} \left(1 - \frac{a_i^\dagger a_i}{4S}\right) a_i \left(1 - \frac{b_j^\dagger b_j}{4S}\right) b_j
\end{aligned}$$

$$
\begin{aligned}
-2\mathbf{J}S \quad & \sum_{\uparrow\uparrow}\left(1-\frac{a_i^\dagger a_i}{4S}\right)a_i a_j^\dagger\left(1-\frac{a_j^\dagger a_j}{4S}\right)\\
-2\mathbf{J} \quad & \sum_{\uparrow\downarrow}\left(S-a_i^\dagger a_i\right)\left(b_j^\dagger b_j-S\right)\\
-2\mathbf{J} \quad & \sum_{\uparrow\uparrow}\left(S-a_i^\dagger a_i\right)\left(S-a_j^\dagger a_j\right)
\end{aligned}
\tag{A.14}
$$

After multiplication, the higher order terms can be removed as justified previously, leaving:

$$
\begin{aligned}
H_{nn} = \quad -2\mathbf{J}S \quad & \sum_{\uparrow\downarrow}\left[a_i^\dagger b_j^\dagger + a_i b_j + b_j^\dagger b_j + a_i^\dagger a_i - S\right]\\
-2\mathbf{J}S \quad & \sum_{\uparrow\uparrow}\left[a_i^\dagger a_j + a_i a_j^\dagger + S - a_j^\dagger a_j - a_i^\dagger a_i\right]
\end{aligned}
\tag{A.15}
$$

The Hamiltonian is expanded in a similar way for the second magnetic sublattice and, again, the higher order terms are neglected:

$$
\begin{aligned}
H_{nn} = \quad -2\mathbf{J}S \quad & \sum_{\uparrow\downarrow}\left[b_j a_i + b_j^\dagger a_i^\dagger + b_j^\dagger b_j + a_i^\dagger a_i - S\right]\\
-2\mathbf{J}S \quad & \sum_{\uparrow\uparrow}\left[b_j b_i^\dagger + b_j^\dagger b_i + S - b_j^\dagger b_j - b_i^\dagger b_i\right]
\end{aligned}
\tag{A.16}
$$

The total Hamiltonian for both sublattices is simply the sum of equations A.15 and A.16. The addition may be simplified by noting that i and j are separate sites and so operators on both of these sites commute.

$$
\begin{aligned}
H_{nn}^{total} = \quad -4\mathbf{J}S \quad & \sum_{\uparrow\downarrow}\left[a_i^\dagger b_j^\dagger + a_i b_j + b_j^\dagger b_j + a_i^\dagger a_i - S\right]\\
-4\mathbf{J}S \quad & \sum_{\uparrow\uparrow}\left[a_i^\dagger a_j + b_j^\dagger b_i + S - a_i^\dagger a_i - b_i^\dagger b_i\right]
\end{aligned}
\tag{A.17}
$$

The next step in solving these equations is to Fourier transform the Hamiltonian. In order to do so, the following Fourier decompositions of the operators are defined:

$$
\begin{aligned}
a_j^\dagger = N^{-\frac{1}{2}}\sum_{\mathbf{q}} e^{-i\mathbf{q}.\mathbf{R_j}}a_q^\dagger \quad a_j = N^{-\frac{1}{2}}\textstyle\sum_q e^{i\mathbf{q}.\mathbf{R_j}}a_q\\
b_j^\dagger = N^{-\frac{1}{2}}\sum_{\mathbf{q}} e^{i\mathbf{q}.\mathbf{R_j}}b_q^\dagger \quad b_j = N^{-\frac{1}{2}}\textstyle\sum_{\mathbf{q}} e^{-i\mathbf{q}.\mathbf{R_j}}b_q
\end{aligned}
\tag{A.18}
$$

where $\boldsymbol{q}$ is the wavevector, $\boldsymbol{R}$ a position vector between spin sites and N the number of spin sites. It is possible, using these FT identities to write down the

FT of the Hamiltonian in equation A.17. For example, the summation containing the term $a_i^\dagger a_j$ may be expressed as:

$$\begin{aligned}
&\sum_{\uparrow\uparrow} a_i^\dagger a_j \\
&\quad = \sum_{\uparrow\uparrow} \frac{1}{N} \sum_{\mathbf{qk}} e^{-i\mathbf{q}.\mathbf{R_i}} a_q^\dagger e^{i\mathbf{k}.\mathbf{R_j}} a_k \\
&\quad = \sum_{\uparrow\uparrow} \frac{1}{N} \sum_{\mathbf{qk}} e^{-i\mathbf{q}.\mathbf{R_i}} a_q^\dagger e^{i\mathbf{k}.\left(\mathbf{R_i}+\boldsymbol{\delta_j}\right)} a_k \\
&\quad = \sum_{\uparrow\uparrow} \frac{1}{N} \sum_{\mathbf{qk}} e^{i(\mathbf{k}-\mathbf{q}).\mathbf{R_i}} a_q^\dagger e^{i\mathbf{k}.\boldsymbol{\delta_j}} a_k \\
&\quad = \sum_{\mathbf{qk}} \delta\left(\mathbf{k}-\mathbf{q}\right) e^{i\mathbf{k}.\boldsymbol{\delta_j}} a_q^\dagger a_k \\
&\quad = \sum_{\mathbf{q}} e^{i\mathbf{q}.\boldsymbol{\delta_j}} a_q^\dagger a_q
\end{aligned} \tag{A.19}$$

where the identity $\frac{1}{N}\sum e^{i\mathbf{R_i}.(\mathbf{k}-\mathbf{q})} = \delta\left(\mathbf{k}-\mathbf{q}\right)$ has been used and $\boldsymbol{\delta_j}$ is the vector between sites i and j. All the other terms in the Hamiltonian can be worked out in a similar fashion. Due to the commutation relations, as described above, there are just four independent terms in the Hamiltonian, which is now of the form:

$$H_{nn}^{total} = a\sum_{\mathbf{q}} a_q^\dagger a_q + b\sum_{\mathbf{q}} b_q^\dagger b_q + c\sum_{\mathbf{q}} a_q^\dagger b_q^\dagger + d\sum_{\mathbf{q}} a_q b_q \tag{A.20}$$

The standard approach used to solve this problem is to perform a Bogoliubov transformation, where the FT of the operators are defined as:

$$a_q^\dagger = \cosh\left(\theta_q\right)\alpha_q^\dagger - \sinh\left(\theta_q\right)\beta_q \tag{A.21}$$

$$a_q = \cosh\left(\theta_q\right)\alpha_q - \sinh\left(\theta_q\right)\beta_q^\dagger \tag{A.22}$$

$$b_q^\dagger = -\sinh\left(\theta_q\right)\alpha_q + \cosh\left(\theta_q\right)\beta_q^\dagger \tag{A.23}$$

$$b_q = -\sinh\left(\theta_q\right)\alpha_q^\dagger + \cosh\left(\theta_q\right)\beta_q \tag{A.24}$$

The Hamiltonian (equation A.20) can be written out in full as:

$$\begin{aligned}
H_{nn}^{total} &= \sum_q a\left(\cosh\left(\theta_q\right)\alpha_q^\dagger - \sinh\left(\theta_q\right)\beta_q\right)\left(\cosh\left(\theta_q\right)\alpha_q - \sinh\left(\theta_q\right)\beta_q^\dagger\right) \\
&+ \sum_q b\left(-\sinh\left(\theta_q\right)\alpha_q + \cosh\left(\theta_q\right)\beta_q^\dagger\right)\left(-\sinh\left(\theta_q\right)\alpha_q^\dagger + \cosh\left(\theta_q\right)\beta_q\right) \\
&+ \sum_q c\left(\cosh\left(\theta_q\right)\alpha_q^\dagger - \sinh\left(\theta_q\right)\beta_q\right)\left(-\sinh\left(\theta_q\right)\alpha_q + \cosh\left(\theta_q\right)\beta_q^\dagger\right)
\end{aligned}$$

$$+ \quad \sum_q d\left(\cosh(\theta_q)\alpha_q - \sinh(\theta_q)\beta_q^\dagger\right)\left(-\sinh(\theta_q)\alpha_q^\dagger + \cosh(\theta_q)\beta_q\right) \tag{A.25}$$

Each line of equation A.25 is multiplied out and like terms collected together. Then, using the identity $\cosh(\theta_q)^2 - \sinh(\theta_q)^2 = 1$:

$$(a+b)\cosh(\theta_q)\sinh(\theta_q) - c\cosh(\theta_q)^2 + d\sinh(\theta_q)^2 = 0 \tag{A.26}$$

$$(a+b)\cosh(\theta_q)\sinh(\theta_q) - d\cosh(\theta_q)^2 + c\sinh(\theta_q) = 0 \tag{A.27}$$

Adding the above two equations:

$$\begin{aligned} 2(a+b)\cosh(\theta_q)\sinh(\theta_q) &= (c+d)\left(\cosh(\theta_q)^2 + \sinh(\theta_q)^2\right) \\ (a+b)\sinh(2\theta_q) &= (c+d)\cosh(2\theta_q) \\ \Rightarrow \tanh(2\theta_q) &= \frac{(c+d)}{(a+b)} \end{aligned} \tag{A.28}$$

Now $\cosh(\theta_q)$ and $\sinh(\theta_q)$ can be rewritten in terms of $\tanh 2(\theta_q)$:

$$\begin{aligned} \sinh(\theta_q)\cosh(\theta_q) &= \frac{\sinh(2\theta_q)}{2} \\ &= \frac{1}{2}\frac{\tanh(2\theta_q)}{\sqrt{1-\tanh(2\theta_q)^2}} \\ &= \frac{1}{2}\frac{(c+d)}{\sqrt{(a+b)^2-(c+d)^2}}; \end{aligned} \tag{A.29}$$

$$\begin{aligned} \sinh(\theta_q)^2 &= \frac{1}{2}(\cosh(2\theta_q) - 1) \\ &= \frac{1}{2}\left(\frac{1}{\sqrt{1-\tanh(2\theta_q)^2}} - 1\right) \\ &= \frac{1}{2}\left(\frac{(a+b)}{\sqrt{(a+b)^2-(c+d)^2}} - 1\right); \end{aligned} \tag{A.30}$$

$$\begin{aligned} \cosh(\theta_q)^2 &= \frac{1}{2}(\cosh(2\theta_q) + 1) \\ &= \frac{1}{2}\left(\frac{1}{\sqrt{1-\tanh(2\theta_q)^2}} + 1\right) \\ &= \frac{1}{2}\left(\frac{(a+b)}{\sqrt{(a+b)^2-(c+d)^2}} + 1\right) \end{aligned} \tag{A.31}$$

These identities may now be used to expand equation A.25:

$$\begin{aligned} H_{nn}^{total} &= \sum_{\mathbf{q}} \alpha_q^\dagger \alpha_q \left[\frac{a-b}{2} + \frac{\sqrt{(a+b)^2 - (c+d)^2}}{2} \right] \\ &+ \sum_{\mathbf{q}} \beta_q^\dagger \beta_q \left[\frac{b-a}{2} + \frac{\sqrt{(a+b)^2 - (c+d)^2}}{2} \right] \\ &+ \sum_{\mathbf{q}} \frac{\sqrt{(a+b)^2 - (c+d)^2}}{2} - \frac{(a+b)}{2} \end{aligned} \tag{A.32}$$

There are therefore two dispersion modes, with frequencies of:

$$\omega^{\pm} = \pm \frac{a-b}{2} + \frac{\sqrt{(a+b)^2 - (c+d)^2}}{2} \tag{A.33}$$

The formalism is now in place to write down the spin dispersion of a system. All that remains is to convert the individual terms in the Hamiltonian into their Fourier transformed counterparts as defined by A.18. We first start with the easy-axis anisotropy term (equations A.11 and A.12).

$$\begin{aligned} & -D \sum_i S_{iz}^2 - D \sum_j S_{jz}^2 \\ &= -D \sum_i \left(S^2 - (2S-1) a_i^\dagger a_i \right) - D \sum_j \left(S^2 - (2S-1) b^\dagger b_j b_j \right) \\ &= -DNS^2 + D(2S-1) \sum_{\mathbf{q}} \left(b_q^\dagger b_q + a_q^\dagger a_q \right) \end{aligned} \tag{A.34}$$

Next, the Hamiltonian for nearest neighbour interactions as defined in equation A.17:

$$\begin{aligned} H_{nn}^{total} &= 2\mathbf{J} S^2 N \left(z_{\uparrow\downarrow} - z_{\uparrow\uparrow} \right) \\ &- 2\mathbf{J} S \sum_{\mathbf{q}\uparrow\downarrow} \left(e^{-iq.\boldsymbol{\delta}_{\uparrow\downarrow}} a_q b_q + e^{iq.\boldsymbol{\delta}_{\uparrow\downarrow}} a_q^\dagger b_q^\dagger - z_{\uparrow\downarrow} \left(b_q^\dagger b_q + a_q^\dagger a_q \right) \right) \\ &- 2\mathbf{J} S \sum_{\mathbf{q}\uparrow\uparrow} \left(e^{iq.\boldsymbol{\delta}_{\uparrow\uparrow}} b_q^\dagger b_q + e^{iq.\boldsymbol{\delta}_{\uparrow\uparrow}} a_q^\dagger a_q - z_{\uparrow\uparrow} \left(b_q^\dagger b_q + a_q^\dagger a_q \right) \right) \end{aligned} \tag{A.35}$$

where $\boldsymbol{\delta}_{\uparrow\downarrow[\uparrow\uparrow]}$ are the vectors between anti-parallel [parallel] spins and $z_{\uparrow\downarrow[\uparrow\uparrow]}$ are the number of nearest neighbours with anti-parallel [parallel] spins. Collecting like terms:

$$H_{nn}^{total} = 2\mathbf{J} S^2 N \left(z_{\uparrow\downarrow} - z_{\uparrow\uparrow} \right) - 2JS \sum_{\mathbf{q}} \left(\sum_{\uparrow\downarrow} e^{-iq.\boldsymbol{\delta}_{\uparrow\downarrow}} a_q b_q + \sum_{\uparrow\downarrow} e^{iq.\boldsymbol{\delta}_{\uparrow\downarrow}} a_q^\dagger b_q^\dagger \right)$$

$$-2\mathbf{J}S\sum_{\mathbf{q}}\left(b_q^{\dagger}b_q\left(\sum_{\uparrow\uparrow}e^{-iq.\boldsymbol{\delta}_{\uparrow\uparrow}}-z_{\uparrow\downarrow}-z_{\uparrow\uparrow}\right)+a_q^{\dagger}a_q\left(\sum_{\uparrow\uparrow}e^{iq.\boldsymbol{\delta}_{\uparrow\uparrow}}-z_{\uparrow\downarrow}-z_{\uparrow\uparrow}\right)\right) \tag{A.36}$$

Finally, everything is in place for the determination of a real spin wave excitation. The Hamiltonian should be written down based on the possible exchange pathways leading to magnetic ordering in the crystal structure. If the excitation is gapped, a term for the anisotropy must be included. The components a_n, b_n, c_n and d_n can be written down for the n terms in the Hamiltonian based on the components of the Fourier transformed creation and annihilation operators by directly comparing the coefficients of equations A.34 and A.36 with equation A.20.

Explicitly, for a spin system with a Hamiltonian with two terms:

$$H=-2\mathbf{J}S\sum_{<ij>}^{nn}\boldsymbol{S}_i.\boldsymbol{S}_j-D\sum_i\boldsymbol{S}_{iz}^2 \tag{A.37}$$

i.e. one containing interactions between nearest neighbour spins (denoted interaction 1) and a single axis anisotropy term (denoted interaction 2):

$$\begin{aligned}
a_1 &= -2\mathbf{J}S\left(\sum_{\uparrow\uparrow}e^{iq.\boldsymbol{\delta}_{\uparrow\uparrow}}-z_{\uparrow\downarrow}-z_{\uparrow\uparrow}\right)\\
b_1 &= -2\mathbf{J}S\left(\sum_{\uparrow\uparrow}e^{-iq.\boldsymbol{\delta}_{\uparrow\uparrow}}-z_{\uparrow\downarrow}-z_{\uparrow\uparrow}\right)\\
c_1 &= -2\mathbf{J}S\sum_{\uparrow\downarrow}e^{iq.\boldsymbol{\delta}_{\uparrow\downarrow}}\\
d_1 &= -2\mathbf{J}S\sum_{\uparrow\downarrow}e^{-iq.\boldsymbol{\delta}_{\uparrow\downarrow}}\\
a_2 &= 2DS\\
b_2 &= 2DS\\
c_2 &= 0\\
d_2 &= 0
\end{aligned} \tag{A.38}$$

The coefficient terms are added and put into directly into equation A.33. The resulting form of the dispersion is thus:

$$\omega=S\sqrt{\left(2D-2\mathbf{J}\left(\sum_{\uparrow\uparrow}e^{iq.\boldsymbol{\delta}_{\uparrow\uparrow}}-z_{\uparrow\downarrow}-z_{\uparrow\uparrow}\right)\right)^2-\left(2\mathbf{J}\sum_{\uparrow\downarrow}e^{iq.\boldsymbol{\delta}_{\uparrow\downarrow}}\right)^2} \tag{A.39}$$

Appendix B

Configurational Entropy Calculation

Configurational entropy in solid solutions describes the entropy involved during an order-disorder transition, in which one or more atomic species are distributed onto specific sites within a crystal lattice. There are an extremely large number of macroscopically indistinguishable configurational microstates in this case. Specifically there are:

$$W = \frac{N!}{yN!\left[(1-y)\,N\right]!} \tag{B.1}$$

ways of of arranging yN atoms atoms of type A and $(1-y)\,N$ atoms of type B over N sites, where 0$\geq$ y $\geq$1. In case of the sodium ordering transition in Na_xCoO_2 the order-disorder transition is modelled by the distribution of Na atoms (type A) and Na vacancies (type B) over the $2b$, $2c$ and $6h$ sites. The entropy is simply calculated as $S = k_B \ln W$ from equation B.1:

$$S = k_B \left\{\ln\left(N!\right) - \ln\left(yN!\right) - \ln\left(\left[(1-y)\,N\right]!\right)\right\} \tag{B.2}$$

The above equation may be simplified using Stirling's approximation $\ln N! = N\ln N - N$ giving:

$$\begin{aligned}\frac{S}{k_B} = \quad & N\ln\left(N\right) - N - \left[yN\ln\left(yN\right) - yN\right] \\ & - \left[(1-y)\,N\ln\left((1-y)\,N\right) - (1-y)\,N\right]\end{aligned}$$

$$= -\{yN\ln(yN) - [(1-y)N\ln((1-y)N)] - N\ln(N)\} \quad \text{(B.3)}$$

Using the definition of the molar gas constant $R = k_B N_A$ equation B.3 can be further simplified for one mole of the substance:

$$S = -R\{y\ln y + (1-y)\ln(1-y)\} \quad \text{(B.4)}$$

For the $x = 0.75$ powder, the entropy involved in arranging half of the sodium onto the $2b$ site and the remaining 0.25 fraction onto the $2c$ site is consequently equal to:

$$\begin{aligned} S &= -R\left\{\frac{1}{2}\ln\frac{1}{2} + \frac{1}{2}\ln\frac{1}{2} + 0.25\ln 0.25 + 0.75\ln 0.75\right\} \\ &= 1.255R \end{aligned} \quad \text{(B.5)}$$

which is equivalent to 10.43 J mol^{-1} K^{-1}.

Appendix C

The Reciprocal Lattice

In order to understand the effects of the different superlattices on the observed Bragg reflections, it is necessary to understand the relative sizes and orientations of the reciprocal lattices. The reciprocal lattice vectors of a unit cell ($\mathbf{a}^*$, $\mathbf{b}^*$ and $\mathbf{c}^*$) relate to the real space vectors ($\mathbf{a}$, $\mathbf{b}$ and $\mathbf{c}$) by the following equations:

$$\mathbf{a}^* = \frac{\mathbf{b} \times \mathbf{c}}{\mathbf{a}.(\mathbf{b} \times \mathbf{c})} \qquad \mathbf{b}^* = \frac{\mathbf{c} \times \mathbf{a}}{\mathbf{a}.(\mathbf{b} \times \mathbf{c})} \qquad \mathbf{c}^* = \frac{\mathbf{a} \times \mathbf{b}}{\mathbf{a}.(\mathbf{b} \times \mathbf{c})} \tag{C.1}$$

where the denominator in the fractions equates to the real space unit cell volume $V = \frac{\sqrt{3}}{2}a^2c$. Writing the vectors for the hexagonal unit cell (depicted by broken blue lines in figure C.1) in terms of cartesian coordinates:

$$\mathbf{a} = a\,\mathbf{x} \qquad \mathbf{b} = -\frac{1}{2}a\,\mathbf{x} + \frac{\sqrt{3}}{2}a\,\mathbf{y} \qquad \mathbf{c} = c\,\mathbf{z} \tag{C.2}$$

and evaluating the cross products, the reciprocal hexagonal lattice vectors are calculated as:

$$\mathbf{a}^* = \frac{1}{a}\mathbf{x} + \frac{1}{\sqrt{3}a}\mathbf{y} \qquad \mathbf{b}^* = \frac{2}{\sqrt{3}a}\mathbf{y} \qquad \mathbf{c}^* = \frac{1}{c}\mathbf{z} \tag{C.3}$$

i.e. the reciprocal lattice is another rhombus but with $\mathbf{a}^*[\mathbf{b}^*]$ rotated 30°[-30°] from its original direction. The $(2a \times 2a)$ superstructural lattice is simply a direct copy of the parent lattice but with half dimensions in reciprocal space. In the $(3a \times \sqrt{3}a)$ superlattice however, there is no rotation in transforming from the real to reciprocal lattice and hence $\mathbf{a}^*_{orth}$ is not coincident with $\mathbf{a}^*_{hex}$. Its unit cell

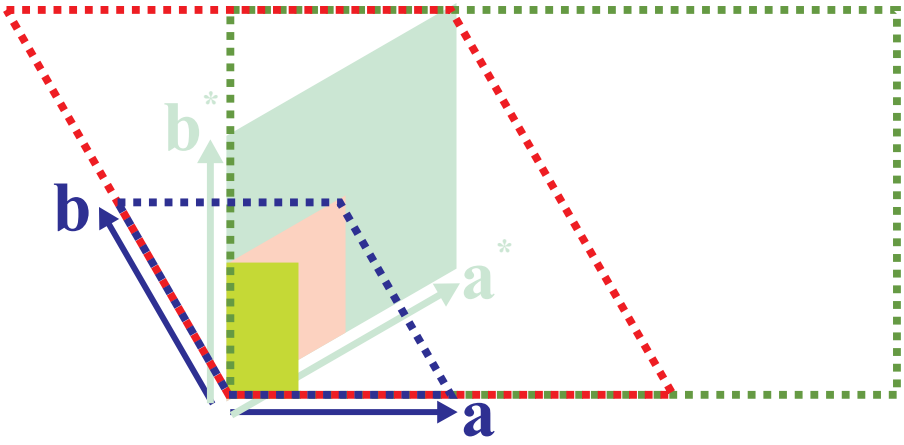

Figure C.1: The real (broken lines) and reciprocal (shaded areas) lattices of the parent hexagonal unit cell (blue), the $(2a \times 2a)$ superstructure cell (red) and the $(3a \times \sqrt{3}a)$ superstructure cell (green).

has dimensions of $\frac{\sqrt{3}}{6}a^*$ along the hexagonal reciprocal direction $(2\overline{1}0)$ and $\frac{1}{2}a^*$ collinear with $\mathbf{b}^*_{hex}$. The transformation matrix for translating from hexagonal to orthorhombic (hkl) values is therefore:

$$\begin{bmatrix} h \\ k \\ l \end{bmatrix}_{orth} = \begin{bmatrix} 3 & 0 & 0 \\ 1 & 2 & 0 \\ 0 & 0 & 3 \end{bmatrix} \begin{bmatrix} h \\ k \\ l \end{bmatrix}_{hex} \tag{C.4}$$

Bibliography

[1] S. Blundell. *Magnetism in Condensed Matter*. Oxford University Press, New York, 2001.

[2] P. Mohn. *Magnetism in the Solid State: An Introduction*. Springer, Berlin, 2006.

[3] M. Cryot and D. Pavuna. *Introduction to Superconductivity and High* T_C *materials*. World Scientific, Singapore, 1992.

[4] G. L. Squires. *Introduction to the theory of thermal neutron scattering*. Dover Publications Inc. New York, 1996.

[5] W. Marshall and S. W. Lovesey. *Theory of Thermal Neutron Scattering*. Oxford University Press, London, 1971.

[6] Y. Wang, N. S. Rogado, R. J. Cava, and N. P. Ong. Spin entropy as the likely source of enhanced thermopower in $\mathrm{Na}_x\mathrm{Co}_2\mathrm{O}_4$. *Nature*, 423:425, 2003.

[7] K. Takada, H. Sakurai, E. Takayama-Muromachi, F. Izumi, R. A. Dilanian, and T. Sasaki. Superconductivity in two dimensional CoO_2 layers. *Nature*, 422:53, 2003.

[8] J. D. Jorgensen, M. Avdeev, D. G. Hinks, J. C. Burley, and S. Short. Crystal structure of the sodium cobaltate deuterate superconductor $\mathrm{Na}_x\mathrm{CoO}_2\cdot$ 4x$\mathrm{D}_2\mathrm{O}$ (x $\approx (1/3)$). *Phys. Rev. B*, 68:214517, 2003.

[9] M. Jansen and R. Hoppe. Notiz zur kenntnis der oxocobaltate des natriums. *Z. Anorg. Allg. Chem.*, 408:104, 1974.

[10] Q. Huang, M. L. Foo, Jr. R. A. Pascal, J. W. Lynn, B. H. Toby, Tao He, H. W. Zandbergen, and R. J. Cava. Coupling between electronic and structural degrees of freedom in the triangular lattice conductor $\mathrm{Na}_x\mathrm{CoO}_2$. *Phys. Rev. B*, 70:184110, 2004.

[11] C. Fouassier, G. Matejka, J. M. Reau, and P Hagenmuller. New oxygenated bronzes of the formula $\mathrm{Na}_x\mathrm{CoO}_2$ (x$\leq$1). Cobalt-oxygen-sodium system. *J. Solid State Chem.*, 6:532, 1973.

[12] M. L. Foo, R. E. Schaak, V. L. Miller, T. Klimczuk, N. S. Rogado, Y. Wang, G. C. Lau, C. Craley, H. W. Zandbergen, N. P. Ong, and R. J. Cava. Chemical instability of the cobalt oxyhydrate superconductor under ambient conditions. *Solid State Commun.*, 127:33, 2003.

[13] D. N. Argyriou, P. G. Radaelli, C. J. Milne, N. Aliouane, L. C. Chapon, A. Chemseddine, J. Veira, S. Cox, N. D. Mathur, and P. A. Midgley. Crystal structure of the superconducting layered cobaltate $\mathrm{Na}_x\mathrm{CoO}_2\cdot$ y $\mathrm{D}_2\mathrm{O}$. *J. Phys.: Condens. Matt.*, 17:3293, 2005.

[14] M. Bañobre-López, F. Rivadulla, R. Caudillo, M. A. López-Quintela, J. Rivas, and J. B. Goodenough. The role of doping and dimensionality in the superconductivity of $\mathrm{Na}_x\mathrm{CoO}_2$. cond-mat/0409606, 2004.

[15] C. de Vaulx, M. H. Julien, C. Berthier, M. Horvatić, P. Bordet, V. Simonet, D. P. Chen, and C. T. Lin. Nonmagnetic insulator state in $\mathrm{Na}_1\mathrm{CoO}_2$ and phase separation of Na vacancies. *Phys. Rev. Lett.*, 95:186405, 2005.

[16] L. M. Helme, A. T. Boothroyd, R. Coldea, D. Prabhakaran, D. A. Tennant, A. Hiess, and J. Kulda. Three-dimensional spin fluctuations in $\mathrm{Na}_{0.75}\mathrm{CoO}_2$. *Phys. Rev. Lett.*, 94:157206, 2005.

[17] S. P. Bayrakci, I. Mirebeau, P. Bourges, Y. Sidis, M. Enderle, J. Mesot, D. P. Chen, C. T. Lin, and B. Keimer. Magnetic ordering and spin waves in $\mathrm{Na}_{0.82}\mathrm{CoO}_2$. *Phys. Rev. Lett.*, 94:157205, 2005.

[18] F. C. Chou, J. H. Cho, and Y. S. Lee. Magnetic susceptibility study of hydrated and nonhydrated $\mathrm{Na}_x\mathrm{CoO}_2{\cdot}\mathrm{yH}_2\mathrm{O}$ single crystals. *Phys. Rev. B*, 70:144526, 2004.

[19] P. Mendels, D. Bono, J. Bobroff, G. Collin, D. Colson, N. Blanchard, H. Alloul, I. Mukhamedshin, F. Bert, A. Amato, and A. D. Hillier. Cascade of bulk mangetic phase transition in $\mathrm{Na}_x\mathrm{CoO}_2$ as studied by muon spin rotation. *Phys. Rev. Lett.*, 94:136403, 2005.

[20] T. Motohashi, R. Ueda, E. Naujalis, T. Tojo, I. Terasaki, T. Atake, M. Karppinen, and H. Yamauchi. Unconventional magnetic transition and transport behavior in $\mathrm{Na}_{0.75}\mathrm{CoO}_2$. *Phys. Rev. B*, 67:064406, 2003.

[21] H. Sakurai, S. Takenouchi, N. Tsujii, and E. Takayama-Muromachi. Synthesis, characterization, and magnetic properties of γ-$\mathrm{Na}_x\mathrm{CoO}_2$ ($0.70<x<0.84$). *J. Phys. Soc. Japan*, 73:2081, 2004.

[22] B. C. Sales, R. Jin, K. A. Affholter, P. Khalifah, G. M. Veith, and D. Mandrus. Magnetic, thermodynamic, and transport characterization of $\mathrm{Na}_{0.75}\mathrm{CoO}_2$ single crystals. *Phys. Rev. B*, 70:174419, 2004.

[23] J. Sugiyama, H. Itahara, J. H. Brewer, E. J. Ansaldo, T. Motohashi, M. Karppinen, and H. Yamauchi. Static magnetic order in $\mathrm{Na}_{0.75}\mathrm{CoO}_2$ detected by muon spin rotation and relaxation. *Phys. Rev. B*, 67:214420, 2003.

[24] S. P. Bayrakci, C. Bernhard, D. P. Chen, B. Keimer, R. K. Kremer, P. Lemmens, C. T. Lin, C. Niedermayer, and J. Strempfer. Bulk antiferromagnetism in $\mathrm{Na}_{0.82}\mathrm{CoO}_2$ single crystals. *Phys. Rev. B*, 69:100410, 2004.

[25] M. L. Foo, Y. Wang, S. Watauchi, H. W. Zandbergen, T. He, R. J. Cava, and N. P. Ong. Charge ordering, commensurability, and metallicity in the phase diagram of the layered $\mathrm{Na}_x\mathrm{CoO}_2$. *Phys. Rev. Lett.*, 92:247001, 2004.

[26] A. Zorkovská, M. Orendáč, J. Šebek, E. Šantavá, P Svoboda, I. Bradarić, I. Savić, and A Feher. Interplay between mesoscopic phase separation and bulk magnetism in the layered $\mathrm{Na}_x\mathrm{CoO}_2$. *Phys. Rev. B*, 72:132412, 2005.

[27] J. Sugiyama, J. H. Brewer, E. J. Ansaldo, H. Itahara, T. Tani, M. Mikami, Y. Mori, T. Sasaki, S. Hebert, and A. Maignan. Dome-shaped magnetic phase diagram of thermoelectric layered cobaltites. *Phys. Rev. Lett.*, 92:017602, 2004.

[28] G. Gašparović, R. A. Ott, J.-H. Cho, F. C. Chou, Y. Chu, J. W. Lynn, and Y. S. Lee. Neutron scattering study of novel magnetic order in $\mathrm{Na}_{0.5}\mathrm{CoO}_2$. *Phys. Rev. Lett.*, 96:046403, 2006.

[29] C. H. Wang, X. H. Chen, J. L. Luo, G. T. Liu, X. X. Lu, H. T. Zhang, G. Y. Wang, X. G. Luo, and N. L. Wang. Dimensional crossover and anomalous magnetoresistivity of superconducting $\mathrm{Na}_x\mathrm{CoO}_2$ single crystals. *Phys. Rev. B*, 71:224515, 2005.

[30] Q. Huang, M. L. Foo, J. W. Lynn, H. W. Zandbergen, G. Lawes, Y. Wang, B. H. Toby, A. P. Ramirez, N. P. Ong, and R. J. Cava. Low temperature phase transitions and crystal structure of $\mathrm{Na}_{0.5}\mathrm{CoO}_2$. *J. Phys.: Condens. Matter*, 16:5803, 2004.

[31] J. Bobroff, G. Lang, H. Alloul, N. Blanchard, and G. Collin. NMR study of the magnetic and metal-insulator transitions in $\mathrm{Na}_{0.5}\mathrm{CoO}_2$: A nesting scenario. *Phys. Rev. Lett.*, 96:107201, 2006.

[32] A. J. Williams, J. P. Attfield, M. L. Foo, and R. J. Cava. Absence of conventional charge ordering in $\mathrm{Na}_{0.5}\mathrm{CoO}_2$ from a high resolution neutron diffraction study. *Phys. Rev. B*, 73:134401, 2006.

[33] G. Cao, C. Feng, Y. Xu, W. Lu, J. Shen, M. Fang, and Z. A. Xu. Superconductivity in a layered cobalt oxyhydrate $\mathrm{Na}_{0.31}\mathrm{CoO}_2.1.3\mathrm{H}_2\mathrm{O}$. *J. Phys.: Condens. Matt.*, 15:L519, 2003.

[34] H. Sakurai, K. Takada, S. Yoshii, T. Sasaki, K. Kindo, and E. Takayama-Muromachi. Unconventional upper- and lower-critical fields and normal-state magnetic susceptibility of the superconducting compound $\mathrm{Na}_{0.35}\mathrm{CoO}_2{\cdot}1.3\mathrm{H}_2\mathrm{O}$. *Phys. Rev. B*, 68:132507, 2003.

[35] B. Lorenz, J. Cmaidalka, R. L. Meng, and C. W. Chu. Thermodynamic properties in the normal and superconducting states of $\mathrm{Na}_x\mathrm{CoO}_2 \cdot y\mathrm{H}_2\mathrm{O}$ powder measured by heat capacity experiments. *Physica C*, 402:106, 2004.

[36] C. J. Milne, D. N. Argyriou, A. Chemseddine, N. Aliouane, J. Veira, S. Landsgesell, and D. Alber. Revised superconducting phase diagram of hole-doped $\mathrm{Na}_x(\mathrm{H_3O})_z\mathrm{CoO}_2 \cdot y\mathrm{H}_2\mathrm{O}$. *Phys. Rev. Lett.*, 93:247007, 2004.

[37] R. E. Schaak, T. Klimczuk, M. L. Foo, and R. J. Cava. Superconductivity phase diagram of $\mathrm{Na}_x\mathrm{CoO}_2{\cdot}1.3\mathrm{H}_2\mathrm{O}$. *Nature*, 424:527, 2003.

[38] D. P. Chen, H. C. Chen, A. Maljuk, A. Kulakov, H. Zhang, P. Lemmens, and C. T. Lin. Single-crystal growth and investigation of $\mathrm{Na}_x\mathrm{CoO}_2$ and $\mathrm{Na}_x\mathrm{CoO}_2.\mathrm{yH}_2\mathrm{O}$. *Phys. Rev. B*, 70:024506, 2004.

[39] H. Sakurai, K. Takada, T. Sasaki, and E. Takayama-Muromachi. Phase diagram of superconducting $\mathrm{Na}_x\mathrm{CoO}_2{\cdot}y\mathrm{H}_2\mathrm{O}$. *Phys. Rev. Lett.*, 93:247007, 2004.

[40] A. T. Boothroyd, R. Coldea, D. A. Tennant, D. Prabhakaran, L. M. Helme, and C. D. Frost. Ferromagnetic in-plane spin fluctuations in $\mathrm{Na}_x\mathrm{CoO}_2$ observed by neutron inelastic scattering. *Phys. Rev. Lett.*, 92:197201, 2004.

[41] D. J. Singh. Quantum critical behavior and possible triplet superconductivity in electron-doped CoO_2 sheets. *Phys. Rev. B*, 68:020503, 2003.

[42] T. Fujimoto, G. Q. Zheng, Y. Kitaoka, R. L. Meng, J. Cmaidalka, and C. W. Chu. Unconventional superconductivity and electron correlations in the cobalt oxyhydrate $\mathrm{Na}_{0.35}\mathrm{CoO}_2 \cdot y\mathrm{H}_2\mathrm{O}$ from nuclear quadrupole resonance. *Phys. Rev. Lett.*, 92:047004, 2004.

[43] K. Ishida, Y. Ihara, Y. Maeno, C. Michioka, M. Kato, K. Yoshimura, K. Takada, T. Sasaki, H. Sakurai, and E. Takayama-Muromachi. Unconventional superconductivity and nearly ferromagnetic spin fluctuations in $\mathrm{Na}_{0.35}\mathrm{CoO}_2 \cdot y\mathrm{H}_2\mathrm{O}$. *J. Phys. Soc. Jpn.*, 72:3041, 2003.

[44] Y. Kobayashi, M. Yokoi, and M. Sato. $^{59}\mathrm{Co\text{-}NMR}$ knight shift of superconducting $\mathrm{Na}_{0.35}\mathrm{CoO}_2 \cdot y\mathrm{H}_2\mathrm{O}$. *J. Phys. Soc. Jpn.*, 72:2453, 2003.

[45] R. Jin, B.C. Sales, S. Li, and D. Mandrus. Variation of specific heat with x and y in $\mathrm{Na}_x\mathrm{CoO}_2 \cdot y\mathrm{H}_2\mathrm{O}/\mathrm{D}_2\mathrm{O}$. cond-mat/0410517, 2004.

[46] H. D. Yang, J.-Y. Lin, C. P. Sun, Y. C. Kang, C. L. Huang, K. Takada, T. Sasaki, H. Sakurai, and E. Takayama-Muromachi. Evidence of nodal superconductivity in $\mathrm{Na}_{0.35}\mathrm{CoO}_2{\cdot}1.3\mathrm{H}_2\mathrm{O}$: A specific-heat study. *Phys. Rev. B*, 71:020504, 2005.

[47] T. Sasaki, P. Badica, N. Yoneyama, K. Yamada, K. Togano, and N. Kobayashi. Superconducting properties under magnetic field in $\mathrm{Na}_{0.35}\mathrm{CoO}_2{\cdot}1.3\mathrm{H}_2\mathrm{O}$ single crystal. *J. Phys. Soc. Jpn.*, 73:1131, 2004.

[48] N. Oeschler, R. A. Fisher, N. E. Phillips, J. E. Gordon, M. L. Foo, and R. J. Cava. Heat capacity of $\mathrm{Na}_{0.3}\mathrm{CoO}_2{\cdot}1.3\mathrm{H}_2\mathrm{O}$, a new two-gap superconductor: Comparison with the heat capacity of MgB_2. *Chin. J. Phys.*, 43:574, 2005.

[49] I. I. Mazin and M. D. Johannes. A critical assessment of the superconducting pairing symmetry in $\mathrm{Na}_x\mathrm{CoO}_2 \cdot y\mathrm{H}_2\mathrm{O}$. *Nature Physics*, 1:91, 2005.

[50] P. H. Zhang, W. D. Luo, M. L. Cohen, and S. G. Louie. Fermi surface of $\mathrm{Na}_x\mathrm{CoO}_2$. *Phys. Rev. Lett.*, 93:236402, 2004.

[51] S. Zhou, M. Gao, H. Ding, P. A. Lee, and Z. Q. Wang. Electron correlation and Fermi surface topology of Na_xCoO_2. *Phys. Rev. Lett*, 94:206401, 2005.

[52] D. Qian, D. Hsieh, L. Wray, Y.-D. Chuang, A. Fedorov, D. Wu, J. L. Luo, N. L. Wang, L. Viciu, R. J. Cava, and M. Z. Hasan. Low-lying quasiparticle states and hidden collective charge instabilities in parent cobaltate superconductors. *Phys. Rev. Lett.*, 96:216405, 2006.

[53] D. Qian, L. Wray, D. Hsieh, D. Wu, J. L. Luo, N. L. Wang, A. Kuprin, A. Fedorov, R. J. Cava, L. Viciu, and M. Z. Hasan. Quasiparticle dynamics in the vicinity of metal-insulator phase transition in Na_xCoO_2. *Phys. Rev. Lett.*, 96:046407, 2006.

[54] H.-B. Yang, Z.-H. Pan, A. K. P. Sekharan, T. Sato, S. Souma, T. Takahashi, R. Jin, B. C. Sales, D. Mandrus, A. V. Fedorov, Z. Wang, and H. Ding. Fermi surface evolution and luttinger theorem in Na_xCoO_2: A systematic photoemission study. *Phys. Rev. Lett.*, 95:146401, 2005.

[55] H.-B. Yang, S.-C. Wang, A. K. P. Sekharan, H. Matsui, S. Souma, T. Sato, T. Takahashi, T. Takeuchi, J. C. Campuzano, R. Jin, B. C. Sales, D. Mandrus, Z. Wang, and H. Ding. ARPES on $Na_{0.6}CoO_2$: Fermi surface and unusual band dispersion. *Phys. Rev Lett.*, 92:246403, 2004.

[56] D. J. Singh and D. Kasinathan. Destruction of the small Fermi surface in Na_xCoO_2 by Na disorder. cond-mat/0604002, 2006.

[57] K. Yada and H. Kontani. Origin of weak pseudogap behaviours in $Na_{0.35}CoO_2$: Absence of small hole pockets. *J. Phys. Soc. Jpn*, 74:2161, 2005.

[58] J. Laverock, S. B. Dugdale, J. A. Duffy, J. Wooldridge, G. Balakrishnan, M. R. Lees, G. Q. Zheng, D. Chen, C. Lin, A. Andrejczuk, M. Itou, and

Y. Sakurai. Elliptical hole pockets in the Fermi surfaces of unhydrated and hydrated sodium cobalt oxides. Submitted to Phys. Rev. Lett., 2006.

[59] Laboratoire des Materiaux et du Gnie Physique de l'Ecole Suprieure de Physique de Grenoble. http://www.lmgp.inpg.fr/.

[60] F. C. Chou, J. H. Cho, P. A. Lee, E. T. Abel, K. Matan, and Y. S. Lee. Thermodynamic and transport measurements of superconducting $\mathrm{Na_{0.3}CoO_2}.1.3\mathrm{H_2O}$ single crystals prepared by electrochemical deintercalation. *Phys. Rev. Lett.*, 92:157004, 2004.

[61] http://www.warwickanalytical.co.uk.

[62] http://www.easylab.co.uk/.

[63] L. B. McCusker, R. B. Von Dreele, D. E. Cox, D. Lour, and P. Scardi. Rietveld refinement guidelines. *J. Appl. Cryst.*, 32:36, 1999.

[64] R. L. Carlin. *Magnetic properties of transition metal compounds*. New York : Springer, 1978.

[65] J. Sugiyama, C. Xia, and T. Tani. Anisotropic magnetic properties of $\mathrm{Ca_3Co_4O_9}$: Evidence for a spin-density-wave transition at 27 K. *Phys. Rev. B*, 67:104410, 2003.

[66] H. Sakurai, K. Takada, T. Sasaki, F. Izumi, R. A. Dilanian, and E. Takayama-Muromachi. Correlation between T_c and lattice parameters of novel superconducting $\mathrm{Na}_x\mathrm{CoO_2} \cdot y\mathrm{H_2O}$. cond-mat/0408428, 2004.

[67] C. Kittel. *Introduction to Solid State Physics - 7th Edition*. John Wiley $\&$ Sons, New York, 1996.

[68] P. Lemmens, V. Gnezdilov, N. N. Kovaleva, K. Y. Choi, H. Sakurai, E. Takayama-Muromachi, K. Takada, T. Sasaki, F. C. Chou, D. P. Chen,

C. T. Lin, and B. Keimer. Effect of Na content and hydration on the excitation spectrum of the cobaltite $\mathrm{Na}_x\mathrm{CoO}_2$˙ y $\mathrm{H}_2\mathrm{O}$. *J. Phys.: Condens. Matt.*, 16:S857, 2004.

[69] R. Jin, B. C. Sales, P. Khalifah, and D. Mandrus. Observation of bulk superconductivity in $\mathrm{Na}_x\mathrm{CoO}_2.\mathrm{yH}_2\mathrm{O}$ and $\mathrm{Na}_x\mathrm{CoO}_2.\mathrm{yD}_2\mathrm{O}$ powder and single crystals. *Phys. Rev. Lett.*, 91:217001, 2003.

[70] S. Nakamura, J. Ohtake, N. Yonezawa, and S. Iida. Metallic conduction in hexagonal potassium cobalt oxide $\mathrm{KCo}_2\mathrm{O}_4$. *J. Phys. Soc. Jpn.*, 65:358, 1996.

[71] M. Blangero, R. Decourt, D. Carlier, G. Ceder, M. Pollet, J. P. Doumerc, J. Darriet, and C. Delmas. First experimental evidence of potassium ordering in layered $\mathrm{K}_4\mathrm{Co}_7\mathrm{O}_{14}$. *Inorg. Chem.*, 44:9299, 2005.

[72] Y. Ando, N. Miyamoto, K. Segawa, T. Kawata, and I. Terasaki. Specific-heat evidence for strong electron correlations in the thermoelectric material $(\mathrm{Na,Ca})\mathrm{Co}_2\mathrm{O}_4$. *Phys. Rev. B*, 60:10580, 1999.

[73] M. Brühwiler, B. Batlogg, S. M. Kazakov, and J. Karpinski. Evidence for two electronic components in $\mathrm{Na}_x\mathrm{CoO}_2$ (x = 0.7-0.75). cond-mat/0309311, 2003.

[74] F. Rivadulla, J.-S. Zhou, and J. B. Goodenough. Chemical, structural, and transport properties of $\mathrm{Na}_{1-x}\mathrm{CoO}_2$. *Phys. Rev. B*, 68:075108, 2003.

[75] L. M. Helme, A. T. Boothroyd, R. Coldea, D. Prabhakaran, A. Stunault, G. J. McIntyre, and N. Kernavanois. Spin gaps and magnetic structure of $\mathrm{Na}_x\mathrm{CoO}_2$. *Phys. Rev. B*, 73:054405, 2006.

[76] H. Lin, L. Rebelsky, M. F. Collins, J. D. Garrett, and W. J. L. Buyers. Magnetic structure of $\mathrm{UNi}_2\mathrm{Si}_2$. *Phys. Rev. B*, 43:13232, 1991.

[77] Y.G. Shi, H. C. Yu, C. J. Nie, and J.Q. Li. Superstructure, sodium ordering and antiferromagnetism in $\mathrm{Na}_x\mathrm{CoO}_2$ (0.75$< x <$1.0). cond-mat/0401052, 2004.

[78] K. Biljakovic, F. Nad, J. C. Lasjaunias, P. Monceau, and K. Bechgaard. The dynamics around the glass transition in the spin density wave ground state of $\mathrm{TMTSF}_2\mathrm{PF}_6$. *J. Phys.: Condens. Matt.*, 6:L135, 1994.

[79] M. Yokoi, T. Moyoshi, Y. Kobayashi, M. Soda, Y. Yasui, M. Sato, and K. Kakurai. Magnetic correlation of $\mathrm{Na}_x\mathrm{CoO}_2$ and successive phase transitions of $\mathrm{Na}_{0.5}\mathrm{CoO}_2$ - NMR and neutron diffraction studies -. *J. Phys. Soc. Jpn.*, 74:3046, 2005.

[80] I. Terasaki, Y. Sasago, and K. Uchinokura. Large thermoelectric power in $\mathrm{NaCo}_2\mathrm{O}_4$ single crystals. *Phys. Rev. B*, 56:12685, 1997.

[81] P. Carretta, M. Mariani, C. B. Azzoni, M. C. Mozzati, I. Bradarić, I. Savić, A. Feher, and J. Šebek. Mesoscopic phase separation in $\mathrm{Na}_x\mathrm{CoO}_2$ (0.65$\leq x \leq$0.75). *Phys. Rev. B*, 70:024409, 2004.

[82] J. S. Brooks, X. Chen, S. J. Klepper, S. Valfells, G. J. Athas, Y. Tanaka, T. Kinoshita, N. Kinoshita, M. Tokumoto, H. Anzai, and C. C. Agosta. Pressure effects on the electronic structure and low-temperature states in the α-$(\mathrm{BEDT\text{-}TTF})_2\mathrm{MHg}(\mathrm{SCN})_4$ organic-conductor family ($\mathrm{M{=}K}$, Rb, Tl, NH_4). *Phys. Rev. B*, 52:14457, 1995.

[83] N. Hanasaki, S. Kagoshima, N. Miura, and G. Saito. Pressure effects to the anomalous state of quasi two-dimensional conductor α-$(\mathrm{BEDT\text{-}TTF})_2\mathrm{KHg}(\mathrm{SCN})_4$. *J. Phys. Soc. Jpn.*, 65:1010, 1996.

[84] J. Sigiyama, D. Andreica, H. Itahara, and T. Tani. The effect of pressure on the spin density wave transition in the layered cobaltites $[\mathrm{Ca}_2\mathrm{CoO}_3]_{0.62}[\mathrm{CoO}_2]$ and $[\mathrm{Ca}_2\mathrm{Co}_{4/3}\mathrm{Cu}_{2/3}\mathrm{O}_4]_{0.62}[\mathrm{CoO}_2]$. *Solid State Commun.*, 135:263, 2005.

[85] M. D. Johannes, I. I. Mazin, and D. J. Singh. Three-dimensional magnetic interactions in $\mathrm{Na}_x\mathrm{CoO}_2$: First-principles calculations and analysis of exchange mechanisms. *Phys. Rev. B*, 71:214410, 2005.

[86] Y. J. Uemura, P. L. Russo, A. T. Savici, C. R. Wiebe, G. J. MacDougall, G. M. Luke, M. Mochizuki, Y. Yanase, M. Ogata, M. L. Foo, and R. J. Cava. Unconventional superconductivity in $\mathrm{Na}_{0.35}\mathrm{CoO}_2{\cdot}1.3\mathrm{D}_2\mathrm{O}$ and proximity to a magnetically ordered phase. cond-mat/0403031, 2004.

[87] J. W. Lynn, Q. Huang, C. M. Brown, V. L. Miller, M. L. Foo, R. E. Schaak, C. Y. Jones, E. A. Mackey, and R. J. Cava. Structure and dynamics of superconducting $\mathrm{Na}_x\mathrm{CoO}_2$ hydrate and its unhydrated analog. *Phys. Rev. B*, 68:214516, 2003.

[88] Q. Huang, J. W. Lynn, B. H. Toby, M. L. Foo, and R. J. Cava. Characterization of the structural transition in $\mathrm{Na}_{0.75}\mathrm{CoO}_2$. *J. Phys.: Condens. Matter*, 17:1831, 2005.

[89] Q. Huang, B. Khaykovich, F. C. Chou, J. H. Cho, J. W. Lynn, and Y. S. Lee. Structural transition in $\mathrm{Na}_x\mathrm{CoO}_2$ with x near 0.75 due to Na rearrangement. cond-mat/0405677, 2004.

[90] T. Motohashi, E. Naujalis, R. Ueda, K. Isawa, M. Karppinen, and H. Yamauchi. Simultaneously enhanced thermoelectric power and reduced resistivity of $\mathrm{Na}_x\mathrm{Co}_2\mathrm{O}_4$ by controlling Na nonstoichiometry. *App. Phys. Lett.*, 79:1480, 2001.

[91] A. Venimadhav, A. Soukiassian, D. A. Tenne, Q. Li, X. X. Xi, D. G. Schlom, R. Arroyave, Z. K. Liu, H. P. Sun, X. Pan, M. Lee, and N. P. Ong. Structural and transport properties of epitaxial $\mathrm{Na}_x\mathrm{CoO}_2$ thin films. *App. Phys. Lett.*, 87:172104, 2005.

[92] J. Rodriguez-Carvajal. Recent advances in magnetic structure determination by neutron powder diffraction. *Physica B*, 192:55, 1993.

[93] C. A. Marianetti, G. Kotliar, and G. Ceder. The role of hybridization in $\mathrm{Na}_x\mathrm{CoO}_2$ and the effect of hydration. cond-mat/0312514, 2003.

[94] J. Wooldridge, D. McK. Paul, G. Balakrishnan, and M. R. Lees. Investigation of the spin density wave in $\mathrm{Na}_x\mathrm{CoO}_2$. *J. Phys.: Condens. Matter*, 17:707, 2005.

[95] http://www-llb.cea.fr/fullweb/winplotr/winplotr.htm.

[96] J. L. Gavilano, D. Rau, B. Pedrini, J. Hinderer, H. R. Ott, S. M. Kazakov, and J. Karpinski. Unconventional charge ordering in $\mathrm{Na}_{0.70}\mathrm{CoO}_2$ below 300 K. *Phys. Rev. B*, 69:100404, 2004.

[97] P. Zhang, R. B. Capaz, M. L. Cohen, and S. G. Louie. Theory of sodium ordering in $\mathrm{Na}_x\mathrm{CoO}_2$. cond-mat/0502072, 2005.

[98] R. Roger, D. J. P. Morris, D. A. Tennant, M. J. Gutmann, J. P. Goff, D. Prabhakaran, N. Shannon, B. lake, A. T. Boothroyd, R. Coldea, and P. Deen. On the ordering of Na^+ ions in $\mathrm{Na}_x\mathrm{CoO}_2$. cond-mat/0510468, 2005.

[99] H. W. Zandbergen, M. Foo, Q. Xu, V. Kumar, and R. J. Cava. Sodium ion ordering in $\mathrm{Na}_x\mathrm{CoO}_2$: Electron diffraction study. *Phys. Rev. B*, 70:024101, 2004.

[100] J. Geck, M. v. Zimmermann, H. Berger, S. V. Borisenko, H. Eschrig, K. Koepernik, M. Knupfer, and B. Büchner. Stripe correlations in $\mathrm{Na}_{0.75}\mathrm{CoO}_2$. cond-mat/0511554, 2005.

[101] S. Lupi, M. Ortolani, L. Baldassarre, and P. Calvani. Optical conductivity and charge ordering in $\mathrm{Na}_x\mathrm{CoO}_2$. cond-mat/0501746, 2005.

[102] http://www.isis.rl.ac.uk/excitations/mslice/.

[103] J. M. Tranquada, G. Shirane, B. Keimer, S. Shamoto, and M. Sato. Neutron scattering study of magnetic excitations in $\mathrm{YBa_2Cu_3O_{6+x}}$. *Phys. Rev. B*, 40:4503, 1989.

[104] P. W. Anderson. An approximate quantum theory of the antiferromagnetic ground state. *Phys. Rev.*, 86:694, 1952.

[105] S. K. Burke, W. G. Stirling, K. R. A. Ziebeck, and J. G. Booth. Magnetic excitations in the incommensurate phases of chromium metal. *Phys. Rev. Lett.*, 51:494, 1983.

[106] S. Tomiyoshi, Y. Yamaguchi, M. Ohashi, E. R. Cowley, and G. Shirane. Magnetic excitations in the itinerant antiferromagnets $\mathrm{Mn_3Si}$ and Fe-doped $\mathrm{Mn_3Si}$. *Phys. Rev. B*, 36:2181, 1987.

[107] H. G. Bohn, W. Zinn, B. Dorner, and A. Kollmar. Neutron scattering study of spin waves and exchange interactions in ferromagnetic EuS. *Phys. Rev. B*, 22:5447, 1980.

[108] H. A. Mook. Temperature dependence of the spin dynamics of EuO. *Phys. Rev. Lett.*, 46:508, 1981.

[109] N. R. Bernhoeft, G. G. Lonzarich, P. W. Mitchell, and D. McK. Paul. Magnetic excitations in $\mathrm{Ni_3Al}$ at low energies and long wavelengths. *Phys. Rev. B*, 28:422, 1983.

[110] H. A. Mook. Neutron scattering studies of the high temperature spin dynamics of ferromagnetic materials. *J. Magn. & Magn. Mater.*, 31-34:305, 1983.

[111] N. L. Wang, Dong Wu, G. Li, X. H. Chen, C. H. Wang, and X. G. Luo. Infrared spectroscopy of the charge ordering transition of $\mathrm{Na_{0.5}CoO_2}$. *Phys. Rev. Lett.*, 93:147403, 2004.

[112] M. L. Foo, T. Klimczuk, and R. J. Cava. Hydration phase diagram for sodium cobalt oxide $\mathrm{Na}_{0.3}\mathrm{CoO}_2 \cdot y\mathrm{H}_2\mathrm{O}$. *Mater. Res. Bull.*, 40:665, 2005.

[113] Y. C. Kim, J. R. Thompson, D. K. Christen, Y. R. Sun, M. Paranthaman, and E. D. Specht. Surface barriers, irreversibility line, and pancake vortices in an aligned $\mathrm{HgBa}_2\mathrm{Ca}_2\mathrm{Cu}_3\mathrm{O}_{8+\delta}$ superconductor. *Phys. Rev. B*, 52:4438, 1995.

[114] M. M. Maská, M. Mierzejewski, B. Andrzejewski, M. L. Foo, R. J. Cava, and T. Klimczuk. Possible singlet-to-triplet pairing transition in $\mathrm{Na}_x\mathrm{CoO}_2 \cdot y\mathrm{H}_2\mathrm{O}$. *Phys. Rev. B*, 70:144516, 2004.

[115] H. Sakurai, K. Takada, T. Sasaki, and E. Takayama-Muromachi. Phase diagram of superconducting $\mathrm{Na}_x\mathrm{CoO}_2 \cdot y\mathrm{H}_2\mathrm{O}$. *J. Phys. Soc. Jpn.*, 74:2909, 2005.

[116] A. Kanigel, A. Keren, L. Patlagan, K. B. Chashka, P. King, and A. Amato. Muon spin relaxation measurements of $\mathrm{Na}_x\mathrm{CoO}_2 \cdot y\mathrm{H}_2\mathrm{O}$. *Phys. Rev. Lett.*, 92:257007, 2004.

[117] http://www.ncnr.nist.gov/programs/crystallography/software/expgui/.

[118] M. Kato, C. Michioka, T. Waki, Y. Itoh, K. Yoshimura, K. Ishida, H. Sakurai, E. Takayama-Muromachi, K. Takada, and T. Sasaki. Possible spin triplet superconductivity in $\mathrm{Na}_x\mathrm{CoO}_2 \cdot y\ \mathrm{H}_2\mathrm{O}$ - $^{59}\mathrm{Co}\ \mathrm{NMR}$ studies. *J. Phys.: Condens. Matt.*, 18:669, 2006.

[119] Q. H. Wang, D. H. Lee, and P. A. Lee. Doped t-J model on a triangular lattice: Possible application to $\mathrm{Na}_x\mathrm{CoO}_2 \cdot y\mathrm{H}_2\mathrm{O}$ and $\mathrm{Na}_{1-x}\mathrm{TiO}_2$. *Phys. Rev. B*, 69:092504, 2004.

[120] W. Higemoto, K. Ohishi, A. Koda, S. R. Saha, R. Kadono, K. Ishida, K. Takada, H. Sakurai, E. Takayama-Muromachi, and T. Sasaki. Possi-

ble unconventional superconductivity in $\mathrm{Na}_x\mathrm{CoO}_2 \cdot y\mathrm{H}_2\mathrm{O}$ probed by muon spin rotation and relaxation. *Phys. Rev. B*, 70:134508, 2004.

[121] K. Takada, K. Fukuda, M. Osada, I. Nakai, F. Izumi, R. A. Dilanian, K. Kato, M. Takata, H. Sakurai, E. Takayama-Muromachi, and T. Sasaki. Chemical composition and crystal structure of superconducting sodium cobalt oxide bilayer-hydrate. *J. Mater. Chem.*, 14:1448, 2004.

[122] D. Prabhakaran, A. T. Boothroyd, R. Coldea, and N. R. Charnley. Crystal growth of $\mathrm{Na}_x\mathrm{CoO}_2$ under different atmospheres. *J. Crys. Grow.*, 271:74, 2004.

[123] T. Holstein and H. Primakoff. Field dependence of the intrinsic domain magnetization of a ferromagnet. *Phys. Rev.*, 58:1098, 1940.